

A Measurement of Λ -Hyperon Spin Polarization in Au+Au Collisions at $\sqrt{s_{\text{NN}}}=3$ GeV with STAR

Dissertation

Presented in Partial Fulfillment of the Requirements for the
Degree Doctor of Philosophy in the Graduate School of The
Ohio State University

Joseph Richard Adams, B.S. & M.S.

Graduate Program in Physics
2021

Dissertation Committee

Dr. Michael Lisa, ADVISOR

Dr. Thomas Humanic

Dr. Michael Poirier

Dr. Ulrich Heinz

©
Copyright by Joseph R. Adams
2021

Abstract

Non-central collisions of relativistic atomic nuclei contain enormous angular momentum, $|\vec{J}| \sim \mathcal{O}(10^0 - 10^2 \frac{\text{TeV} \cdot \text{fm}}{c} \approx 10^3 - 10^5 \hbar)$ in the collision energy range spanned by the capabilities of the Relativistic Heavy Ion Collider (RHIC) at Brookhaven National Lab (BNL). The energy densities that exist in the collision interaction region are sufficient to deconfine constituent quarks from their bound nucleon states and thereby facilitate the short-lived ($\mathcal{O}(1\text{fm}/c)$) formation of the so-called Quark-Gluon Plasma (QGP), to which some of the net \vec{J} is transferred. The Solenoid Tracker At RHIC (STAR) is a set of detectors working in unison to reconstruct collision information, and is an indispensable tool used to study the QGP. I present here work surrounding \vec{J} , ranging from detector construction for STAR in order to accurately measure \hat{J} , experimental analysis of phenomena driven by \vec{J} using the STAR detector, and theoretical calculations involving the direction of \vec{J} affected by event-by-event fluctuations.

The “Event-Plane Detector” (EPD), after years of prototyping and design, was largely constructed at Ohio State University in 2017-2018 and officially replaced its predecessor, the Beam Beam Counter (BBC), at STAR. While similar detectors have been constructed, including the BBC, unique challenges were faced in the construction of the EPD. Due to many factors, including careful construction, the EPD’s performance was and remains phenomenal, providing experimentalists in the STAR collaboration with far-improved resolution on \hat{J} . The use of the EPD was essential for drastically reducing the statistical uncertainties on a number of analyses, including the

spin alignment of Λ hyperons with \hat{J} , \bar{P}_Λ .

In this thesis is detailed the process of extracting the \vec{J} -driven \bar{P}_Λ at the relatively low center-of-momentum nucleon-nucleon collision energy of $\sqrt{s_{\text{NN}}} = 3$ GeV. In order to achieve such a low $\sqrt{s_{\text{NN}}}$, the lowest yet achieved by RHIC, a “beam” of Au ions was made to hit a fixed Au foil target instead of two oppositely moving ion beams colliding; however, this fixed-target setup introduced numerous nuanced complications in order to extract \bar{P}_Λ . A new experimental method to measure \bar{P}_Λ is introduced in this work to deal with such complicating details. I present here the observation of the largest yet-observed \bar{P}_Λ at the lowest $\sqrt{s_{\text{NN}}}$ yet studied, as well as its dependences on event and Λ -hyperon kinematic variables.

An inconclusive search for the magnetic field sustained in the QGP, $|\vec{B}_{\text{QGP}}|$, is also presented here. While \vec{J} drives \bar{P}_Λ as well as that of its anti-particle the $\bar{\Lambda}$ hyperons, $\bar{P}_{\bar{\Lambda}}$, \vec{B}_{QGP} drives an enhancement of $\bar{P}_{\bar{\Lambda}}$ and a suppression of \bar{P}_Λ , leading to $\bar{P}_{\bar{\Lambda}} - \bar{P}_\Lambda$ splitting. This splitting has been observed in previous studies across a wide range of $\sqrt{s_{\text{NN}}}$, but without sufficient statistical significance. A high-statistics data set at $\sqrt{s_{\text{NN}}} = 27$ GeV was performed by RHIC and collected by STAR which served as a promising tool to see a statistically significant splitting. The effort to measure the splitting at $\sqrt{s_{\text{NN}}} = 27$ GeV is briefly described in this thesis, but ultimately numerous complicated problems with the collider facility and the STAR detector presented nuanced dependences of the splitting; sufficient confidence could not be gained that unaccounted-for systematic effects would not be present.

Also studied in this thesis were the effects of event-by-event nucleon-

position fluctuations on the orientation of \hat{J} . Theoretical models of heavy-ion collisions were used to describe the positions of nucleons at the momentum of impact, as well as the time evolution of the system. Unsurprisingly, the directions of angular momentum of the nucleons (and deconfined quarks) that participated in the collision, \hat{J}_{part} , and that of the “spectator” nucleons, \hat{J}_{spec} , fluctuate on an event-by-event basis due to the randomness inherent in the system. Theoretical calculations of \overline{P}_{Λ} correlate the Λ -hyperon spin with the angular momentum direction of the system, \hat{J}_{syst} , and the function form of \overline{P}_{Λ} used to extract the signal experimentally uses the measurable \hat{J}_{spec} as an approximation of \hat{J}_{syst} ; however, we discover an additional decorrelation between \vec{J}_{spec} and \vec{J}_{part} driven by conservation of angular momentum. More importantly, we find a much more significant decorrelation between \vec{J}_{spec} and \vec{J}_{part} when looking at the more restricted region of particles used for measuring \overline{P}_{Λ} , driven by random fluctuations. We also find, importantly, that this decorrelation becomes larger with increasing $\sqrt{s_{\text{NN}}}$ and therefore serves as a crucial correction to apply to the observable \overline{P}_{Λ} .

This dissertation is dedicated to Richard Mattson and David Adams.

Acknowledgements

Midway through my first physics class I happily dropped my aspirations for my newfound love of math and science. While the journey so far has been incredibly rewarding, there is not a doubt in my mind I would not have made it this far without the important people in my life.

At times the ground beneath my feet felt like it would give; without the stable and encouraging world built by my Grandparents Dave and Karen, Bob and Chuckie, my parents Bob and Nancy, my brothers Brian and Kevin, and my sisters-in-law Andrea and Ali, I would not have been able to do push through the hardest parts.

Many times I was convinced of my complete ineptitude; I felt unqualified to even be a graduate student, let alone one who leads analyses. Had Mike and Isaac not believed wholeheartedly in my capabilities, I am convinced I would not have finished this program.

At times I felt detached and alone; without my close friends in Columbus, BC, Cristiana, and Montague; Bryan and Rebecca; Humberto, I would have been lost.

To each of you — thank you.

VITA

January, 1992..... Born
Munster, IN
May, 2015..... B.S. Physics, University of Illinois
Chicago, IL
August, 2017..... M.S. Physics, Ohio State University
Columbus, OH

Publications

1. “Azimuthal anisotropy measurements of strange and multistrange hadrons in U+U collisions at $\sqrt{s_{NN}}=193$ GeV at the BNL Relativistic Heavy Ion Collider”
Phys. Rev. C 103 (2021) 64907
2. “Longitudinal double-spin asymmetry for inclusive jet and dijet production in polarized proton collisions at $\sqrt{s} = 200$ GeV”
Phys. Rev. D 103 (2021) 0
3. “Methods for a blind analysis of isobar data collected by the STAR collaboration”

NST 32 (2021) 48

4. “Global polarization of Xi and Omega hyperons in Au+Au collisions at $\sqrt{s_{NN}} = 200$ GeV”
Phys. Rev. Lett. 126 (2022) 162301
5. “Measurement of transverse single-spin asymmetries of π^0 and electromagnetic jets at forward rapidity in 200 and 500 GeV transversely polarized proton-proton collisions”
Phys. Rev. D 103 (2021) 92009
6. “Comparison of transverse single-spin asymmetries for forward π^0 production in polarized pp, pAl and pAu collisions at nucleon pair c.m. energy $\sqrt{s_{NN}} = 200$ GeV”
Phys. Rev. D 103 (2021) 72005
7. “Measurements of W and Z/ γ^* cross sections and cross-section ratios in p+p collisions at RHIC”
Phys. Rev. D 103 (2021) 12001
8. “Measurements of Dihadron Correlations Relative to the Event Plane in Au+Au Collisions at $\sqrt{s_{NN}} = 200$ GeV”
Chinese Phys. C 45 (2021) 44002
9. “Nonmonotonic Energy Dependence of Net-Proton Number Fluctuations”
Phys. Rev. Lett. 126 (2021) 92301
10. “Flow and interferometry results from Au+Au collisions at $\sqrt{s_{NN}} =$

- 4.5 GeV”
 Phys. Rev. C 103 (2021) 34908
11. “Beam-energy dependence of the directed flow of deuterons in Au+Au collisions”
 Phys. Rev. C 102 (2020) 44906
 12. “Measurement of inclusive J/psi polarization in p+p collisions at $\sqrt{s} = 200$ GeV by the STAR experiment”
 Phys. Rev. D 102 (2020) 92009
 13. “Investigation of the linear and mode-coupled flow harmonics in Au+Au collisions at $\sqrt{s_{NN}} = 200$ GeV”
 Phys. Lett. B 809 (2020) 135728
 14. “Measurement of inclusive charged-particle jet production in Au+Au collisions at $\sqrt{s_{NN}} = 200$ GeV”
 Phys. Rev. C 102 (2020) 54913
 15. “Measurement of the central exclusive production of charged particle pairs in proton-proton collisions at $\sqrt{s} = 200$ GeV with the STAR detector at RHIC”
 JHEP 7 (2020) 178
 16. “Results on Total and Elastic Cross Sections in Proton-Proton Collisions at $\sqrt{s}=200$ GeV”
 Phys. Lett. B 808 (2020) 135663

17. “Measurement of Groomed Jet Substructure Observables in pp Collisions at $\sqrt{s}=200$ GeV with STAR”
Phys. Lett. B 811 (2020) 135846
18. “Beam energy dependence of net-Lambda fluctuations measured by the STAR experiment at the BNL Relativistic Heavy Ion Collider”
Phys. Rev. C 102 (2020) 24903
19. “The STAR Event Plane Detector”
Nucl. Instrum. Meth. A 968 (2020) 163970
20. “Underlying event measurements in p+p collisions at $\sqrt{s}=200$ GeV at RHIC”
Phys. Rev. D 101 (2020) 52004
21. “Measurement of D0-meson + hadron two-dimensional angular correlations in Au+Au collisions at $\sqrt{s_{NN}}=200$ GeV”
Phys. Rev. C 102 (2020) 14905
22. “First measurement of Lambda c baryon production in Au+Au collisions at $\sqrt{s_{NN}} = 200$ GeV”
Phys. Rev. Lett. 124 (2020) 172301
23. “Bulk Properties of the System Formed in Au+Au Collisions at $\sqrt{s_{NN}} = 14.5$ GeV”
Phys. Rev. C 101 (2020) 24905
24. “Beam-energy dependence of identified two-particle angular correlations in Au+Au collisions at RHIC”
Phys. Rev. C 101 (2020) 14916

25. “Measurement of away-side broadening with self-subtraction of flow in Au+Au collisions at $\sqrt{s_{NN}}=200$ GeV”
Chinese Phys. C 44 (2020) 104001
26. “Strange hadron production in Au+Au collisions at $\sqrt{s_{NN}} = 7.7, 11.5, 19.6, 27,$ and 39 GeV”
Phys. Rev. C 102 (2020) 34909
27. “Charge-dependent pair correlations relative to a third particle in p+Au and d+Au collisions at RHIC”
Phys. Lett. B 798 (2019) 134975
28. “Longitudinal double-spin asymmetry for inclusive jet and dijet production in pp collisions at $\sqrt{s}=510$ GeV”
Phys. Rev. D 100 (2019) 52005
29. “Measurement of inclusive J/ψ suppression in Au+Au collisions at $\sqrt{s_{NN}} = 200$ GeV through the dimuon channel at STAR”
Phys. Lett. B 797 (2019) 134917
30. “Polarization of Lambda (anti-Lambda) hyperons along the beam direction in Au+Au collisions at $\sqrt{s_{NN}} = 200$ GeV”
Phys. Rev. Lett. 123 (2019) 132301
31. “Measurements of the transverse-momentum-dependent cross sections of J/ψ production at mid-rapidity in proton+proton collisions at $\sqrt{s} = 510$ and 500 GeV with the STAR detector”
Phys. Rev. D 100 (2019) 52009

- 32. “First observation of the directed flow of D0 and D0bar in Au+Au collisions at $\sqrt{s_{NN}} = 200$ GeV”
Phys. Rev. Lett. 123 (2019) 162301
- 33. “Observation of excess J/psi yield at very low transverse momenta in Au+Au collisions at $\sqrt{s_{NN}} = 200$ GeV and U+U collisions at $\sqrt{s_{NN}} = 193$ GeV”
Phys. Rev. Lett. 123 (2019) 132302
- 34. “Precise measurement of the mass difference and the binding energy of hypertriton and antihypertriton”
Nature Physics 16 (2020) 409
- 35. “Beam energy dependence of (anti-)deuteron production in Au+Au collisions at RHIC”
Phys. Rev. C 99 (2019) 64905
- 36. “Collision energy dependence of second-order off-diagonal and diagonal cumulants of net-charge, net-proton and net-kaon multiplicity distributions in Au+Au collisions”
Phys. Rev. C 100 (2019) 14902
- 37. “Azimuthal harmonics in small and large collision systems at RHIC top energies”
Phys. Rev. Lett. 122 (2019) 172301
- 38. “Collision Energy Dependence of pT Correlations in Au+Au Collisions at RHIC”
Phys. Rev. C 99 (2019) 44918

39. “Centrality and transverse momentum dependence of D0-meson production at mid-rapidity in Au+Au collisions at $\sqrt{s_{NN}} = 200$ GeV”
Phys. Rev. C 99 (2019) 34908
40. “Measurement of the longitudinal spin asymmetries for weak boson production in proton-proton collisions at $\sqrt{s} = 510$ GeV”
Phys. Rev. D 99 (2019) 51102
41. “Erratum: Observation of D0 meson nuclear modifications in Au+Au collisions at $\sqrt{s_{NN}} = 200$ GeV”
Phys. Rev. Lett. 121 (2018) 229901
42. “Transverse spin transfer to Lambda and anti-Lambda hyperons in polarized proton-proton collisions at $\sqrt{s}=200$ GeV”
Phys. Rev. D 98 (2018) 91103
43. “Improved measurement of the longitudinal spin transfer to Lambda and Anti-Lambda hyperons in polarized proton-proton collisions at $\sqrt{s} = 200$ GeV”
Phys. Rev. D 98 (2018) 112009
44. “The Proton-Omega correlation function in Au+Au collisions at $\sqrt{s_{NN}}=200$ GeV”
Phys. Lett. B 790 (2019) 490
45. “Low pT e+e- Pair Production in Au+Au Collisions at $\sqrt{s_{NN}} = 200$ GeV and U+U Collisions at $\sqrt{s_{NN}} = 193$ GeV at STAR”
Phys. Rev. Lett. 121 (2018) 132301

46. “Longitudinal Double-Spin Asymmetries for Dijet Production at Intermediate Pseudorapidity in Polarized pp Collisions at $\sqrt{s} = 200$ GeV”
Phys. Rev. D 98 (2018) 32011
47. “Longitudinal double-spin asymmetries for π^0 s in the forward direction for 510 GeV polarized pp collisions”
Phys. Rev. D 98 (2018) 32013
48. “Global polarization of Lambda hyperons in Au+Au collisions at $\sqrt{s_{NN}}=200$ GeV”
Phys. Rev. C 98 (2018) 14910
49. “J/psi production cross section and its dependence on charged-particle multiplicity in p+p collisions at $\sqrt{s}=200$ GeV”
Phys. Lett. B 786 (2018) 87
50. “MWPC prototyping and performance test for the STAR inner TPC upgrade”
Nucl. Instrum. Meth. A 896 (2018) 90
51. “Beam energy dependence of rapidity-even dipolar flow in Au+Au collisions”
Phys. Lett. B 784 (2018) 26
52. “Correlation Measurements Between Flow Harmonics in Au+Au Collisions at RHIC”
Phys. Lett. B 783 (2018) 459
53. “Azimuthal anisotropy in Cu+Au collisions at $s_{NN} = 200$ GeV”
Phys. Rev. C 98 (2018) 14915

- 54. “Transverse spin-dependent azimuthal correlations of charged pion pairs measured in $p^\uparrow + p$ collisions at $\sqrt{s} = 500$ GeV”
Phys. Lett. B 780 (2018) 332
- 55. “Measurement of hyper triton lifetime in Au+Au collisions at the Relativistic Heavy-Ion Collider”
Phys. Rev. C 97 (2018) 54909
- 56. “The STAR MAPS-based PiXeL detector”
Nucl. Instrum. Meth. A 907 (2018) 60
- 57. “The STAR MAPS-based PiXeL detector”
Nucl. Instrum. Meth. A 907 (2018) 60
- 58. “Collision Energy Dependence of Moments of Net-Kaon Multiplicity Distributions at RHIC”
Phys. Lett. B 785 (2018) 551
- 59. “Azimuthal transverse single-spin asymmetries of inclusive jets and charged pions within jets from polarized-proton collisions at $\sqrt{s} = 500$ GeV”
Phys. Rev. D 97 (2018) 32004
- 60. “Beam-Energy Dependence of Directed Flow of Lambda, Anti-Lambda, K plus, K minus, K0 short and phi in Au+Au Collisions”
Phys. Rev. Lett. 120 (2018) 62301
- 61. “Beam Energy Dependence of Jet-Quenching Effects in Au+Au Collisions at $\sqrt{s_{NN}} = 7.7, 11.5, 14.5, 19.6, 27, 39,$ and 62.4 GeV”
Phys. Rev. Lett. 121 (2018) 32301

Fields of study

Physics

Table of Contents

Abstract	i
Acknowledgements	v
VITA	vi
Table of Contents	xvi
List of Figures	xx
1 Introduction	1
1.1 Heavy-ion collisions	1
The basics	1
Geometry and flow coefficients	5
Commonly used variables	7
1.2 Experimental setup	10
The Relativistic Heavy-Ion Collider	10
The Solenoid Tracker at RHIC	13
1.3 Outline	21
2 Construction of the STAR Event-Plane Detector	24
2.1 Fiber bundles	27
2.2 Epoxy	29
2.3 Scintillator slab to supersector	30
2.4 Testing	38

3	Global Λ polarization in Au+Au collisions at $\sqrt{s_{\text{NN}}} = 3$ GeV	43
3.1	Introduction	43
3.2	Event and Λ selection	46
	Event selection	46
	Λ selection	48
3.3	Event-plane determination	51
	Measuring Ψ_1 with the EPD	51
	\vec{B}_{STAR} -driven $\Psi_{1,\text{EPD}}$ rotation	55
3.4	Polarization observable	61
	The restricted invariant-mass method	61
	The generalized invariant-mass method	65
3.5	Results	74
3.6	Summary	77
4	Initial-state fluctuations and angular momentum in heavy-ion collisions	79
4.1	Introduction	79
4.2	Models	81
4.3	Correlation results	90
	\hat{J}_{part} correlations with \hat{J}_{syst} and \hat{J}_{spec}	90
	\hat{J}_{part} correlations with geometry	96
4.4	Summary	99
5	Summary and future work	101
A	Details on event and Λ selection	105
A.1	Details on event selection	105

A.2	Details on Λ selection	110
B	Determination of subevents	117
B.1	EPD	117
B.2	TPC	123
C	Flattening of the event-plane distributions	125
D	Position of EPD tile hit	134
E	Efficiency Corrections	139
E.1	Trigger Efficiency	139
E.2	Λ -measurement efficiency	140
E.3	Acceptance efficiency	141
F	Systematic uncertainties	147
F.1	Overview	147
F.2	Checks for systematic mistakes	148
F.3	Contributions to the total systematic uncertainty	152
G	Comparing \overline{P}_Λ measurements with theory	154
G.1	Extracting centrality from impact parameter	154
G.2	Extracting exclusive y ranges from inclusive y ranges	161
H	Model-based determinations of centrality	162
H.1	Monte-Carlo Glauber	162
H.2	AMPT	167
I	Angular-momentum conservation in AMPT	171

J	A search for the magnetic field in the QGP	176
J.1	Introduction	176
J.2	Ψ_1 flatness and $\overline{P}_\Lambda, \overline{P}_{\overline{\Lambda}}$ variations	177
J.3	Summary, and search at $\sqrt{s_{\text{NN}}} = 19$ GeV	194
	Bibliography	196

List of Figures

Figure 1	The standard model of elementary particle physics. Here is shown the six quarks and their force carrier, the gluon.	2
Figure 2	The QCD phase diagram, with a degree of speculation on the features. Experimentally testing the features is achiev- able through relativistic heavy-ion collisions. Figure from [10].	4
Figure 3	A typical heavy-ion collision, viewed in the transverse plane. The reaction plane is spanned by the impact parameter and the beam direction. Figure from [64].	6
Figure 4	Normalized multiplicity distribution of negatively charged hadrons h^- with transverse momentum $p_T > 100$ MeV/ c and pseudorapidity $ \eta < 0.5$ in Au+Au collisions at $\sqrt{s_{NN}} =$ 130 GeV as measured by the STAR collaboration. σ is the cross section, measured in millibarnes. The shaded region is the multiplicity distribution for the 0-5% most central colli- sions with the impact parameter determined by the ZDC. The solid curve is a simulation (using the HIJING model). Figure from [9].	8
Figure 5	A small section of the nearly circular, roughly 2.5 mile- long collider rings. These rings must be kept a sufficiently low internal temperature for the magnets to remain superconduct- ing. Figure from [1].	11

Figure 6	An aerial view of the RHIC collider and accelerators feeding low-energy ions into RHIC. We see the yellow and blue RHIC rings crossing at each of the six intersection points. Figure from [1].	12
Figure 7	One side of the STAR detector and the surrounding structure. One can make out the small beam passing into the center, which carries relativistic nuclei. The small, black circle surrounding the beampipe's entry point is the Beam Beam Counter (BBC); the larger cyan circle on which the BBC is mounted is the Event Plane Detector (EPD). Many remaining detectors are obstructed. An image of the STAR detector is viewable in 3D in Fig. 8.	14
Figure 8	A crossview image of the STAR detector. To achieve perception of 3 spatial dimensions one must cross their eyes until the two images overlap and then adjust the plane of focus as if the object is behind the screen, until the image becomes clear. Achieving the perception may take some practice. . . .	15
Figure 9	A rough schematic of the TPC; the charged membrane lies in the center and the large, empty chamber typically filled with gas. The beam pipe passes through the central axis of the TPC's cylindrical form.	16

Figure 10	The STAR TPC's Front-End Electronics (FEEs) are visible when the STAR magnet is pulled back. We see scaffolding erected for maintenance. This is a crossview image; to achieve perception of 3 spatial dimensions one must cross their eyes until the two images overlap and then adjust the plane of focus as if the object is behind the screen, until the image becomes clear. Achieving the perception may take some practice.	17
Figure 11	The energy loss in the TPC as a function of particle charge and momentum. At the low energy shown of $\sqrt{s_{NN}} = 3$ GeV, one can easily separate bands associated with different particles. At higher energies, the bands merge at higher $ \vec{p} $ and further information is required from the BTOF detector to discern particle species.	18
Figure 12	The basic setup of the TOF detector. Charged particles ionize gas molecules between stacked plates of glass which leads to small but measurable changes in potential that are read by pick-up electrodes. Figure from [28].	19
Figure 13	A rough schematic of the EPD. We can see the $31 \times 12 = 372$ tiles belonging to one "wheel" of the EPD. Photons generated by charged particles passing through the tiles travel down fiber-optic cables to a series of electronics that digitize the signal. Figure from [8].	21

Figure 14	A rough schematic of the STAR BBC. The width is roughly 2 m. The black numbers indicate the tile number while the blue numbers indicate the PMT number; it is apparent that many large tiles are paired together and provide very little information about hit positions. Previous analyses using the BBC restricted themselves to the inner tiles only.	25
Figure 15	A single EPD supersector; twelve supersectors make a wheel and two wheels make an EPD. The unit of length is cm. Figure from [56].	25
Figure 16	$R_{\text{EP}}^{(1)}$ for the EPD is drastically improved over its predecessor, the BBC.	27
Figure 17	A finished fiber bundle. The green WLS fibers are all cut to different length. The ends of the fibers at the connector are polished painstakingly. Partial lengths of the fibers are painted with reflective paint, as are the tips.	28
Figure 18	The tip of a WLS fiber through various stages in polishing. The improvements are dramatic. Figure from [56]. . . .	29
Figure 19	Removing the air bubbles from optical epoxy with a small vacuum chamber.	30
Figure 20	A rectangular scintillator slab of 1.2 cm-thick Eljen EJ-200.	31
Figure 21	A supersector in the process of its first milling stage. The outline of the supersector has been cut out and is being prepared for milling tile-separation grooves at half depth. . . .	32

Figure 22	The supersector edge is taped after the first step of milling so that the epoxy filling the grooves does not pour out of the sides. Here is seen tape peeled back after the epoxy has dried. Figure from [8].	33
Figure 23	A supersector after the second stage of milling; we see the epoxy binding the tiles together while the second half of the tile-separation grooves were milled. We also see the sigma grooves for fiber optics. Figure from [8].	34
Figure 24	After cleaning the supersectors following the final milling step, wide, ultra-low-friction Teflon PTFE tape was used on the face of each tile to help avoid optical-epoxy spillover. Carefully guiding a knife along the edge of the sigma grooves, excess tape was removed.	34
Figure 25	Here the fiber is completely inserted as a worker carefully applies enough optical epoxy to top off the groove. The central groove through which all fibers pass is visible in the bottom right corner. Figure from [8].	35
Figure 26	A supersector tip after polishing the sides. One can clearly see the embedded wavelength shifting fiber as well as the white walls of epoxy, optically isolating the tiles completely. Figure from [8].	36
Figure 27	A flashlight held to a tile in the dark; no light apparently travels to neighboring tiles.	36
Figure 28	Wrapping the supersectors in Tyvek fabric cut to shape.	37
Figure 29	A fully completed supersector.	37

Figure 30	A cartoon demonstrating the cosmic test-stand setup. Four supersectors were stacked vertically. The top and bottom supersectors functioned as trigger detectors while the inner two supersectors were studied for quality of MIP peaks. After measuring SiPM signals for over a day, signals for a given tile number were examined when signals from the same tile numbers of the trigger detectors crossed a threshold.	39
Figure 31	Using the offline trigger selection, it is possible to iso- late ADC distributions of vertical cosmic rays from those of all incident cosmic rays as shown in Fig. 30.	40
Figure 32	The Sr source used, and wrapped in thin Pb sheets. A small opening of diameter 5 mm allows the radiation to travel nearly vertical.	41
Figure 33	The Sr source mounted indirectly to the x-y motors that can be programmed to follow a series of step-wait-step. .	41
Figure 34	The signal outputs from a handfull of EPD tiles as the Sr source covers a surface area. It is clear that each tile “lights up” when the source is directly underneath, and there is no apparent cross-talk. Figure from [8].	42
Figure 35	Here is shown the current above the background value when the laboratory lights are completely off and no Sr source is near. There is no apparent cross-talk between adjacent tiles. Figure from [8].	42

Figure 36	\bar{P}_Λ measured by the STAR collaboration in [7] across the BES range of $\sqrt{s_{\text{NN}}}$. Clearly, as $\sqrt{s_{\text{NN}}}$ decreases, \bar{P}_Λ increases. Earlier measurements at higher $\sqrt{s_{\text{NN}}}$ are shown, studied in [2], that are consistent with zero.	45
Figure 37	A slide from [48], demonstrating the Au target’s position.	47
Figure 38	$m_{\text{inv.}}$ distribution for Λ s found using the traditional method compared to that with those found using the KFParticle package.	50
Figure 39	The nMIP distribution of inner EPD rings along with the multiple Landau fits each corresponding to a different number of MIPs passing through the tile in an event. The data shown is taken at $\sqrt{s_{\text{NN}}} = 27$ GeV where multi-hit probability is large relative to that at $\sqrt{s_{\text{NN}}} = 3$ GeV. Image courtesy of Xiaoyu Liu.	52
Figure 40	The Ψ_1 correlation between the EPD and the first TPC reference subevent as a function of centrality.	54
Figure 41	The Ψ_1 correlation between the EPD and the second TPC reference subevent as a function of centrality.	54
Figure 42	The Ψ_1 correlation between the two TPC reference subevents as a function of centrality.	54
Figure 43	The $\Psi_{1,\text{EPD}}$ resolution as a function of centrality, using the correlations between each subevent pair (Figures 40, 41, and 42) using Eq. 9.	54
Figure 44	Azimuthal rotation of charged tracks due to \vec{B}_{STAR} as a function of p_z . Eq. 22 and Helix calculations agree.	58

Figure 45	Another way to quantify the rotational effects of \vec{B}_{STAR} on $\Psi_{1,\text{EPD}}$; although we might expect this to look similar to Fig. 47, the observed rotation is smaller. The dependence on TPC subevent is expected because here $R_{\text{EP}}^{(1)}$ effects come into play. TPC subevent 0 covers $-1 < \eta < -0.9$, subevent 1 covers $-0.9 < \eta < -0.8$, and so on.	60
Figure 46	$\Psi_{1,\text{TPC}} - \phi_{\text{EPDhit}}$ for 45-50% centrality. The distribution is fitted with a cosine of vertical offset $p0$, amplitude $p1$, and phase $p2$; the phase is due to the \vec{B}_{STAR} -induced azimuthal rotation.	60
Figure 47	The extracted phase shifts of cosine fits to $\Psi_{1,\text{TPC}} - \phi_{\text{EPDhit}}$ are plotted against collision centrality and TPC subevent (excuse the label; TPC subevent 0 covers $-1 < \eta < -0.9$, subevent 1 covers $-0.9 < \eta < -0.8$, and so on). The shift by π is included because there is no rapidity weighting; the TPC and EPD lie on opposite sides of mid-rapidity. We see here a dependence on TPC subevent, which indicates a problem.	61
Figure 48	Phase shifts of cosine fits to $\Psi_{1,\text{TPC}} - \phi_{\text{EPDhit}}$ across centrality, with the uncertainties displaying the range in values determined by different TPC subevents. In principle they should all agree, and they do up to around 50% centrality. . .	61

Figure 49 Here, we visually see the procedure known as the invariant-mass method. On the left panel, a second-degree polynomial fits the background (in green) and two summed Gaussian distributions fit the signal (in red). The ratios of these fits give $f^{\text{sig.}}(m_{\text{inv.}})$ (in blue) and $f^{\text{bgd.}}(m_{\text{inv.}})$ (in black). On the right panel, we see those used to fit $\langle \sin(\Psi_1 - \phi_p^*) \rangle$ with Eq. 25. It is apparent here that the fit function is not appropriate for the data, and that this method is invalid in this situation. 63

Figure 50 Polarization as a function of rapidity using the standard (and in this case invalid) method; we see dramatic behavior such that the polarization increases strongly with y , and the statistical uncertainties are such that we would quote such a dependence with certainty. 64

Figure 51 Polarization as a function of p_T using the standard (and in this case invalid) method; we see dramatic behavior such that the polarization increases strongly with p_T before sharply dropping off, and the statistical uncertainties are such that we would quote such a dependence with certainty. 64

Figure 52 Polarization as a function of centrality using the standard (and in this case invalid) method; we see dramatic behavior such that the polarization increases strongly with centrality besides a sharp drop at 10-20% centrality, and the statistical uncertainties are such that we would quote such a dependence with certainty. 65

Figure 53 Here is an illustration of the simplified explanation of the observed peaking and dipping structure in $\langle \sin(\Psi_1 - \phi_p^*) \rangle (m_{\text{inv.}})$ that makes the “traditional” invariant-mass method invalid for this analysis. Because of inefficiencies in the STAR TPC, Λ decays with $0 < \phi_\Lambda - \phi_p^* < \pi$ $m_{\text{inv.}}$ distributions peaked more sharply around $m_{\Lambda, \text{PDG}}$ while those with $\pi < \phi_\Lambda - \phi_p^* < 2\pi$ are more broad. Alone this would not be problematic, but with the additional detector asymmetry present in fixed-target mode wherein we mostly measure Λ s with positive v_1 (because we measure mostly positive-rapidity tracks) (simplified with $\phi_\Lambda = \Psi_1$), there is a correlation between Ψ_1 and ϕ_p^* that depends on $\phi_\Lambda - \phi_p^*$ and has absolutely nothing to do with any sort of physical polarization. 68

Figure 54 Here is an illustration of the daughter tracks crossing in the transverse plane. This broken symmetry comes from the STAR magnetic field, which is along the beam axis ($\vec{B}_{\text{STAR}} = -|\vec{B}_{\text{STAR}}|\hat{z}$); the $p - \pi$ tracks from Λ s with $0 < \phi_\Lambda - \phi_p^* < \pi$ cross each other in the transverse plane while $p - \pi$ tracks from Λ s with $\pi < \phi_\Lambda - \phi_p^* < 2\pi$ immediately diverge in the transverse plane after the Λ decay. 69

Figure 55	We impose a non-zero $v_{1,\Lambda}$ on embedded Λ s, which have $v_1 = 0$ and $\overline{P}_\Lambda = 0$ by default, by preferentially selecting those aligned with Ψ_1 . We simply roughly replicate the $v_{1,\Lambda}(y)$ observed with this data set. From this change alone, we measure a significant $\overline{P}_\Lambda > 0$ using the “traditional” invariant-mass method.	69
Figure 56	Here is shown the $m_{\text{inv.}}$ distribution as a function of $\phi_\Lambda - \phi_p^*$, and it is clear that the width of the distribution depends significantly on $\phi_\Lambda - \phi_p^*$	71
Figure 57	Here is shown the same procedure used in the “traditional” invariant-mass method except we constrain ourselves to regions of $\phi_\Lambda - \phi_p^*$. We see here that $\langle \sin(\Psi_1 - \phi_p^*) \rangle (m_{\text{inv.}})$ clearly follows the form expected, according to Eq. 25.	71
Figure 58	Here is shown the extracted $\langle \sin(\Psi_1 - \phi_p^*) \rangle^{\text{sig.}}$ with respect to $\phi_\Lambda - \phi_p^*$. We fit with a sine because of the correlation between v_1 and Ψ_1 ; the amplitude corresponds to the strength of v_1 and the vertical shift is the true, vorticity-driven polarization, $\overline{P}_H^{\text{true}}$	72
Figure 59	The true, vorticity-driven polarization extracted using the generalized invariant-mass method for negative and positive rapidity; this is fit with a horizontal line to extract the average value and statistical uncertainty.	73

Figure 60	Measured polarization vs. input polarization for embedded Λ s with induced $v_1(y)$; we see that the polarization is under-reported if we use the generalized invariant-mass method on negative- and positive-rapidity Λ s together (“1 y bins”), but as long as we treat these two cases separately and average the results (“S y bins”, meaning symmetric bins in rapidity) then the polarization is accurately measured. More finely separating these rapidity bins neither helps nor hurts.	73
Figure 61	Statistically significant \overline{P}_Λ at $\sqrt{s_{\text{NN}}} = 3$ GeV is measured and plotted alongside previous studies [3, 7, 5, 4] and model predictions [37, 59, 29, 24, 31].	75
Figure 62	\overline{P}_Λ at $\sqrt{s_{\text{NN}}} = 3$ GeV, plotted with respect to centrality and alongside theory predictions at this energy [29, 24, 33]. We observe significant monotonic dependence of \overline{P}_Λ on centrality.	76
Figure 63	\overline{P}_Λ at $\sqrt{s_{\text{NN}}} = 3$ GeV, plotted with respect to p_T and alongside AMPT predictions at this energy [29]. We observe no significant dependence of \overline{P}_Λ on p_T	76
Figure 64	\overline{P}_Λ at $\sqrt{s_{\text{NN}}} = 3$ GeV, plotted with respect to y and alongside AMPT predictions at this energy [29]. We observe no significant dependence of \overline{P}_Λ on y	77

Figure 65 The magnitudes of angular momenta of the system, the participants, and the spectators, and the fraction of $|\vec{J}_{\text{syst}}|$ carried by the participants and spectators, as a function of b at $\sqrt{s_{\text{NN}}} = 27$ GeV in the Monte-Carlo Glauber model. Above $b \gtrsim 1$ fm we see $|\vec{J}_{\text{spec}}|$ take a larger fraction of $|\vec{J}_{\text{syst}}|$ as b becomes larger, since the number of spectators continually increases as does their average distance from the center of mass. Below $b \lesssim 1$ fm, however, we see $|\vec{J}_{\text{spec}}|/|\vec{J}_{\text{syst}}|$ as well as $|\vec{J}_{\text{part}}|/|\vec{J}_{\text{syst}}|$ rapidly increase as b becomes smaller, even to the point of becoming larger than 1. This is due to the fact that $|\vec{J}_{\text{syst}}| \rightarrow 0$ as $b \rightarrow 0$ while $\langle |\vec{J}_{\text{part}}| \rangle$ and $\langle |\vec{J}_{\text{spec}}| \rangle$ remain finite at $b = 0$ due to the extreme likelihood of spectators still existing for these cases. 80

Figure 66 A $^{197}_{97}\text{Au}$ nucleus generated by random sampling of the appropriate distributions. The nucleon diameters are drawn as d_{\perp} (Eq. 28). From this picture we gain an intuitive sense of the level of nucleon position fluctuations. 83

Figure 67 Averaged over many $^{197}_{97}\text{Au}$ nuclei, we see that the density profile is quite smooth and spherical symmetry holds to a very good degree of approximation. 83

Figure 68	A $^{197}_{97}\text{Au} + ^{197}_{97}\text{Au}$ collision at $b = 8$ fm with nucleon diameters drawn as d (Eq. 28). In the upper panel, we see a three-dimensional cartoon where gray nucleons are spectators and the darkness of the red corresponds to the number of collisions a given participant nucleon undergoes. In the lower panel, we see a two-dimensional cartoon in the transverse ($x - y$) plane where participant nucleons are outlined in black. . . .	84
Figure 69	The nucleon density profile for collisions of $b = 8$ fm, averaged over many events; although a given collision's overlap region will be lumpy (Fig. 68), the overlap region is <i>on average</i> smooth.	84
Figure 70	The angular-momentum correlation between participants in the MCG model with respect to collision centrality as determined by b or multiplicity. There is clearly no difference between the two methods of centrality determination. . .	85
Figure 71	The distribution of impact parameter for all input events and input events that resulted in at least one nucleon-nucleon collision. Clearly the collision event yield above $b \approx 2R_0$ drops, but the drop is smooth due to nucleon position fluctuations. .	87

Figure 72 The MCG model is used to generate a handful of collisions at varying b . The z dimension is irrelevant in this model and the collisions are viewed in the transverse plane. Black outlines denote participant nucleons, and yellow dashed lines denote the elliptic fit to the collision overlap region. Each event is typical, in that $\hat{J}_{\text{spec}} \cdot \hat{J}_{\text{part}}|_b \approx \left\langle \hat{J}_{\text{spec}} \cdot \hat{J}_{\text{part}} \right\rangle|_b$ and $\Phi_2|_b \approx \langle \Phi_2 \rangle|_b$ 89

Figure 73 The correlation between \hat{J}_{syst} and \hat{J}_{part} . There is significant decorrelation for peripheral and central events, but good correlation for mid-central collisions. There is an enhanced correlation between \hat{J}_{syst} and \hat{J}_{part} which arises from conservation of angular momentum. In AMPT, spectators are defined with $|y| > 2$ 90

Figure 74 The correlation between \hat{J}_{part} and \hat{J}_{spec} becomes smaller as we further constrain the size of the rapidity window used for the calculation of \hat{J}_{part} where initial-state fluctuations play a larger role. Experiments typically are limited to $|y| < 1$. . . 93

Figure 75 The correlation between \hat{J}_{part} and \hat{J}_{spec} becomes smaller as we increase $\sqrt{s_{\text{NN}}}$ where a given rapidity window includes a smaller fraction of all particles and initial-state fluctuations play a larger role. This is similar to the effects driving the observation in Fig. 74. The values of $\sqrt{s_{\text{NN}}}$ are chosen to match those of the RHIC Beam Energy Scan (BES). 94

Figure 76	The correlation between \hat{J}_{part} and \hat{J}_{spec} for mid-central collisions, the event class used when studying angular-momentum-driven phenomena, falls with $\sqrt{s_{\text{NN}}}$. $3 < b < 8$ fm describes the region from Fig. 75 where the correlation is flat, and $6.5 < b < 10.3$ fm and $7.5 < b < 8.5$ fm are two ways of approximating 20-50% central collisions.	95
Figure 77	Here we examine the behavior of $\frac{\langle \vec{J}_{\text{spec}} \cdot \vec{J}_{\text{part}} \rangle}{\langle \vec{J}_{\text{spec}} \rangle \langle \vec{J}_{\text{part}} \rangle}$ and see it is nearly identical to that of $\hat{J}_{\text{spec}} \cdot \hat{J}_{\text{part}}$	96
Figure 78	The correlation between the orientation of the elliptic overlap region and \hat{J}_{syst} is largest for mid-central collisions, in line with expectations. Counter-intuitively, however, there is a smaller correlation between the orientation of the ellipse and \hat{J}_{part} . The absolute value of $\sin(\Phi_2 - \phi_{\vec{J}_{\text{ref}}})$ is used since Φ_2 is physically indistinguishable from $\Phi_2 \pm \pi$	98
Figure 79	The v_z distribution is sharply peaked about $\langle v_z \rangle = 200.7$ cm. This cut is actually redundant, as the trigger ID selection excludes events with v_z outside of 200 ± 2 cm. Without the trigger selection, many smaller peaks appear due to out-of-time events/tracks. The peak is wider than the target width in \hat{z} of 1 mm; this is due to peripheral events which have poor resolution of the primary vertex.	106
Figure 80	We impose a cut on v_T about the beam spot (0,-2) instead of (0,0) (as is typically done in collider mode) because the beam is steered downwards.	107

Figure 81	We impose a cut on v_T about the beam spot (0,-2) instead of (0,0) (as is typically done in collider mode) because the beam is steered downwards.	107
Figure 82	Comparing the distribution of number of primary tracks in an event to a Glauber model. Glauber fits the data well besides low multiplicity where triggering becomes difficult and high multiplicity where pileup is evident. Events with more than 195 primary tracks are obviously dominated by pileup. This slide from [21].	108
Figure 83	Comparing the distribution of number of primary tracks in an event to fixed-target E895 data. This slide from [21]. . .	109
Figure 84	The bad run list compiled through various QA studies performed by the UC Davis group. Figure from [39].	110
Figure 85	The Λ $m_{\text{inv.}}$ distribution before and after applying the Thunderdome filter. The effect is small and mostly concentrated at $m_{\text{inv.}} > m_{\Lambda, \text{PDG}}$	114
Figure 86	The rapidity distribution of measured Λ s using the final set of cuts.	115
Figure 87	The p_T distribution of measured Λ s using the final set of cuts.	115
Figure 88	The $y - p_T$ distribution of measured Λ s using the final set of cuts.	115
Figure 89	The $y - p_T$ distribution of measured Λ s using the final set of cuts.	115

Figure 90	The $m_{\text{inv.}}$ distribution of measured Λ s using the final set of cuts.	116
Figure 91	Λ yield as a function of centrality; the drop in yield is significant.	116
Figure 92	$R_{\text{EP}}^{(1)}$ for the EPD with no momentum-conservation considerations (i.e. using large subevents that capture a significant fraction of all produced particles. Here, especially at more central events (smaller “centrality bin” is shown), $R_{\text{EP}}^{(1)}$ is noticeably and artificially enhanced.	117
Figure 93	The $dN/d\eta$ distribution, using the TPC and EPD; the η gap between the two detectors is clear. In the TPC, we can see the tracking efficiency dropping sharply around $\eta \sim -1.4$. In the EPD, we can see small spikes, which are attributed to individual tiles; when choosing a random point in tile, the associated η distribution does not match reality, so a more ideal choice would be to have η bin widths match the widths of EPD rings in η . We can see jumps in yield at $\eta \sim -3$ and $\eta \sim -4.4$; these may or may not be physical, and no model would be very useful at describing behavior at such forward rapidities.	119
Figure 94	The distribution of number of tracks for each TPC subevent (excuse the label; TPC subevent 0 covers $-1 < \eta < -0.9$, subevent 1 covers $-0.9 < \eta < -0.8$, and so on). We see here that if the subevents were any smaller than 0.1 in η , we would see too many events with “empty” TPC subevents.	120

Figure 95	The Ψ_1 correlation of the two TPC subevents chosen for this momentum-conservation study; we see that, although the subevents often have only a small handful of tracks, the correlation between the subevents is still meaningful.	121
Figure 96	The difference between polarization measurements using various EPD Ring Groups and that using EPD Ring Group 3, with the uncertainties subtracted in quadrature. There is no observable drop in polarization with EPD Ring Group that would arise from momentum-conservation effects.	122
Figure 97	$R_{\text{EP}}^{(1)}$ of the EPD with a variety of TPC subevent choices (excuse the label; TPC subevent 0 covers $-1 < \eta < -0.9$, subevent 1 covers $-0.9 < \eta < -0.8$, and so on). As TPC reference subevents approach zero (i.e. approach $\eta = -1$), $R_{\text{EP}}^{(1)}$ is artificially inflated due to non-flow correlations with the EPD; however, the η gap between TPC subevents is not relevant as such non-flow correlations are cancelled out (see Eq. 9).	124
Figure 98	Here is the same plot as in Fig. 97, zoomed and re-scaled onto the region of the TPC far enough from the EPD to have no observable non-flow contributions to $R_{\text{EP}}^{(1)}$	124
Figure 99	TPC Positive-track yield as a function of p_T and η . . .	125
Figure 100	TPC Positive-track yield as a function of p_T and ϕ ; sector boundaries and TPC non-uniformity are obvious. . . .	126
Figure 101	TPC Positive-track yield as a function of η and ϕ ; sector boundaries and TPC non-uniformity are obvious.	126
Figure 102	TPC Negative-track yield as a function of p_T and η . . .	127

Figure 103	TPC Negative-track yield as a function of p_T and ϕ ; sector boundaries and TPC non-uniformity are obvious. . . .	127
Figure 104	TPC Negative-track yield as a function of η and ϕ ; sector boundaries and TPC non-uniformity are obvious. . . .	128
Figure 105	The raw Ψ_1 distribution with respect to centrality; non- uniformity is obvious.	129
Figure 106	The shifted Ψ_1 distribution with respect to centrality; flatness is obvious.	129
Figure 107	The projection of the above histogram across centrality; flatness is obvious.	130
Figure 108	The raw Ψ_1 distribution with respect to centrality; non- uniformity is obvious.	130
Figure 109	The shifted Ψ_1 distribution with respect to centrality; flatness is obvious.	131
Figure 110	The projection of the above histogram across centrality; flatness is obvious.	131
Figure 111	The raw Ψ_1 distribution with respect to centrality; non- uniformity is obvious.	132
Figure 112	The shifted Ψ_1 distribution with respect to centrality; flatness is obvious.	132
Figure 113	The projection of the above histogram across centrality; flatness is obvious.	133

Figure 114	Fourier-shifted Ψ_1 distributions of an arbitrarily selected EPD ring with 48 terms. Using the tile center for the ϕ of each EPD hit (shown in blue) reveals the azimuthal structure of the EPD and using a random point within the tile of each EPD hit (shown in red) “washes out” the structure and allows for a flat distribution.	136
Figure 115	Fourier-shifting terms for the EPD, using the tile center for the ϕ of the EPD hit, excluding the $i_{\text{Fourier}} = 1$ since it is the largest and dominates the color scale. We see significant behavior for $i_{\text{Fourier}} \sim n24$, corresponding the the number of azimuthal divisions (sectors) in the EPD.	137
Figure 116	Despite the structure in the Ψ_1 distribution when using the tile center (seen in Fig. 114), we see no preferred direction.	138
Figure 117	Correlating Ψ_1 measurements between the EPD and TPC and taking the ratio of the results between the two methods (using EPD tile centers or random points on the tile), we see virtually no difference besides in the first ring, where the tiles have twice the azimuthal width as any other.	138
Figure 118	Trigger efficiency as a function of collision centrality.	139
Figure 119	The ratio of embedded Λ s to <i>measured</i> embedded Λ s with respect to p_T and y ; this ratio measures the efficiency of identifying Λ s as affected by both the STAR detector and the Λ -finding algorithm.	141

Figure 120	The second-harmonic acceptance-correction term A_2 , from Eq. 36; we see that, although there is a dependence on $m_{\text{inv.}}$, the term is less than 10% within the Λ mass peak. . . .	142
Figure 121	The second-harmonic polarization term $P_{\text{H}}^{(2)}$, from Eq. 36; we don't see a strong dependence on $m_{\text{inv.}}$, and the term is less than 0.1% within the Λ mass peak.	142
Figure 122	The A_0 term from Eq. 36 as a function of $m_{\text{inv.}}$; the dependence is quite strong.	143
Figure 123	The A_0 term from Eq. 36 as a function of $m_{\text{inv.}}$ and y .	144
Figure 124	The A_0 term from Eq. 36 as a function of $m_{\text{inv.}}$ and p_{T} .	145
Figure 125	The A_0 term from Eq. 36 as a function of $m_{\text{inv.}}$ and Centrality.	146
Figure 126	Difference between polarization using the standard KFParticle- found Lambdas and using the “manually”-found Lambdas (us- ing the first cut set). This is the integrated result and the x axis is simply a meaningless placeholder.	148
Figure 127	Difference between polarization using the standard KFParticle- found Lambdas and using the “manually”-found Lambdas (us- ing the first cut set).	149
Figure 128	Difference between polarization using the standard KFParticle- found Lambdas and using the “manually”-found Lambdas (us- ing the first cut set).	149
Figure 129	Difference between polarization using the standard KFParticle- found Lambdas and using the “manually”-found Lambdas (us- ing the first cut set).	150

Figure 130	Difference between polarization using the standard KFParticle-found Lambdas and using the “manually”-found Lambdas (using the second cut set). This is the integrated result and the x axis is simply a meaningless placeholder. Note: this is not simply a plot of \overline{P}_Λ vs. Placeholder; we subtract the integrated result <i>and</i> subtract the statistical uncertainties in quadrature.	150
Figure 131	Difference between polarization using the standard KFParticle-found Lambdas and using the “manually”-found Lambdas (using the second cut set). Note: this is not simply a plot of \overline{P}_Λ vs. Pt; we subtract the integrated result <i>and</i> subtract the statistical uncertainties in quadrature.	151
Figure 132	Difference between polarization using the standard KFParticle-found Lambdas and using the “manually”-found Lambdas (using the second cut set). Note: this is not simply a plot of \overline{P}_Λ vs. ComRapidity; we subtract the integrated result <i>and</i> subtract the statistical uncertainties in quadrature.	151
Figure 133	Difference between polarization using the standard KFParticle-found Lambdas and using the “manually”-found Lambdas (using the second cut set). Note: this is not simply a plot of \overline{P}_Λ vs. Centrality; we subtract the integrated result <i>and</i> subtract the statistical uncertainties in quadrature.	152
Figure 134	The impact-parameter distribution using a Glauber model	154

Figure 135	The multiplicity distributions from both data and Glauber. For Glauber, we can also see the multiplicity distributions corresponding to each 1 fm impact-parameter window. The trigger efficiency at low multiplicity is obvious.	157
Figure 136	The ratio of multiplicity distributions from both data and Glauber. In the range $40 \lesssim \text{multiplicity} \lesssim 190$ the Glauber model reproduces the observed multiplicity fairly well.	157
Figure 137	The estimated trigger-efficiency-corrected Λ yield vs. multiplicity distribution for each 1 fm impact-parameter window. We see a stark difference compared to Fig. 135; here, above $b = 3$ fm, Λ yield falls with centrality whereas event yield rises.	158
Figure 138	Theory polarization extrapolated from three given impact parameters across the range $0 < b < 16$ fm. We assume zero polarization and vorticity at $b = 0$ fm and take the last linear fit beyond the last data point. The values shown here are from UrQMD predictions at low energy [24].	159
Figure 139	Λ yield vs. impact parameter for the 20-50% centrality window.	159
Figure 140	Polarization vs. centrality, compared to UrQMD [24] using the two methods described here. The “simple picture” uses Eq. 40 and only the three impact parameters given by the model calculation, and the “full correction” uses the Glauber-model Λ -yield weighting and theory extrapolation described above.	160

Figure 141	Polarization calucations using the 3-Fluid-Dynamics model [31]. Three inclusive <i>hydrodynamic</i> rapidity windows are shown as the uncertainties.	161
Figure 142	The distribution of participant count over many events; we see a peak near zero due to the relatively large number of peripheral events and a sudden drop-off near $2 * 197 = 394$, which is of course the maximum number of participants allowed in a $^{197}_{97}\text{Au} + ^{197}_{97}\text{Au}$ collision. Interestingly, we see no counts at the maximum number of allowed participants due to the extreme rarity of spectator-free collisions, <i>even in 100% central events</i>	164
Figure 143	The distribution of binary collision count over many events; we see a peak near zero due to the relatively large number of peripheral events and a drop-off more gradual than in Fig. 142 due of course to the fact that a given nucleon may collide with more than one nucleon.	164
Figure 144	The negative binomial distribution (Eq. 47 with $\mu = 0.9$ and $k = 39.984$. This describes the distribution of produced charged particles per participant. Clearly this drops sharply after a few non-negligible values.	165
Figure 145	The multiplicity distribution achieved by randomly sampling Eq. 47 for each participant; we see a peak near zero due to the relatively large number of peripheral events and a drop-off more gradual than in Fig. 142 due to the “smearing” effect of Eq. 47.	165

Figure 146	Centrality as a function of b ; we simply take from Fig. 71 the fraction of total collision events at or below a given impact parameter.	166
Figure 147	Centrality as a function of MCG multiplicity; we simply take from Fig. 145 the fraction of total collision events at or above a given multiplicity.	166
Figure 148	The impact-parameter distribution in AMPT without event filtering; we see that “non-collision events are not stored. Clearly, at $b \gtrsim 2R_A$, we see a gradual drop consistent with the fluctuating nucleon positions on the “skin” of the nucleus as opposed to a sudden drop-off as one would expect from a hard-shell model.	167
Figure 149	The multiplicity distribution of $ \eta < 1$ in AMPT. . . .	168
Figure 150	Centrality as a function of b ; we simply take from the impact parameter distribution the fraction of total collision events at or below a given impact parameter.	169
Figure 151	Centrality as a function of multiplicity in the range $ \eta < 1$; we simply take from Fig. 149 the fraction of total collision events at or above a given multiplicity.	169
Figure 152	AMPT system angular momentum estimated according to Eq. 48; we see that it does not follow the form of Eq. 49. In fact, the dependence on b seems completely incorrect; this turns out to be a problem with running AMPT “out of the box” with low precision.	172

Figure 153	AMPT system angular momentum along $-y$ estimated according to Eq. 48; we see that it is not roughly constant at 1. In fact, the dependence on b seems completely incorrect; this turns out to be a problem with running AMPT “out of the box” with low precision.	173
Figure 154	AMPT system angular momentum estimated according to Eq. 48, with increased output-file precision; we see that it does closely follow the form of Eq. 49.	174
Figure 155	AMPT system angular momentum along $-y$ estimated according to Eq. 48; we see that it is roughly constant at 1. The dot product falling below 1 for more central collisions comes from the fact that incoming nuclei are build from nucleons randomly generated according to the appropriate distributions with nuclei separation according to a randomly-chosen b . The centers-of-mass of the two nuclei thus have a variation from the point about which the nucleons were generated which becomes more noticeable by this dot product as $b \rightarrow 0$ fm. . .	175
Figure 156	The raw Ψ_1 distribution for each EPD wheel. The red lines are sinusoidal fits, which approximate the data quite well.	178
Figure 157	The amplitude of the sinusoidal fit to the normalized Ψ_1 distribution over time. We see clearly that the sizes of the uncertainties do not match the scatter, indicating that the amplitude is changing significantly on a run-by-run basis. . . .	179

Figure 158	The phase shift of the sinusoidal fit to the normalized Ψ_1 distribution over time. We see clearly that the sizes of the uncertainties do not match the scatter, indicating that the phase is changing significantly on a run-by-run basis.	180
Figure 159	Here is shown that the characteristics of the Ψ_1 distribution shape evolve smoothly with time within fills. In between fills (as indicated with solid black vertical lines in time) we do not see jumps.	181
Figure 160	Here, in contrast to Fig. 159, we see that the characteristics of the Ψ_1 distribution shape can jump suddenly between runs, even without a fill in between.	182
Figure 161	The Ψ_1 distribution with respect to $v_{z,\text{TPC}}$ is apparently flat.	183
Figure 162	The Ψ_1 distribution with respect to $ v_{z,\text{TPC}} - v_{z,\text{VPD}} $ is obviously non-flat.	183
Figure 163	We shift Ψ_1 with respect to $ v_{z,\text{TPC}} - v_{z,\text{VPD}} $ to ensure its flatness.	184
Figure 164	The behavior of \overline{P}_Λ vs. $ v_{z,\text{TPC}} - v_{z,\text{VPD}} $ is drastically different than that of $\overline{P}_{\overline{\Lambda}}$ vs. $ v_{z,\text{TPC}} - v_{z,\text{VPD}} $	185
Figure 165	The so-called “helicity efficiency effect” wherein a Λ emitting its pion daughter “backwards” in the Λ rest frame has substantially lower p_T than a pion emitted “forward” in the Λ frame. The proton’s momentum is only slightly affected. Lower- p_T tracks are more difficult to measure in the STAR TPC.	186

Figure 166	The difference in behavior seen in Fig. 164 is dramatically worse on the East side of the TPC, due to a missing iTPC sector.	187
Figure 167	Here is shown the suggested jump in $\bar{P}_{\bar{\Lambda}}$ and \bar{P}_{Λ} between the two productions. \bar{P}_{Λ} seems to rise and $\bar{P}_{\bar{\Lambda}}$ seems to fall. This is within statistical uncertainties, however, and only suggests a problem.	188
Figure 168	Here is shown the suggested jump in $\bar{P}_{\bar{\Lambda}}$ and \bar{P}_{Λ} between the two productions, which remains when isolating the missing iTPC section of y_{Λ} . For both sections, \bar{P}_{Λ} still seems to rise and $\bar{P}_{\bar{\Lambda}}$ seems to fall. This is within statistical uncertainties, however, and only suggests a problem.	189
Figure 169	Here is shown a more detailed dependence of $\bar{P}_{\bar{\Lambda}}$ and \bar{P}_{Λ} on time; for \bar{P}_{Λ} especially, the dependence appears to be linear, but the linear fit term (fitting with $p_0 + p_1\bar{P}_{\Lambda}$ is only of significance 2.3σ	190
Figure 170	There is no apparent dependence of $R_{\text{EP}}^{(1)}$ on time, which would be a potential explanation of the behavior seen in Fig. 169	191
Figure 171	The dependence of multiplicities and particle quantities on time; there is an obvious jump between the two productions.	192
Figure 172	The dependence of particle matches and hits on time; there is an obvious jump between the two productions. . . .	193

Figure 173	$R_{\text{EP}}^{(1)}$ in uncalibrated $\sqrt{s_{\text{NN}}} = 19.6$ GeV data; there is a 15% increase over $R_{\text{EP}}^{(1)}$ seen at $\sqrt{s_{\text{NN}}} = 27$ GeV, with comparable Λ statistics. v_1 weighting is achieved on a η -dependent basis (Fig. 174).	194
Figure 174	v_1 weights are achieved by measuring $\langle \cos(\Psi_1 - \phi) \rangle (\eta)$ where Ψ_1 is determined by the opposite EPD wheel.	195

1 Introduction

1.1 Heavy-ion collisions

The basics

The 20th century witnessed the discovery of a plethora of new particles; physicists theorized and demonstrated that these particles were not fundamental but instead comprised of what came to be called “quarks”. Like other “matter particles” (see Fig. 1), quarks interact through the exchange of force-carrier particles. Quarks carry with them a so-called color charge, and forces between them are mediated by gluons in quantum chromodynamics (QCD); these are the analog of photons, which mediate the forces between electric charges in quantum electrodynamics (QED).

Unlike in QED, the force carriers in QCD are self interacting; furthermore, while the potential between charges in QED falls as r^{-1} , the potential between color charges in QCD rises as r at large separation. Color charges in QCD could be pulled apart while the force between them remains roughly constant with separation until a breaking point is reached. In QCD, that breaking point occurs when the potential energy is sufficient to create a new quark and anti-quark that then bind to the original, separated pair.

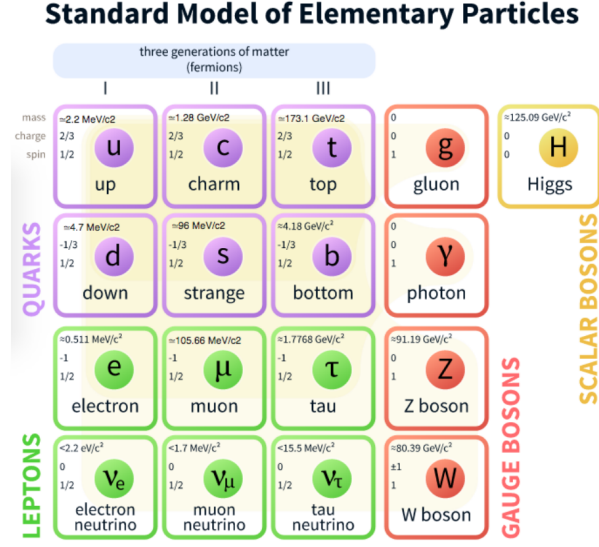


Figure 1: The standard model of elementary particle physics. Here is shown the six quarks and their force carrier, the gluon.

For high-enough energy densities (corresponding to very small separation between them), quarks and gluons are no longer bound into hadrons; they enter a new state of matter called the Quark-Gluon Plasma (QGP) [10]. In order to create the QGP, atomic nuclei must be accelerated to speeds very near the speed of light (so fast that the nuclei are almost entirely flat in the lab frame) and collided head-on so that the colliding nucleons (called participants) have a high-enough energy density to “melt” into the QGP state. When the QGP is formed, it is extremely hot (at about 100,000 times the temperature of the sun’s core) and has an extremely high pressure. This causes the QGP to undergo such a violent expansion that within a few yoctoseconds ($1 \text{ ys} = 10^{-24} \text{ s} \approx 3 \text{ fm}/c$), the temperature is too low on the outer shell to remain deconfined, and so quarks and gluons fuse again into hadrons; this process is called “hadronization” or “chemical freezeout”. The

QGP formed in a typical heavy-ion collision is entirely hadronized within about 10 ys, but the hadrons are still close enough to interact at this point. At “kinetic freezeout” the hadrons’ interactions become negligible and they travel outward at very high speeds to be detected.

By colliding nuclei at a variety of center-of-momentum nucleon-nucleon energies, $\sqrt{s_{\text{NN}}}$, one may probe the phase diagram of QCD 2; the primary objective of studying heavy-ion collisions. “Lattice QCD” calculations at low baryon chemical potential predict a smooth crossover between baryonic and partonic matter [22]; however, model calculations at high baryon chemical potential predict a first-order phase transition between these two states [11, 57]. There is therefore enormous experimental motivation to find the QCD first-order phase transition and critical point and, in a larger sense, characterize the QGP.

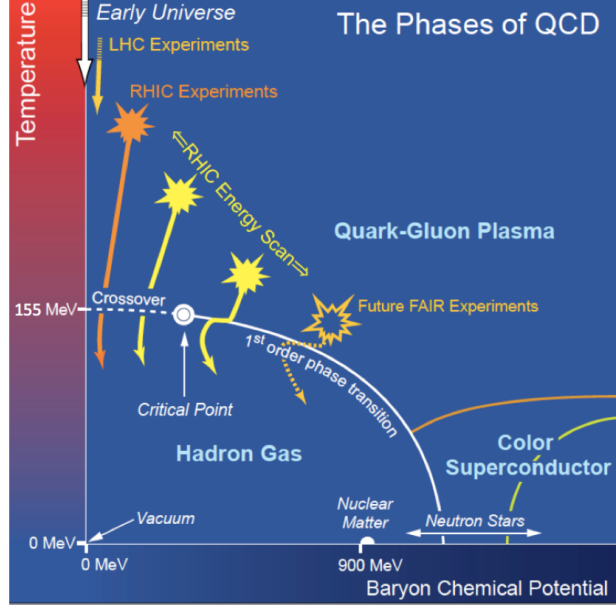


Figure 2: The QCD phase diagram, with a degree of speculation on the features. Experimentally testing the features is achievable through relativistic heavy-ion collisions. Figure from [10].

Particle detectors, such as the Solenoid Tracker At RHIC (STAR), are really combinations of many detectors, and are capable of reconstructing information about the collisions. The most important detector in STAR (often referred to as the “heart” of the operation) is the Time Projection Chamber (TPC). The TPC is filled with gas and has parallel electric and magnetic fields in the direction the long axis of its cylindrical shape. As charged particles travel outward from the center, where the QGP was formed, they bend in the strong magnetic field (0.5 T), their paths creating helices that yield information about the momenta of the particles. The charged particles ionize the gas as they travel in their helical paths through the TPC, and the electric field in the TPC drifts the freed electrons to sensors on one

end of the cylinder; this information is used to reconstruct the helices. Using such tools as the TPC, experimentalists can “take pictures” of heavy-ion collisions, extracting crucial information to understand the evolution of the QGP.

Geometry and flow coefficients

When heavy ions collide, they usually collide off-center. The parts of the Lorentz-contracted nuclei that collide form the “overlap region” which then forms the QGP, and the parts that miss the collision are called the spectators, which continue their motion before disintegrating. This overlap region is often depicted as a perfect football shape which helps form some basic intuitions, but often fails; pictures of atoms often depict stationary nucleons packed as tightly as possible in a ball, but this is not accurate.

Nucleons are moving non-relativistically with a momentum of about $0.25 \text{ GeV}/c$ inside the nucleus, and they are not packed tightly. When QGP from a heavy-ion collision is formed, it has an initial-state geometry that is determined by the random position of the nucleons within the nucleus and the separation of the centers of the two colliding nuclei (impact parameter $|\vec{b}|$) at the moment of impact (see Fig. 3).

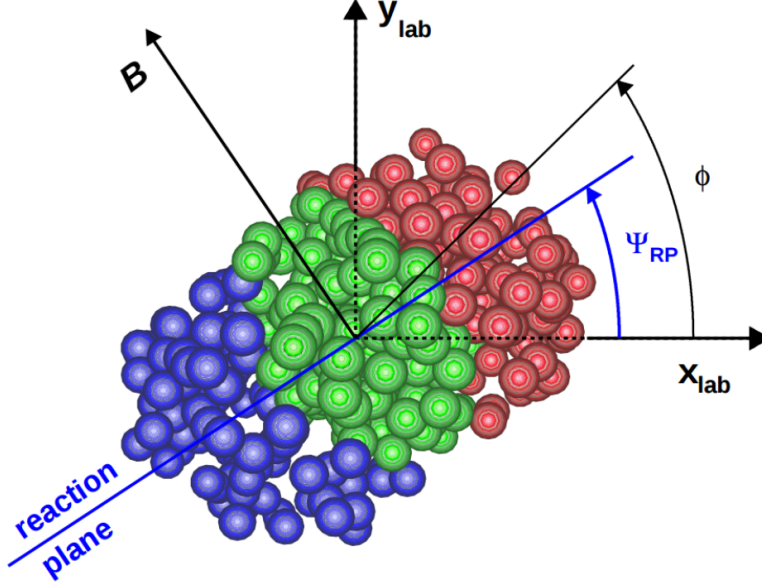


Figure 3: A typical heavy-ion collision, viewed in the transverse plane. The reaction plane is spanned by the impact parameter and the beam direction. Figure from [64].

The overlap region can also look triangular, square, etc.; however, it often seems not to take on the form of any basic shape. In fact, the overlap region has some degree of being elliptic, some different degree of being triangular, and so on [62].

These “degrees” translate into momentum anisotropies which are quantified with flow coefficients, v_n , so-called because the initial-state geometry dictates how strongly the QGP will expand in any given direction. The shape of the initial-state geometry tells us the probability of a particle to be emitted in a given azimuthal direction, since the “shorter” sides of any shape (e.g. the minor axis of an ellipse) have larger pressure gradients than the “longer” sides. This probability density is often described with a Fourier

decomposition [12]:

$$\frac{dN}{d\Delta\phi} \propto 1 + 2v_{1,\alpha} \cos(\Delta\phi) + 2v_{2,\alpha} \cos(2\Delta\phi) + \dots, \quad (1)$$

where v_1 is the “directed flow” and v_2 is the “elliptic” flow, α indicates a particle type, and the angles $\Delta\phi$ are the angles of particles’ momenta at the point of hadronization measured with respect to the relevant “event-plane” angle,

$$\Psi_{\text{EP},i} = \frac{1}{i} \text{atan2} \left(\sum_i w_i \sin(i\phi_i), \sum_i w_i \cos(i\phi_i) \right), \quad (2)$$

so that $\Delta\phi = \phi - \Psi_{\text{EP},i}$ (see Fig. 3). The sine terms of the Fourier decomposition are left out due to reflection symmetry with respect to the reaction plane.

There are two planes relevant to the collision that are often used. The transverse plane is the plane in which the Lorentz-contracted nuclei are almost entirely flat; it is orthogonal to the beam direction. A given particle’s momentum in the transverse plane is often used, and is denoted in this paper by p_T . The reaction plane is the plane spanned by the beam direction (\hat{z}) and \vec{b} . The reaction plane is not exactly measureable, so it is often estimated with the first- or second-order event plane angle, which measures the tilt of the overlap region. Besides very central ($|\vec{b}| \lesssim 1$ fm) or very peripheral ($|\vec{b}| \gtrsim 10$ fm for Au+Au) collisions, this approximation is valid.

Commonly used variables

Although $|\vec{b}|$ is a useful quantity in theory and in simulations, it is not a measurable quantity in the lab. To a first-order approximation, collisions with

smaller impact parameters deposit more energy into the QGP and therefore produce more particles than do collisions with larger impact parameters; however, fluctuations of nucleon positions within the nuclei at the moment of impact make the relationship between $|\vec{b}|$ and number of particles produced (multiplicity N) dispersive. For example, a central (e.g. $|\vec{b}| \approx 1$ fm) collision where the majority of nucleons happen (through statistical fluctuations) to overlap at the moment of impact will produce more particles than a very central (e.g. $|\vec{b}| \approx 0$ fm) collision where a significant fraction of nucleons do *not* happen to overlap.

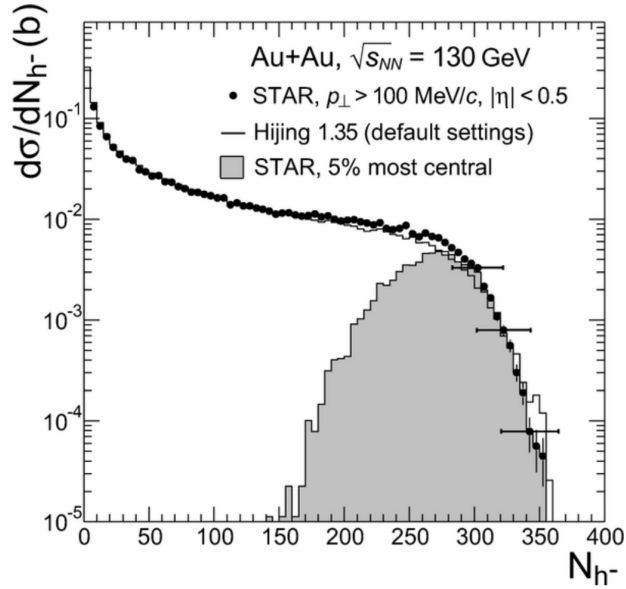


Figure 4: Normalized multiplicity distribution of negatively charged hadrons h^- with transverse momentum $p_T > 100$ MeV/ c and pseudorapidity $|\eta| < 0.5$ in Au+Au collisions at $\sqrt{s_{NN}} = 130$ GeV as measured by the STAR collaboration. σ is the cross section, measured in millibarns. The shaded region is the multiplicity distribution for the 0-5% most central collisions with the impact parameter determined by the ZDC. The solid curve is a simulation (using the HIJING model). Figure from [9].

The nomenclature may be confusing, but very central collisions (with small impact parameters) have a *smaller* “centrality” (e.g. 0-5% centrality) and very peripheral collisions (with large impact parameters) have a *larger* centrality (e.g. 90-100% centrality). Events are typically broken into different “centrality classes” that fit within a given centrality range, and centrality ranges are experimentally chosen by windows in multiplicity. In Fig. 4 is shown an experimentally measured and model-based multiplicity distribution plotted together. Additionally, we see the multiplicity distribution corresponding to very central collisions within a model, where b can be known exactly; we see a broad distribution that spans half of the entire multiplicity range. In Fig. 136 we can see the multiplicity distributions from another model corresponding to different ranges in b . These plots demonstrate that one can only approximate b using multiplicity; however, there is no known method to better measure b experimentally.

A particle’s momentum in the transverse plane, p_T , is valuable in part because the transverse plane is orthogonal to the direction of the external magnetic field used in experiments, which is aligned with the beam direction (along \hat{z}). Because of this, we can experimentally have access to momentum information purely from the radius of a particle’s curvature in the transverse plane, without needing to identify its species.

Another very useful and often-used variable is rapidity, y , which is defined as:

$$y = \frac{1}{2} \ln \frac{E + p_z}{E - p_z}. \quad (3)$$

A particle’s y is valuable information experimentally because it is additive under longitudinal boosts; however, particle identification is required which

is more experimentally challenging. For relativistic ($E/p \approx 1$) particles, however, we can make the approximation

$$y \approx \frac{1}{2} \ln \frac{p + p_z}{p - p_z} = -\ln \left(\arctan \frac{\theta}{2} \right) \equiv \eta, \quad (4)$$

where η is the appropriately named “pseudo-rapidity” and θ is the angle that the particle makes with \hat{z} . The advantages of the usage of η include the fact that particle identification (e.g. mass determination) is not required, and that it is explicitly related to geometry.

1.2 Experimental setup

The Relativistic Heavy-Ion Collider

The Relativistic Heavy-Ion Collider (RHIC) is truly a feat of engineering: two side-by-side “rings” (Fig. 5) are cooled to within a few Kelvin of absolute zero and carry superconducting magnets. These two rings are each nearly 2.5 miles in circumference, making for a total of nearly 5 miles of superconducting, supercooled rings. Because of the intense radiation emitted by the accelerated nuclei, these rings are kept underground to keep radiation levels within Brookhaven National Laboratory (BNL) at tolerable levels. At six evenly spaced points, the rings intersect in order to facilitate heavy-ion collisions.

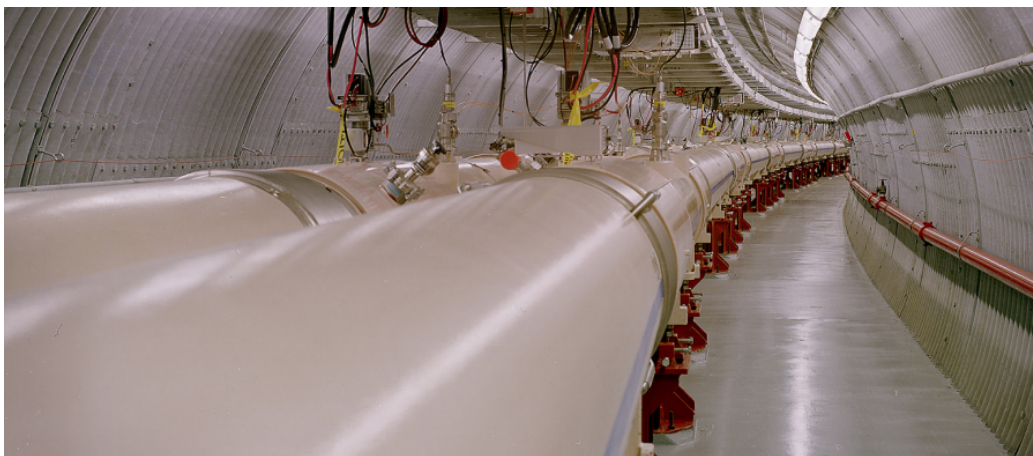


Figure 5: A small section of the nearly circular, roughly 2.5 mile-long collider rings. These rings must be kept a sufficiently low internal temperature for the magnets to remain superconducting. Figure from [1].

In Fig. 6 is shown an aerial view of the RHIC facility at BNL. The yellow ring carries counter-clockwise-going ions while the blue carries clockwise-going ions. There are six intersection points at which these rings cross paths.

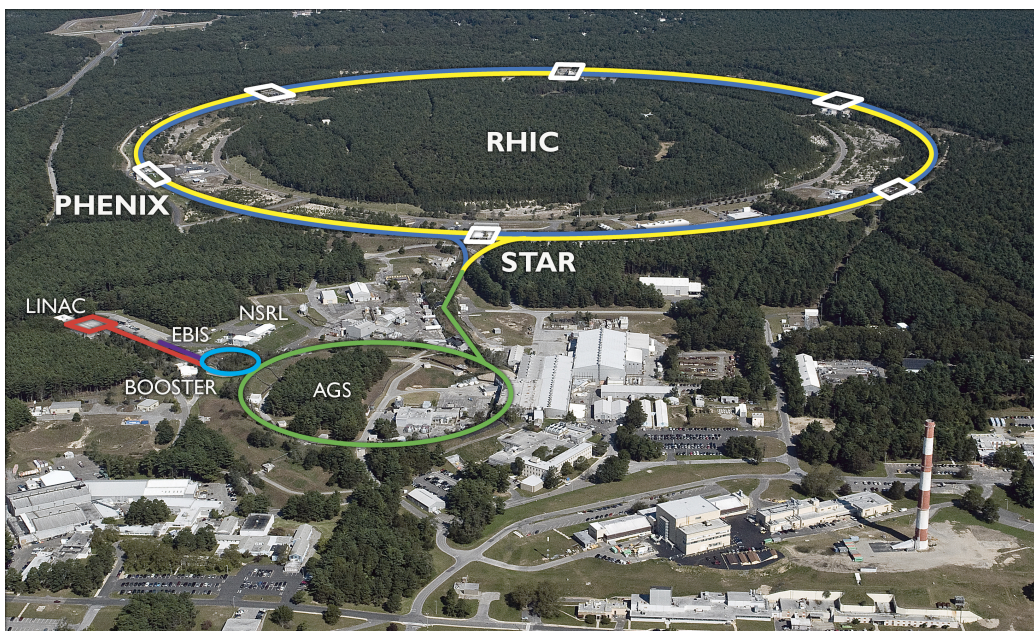


Figure 6: An aerial view of the RHIC collider and accelerators feeding low-energy ions into RHIC. We see the yellow and blue RHIC rings crossing at each of the six intersection points. Figure from [1].

RHIC is fed by a series of accelerators that gradually ramp up the ions to sufficient energies. The beam either starts from the Electron Beam Ion Source (EBIS) as a source of heavy ions or the Linear Accelerator (Linac) as a source of protons, occasionally used for $p+p$ or $p+A$ collisions. These are shown in red and purple in Fig. 6. Further acceleration is provided by the Booster Synchrotron, shown in light blue, before passing into the Alternating Gradient Synchrotron (AGS), shown in green. Prior to the construction of RHIC, the AGS served $p+p$ collisions and acted as a true workhorse of experimental particle physics. With the construction of RHIC, the primary function of the AGS became to carry heavy nuclei in order to feed RHIC.

The Solenoid Tracker at RHIC

At one of the intersection points of the RHIC beampipes sits the Solenoid Tracker At RHIC (STAR), which is essentially an enormous collection of detectors, cabling, electronics, water-cooling lines, power lines, magnets, etc. To see it in person is humbling. In Fig. 7 is shown a picture of the STAR detector, where a few of the subsystem detectors are discernable.

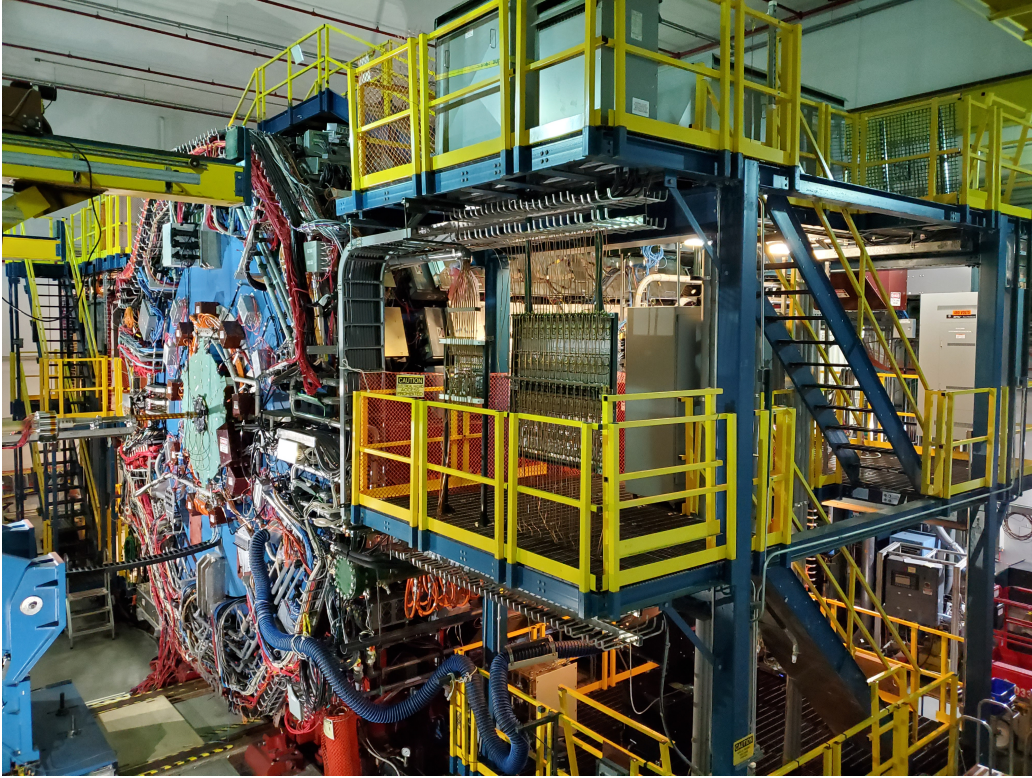


Figure 7: One side of the STAR detector and the surrounding structure. One can make out the small beam passing into the center, which carries relativistic nuclei. The small, black circle surrounding the beampipe's entry point is the Beam Beam Counter (BBC); the larger cyan circle on which the BBC is mounted is the Event Plane Detector (EPD). Many remaining detectors are obstructed. An image of the STAR detector is viewable in 3D in Fig. 8.

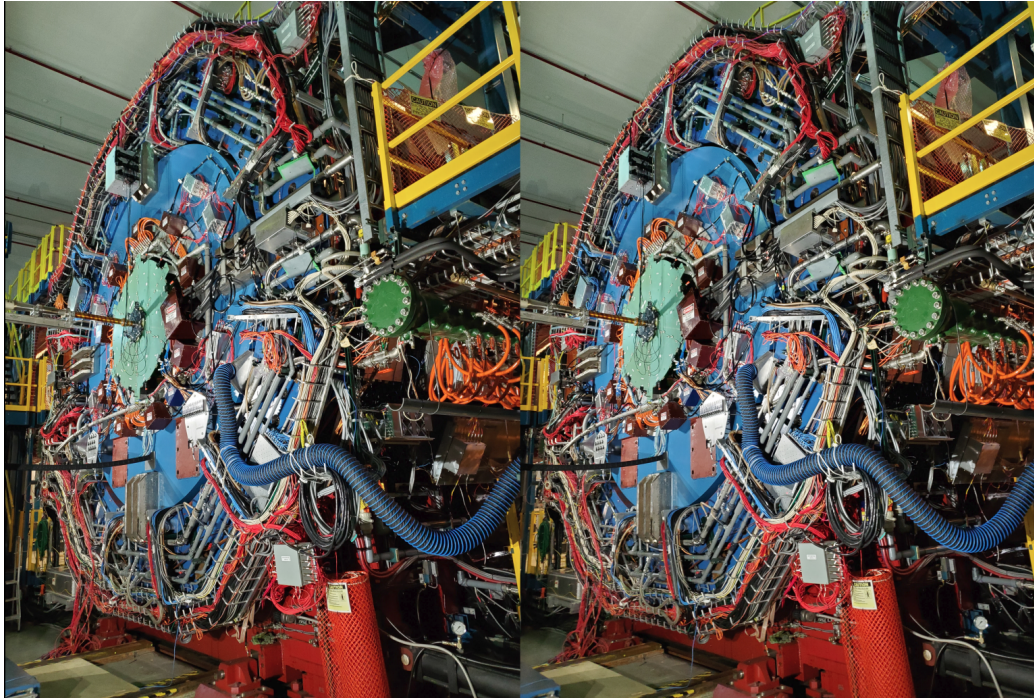


Figure 8: A crossview image of the STAR detector. To achieve perception of 3 spatial dimensions one must cross their eyes until the two images overlap and then adjust the plane of focus as if the object is behind the screen, until the image becomes clear. Achieving the perception may take some practice.

The Time Projection Chamber

There is a strong magnetic field (0.5 T) that runs parallel to the beam direction. When the QGP hadronizes, particles travel radially outwards at very high speeds; charged particles therefore bend in the strong magnetic field, their paths creating helices. Valuable information can be gained from these helices, and so a time projection chamber (TPC) [13] is used to measure them. A TPC is filled with a gas so that the charged particles bending in the magnet interact electromagnetically with the gas, ionizing atoms along the way.

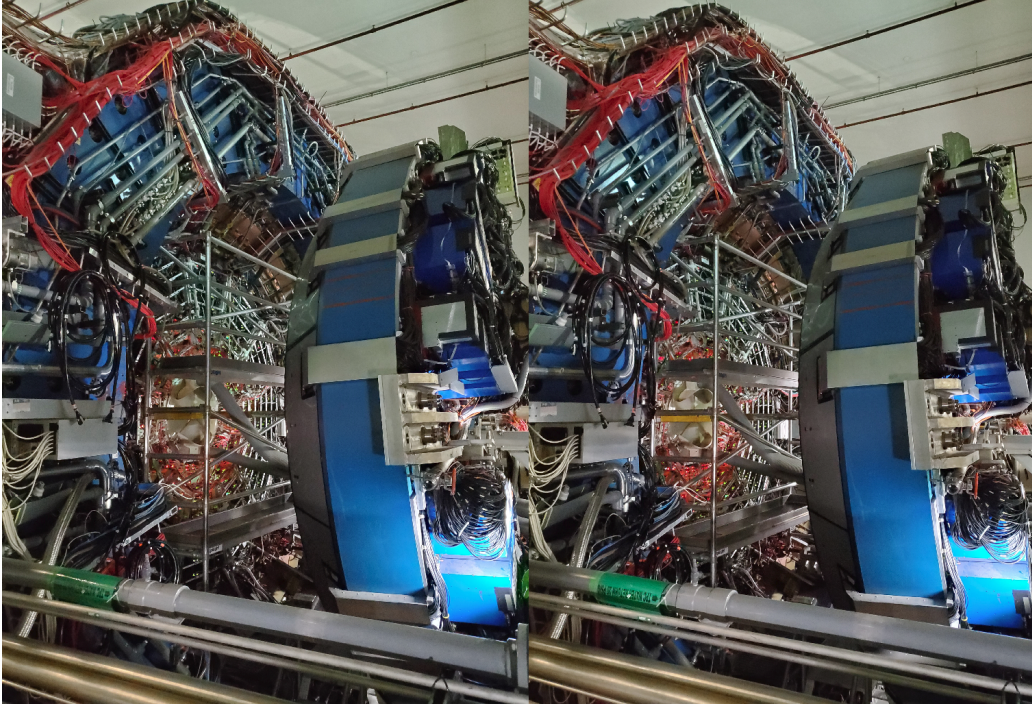


Figure 10: The STAR TPC's Front-End Electronics (FEEs) are visible when the STAR magnet is pulled back. We see scaffolding erected for maintenance. This is a crossview image; to achieve perception of 3 spatial dimensions one must cross their eyes until the two images overlap and then adjust the plane of focus as if the object is behind the screen, until the image becomes clear. Achieving the perception may take some practice.

Among other things, the TPC is used for measuring the energy loss of a particle as it passes through the gas as a function of the magnitude of the track's momentum. For a given particle at a given momentum, this energy loss is well known; however, the dE/dx vs. \vec{p} curves (see Fig. 11) have a non-zero thickness due to finite resolution. Particle identification can be achieved to first order by selecting tracks whose value of dE/dx falls close enough to its predicted value. For larger particle momenta, $|\vec{p}| \gtrsim 1.5 - 2 \text{ GeV}/c$, the bands begin to merge and dE/dx becomes less useful in terms

of identifying particles. At higher collision energies than what is used in Fig. 11, a significant fraction of particles lie in the dE/dx overlap region.

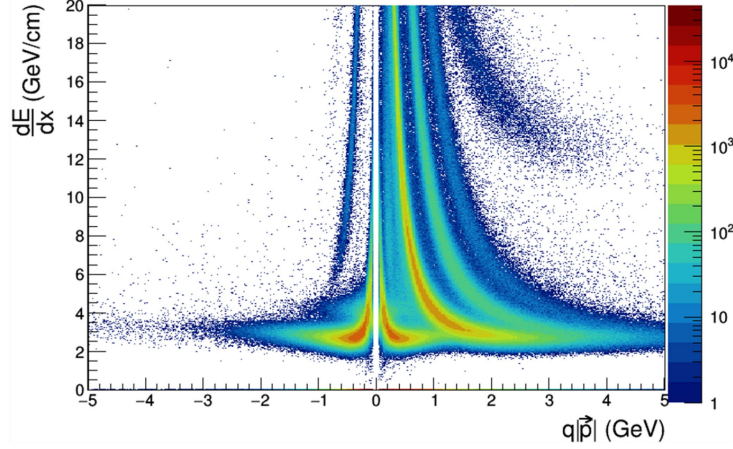


Figure 11: The energy loss in the TPC as a function of particle charge and momentum. At the low energy shown of $\sqrt{s_{NN}} = 3$ GeV, one can easily separate bands associated with different particles. At higher energies, the bands merge at higher $|\vec{p}|$ and further information is required from the BTOF detector to discern particle species.

The Time-Of-Flight Detector

To aid particle identification, a cylindrical detector wraps around the TPC; it measures the time at which particles exit the TPC, and is appropriately named the time of flight (TOF) detector [43]. The TOF is essentially a stack of thin glass plates that are electrically floating and separated by less than a quarter of a millimeter of gas, with high-voltage electrodes on the top and bottom of the stack creating a strong electric field orthogonal to the plates. Charged particles passing through the gaseous gaps ionize molecules, and the liberated electrons create “avalanches” of electrons that do not penetrate the resistive glass plates. Pads sitting just outside of these electrodes measure the voltage drops created by these avalanches and the time is recorded. A

rough schematic of a TOF tray is shown in Fig. 12.

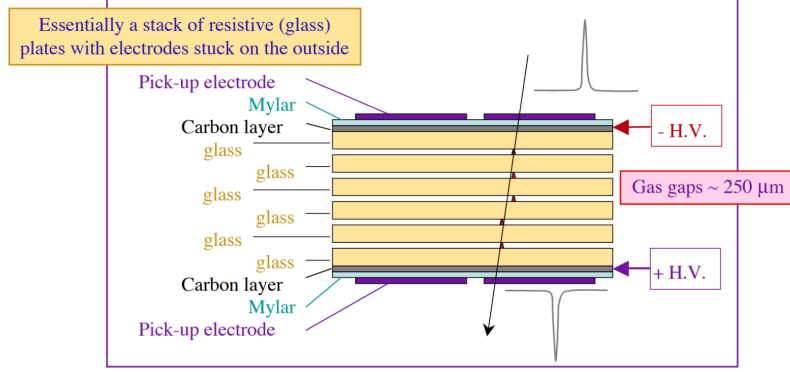


Figure 12: The basic setup of the TOF detector. Charged particles ionize gas molecules between stacked plates of glass which leads to small but measurable changes in potential that are read by pick-up electrodes. Figure from [28].

Tracks from the TPC can then be matched to hits in the TOF, and this information can be used to determine the mass of the particle that made the track. The momentum of the particle is measured by the TPC as well as the path length. The path length along with the time of flight yield the relativistic velocity $\gamma\beta c$ and the mass is achieved with $m = |\vec{p}|/\gamma\beta c$. The TOF thus enables better particle identification when used with the TPC, especially for higher-momenta particles, $|\vec{p}| \gtrsim 1.5 - 2 \text{ GeV}/c$.

The Event-Plane Detector

In many analyses, it is important to know the orientation of the first- or second-order event plane in each collision, which correlate well with the reaction plane [62]. For measuring Lambda polarization, we need to know the orientation of the first-order event plane in order to estimate the direction of the system's angular momentum. This can be done with the TPC or the TOF; however, it is favorable to use particles for the event-plane deter-

mination isolated in η from particles used in the analysis even despite the fact that fluctuations lead to small decorrelations of event planes determined from different regions in η . Because of this, a detector sitting at very high $|\eta|$ is used for event-plane determination; this is the Event-Plane Detector (EPD) [8]. The EPD is a pair of disks consisting of plastic scintillator tiles embedded with wavelength-shifting fibers. Charged particles passing through the scintillator produce photons that are absorbed by the wavelength-shifting fibers and transmitted through clear fiber optics to Silicon Photomultipliers (SiPMs). These SiPMs are essentially a stack of high-voltage electrodes that produce electron avalanches whenever photons are absorbed. Drops in potentials across the electrodes thus correspond to particles passing through a certain region in η and ϕ . The distribution of these particles on an event-by-event basis then are used to determine the first-order event plane angle Ψ_1 , given by Eq. 2. A rough schematic of the EPD is shown in Fig. 13.

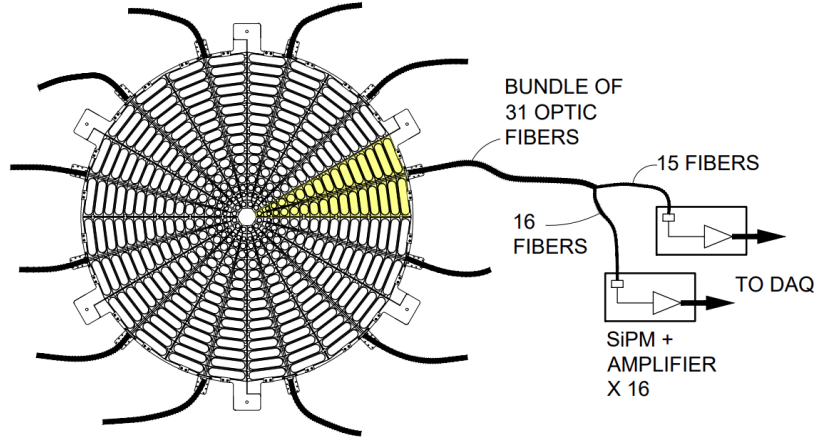


Figure 13: A rough schematic of the EPD. We can see the $31 \times 12 = 372$ tiles belonging to one “wheel” of the EPD. Photons generated by charged particles passing through the tiles travel down fiber-optic cables to a series of electronics that digitize the signal. Figure from [8].

The EPD is one of the STAR subsystems at the heart of the measurement discussed in this dissertation. The following chapter discusses the EPD in greater detail.

1.3 Outline

The spin alignment of Λ hyperons with the direction of angular momentum within the collision, \vec{J} , has been studied intensely both theoretically [42, 15, 17, 3, 7, 4, 16] and experimentally [2, 50, 7]; its discovery confirmed the presence of extreme vorticity within the QGP and can be used as a tool for other important discoveries (see appendix J). Measurements such as that of Λ polarization, \overline{P}_Λ , are “statistics hungry” and typically require $\mathcal{O}(10^6)$ Λ hyperons produced to yield measurements with sufficient statistical precision. As will be discussed in Sec. 3, the statistical uncertainties on \overline{P}_Λ go as

$\sim (R_{\text{EP}}^{(1)}\sqrt{N})^{-1}$, where N is the number of Λ hyperons and $R_{\text{EP}}^{(1)}$ describes a detector's ability to resolve the direction of angular momentum. An increase of $R_{\text{EP}}^{(1)}$ by a factor of two, for example, would correspond (in terms of uncertainties) to an increase of statistics by a factor of four. While a previously existing detector, STAR's Beam-Beam Counter (BBC), yielded large-enough $R_{\text{EP}}^{(1)}$ to measure \overline{P}_Λ across a broad range of $\sqrt{s_{\text{NN}}}$, future measurements are increasingly statistics hungry (see e.g. Sec. 3 and appendix J); the most effective way to achieve these measurements is to implement better detectors with larger $R_{\text{EP}}^{(1)}$.

This dissertation begins with the construction of the STAR Event Plane Detector, an upgrade to the BBC. Meticulous construction, testing, installation, and management of the EPD consumed over a year of my time as a new PhD student, and is something in which I still remain involved. The EPD was crucial to the measurement of Λ -hyperon spin polarization at $\sqrt{s_{\text{NN}}} = 3$ GeV, which is the topic of main concern in this dissertation. Despite subtle and unique complications present in the relevant data set, a successful measurement was made of integrated, mid-central \overline{P}_Λ as well as of the dependences of \overline{P}_Λ on centrality, p_{T} , and y . The integrated \overline{P}_Λ is the largest yet measured, and at the lowest $\sqrt{s_{\text{NN}}}$ at which \overline{P}_Λ has yet been measured. The dependences of \overline{P}_Λ on centrality and p_{T} agree with a previous high-statistics data set at $\sqrt{s_{\text{NN}}} = 200$ GeV [50] and with model-based expectations. The dependence of \overline{P}_Λ (or lack thereof) is significant because, unlike previous measurements, we have access to the most forward-rapidity Λ hyperons and are able to test the abundance of model-based predictions of such a dependence.

Also discussed in this dissertation is the important, model-based study

of the effects of event-by-event fluctuations on the correlation between the angular momentum of the participants, \vec{J}_{part} , and that of the spectators, \vec{J}_{spec} . Experimentally, \vec{J}_{spec} is measured as a proxy for \vec{J}_{part} and they are assumed to be parallel. While such an assumption is valid on average, we found that event-by-event fluctuations significantly suppress this correlation and especially for central and peripheral collisions. Furthermore, this effect is more dramatic for larger $\sqrt{s_{\text{NN}}}$, and without correcting for this, one would measure a false dependence of \overline{P}_{Λ} on $\sqrt{s_{\text{NN}}}$. While the observed dependence of \overline{P}_{Λ} on $\sqrt{s_{\text{NN}}}$ could not fully be explained by this effect, it is nonetheless important to correct for this decorrelation. We furthermore found a decorrelation between the orientation of the elliptic overlap region and the direction of \vec{J}_{part} and therefore demonstrate that this correction cannot be avoided by simply measuring \vec{J}_{part} directly from the produced particles at mid rapidity.

2 Construction of the STAR Event-Plane Detector

Prior to the installation of the STAR EPD, discussed briefly in Sec. 1.2, the Beam-Beam Counter (BBC) served as a “trigger” detector, and as well recorded information about the azimuthal distribution of forward-going particles. The BBC is comprised of a number of hexagonal tiles; the inner tiles are roughly a quarter of the width of the outer tiles. Embedded in the tiles are fiber optics that carry light generated by the passing of particles through the scintillator tiles to photomultiplier tubes (PMTs) that then convert the light into electrical signals. A rough schematic of the BBC is shown in Fig. 14 where the tile IDs and the corresponding PMT IDs are shown. The outer tiles are quite large, and many of them share PMTs; however, most of the inner tiles have a dedicated PMT and they are much smaller.

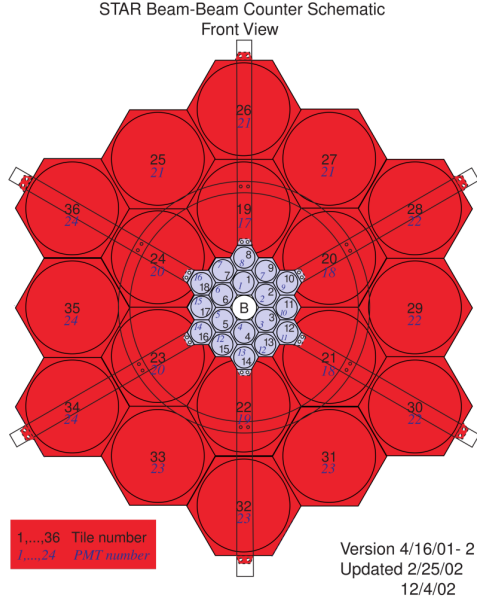


Figure 14: A rough schematic of the STAR BBC. The width is roughly 2 m. The black numbers indicate the tile number while the blue numbers indicate the PMT number; it is apparent that many large tiles are paired together and provide very little information about hit positions. Previous analyses using the BBC restricted themselves to the inner tiles only.

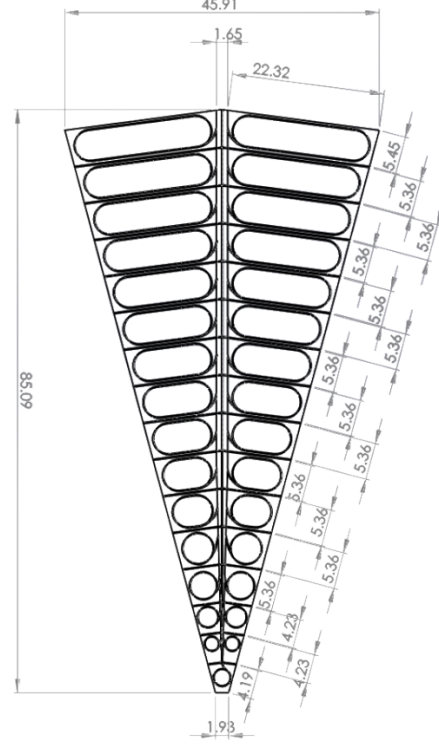


Figure 15: A single EPD supersector; twelve supersectors make a wheel and two wheels make an EPD. The unit of length is cm. Figure from [56].

The azimuthal distribution of forward-going particles yields important information about the event; most notably it reveals, within some degree of precision, the direction of angular momentum of the heavy-ion collision, \hat{J}_{sys} , and yields insight on the orientation of the collision overlap region seen in Fig 3. Recall Sec. 1.1; the first-order event-plane angle is given by Eq. 2

as

$$\Psi_1 = \text{atan2} \left(\sum_i w_i \sin(\phi_i), \sum_i w_i \cos(\phi_i) \right), \quad (5)$$

which is offset from \hat{J}_{syst} by $\approx \pi/2$. Consider the following effect driven by angular momentum: spin alignment of Λ hyperons with \hat{J}_{syst} (discussed later on),

$$\overline{P}_\Lambda \propto \frac{\langle \sin(\phi_p^* - \Psi_1) \rangle}{R_{\text{EP}}^{(1)}} \quad (6)$$

Ignoring ϕ_p^* for the time being, we see this observable involves correlating an angle with Ψ_1 and correcting by $R_{\text{EP}}^{(1)}$, the degree to which Ψ_1 accurately reproduces the reaction plane (“first-order event-plane resolution”). Now \overline{P}_Λ is a statistically challenged measurement and in order to reduce statistical uncertainties one may increase the size of the data set and/or improve $R_{\text{EP}}^{(1)}$, but the two do not stand on even ground; improving $R_{\text{EP}}^{(1)}$ by a factor of two, for example, is statistically equivalent to increasing the data set size by a factor of four. This is precisely the motivation for replacing the BBC with an upgraded detector; the EPD. The granularity of the EPD shown in Fig. 13 is obviously far greater than that of the BBC in Fig. 14, and we see in Fig. 16 the significant improvement in $R_{\text{EP}}^{(1)}$ provided by the EPD over the BBC.

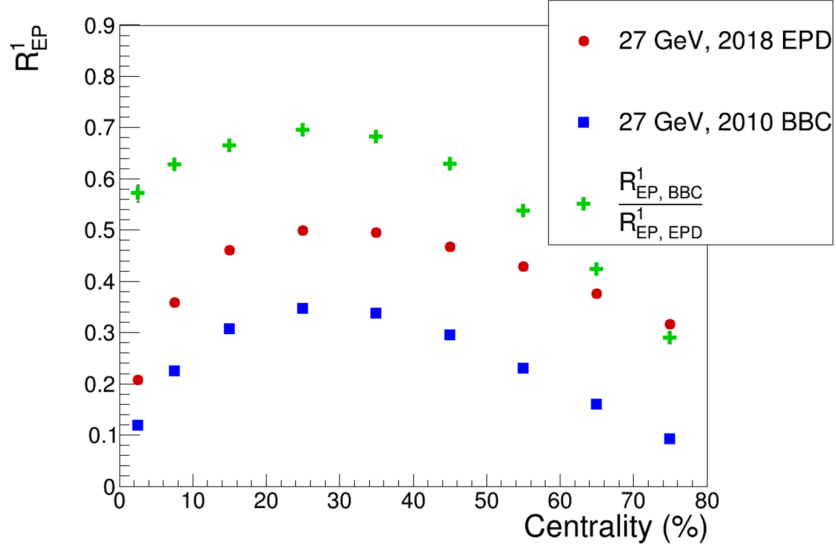


Figure 16: $R_{EP}^{(1)}$ for the EPD is drastically improved over its predecessor, the BBC.

The construction for the EPD was formally proposed in 2016 [56] after years of prototyping and construction took nearly two years before full installation in 2018. While many institutions were involved throughout various stages, the majority of the EPD was constructed at Ohio State University. Isaac Upsal and I were the two OSU laboratory managers for this project; what follows is a summary of the steps in constructing the EPD.

2.1 Fiber bundles

The majority of fiber-bundle construction and preparation was performed by Lehigh University; I therefore only briefly summarize the work here.

WaveLength-Shifting (WLS) fiber-optic cables were necessary to absorb photons generated by charged particles passing through the scintillator tiles

and change their reflective angles to be within that required for total internal reflection. Fibers were cut to length, as the distance from one end of a supersector to a tile is different for each tile. The fibers embedded in the connectors were painstakingly polished in order to facilitate photon transmission to the clear fiber bundles. The sections of fiber between the fiber connectors and the tile insertion points were coated with reflective paint, as were the tips of the fibers. A finished fiber bundle is shown in Fig. 17 and a fiber tip through various stages in fiber polishing is shown in Fig. 18.

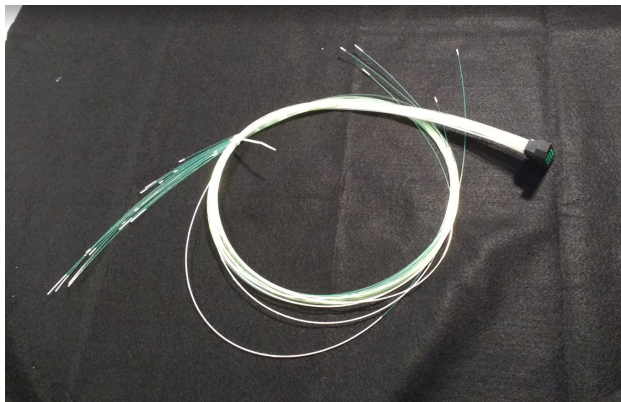


Figure 17: A finished fiber bundle. The green WLS fibers are all cut to different length. The ends of the fibers at the connector are polished painstakingly. Partial lengths of the fibers are painted with reflective paint, as are the tips.

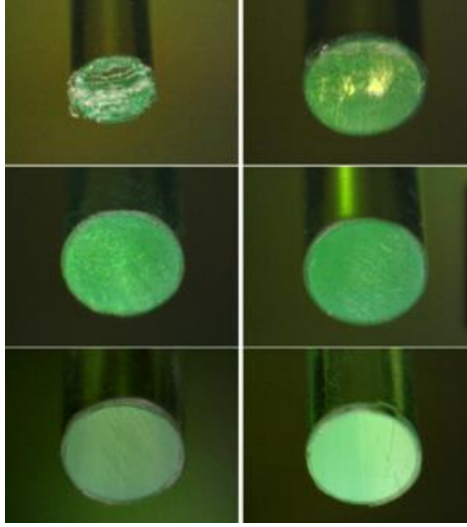


Figure 18: The tip of a WLS fiber through various stages in polishing. The improvements are dramatic. Figure from [56].

2.2 Epoxy

Two types of epoxy were used in the construction of the EPD. White, reflective epoxy was used to optically isolate tiles, creating a solid barrier and strong bond between them. Translucent, optical epoxy was used for embedding the wavelength-shifting fibers into the scintillator tiles and securing them in place, while allowing photons to pass easily through them.

The procedure followed in producing and storing the reflective epoxy was taken from detailed work found in [51]. The epoxy resin “D.E.R. 332” and curing agent “Jeffamine D230” were the structural-integrity ingredients while $44\mu\text{mTiO}_2$ powder was used for reflectivity. Resin and stainless-steel mixing balls were warmed to 62°C for three hours before adding the reflective powder and spinning at 40 rpm for another three hours. This process was repeated before adding the curing agent and spinning at 40 rpm for a few minutes.

Dull-tipped, 10 ml syringes were then filled and immediately flash-frozen in liquid nitrogen and stored in a freezer at 20° C for future use.

For the fiber optics, EJ-500 optical epoxy was activated. Air bubbles needed to be carefully removed by vacuum, without bringing air pressure low enough to boil the epoxy; bubbles in the optical grooves would impact the light transfer the the fibers. An example of this is shown in Fig.

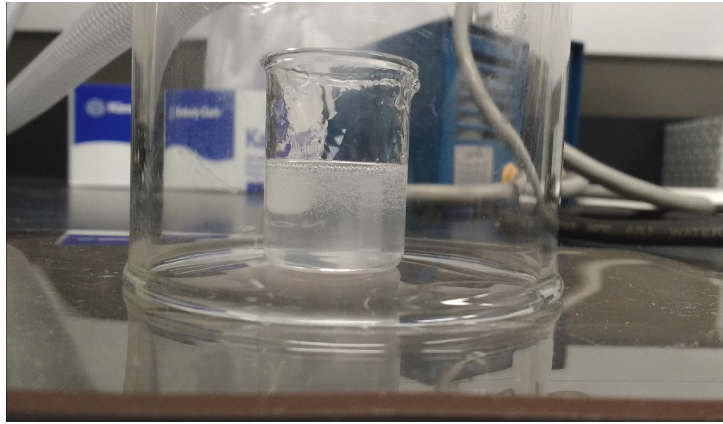


Figure 19: Removing the air bubbles from optical epoxy with a small vacuum chamber.

2.3 Scintillator slab to supersector

Regular shipments of 1.2 cm-thick Eljen EJ-200 plastic scintillator slabs arrived in rectangular form in crates (Fig. 20). The initial step involved milling tile-separation grooves at a depth of half the thickness. In Fig. 21 is shown a supersector in the process of this first milling stage. The outline has been cut out of half of a slab (note: a slab yields two supersectors) and is being prepared for tile-separation-groove milling. A mixture of water and 5% oil during the milling process helped avoid scintillator overheating; as well, the

milling was performed with many increments in depth. The pressure of the clamps holding the supersectors in place during milling (seen in Fig. 21) was carefully set to be as little as possible in order to avoid micro-cracking (to which plastic scintillator is very susceptible).



Figure 20: A rectangular scintillator slab of 1.2 cm-thick Eljen EJ-200.

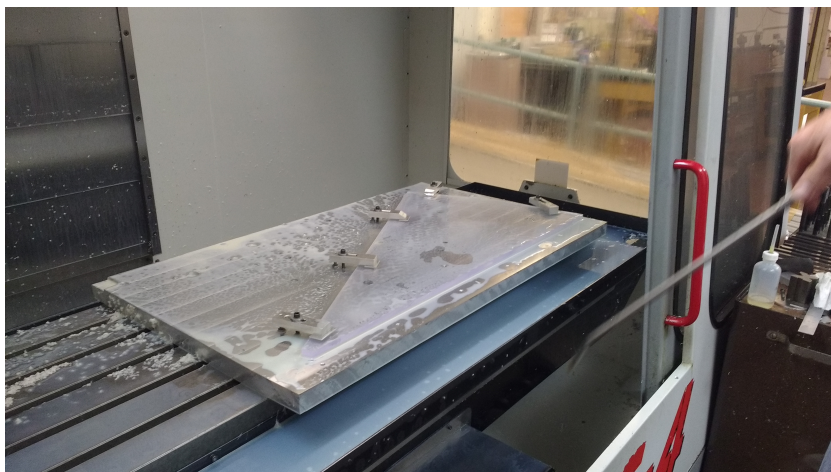


Figure 21: A supersector in the process of its first milling stage. The outline of the supersector has been cut out and is being prepared for milling tile-separation grooves at half depth.

Because of the oil present in the cooling fluid, special care was taken to completely clean the supersectors and especially the grooves after milling steps. Tepid distilled water and gentle detergent were used along with non-scratch towels and cotton swabs; in order to completely remove the oil and soap, cleaning was performed thrice with soap and water and thrice again with pure water. After drying, the sides of the scintillator were taped so that epoxy filling the grooves would not leak out of the sides (see Fig. 22).

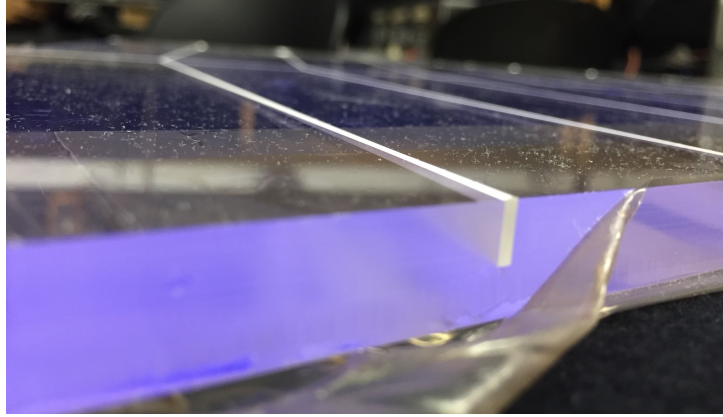


Figure 22: The supersector edge is taped after the first step of milling so that the epoxy filling the grooves does not pour out of the sides. Here is seen tape peeled back after the epoxy has dried. Figure from [8].

With the supersector prepared for epoxy, syringes were removed from the freezer and warmed in an oven. Care was taken to avoid epoxy spilling onto the surface of the supersector. Because the drying epoxy contracts, weights were carefully placed on the three “corners” of the supersector to prevent bowing. After a full day, the epoxy was dry enough to remove the tape as seen in Fig. 22.

The supersectors then began the second stage of milling; with the unmilled side face up, the tile separation grooves were milled again at half depth, and additional “sigma” grooves (so called because of their resemblance to the Greek letter σ) were milled to hold wavelength-shifting fiber optics. A few tiles within a supersector after this next stage are shown in Fig. 23. Following the same cleaning procedure as before, the faces and grooves were carefully cleaned to facilitate strong epoxy bonds. The fiber-bundle connector was glued into place and the sides were then taped as before, but additional taping to the front face of the tiles was performed using ultra-low-friction Teflon

PTFE tape to help avoid optical-epoxy spillover.

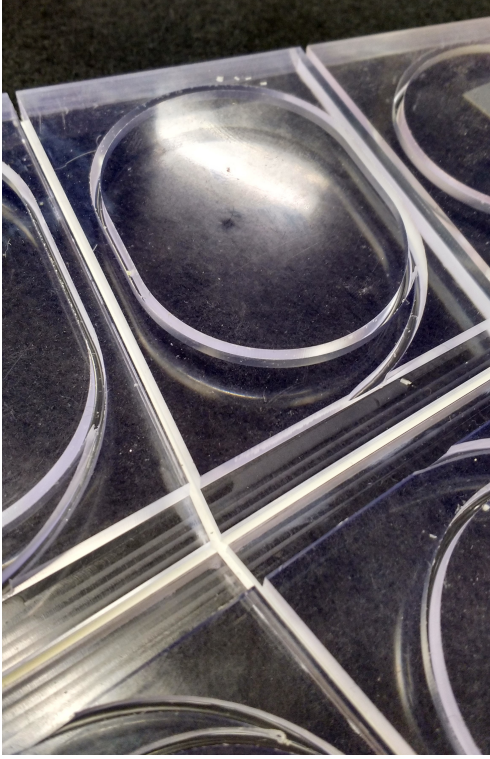


Figure 23: A supersector after the second stage of milling; we see the epoxy binding the tiles together while the second half of the tile-separation grooves were milled. We also see the sigma grooves for fiber optics. Figure from [8].

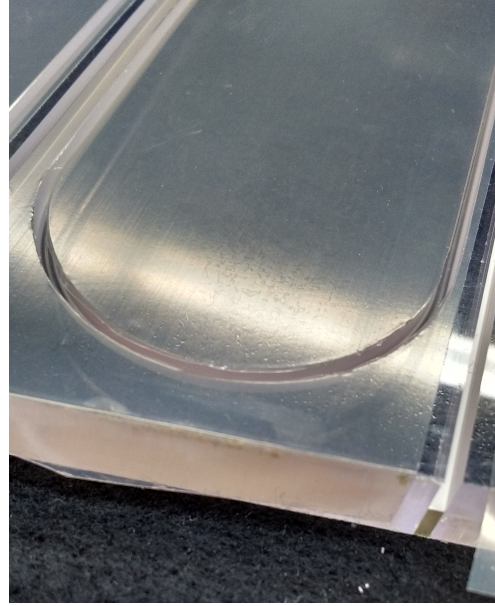


Figure 24: After cleaning the supersectors following the final milling step, wide, ultra-low-friction Teflon PTFE tape was used on the face of each tile to help avoid optical-epoxy spillover. Carefully guiding a knife along the edge of the sigma grooves, excess tape was removed.

Simultaneous placement and gluing of optical fibers into sigma grooves required two people. One person was responsible for slowly (as to avoid creating bubbles) inject epoxy while the other carefully twisted the fiber into place and held it down with bamboo skewers so as to prevent the fiber from twisting out of the groove. Special care had to be taken while injecting so

as to avoid scraping the fiber's coating with the metal-tipped syringe (see Fig. 25).

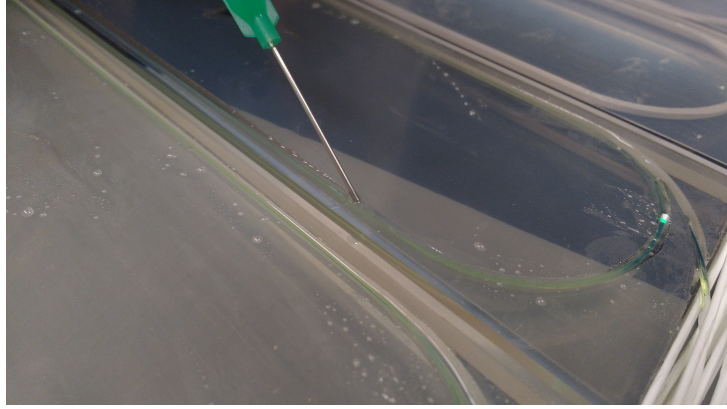


Figure 25: Here the fiber is completely inserted as a worker carefully applies enough optical epoxy to top off the groove. The central groove through which all fibers pass is visible in the bottom right corner. Figure from [8].

After the optical epoxy dried, the second half of the tile separation grooves were filled, along with the central channel through which all fibers pass, visible in the lower-right corner in Fig. 25. At this point, tiles are fully bound to each other, but only with reflective-epoxy bonds and are therefore optically isolated. After all epoxy was dried, the edges of the supersectors were polished using a series of increasingly finer-grit sandpaper and finished with 1200-grit, $5\mu\text{mAl}_2\text{O}_3$ lapping grains. Flashlights at high incident angles revealed any remaining scratches that were carefully polished away. An example of the tip of a supersector after this step is shown in Fig. 26, showing the white epoxy walls and embedded optical fibers.

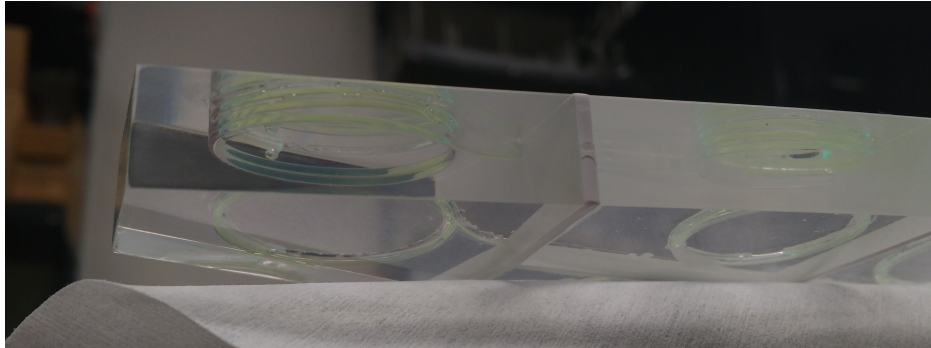


Figure 26: A supersector tip after polishing the sides. One can clearly see the embedded wavelength shifting fiber as well as the white walls of epoxy, optically isolating the tiles completely. Figure from [8].

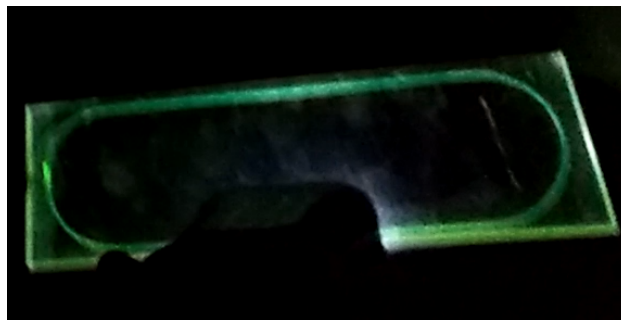


Figure 27: A flashlight held to a tile in the dark; no light apparently travels to neighboring tiles.

After polishing, the supersectors are wrapped in white DuPont 1055B polyethylene Tyvek cut to shape as shown in Fig. 28. This is done to encourage light reflecting into the tiles when exiting the faces. Afterwards, two layers of black paper with fabric on one side were similarly wrapped to keep light from entering the scintillator from external sources. Wide electrical tape was carefully applied to the corners and near the fiber connector which were more prone to light leakage. A fully completed supersector is shown in Fig. 29.

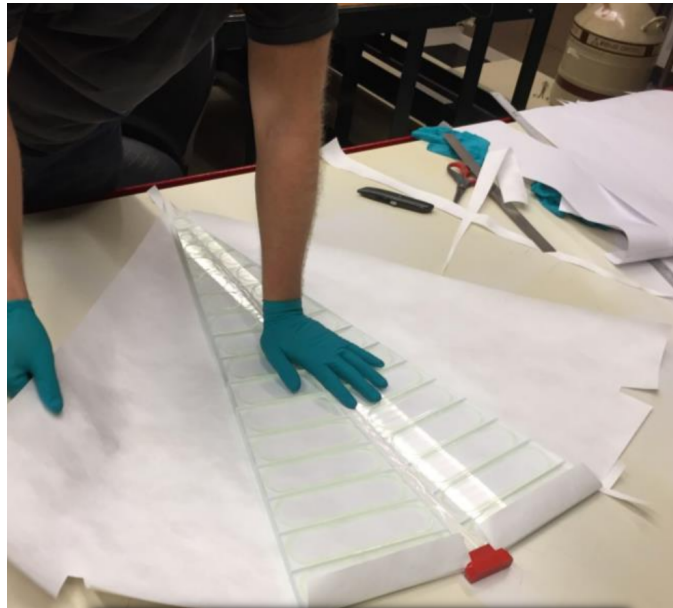


Figure 28: Wrapping the supersectors in Tyvek fabric cut to shape.

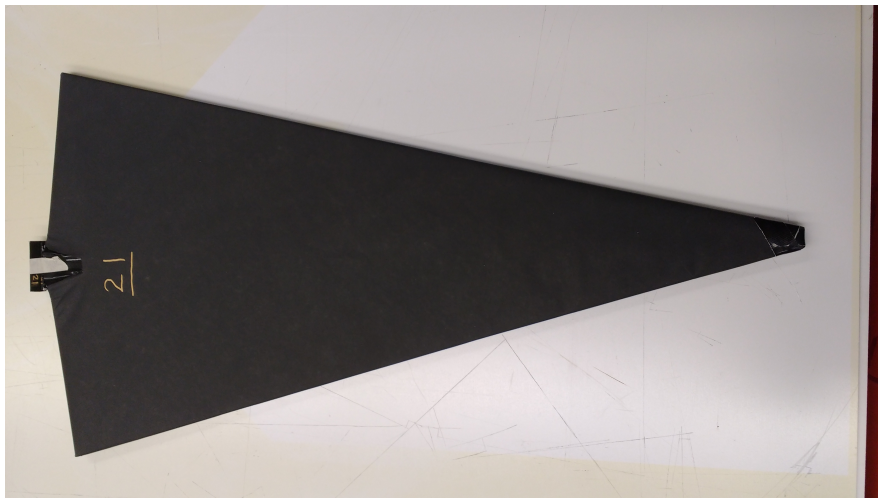


Figure 29: A fully completed supersector.

2.4 Testing

The first stage of supersector testing used cosmic rays. As shown in a cartoon in Fig. 30, four supersectors were stacked vertically and positioned such that any given tile number would be aligned vertically. The fiber connectors were attached indirectly to Silicon PhotoMultipliers (SiPMs) that generate an electric response to a photon; the ADC. The ADC distribution from a tile with no requirements (e.g. triggers) is shown in black in Fig. 31; there is a large peak at low ADC corresponding to “noise” in the SiPM.

The ADC distribution is also wide, which is in part driven by the fact that cosmic rays with varying incident angles travel different distances through the scintillator. In order to remove that contribution, we want to isolate vertical cosmic rays. If we require a “hit”, or ADC value above some threshold, in two corresponding tile numbers (e.g. tile 12 as shown in Fig. 31) from the top and bottom supersectors, then it is very likely attributed to a cosmic ray that passed through the same tile number of the two inner supersectors. We can see in Fig. 31 that making such a requirement on (nearly) vertical cosmic rays removes the noise and reduces the width of the distribution.

That “vertical” ADC distribution in blue can be fit quite well to a Landau distribution, and the width divided by the most probable value serves as a measure of how well the tile can resolve the number of particles passing through a tile at a given time. Typical values for EPD tiles were $0.1 - 0.15$.

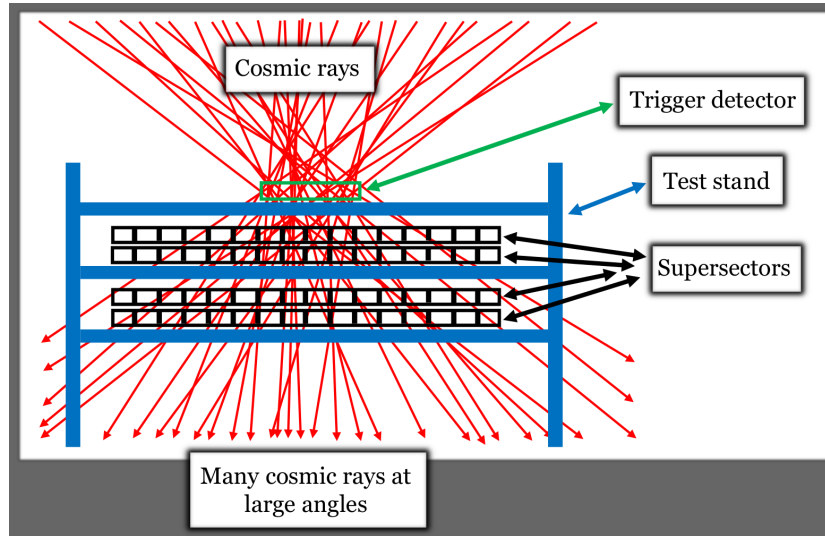


Figure 30: A cartoon demonstrating the cosmic test-stand setup. Four supersectors were stacked vertically. The top and bottom supersectors functioned as trigger detectors while the inner two supersectors were studied for quality of MIP peaks. After measuring SiPM signals for over a day, signals for a given tile number were examined when signals from the same tile numbers of the trigger detectors crossed a threshold.

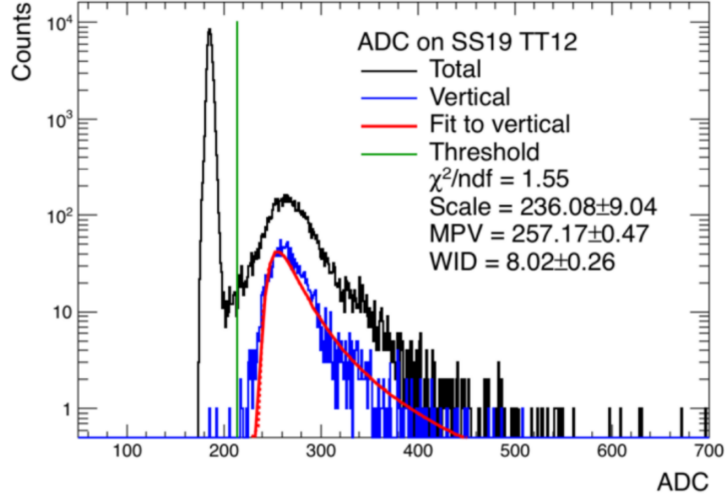


Figure 31: Using the offline trigger selection, it is possible to isolate ADC distributions of vertical cosmic rays from those of all incident cosmic rays as shown in Fig. 30.

We were also careful to check the tiles for “cross talk” where a signal in one tile might generate a false signal in a neighboring tile for various reasons. While the picture shown in the dark in Fig. 27 is visually compelling, we need to test more rigorously. We used a low-radiation Sr source, shown in Fig. 32, with a small opening at the top to approximate vertical radiation. The Sr source was then mounted on a motorized, programmable x-y table as shown in Fig. 33.

The table was aligned and programmed to scan a handful of tiles over the course of a few hours, taking 0.5 cm steps and waiting 2 min. at each step. SiPMs corresponding to individual tiles were then read out and “heat maps” such as the one shown in Fig. 34 revealed at least somewhat compelling tile separation. The background (noise) level is apparent across the entire range scanned. By projecting onto the even or odd tiles, we can examine the signal

above noise for neighboring tiles as the Sr source moves, as in Fig. 35. There, it is clear that cross-talk is negligible. The measured enhanced signal above background is consistently < 2 for all tiles.



Figure 32: The Sr source used, and wrapped in thin Pb sheets. A small opening of diameter 5 mm allows the radiation to travel nearly vertical.



Figure 33: The Sr source mounted indirectly to the x-y motors that can be programmed to follow a series of step-wait-step.

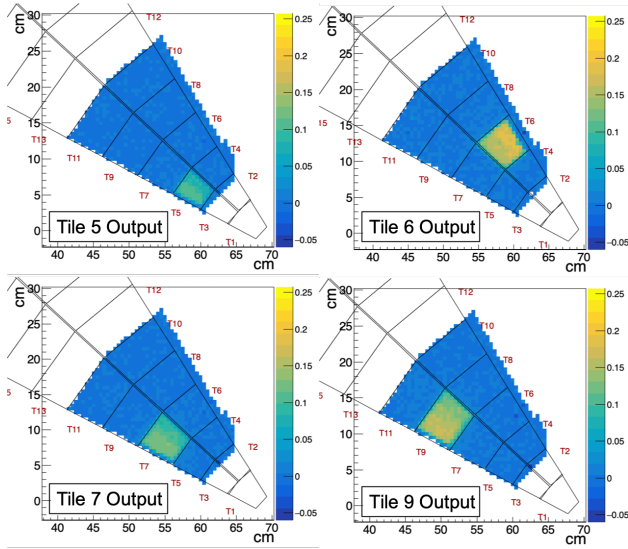


Figure 34: The signal outputs from a handfull of EPD tiles as the Sr source covers a surface area. It is clear that each tile “lights up” when the source is directly underneath, and there is no apparent cross-talk. Figure from [8].

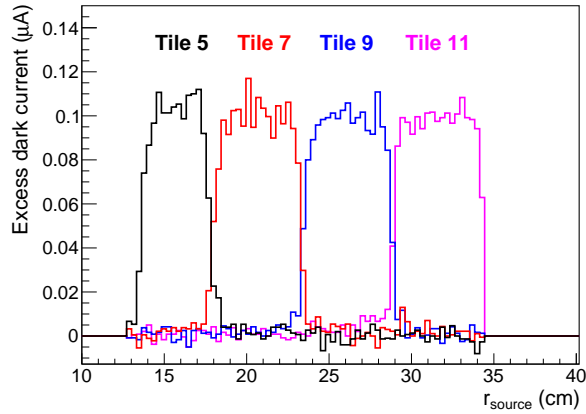


Figure 35: Here is shown the current above the background value when the laboratory lights are completely off and no Sr source is near. There is no apparent cross-talk between adjacent tiles. Figure from [8].

3 Global Λ polarization in Au+Au collisions

at $\sqrt{s_{\text{NN}}} = 3 \text{ GeV}$

3.1 Introduction

In relativistic heavy-ion collisions, there is substantial angular momentum that depends on $\sqrt{s_{\text{NN}}}$; for the energy range spanned by RHIC, $|\vec{J}_{\text{sys.}}| \sim \mathcal{O}(1 - 100 \frac{\text{TeV fm}}{c})$. The majority of this remains in the spectators and forward-going particles while a fraction is transferred to the QGP (see Fig. 65). If the Lorentz-contracted nuclei were disks of uniform thickness this would not be true; however, due to the radially decreasing density profile (as seen as a projection in the transverse plane in Fig. 67) one “side” of the QGP carries more forward-going particles than the other, and there is a net angular momentum in the QGP (defined using “participant” notation, \vec{J}_{part}). Via spin-orbit coupling, this \vec{J}_{part} is transferred in part to the spin polarization of partons within the QGP. Due to angular-momentum conservation, \vec{J}_{part} will be transferred in part to the spin polarization of hadrons.

To measure this experimentally, one would want to correlate the direction of global hadron spin, \hat{S} , with \hat{J}_{syst} (though \hat{J}_{part} may seem a more natural choice; this is discussed later, in Sec. 4). While measuring \hat{S} of a generic particle would be quite difficult experimentally, some particles reveal the direction of their spins by preferential “decay orientations”. The most straightforward

particle to use is the Λ hyperon via the decay channel $\Lambda \rightarrow p^+ + \pi^-$ which accounts for the majority of Λ -hyperon decays. The proton is emitted preferentially along the direction of the Λ hyperon's spin, and the corresponding decay parameter is $\alpha_\Lambda = 0.732 \pm 0.014$ [69]. Recall that the reaction plane is spanned by $\hat{b} \times \hat{p}_{\text{beam}}$ and is orthogonal to \vec{J}_{syst} ; the angle it makes with \hat{x} in the detector system is the reaction-plane angle, Ψ_{RP} . This is estimated by the first-order event-plane angle, Ψ_1 , and the resolution, $R_{\text{EP}}^{(1)}$, describes how well the two are correlated. For a symmetric detector and colliding system, we may write the polarization as

$$\overline{P}_\Lambda \equiv \left\langle \vec{P}_\Lambda \cdot \hat{J}_{\text{sys.}} \right\rangle = \frac{8}{\pi \alpha_\Lambda} \frac{1}{R_{\text{EP}}^{(1)}} \left\langle \sin(\Psi_{\text{EP},1} - \phi_p^*) \right\rangle^{\text{sig}}. \quad (7)$$

In a publication by the STAR collaboration in 2007 at $\sqrt{s_{\text{NN}}} = 62.4, 200$ GeV, this was measured to be consistent with zero; however, studying the effect across a range of lower $\sqrt{s_{\text{NN}}}$ demonstrated a rising \overline{P}_Λ with falling $\sqrt{s_{\text{NN}}}$ (see Fig. 36). Later, higher-statistics data sets at $\sqrt{s_{\text{NN}}} = 200$ GeV by the STAR collaboration [50] and later at $\sqrt{s_{\text{NN}}} = 2.76, 5.02$ GeV by the ALICE collaboration [4] demonstrated $\overline{P}_\Lambda < 0.5\%$.

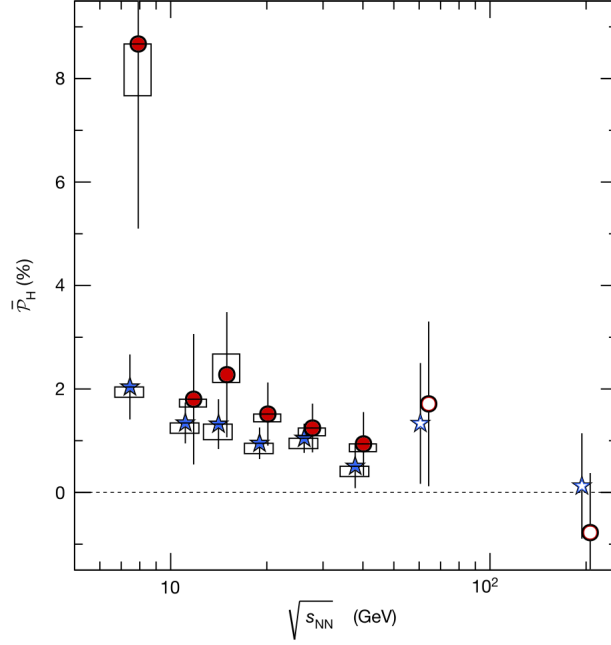


Figure 36: \bar{P}_Λ measured by the STAR collaboration in [7] across the BES range of $\sqrt{s_{NN}}$. Clearly, as $\sqrt{s_{NN}}$ decreases, \bar{P}_Λ increases. Earlier measurements at higher $\sqrt{s_{NN}}$ are shown, studied in [2], that are consistent with zero.

The trend of falling \bar{P}_Λ with $\sqrt{s_{NN}}$ is convincing, and one wonders how low in $\sqrt{s_{NN}}$ the trend can continue. At $\sqrt{s_{NN}} = 2m_N$, $|\vec{J}_{\text{syst}}|$ is zero and therefore so must \bar{P}_Λ . Very recent theoretical calculations find a peak \bar{P}_Λ near $\sqrt{s_{NN}} \approx 3$ GeV [31, 24]. This study aims to achieve the experimental measure of \bar{P}_Λ at $\sqrt{s_{NN}} = 3$ GeV.

3.2 Event and Λ selection

Event selection

In order to achieve the collision energy of $\sqrt{s_{\text{NN}}} = 3$ GeV, the “yellow” ion storage ring (carrying ions counter-clockwise around RHIC when viewed from above and eastward at STAR’s location on the south side of RHIC) held ions with nucleon energy 3.85 GeV and was steered downward by a few centimeters to hit a thin Au foil positioned at $z = 200$ cm (see Fig. 37). An “event” was recorded if there was an above-threshold signal in both the East BBC and in the TOF. A total of over a third of a billion events were recorded, although not all recorded events were usable.

Gold Target Installed for Run 14

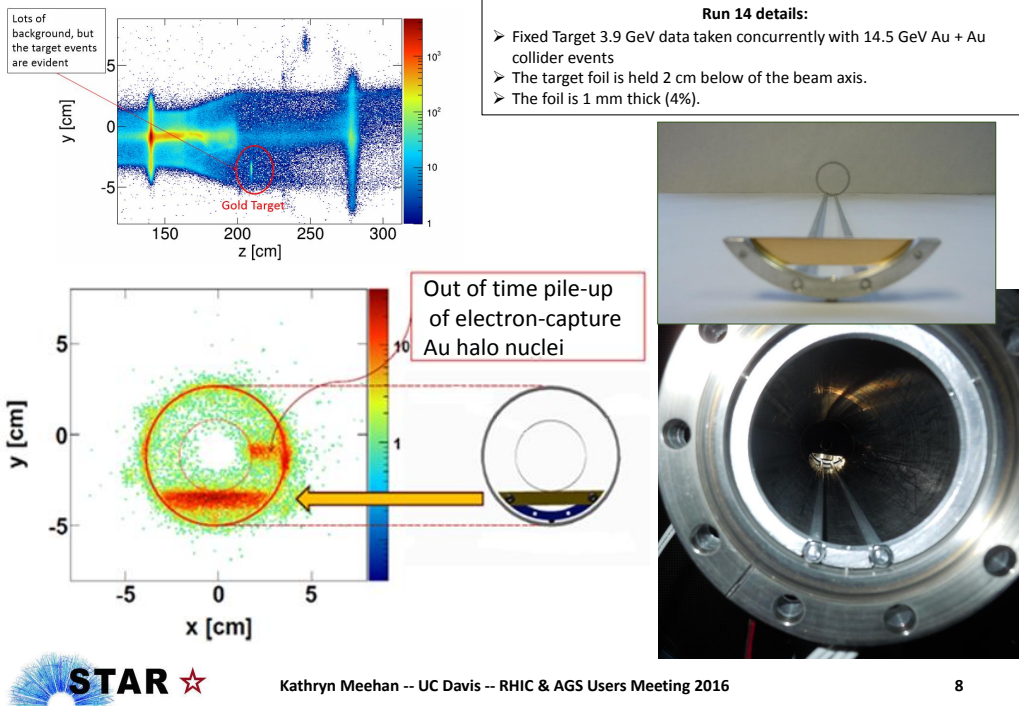


Figure 37: A slide from [48], demonstrating the Au target's position.

The “primary vertex” of an event is determined by tracing the measured particles’ tracks back to a common origin (which is not shared by all tracks; e.g. products of decays) and approximates the point of collision. Figure 37 shows the distribution of the primary vertices in the $y - z$ and $x - y$ planes; it is obvious that a significant number of events occurred as a result of beam interactions with the beam pipe and with the fixed-target support structure. In order to filter these events out, we simply impose appropriate “cuts”, or selections, on v_z and $v_T = \sqrt{v_x^2 + (v_y - 2 \text{ cm})^2}$

Additional cuts are imposed on events with too many “primary tracks” (those whose paths can be traced to within 3 cm of the primary vertex) which correspond to “pileup” events (in which the tracks from multiple collisions were recorded), events that were marked as “bad” by the operators at the time of data taking (for various reasons), and events which were later found to have other problems. In order to maintain consistency across analysis performed on a given data set, standard practice dictates that a dedicated group of people build these qualifications for and lists of bad runs. The experimental nuclear physics group at the University of California at Davis performed these studies; further details can be found in appendix A.1

Λ selection

We are interested in measuring \overline{P}_H using Λ hyperons, through the decay $\Lambda \rightarrow p^+ + \pi^-$. Recall that STAR’s magnetic field is aligned with $-\hat{z}$ and therefore the positively and negatively charged particles curve in opposite directions. Typically [7], one will first identify protons and pions using the track curvatures, energy loss in the TPC, and (if applicable) measured mass using the methods described in Sec. 1.2. Additionally, one will impose a series of quality selections, or “cuts” on each particle. In order to avoid contributions of “spallation” protons originating from beampipe interactions, a standard cut of $p_T \geq 0.4$ GeV/ c is applied to the protons, and to avoid tracking issues associated with low momentum, a cut of $p_T \geq 0.15$ GeV/ c is applied to the pions. In order to neglect very poor position and momentum resolution, a cut on the minimum number of TPC signals associated with a track of ≥ 15 is applied.

Then, a series of cuts are applied to each $[p, \pi]$ pair to determine whether they likely originated from a Λ decay. The most obvious is perhaps on the separation between their helical paths; if the *measured* Distance at Closest Approach (DCA) is larger than, say 1 cm, then the proton and pion probably did not originate from a decay. Furthermore, if the (again, *measured*) DCA between either of the helical paths and the primary vertex is very small, say less than 1 cm, then the relevant particle likely originated from the primary vertex rather than a decay, later on.

Two final cuts are imposed on the Λ “candidate” reconstructed using the $[p, \pi]$ pair. The DCA of the Λ to the primary vertex must be sufficiently close in order to filter out Λ s that were not directly emitted from the collision (i.e. which were a product of another decay). Finally, the decay length of the Λ must be sufficiently large to neglect the abundance of primary protons and pions (those originating directly from the collision) that would pass the prior cuts more easily.

While we ultimately did perform the above procedure for reconstructing Λ hyperons, we did so only in our studies of systematic effects. For the quoted results, we used a machine-learning-based algorithm which achieves overall better purity, called KFParticle [71, 27]. Details on our usage of KFParticle, as well as the specific cuts used in our Λ reconstruction for the systematics study and further Λ kinematic cuts, can be found in appendix A.2

A reconstructed Λ has a measured invariant mass, $m_{\text{inv.}}$, associated with it. The true Λ mass as quoted by the Particle Data Group (PDG), $m_{\Lambda, \text{PDG}}$, is 1.11568 GeV/ c ; we might then expect to see a distribution of $m_{\text{inv.}}$ from reconstructed Λ s to be peaked about $m_{\Lambda, \text{PDG}}$ where a significant fraction

of counts on the peak correspond to legitimate Λ decays and the majority of counts outside the peak to be $[p, \pi]$ pairs that coincidentally passed the series of cuts and are falsely reconstructed Λ s (called the “combinatoric background”). Figure 38 demonstrates the $m_{\text{inv.}}$ distributions of Λ s reconstructed using KFPARTICLE as well as the “manual” cuts used for the systematics study.

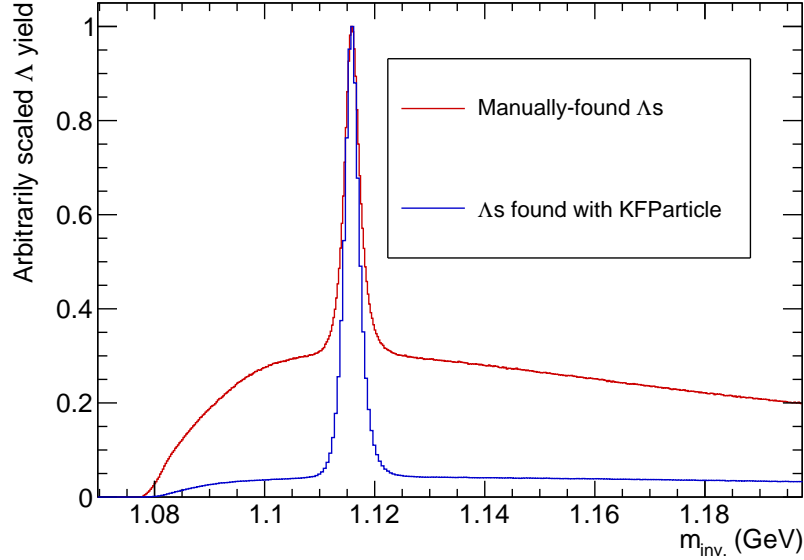


Figure 38: $m_{\text{inv.}}$ distribution for Λ s found using the traditional method compared to that with those found using the KFPARTICLE package.

3.3 Event-plane determination

Measuring Ψ_1 with the EPD

Recall the reaction plane, which is spanned by $\vec{p}_{\text{beam}} \times \vec{b}$. Because of finite statistics and detector acceptance, as well as event-by-event fluctuations, it is impossible to know the orientation of the reaction plane, Ψ_{RP} , exactly. We can only estimate Ψ_{RP} through the azimuthal distribution of emitted particles, which yields an event-plane angle. We are interested in the first-order event-plane angle, $\Psi_{\text{EP},1}$, which is given as [62]

$$\Psi_{\text{EP},1} = \text{atan2} \left(\sum_i w_i \sin \phi_i, \sum_i w_i \cos \phi_i \right), \quad (8)$$

where atan2 is the C++ function and the sum is carried out over the particles in a chosen region of p_{T}, y , etc. In the case of a scintillator detector such as the EPD (used for our determination of $\Psi_{\text{EP},1}$), we don't have access to these variables; we can only choose a region in η . The choice of weight, w_i , varies, but at least should involve $\text{sign}(y)$. Our precision on ϕ_i is limited due to the tile angular width of $\pi/12$ (or $\pi/6$ in the case of the inner EPD ring; see Fig. 15), so we choose a random point within the tile (see appendix D). At larger $\sqrt{s_{\text{NN}}}$ and when using the EPD for $\Psi_{\text{EP},1}$ measurement, an additional factor is included: the strength of the measured signal ("ADC"), which is loosely related to the number of particles that had passed through a tile. At $\sqrt{s_{\text{NN}}} = 3$ GeV, the multi-hit probability is very small, so we do not apply this additional factor to the weight.

In either case, a signal strength must pass a threshold in order to be con-

sidered a “hit”, to exclude detector “noise”. Through fitting performed on the ADC distribution using Landau distributions (carried out separately during the data-calibration process), one can apply this cut in units of “number of minimum-ionizing particles”, or nMIP. The advantage of the nMIP units over the ADC units is that they scale with offsets or gains in ADC. The ADC distribution and its Landau fits are shown in Fig. 39 at higher $\sqrt{s_{NN}}$ where multiple peaks are visible. Regardless of $\sqrt{s_{NN}}$, the effects of noise are negligible above nMIP=0.3 and we therefore apply this cut.

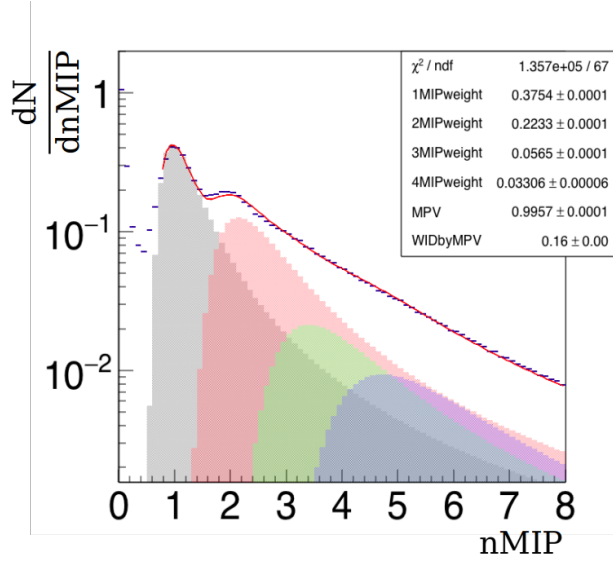


Figure 39: The nMIP distribution of inner EPD rings along with the multiple Landau fits each corresponding to a different number of MIPs passing through the tile in an event. The data shown is taken at $\sqrt{s_{NN}} = 27$ GeV where multi-hit probability is large relative to that at $\sqrt{s_{NN}} = 3$ GeV. Image courtesy of Xiaoyu Liu.

Only the east side of the Event-Plane Detector (EPD) is used since essentially no produced particles pass through the west side of the EPD. Because

we don't have a symmetric collider/detector system for this data set, we use the three-subevent method for determining $R_{\text{EP}}^{(1)}$, comparing Ψ_1 measured using the subevent of choice to Ψ_1 measured using reference subevents $\Psi_{1,\text{Ref.1}}$ and $\Psi_{1,\text{Ref.2}}$ [52]:

$$R_{\text{EP}}^{(1)} = \sqrt{\frac{\langle \cos(\Psi_1 - \Psi_{1,\text{Ref.1}}) \rangle \langle \cos(\Psi_1 - \Psi_{1,\text{Ref.2}}) \rangle}{\langle \cos(\Psi_{1,\text{Ref.1}} - \Psi_{1,\text{Ref.2}}) \rangle}}. \quad (9)$$

Although we could use the entire east EPD wheel for the measurement of Ψ_1 , our $R_{\text{EP}}^{(1)}$ would be overestimated because of momentum-conservation effects that are substantial in collisions of low energy (and therefore low multiplicity); see Sec. B.1. As detailed in appendix B.1, only the outer four wheels of the EPD are used for the determination of $\Psi_{\text{EP},1}$. As detailed in appendix B.2, the two reference subevents are tracks in the TPC with $-0.5 < \eta < -0.4$ and $-0.2 < \eta < -0.1$.

Due to a number of factors, including non-uniformity of detector acceptance, the distribution of $\Psi_{\text{EP},1}$ will not be completely flat. If these “raw” event-plane angles are used, there will be an overall preference of some orientation. The process involved in forcing a flat distribution, and thereby removing any such preference, is detailed in appendix C. After this procedure, we run through all events again to correlate the Ψ_1 s and subsequently calculate $R_{\text{EP}}^{(1)}$ according to Eq. 9.

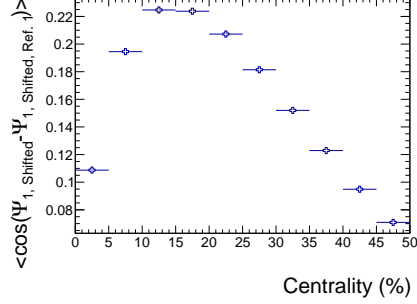


Figure 40: The Ψ_1 correlation between the EPD and the first TPC reference subevent as a function of centrality.

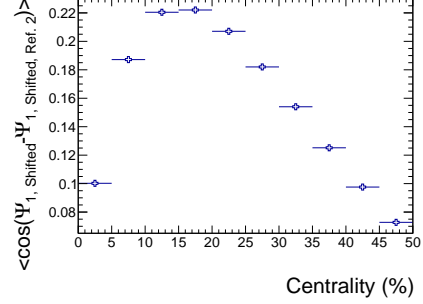


Figure 41: The Ψ_1 correlation between the EPD and the second TPC reference subevent as a function of centrality.

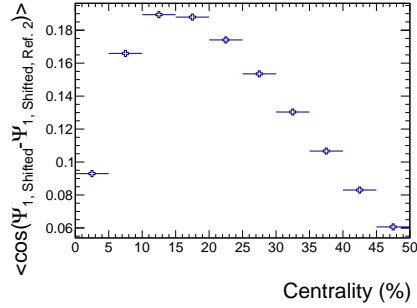


Figure 42: The Ψ_1 correlation between the two TPC reference subevents as a function of centrality.

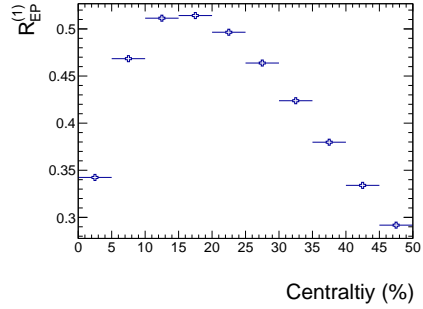


Figure 43: The $\Psi_{1, \text{EPD}}$ resolution as a function of centrality, using the correlations between each subevent pair (Figures 40, 41, and 42) using Eq. 9.

We see in Figs. 40, 41, 42, and 43 these correlations and the resultant $R_{\text{EP}}^{(1)}$ of the EPD rings used, as a function of collision centrality.

\vec{B}_{STAR} -driven $\Psi_{1,\text{EPD}}$ rotation

As we know, the STAR magnetic field, \vec{B}_{STAR} , runs parallel to the beam thereby bending charged-particle tracks in the transverse plane. This is necessary for crucial TPC measurements, but poses a potential problem when measuring Ψ_1 with any detector that lacks tracking; the azimuthal position of a charged particle does not accurately reflect the azimuthal position of that charged particle at its DCA to the primary vertex. This is a simple derivation of the azimuthal angle of relativistic charged particle traveling in a constant magnetic field $\vec{B} = B\hat{z}$; we start from $\vec{F} = \gamma m \vec{a}$:

$$\gamma m \frac{d\vec{v}}{dt} = q\vec{v} \times \vec{B} = qB (v_y \hat{x} - v_x \hat{y}). \quad (10)$$

Looking at the x and y directions separately, and using

$$\vec{\omega} = -\frac{q\vec{B}}{\gamma m}, \quad \omega = -\frac{qB}{\gamma m}, \quad (11)$$

we have

$$\frac{dv_x}{dt} = -\omega v_y, \quad \frac{dv_y}{dt} = \omega v_x, \quad (12)$$

which lead to the familiar

$$\frac{d^2 v_x}{dt^2} = -\omega^2 v_x, \quad \frac{d^2 v_y}{dt^2} = -\omega^2 v_y, \quad (13)$$

which have the solutions

$$v_x = a_1 \sin(\pm\omega t + b_1), \quad v_y = a_2 \sin(\pm\omega t + b_2). \quad (14)$$

We can consider the fact that the initial velocity in the $x - y$ plane is given in terms of the initial azimuthal angle ϕ_0 as

$$v_x = |\vec{v}_\perp| \cos(\phi_0), \quad v_y = |\vec{v}_\perp| \sin(\phi_0) \quad (15)$$

along with Eq. 14 taken at $t = 0$,

$$v_x = a_1 \cos(b_1), \quad v_y = a_2 \cos(b_2), \quad (16)$$

to see that $a_1 = a_2 = |\vec{v}_\perp| \equiv v_\perp$, $b_1 = \phi_0 + \pi/2$, and $b_2 = \phi_0$. Integrating, we then have:

$$x = \frac{v_\perp}{\pm\omega} \sin(\pm\omega t + \phi_0) + c_1, \quad y = \frac{-v_\perp}{\pm\omega} \cos(\pm\omega t + \phi_0) + c_2. \quad (17)$$

Taking $t = 0$ yields

$$c_1 = x_0 - \frac{v_\perp}{\pm\omega} \sin(\phi_0), \quad c_2 = y_0 + \frac{v_\perp}{\pm\omega} \cos(\phi_0), \quad (18)$$

leading to the time-dependent azimuthal angle

$$\phi(t) = \text{atan2}\left(\frac{-v_\perp}{\pm\omega} [\cos(\pm\omega t + \phi_0) - \cos(\phi_0)] + y_0, \frac{v_\perp}{\pm\omega} [\sin(\pm\omega t + \phi_0) - \sin(\phi_0)] + x_0\right), \quad (19)$$

where $\text{atan2}(y,x)$ is the C++ function.

We would like to remove the explicit presence of time. Looking at the z

direction, we have

$$t = \frac{\Delta z}{v_z} = \frac{\gamma m \Delta z}{p_z} \Rightarrow \omega t = -\frac{qB \Delta z}{p_z}. \quad (20)$$

If we take for simplicity a particle with initial momentum $\vec{p} = |\vec{p}|\hat{x}$, starting at the origin, we have

$$x = \frac{v_\perp}{\pm\omega} \sin(\pm\omega t), \quad \frac{-v_\perp}{\pm\omega} [\cos(\pm\omega t) - 1]. \quad (21)$$

We can then use the right-hand rule to determine whether we take the positive or negative sign for the ω , and see that it should be the positive sign. For this simple example, we then have:

$$\phi(p_z) = \text{atan2} \left[1 - \cos \left(-\frac{qB \Delta z}{p_z} \right), \quad \sin \left(-\frac{qB \Delta z}{p_z} \right) \right] \quad (22)$$

For the sake of generality, the momentum-dependent azimuthal angle is

$$\phi(p_z) = \text{atan2} \left(\frac{-v_\perp}{\omega} [\cos(\omega t + \phi_0) - \cos(\phi_0)] + y_0, \right. \\ \left. \frac{v_\perp}{\omega} [\sin(\omega t + \phi_0) - \sin(\phi_0)] + x_0 \right). \quad (23)$$

We see from Eq. 22 that, surprisingly, the azimuthal rotation of a charged track due to \vec{B}_{STAR} is independent of p_T . Intuitively, we might expect p_T dependence because low- p_T tracks have higher curvatures, but over a given distance in z , the azimuthal rotation is independent of this curvature. Checks don't hurt though, so Fig. 44 shows Eq. 22 plotted alongside a simulation of the same scenario using StPhysicalHelix, and the two agree.

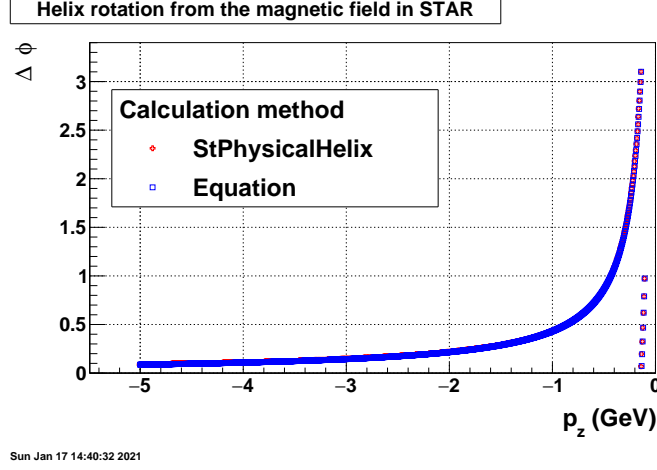


Figure 44: Azimuthal rotation of charged tracks due to \vec{B}_{STAR} as a function of p_z . Eq. 22 and Helix calculations agree.

We also see from Eq. 22 that the collision energy of this analysis presents the worst-case scenario for $\Psi_{1,\text{EPD}}$ rotation; Δz , at 2 m, is twice as large as the average in collider mode, p_z is on average smaller than any other RHIC energy reached so far, and forward-rapidity tracks are almost entirely positive (at higher energies, where there is more charge symmetry, positive and negative tracks curl in opposite directions and the net effect is closer to a smearing rather than a rotation). We can measure this effect through the distribution of $\Psi_{1,\text{TPC}} - \phi_{\text{EPDhit}}$. The charge asymmetry or average p_z may depend on collision centrality, so we check the centrality dependence; Fig. 46 shows such a distribution. The distributions are fitted with a cosine, and the phase shifts are indicative of the \vec{B}_{STAR} -induced azimuthal rotation. There is no apparent reason why the extracted phase shift would depend on the TPC subevent chosen, so we use different TPC subevents as a check. Fig. 47 shows the extracted phase shifts (with an additional shift by π as an effective rapidity weight - the

TPC and EPD lie on opposite sides of mid-rapidity) with respect to collision centrality and TPC subevent of choice. The surprising dependence on TPC subevent is something that indicates a problem; any non-unity $R_{\text{EP}}^{(1)}$ would only impact the amplitude of the cosine fit and any non-flow correlations would only impact $\langle \cos(\Psi_{1,\text{TPC}} - \phi_{\text{EPDhit}}) \rangle$, not $\langle \sin(\Psi_{1,\text{TPC}} - \phi_{\text{EPDhit}}) \rangle$. We can, however, see that this dependence on subevent is dominant only at centralities over 50%; we can, for a given centrality, take the range of phase shifts determined from different TPC subevents as the uncertainty, and plot the average values across centrality (Fig. 48). The disagreement above 50% centrality is not understood, and follows a similar pattern in this analysis of strange behavior above 50% centrality. Below 50% centrality, there is no observed centrality dependence or TPC subevent dependence of the rotation; it is roughly constant at around 0.058 radians, or about 3 degrees. We could take the average value as the angle by which we correct $\Psi_{1,\text{EPD}}$, with its standard deviation of 0.0014 as the systematic uncertainty, but this would be an under-estimation. If we truly want to measure our uncertainty in the value of $\Delta\Psi_{1,\text{EPD}}$ then we ought to take the range in uncertainty with the mid-point of the range as the correction; this leaves us with 0.063 ± 0.011 .

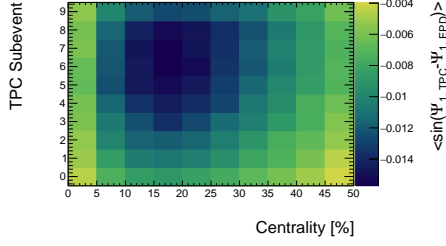


Figure 45: Another way to quantify the rotational effects of \vec{B}_{STAR} on $\Psi_{1, \text{EPD}}$; although we might expect this to look similar to Fig. 47, the observed rotation is smaller. The dependence on TPC subevent is expected because here $R_{\text{EP}}^{(1)}$ effects come into play. TPC subevent 0 covers $-1 < \eta < -0.9$, subevent 1 covers $-0.9 < \eta < -0.8$, and so on.

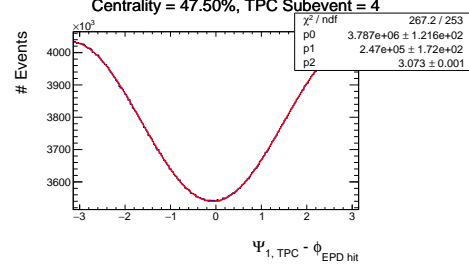


Figure 46: $\Psi_{1, \text{TPC}} - \phi_{\text{EPD hit}}$ for 45-50% centrality. The distribution is fitted with a cosine of vertical offset $p0$, amplitude $p1$, and phase $p2$; the phase is due to the \vec{B}_{STAR} -induced azimuthal rotation.

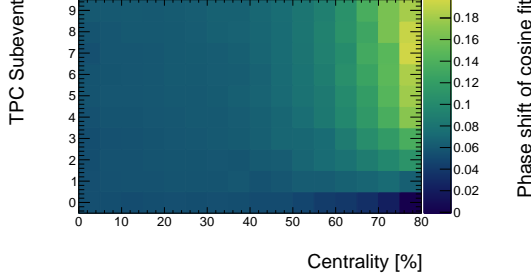


Figure 47: The extracted phase shifts of cosine fits to $\Psi_{1,\text{TPC}} - \phi_{\text{EPDhit}}$ are plotted against collision centrality and TPC subevent (excuse the label; TPC subevent 0 covers $-1 < \eta < -0.9$, subevent 1 covers $-0.9 < \eta < -0.8$, and so on). The shift by π is included because there is no rapidity weighting; the TPC and EPD lie on opposite sides of mid-rapidity. We see here a dependence on TPC subevent, which indicates a problem.

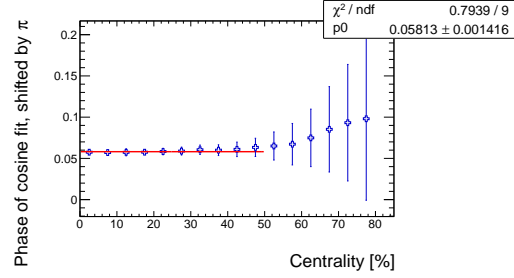


Figure 48: Phase shifts of cosine fits to $\Psi_{1,\text{TPC}} - \phi_{\text{EPDhit}}$ across centrality, with the uncertainties displaying the range in values determined by different TPC subevents. In principle they should all agree, and they do up to around 50% centrality.

3.4 Polarization observable

The restricted invariant-mass method

Absent STAR efficiency corrections, the polarization observable is given by

$$\overline{P}_\Lambda = \frac{8}{\pi \alpha_\Lambda} \frac{1}{R_{\text{EP}}^{(1)}} \langle \sin(\Psi_1 - \phi_p^*) \rangle, \quad (24)$$

where α_Λ is the Λ 's decay parameter and ϕ_p^* is the azimuthal angle of the daughter proton in the Λ rest frame at the decay. We know that when

we reconstruct Λ s, we inevitably have $p - \pi$ pairs that just happen to pass cuts (“the background”). The background, for various reasons, can have a non-zero \overline{P}_Λ , but of course we do not want to include any background polarization in our measurement of \overline{P}_Λ . The typical procedure is as follows: First, fit the $m_{\text{inv.}}$ distribution assuming functional forms for the signal and background regions separately (we found a second-degree polynomial for the background and a set of two Gaussian distributions for the signal to work quite well). Second, simply divide the signal fit function by the background fit function and vice versa to get the signal fraction and background fraction as functions of $m_{\text{inv.}}$ ($f^{\text{sig.}}(m_{\text{inv.}})$ and $f^{\text{bgd.}}(m_{\text{inv.}})$, respectively). Third, plot Eq. 24 vs. $m_{\text{inv.}}$ and fit with the function

$$\overline{P}_\Lambda^{\text{obs.}} = f^{\text{bgd.}}(m_{\text{inv.}})\overline{P}_\Lambda^{\text{bgd.}} + f^{\text{sig.}}(m_{\text{inv.}})\overline{P}_\Lambda^{\text{sig.}} \quad (25)$$

to extract the polarization associated with the true Λ s, $\overline{P}_\Lambda^{\text{sig.}}$. Though this method has worked in previous measurements with different data sets, there are problems when implementing it here. Fig. 49 demonstrates this method being applied for this data set; we see that, rather than $\langle \sin(\Psi_1 - \phi_p^*) \rangle$ following the form of Eq. 25 as it ought to, it peaks sharply near $m_{\text{inv.}} = m_{\Lambda, \text{PDG}}$ and dips sharply on each side of the peak.

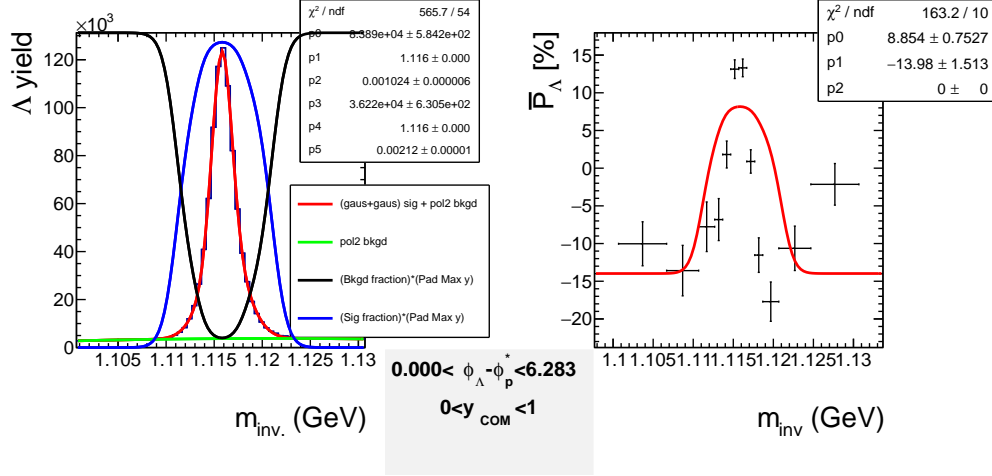


Figure 49: Here, we visually see the procedure known as the invariant-mass method. On the left panel, a second-degree polynomial fits the background (in green) and two summed Gaussian distributions fit the signal (in red). The ratios of these fits give $f^{\text{sig.}}(m_{\text{inv.}})$ (in blue) and $f^{\text{bgd.}}(m_{\text{inv.}})$ (in black). On the right panel, we see those used to fit $\langle \sin(\Psi_1 - \phi_p^*) \rangle$ with Eq. 25. It is apparent here that the fit function is not appropriate for the data, and that this method is invalid in this situation.

Now if we would take the results as they stand here, we would dramatically over-estimate the polarization, almost by a factor of 2; furthermore, we would observe significant dependence of the polarization on y , p_T , centrality, etc..

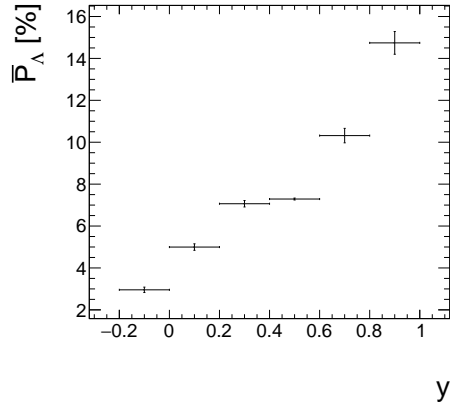


Figure 50: Polarization as a function of rapidity using the standard (and in this case invalid) method; we see dramatic behavior such that the polarization increases strongly with y , and the statistical uncertainties are such that we would quote such a dependence with certainty.

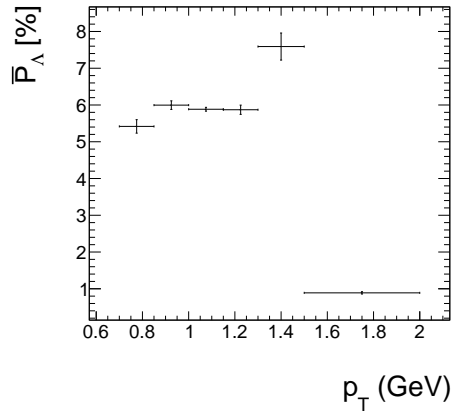


Figure 51: Polarization as a function of p_T using the standard (and in this case invalid) method; we see dramatic behavior such that the polarization increases strongly with p_T before sharply dropping off, and the statistical uncertainties are such that we would quote such a dependence with certainty.

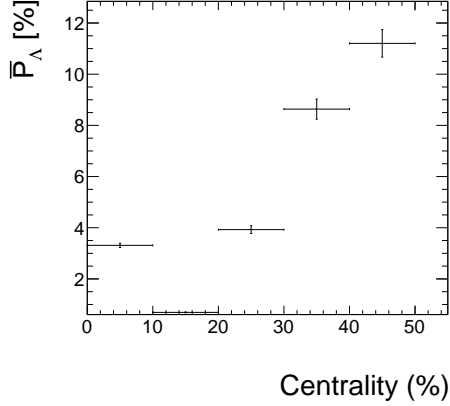


Figure 52: Polarization as a function of centrality using the standard (and in this case invalid) method; we see dramatic behavior such that the polarization increases strongly with centrality besides a sharp drop at 10-20% centrality, and the statistical uncertainties are such that we would quote such a dependence with certainty.

It is clear from Fig. 49 that the standard procedure is, in this case, inappropriate; the measured polarization does not follow the shape of the signal fraction as a function of $m_{\text{inv.}}$. If we were to ignore that fact, we would not only drastically over-estimate the integrated polarization, but we would also measure behavior as a function of y , p_T , and centrality that is completely incorrect.

The generalized invariant-mass method

We can understand this problem through a combination of a TPC tracking inefficiency (present at all energies) and an asymmetry in the detector-collider system (present only in fixed-target mode) working together to give this effect. Consider two classes of decays: those with $0 < \phi_\Lambda - \phi_p^* < \pi$ and those with $\pi < \phi_\Lambda - \phi_p^* < 2\pi$; a perfect detector would reconstruct such Λ s with equal efficiency, but the STAR TPC can better measure decays with $0 < \phi_\Lambda - \phi_p^* < \pi$. This broken symmetry comes from the STAR magnetic

field, which is along the beam axis ($\vec{B}_{\text{STAR}} = -|\vec{B}_{\text{STAR}}|\hat{z}$); the $p - \pi$ tracks from Λ s with $0 < \phi_\Lambda - \phi_p^* < \pi$ cross each other in the transverse plane while $p - \pi$ tracks from Λ s with $\pi < \phi_\Lambda - \phi_p^* < 2\pi$ immediately diverge in the transverse plane after the Λ decay. We can see this illustrated in Figures 53 and 54; keep in mind that \vec{B}_{STAR} is going into the page so that the proton will curve counter-clockwise and the pion will curve clockwise. The $m_{\text{inv.}}$ distributions differ substantially between these two classes; track-crossing decays apparently have a more sharply peaked $m_{\text{inv.}}$ distribution. We briefly pursued the cause of this effect and found that it may be due to the reconstruction algorithm choosing the decay point by minimizing $DCA_{p-\pi}$ (which may not be strictly valid), but we leave this for further study; it is not surprising in principle that these decay classes would not have equal efficiencies in the STAR TPC given that the symmetry is broken by \vec{B}_{STAR} . We henceforth refer to this effect as the “Azimuthal Emission Efficiency”, or AEE. This AEE (which exists at all energies and in both collider modes) in and of itself would not be a problem; however, in fixed-target mode we have another asymmetry that, when paired with the AEE, invalidates the invariant-mass method described above in the case of fixed-target collisions. Because, in the frame of the STAR detector, one beam is in motion while the other is fixed, the vast majority of tracks measured by the TPC are positive rapidity in the center-of-mass (COM) frame; furthermore, we measure much further into positive rapidity in the COM frame than in collider mode. We therefore have an acceptance- and efficiency-driven correlation between Ψ_1 and ϕ_Λ in fixed-target mode, even when integrated over all measured Λ s, and that correlation is strong because of the strong $v_{1,\Lambda}$ at this energy; such a

correlation, having nothing to do with any sort of physical polarization, could be measured with the very polarization correlator itself: $\langle \sin(\Psi_1 - \phi_p^*) \rangle$.

We can take an idealized scenario to understand all of this clearly. Consider two Λ s with $\phi_\Lambda = \Psi_1$ to illustrate the strong $v_{1,\Lambda}$; one decays with $\phi_\Lambda = \pi$ and the other decays with $\phi_\Lambda = 3\pi/2$ to illustrate the two decay classes $0 < \phi_\Lambda - \phi_p^* < \pi$ and $\pi < \phi_\Lambda - \phi_p^* < 2\pi$, respectively. The AEE tells us that the first decay, with $\phi_\Lambda = \pi$, will be more likely to have an $m_{\text{inv.}}$ further from $m_{\Lambda,\text{PDG}}$ than the second decay, which in turn will be more likely to have an $m_{\text{inv.}}$ closer to $m_{\Lambda,\text{PDG}}$. The first decay will also have $\langle \sin(\Psi_1 - \phi_p^*) \rangle = -1$ while the second will have $\langle \sin(\Psi_1 - \phi_p^*) \rangle = 1$; therefore, although the net $\bar{P}_\Lambda = 0$, we see positive \bar{P}_Λ at $m_{\text{inv.}} \approx m_{\Lambda,\text{PDG}}$ and negative \bar{P}_Λ to the sides. This illustration is shown in Fig. 53.

This can also be shown quite clearly with embedded Λ s, which have $v_{1,\Lambda} = 0$ and $\bar{P}_\Lambda = 0$ by default, but still exhibit the characteristic features of the AEE. By preferentially choosing embedded Λ s aligned with Ψ_1 , we can impose a non-zero $v_{1,\Lambda}(y)$ to roughly reproduce what we see in the data. With this change alone, we see the dipping and peaking in $\bar{P}_\Lambda(m_{\text{inv.}})$ characteristic of the AEE in fixed-target mode (Fig. 55). Furthermore, when applying the “traditional” invariant-mass method to this embedded Λ sample, we measure a statistically significant and positive \bar{P}_Λ . Furthermore, if we were to ignore this obvious problem and quote the polarization extracted using the “traditional” invariant-mass method, we would not only over-report \bar{P}_Λ but we would also measure a significant dependence of \bar{P}_Λ on y because v_1 increases with y !

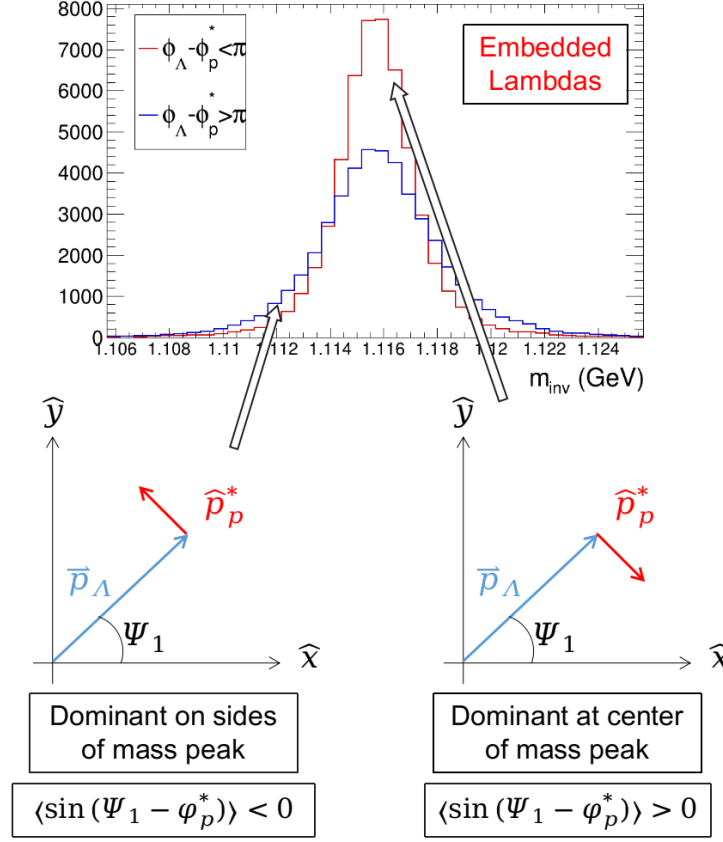


Figure 53: Here is an illustration of the simplified explanation of the observed peaking and dipping structure in $\langle \sin(\Psi_1 - \phi_p^*) \rangle(m_{\text{inv.}})$ that makes the “traditional” invariant-mass method invalid for this analysis. Because of inefficiencies in the STAR TPC, Λ decays with $0 < \phi_{\Lambda} - \phi_p^* < \pi$ $m_{\text{inv.}}$ distributions peaked more sharply around $m_{\Lambda, \text{PDG}}$ while those with $\pi < \phi_{\Lambda} - \phi_p^* < 2\pi$ are more broad. Alone this would not be problematic, but with the additional detector asymmetry present in fixed-target mode wherein we mostly measure Λ s with positive v_1 (because we measure mostly positive-rapidity tracks) (simplified with $\phi_{\Lambda} = \Psi_1$), there is a correlation between Ψ_1 and ϕ_p^* that depends on $\phi_{\Lambda} - \phi_p^*$ and has absolutely nothing to do with any sort of physical polarization.

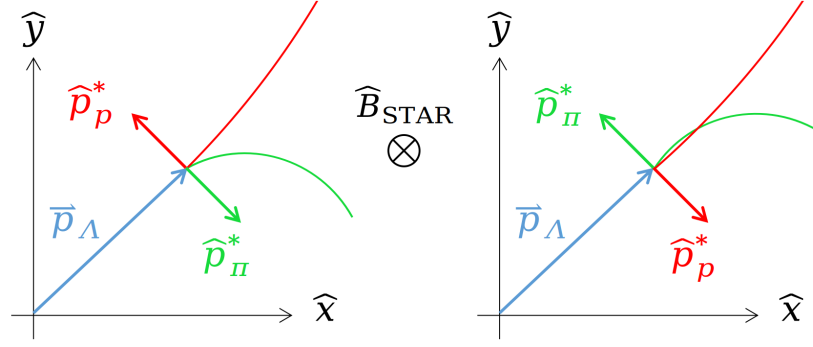


Figure 54: Here is an illustration of the daughter tracks crossing in the transverse plane. This broken symmetry comes from the STAR magnetic field, which is along the beam axis ($\vec{B}_{\text{STAR}} = -|\vec{B}_{\text{STAR}}|\hat{z}$); the $p - \pi$ tracks from Λ s with $0 < \phi_{\Lambda} - \phi_p^* < \pi$ cross each other in the transverse plane while $p - \pi$ tracks from Λ s with $\pi < \phi_{\Lambda} - \phi_p^* < 2\pi$ immediately diverge in the transverse plane after the Λ decay.

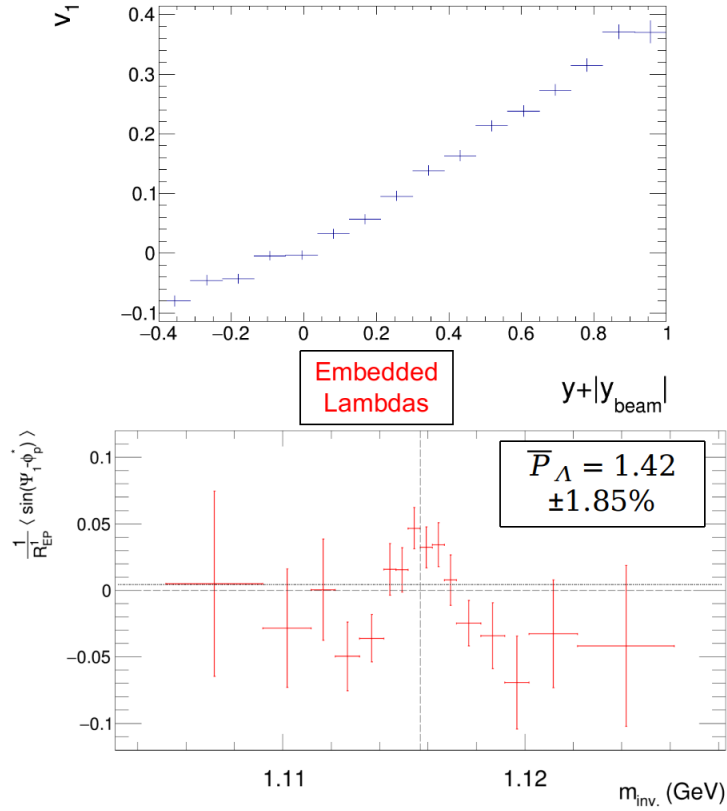


Figure 55: We impose a non-zero $v_{1,\Lambda}$ on embedded Λ s, which have $v_1 = 0$ and $\bar{P}_{\Lambda} = 0$ by default, by preferentially selecting those aligned with Ψ_1 . We simply roughly replicate the $v_{1,\Lambda}(y)$ observed with this data set. From this change alone, we measure a significant $\bar{P}_{\Lambda} > 0$ using the “traditional” invariant-mass method.

The solution to this problem is not to throw away this “traditional” invariant-mass method altogether, but instead to generalize it. Because the $m_{\text{inv.}}$ distribution itself depends on $\phi_\Lambda - \phi_p^*$ (see Fig. 56), we should follow the same steps as in the “traditional” invariant-mass method for bins in $\phi_\Lambda - \phi_p^*$ that are small enough that the AEE is not observable; we found 32 bins (or bin widths of $2\pi/32 \approx 0.2$ to work well and checked that perturbations around that number yielded consistent results. Fig. 57 demonstrates that once we constrain ourselves to small regions of $\phi_\Lambda - \phi_p^*$, the effects of the AEE are not measurable and the polarization correlator, $\langle \sin(\Psi_1 - \phi_p^*) \rangle$, clearly follows the form expected of Eq. 25. Once we do this for all bins we can plot the extracted signals, $\langle \sin(\Psi_1 - \phi_p^*) \rangle^{\text{sig.}}$, against $\phi_\Lambda - \phi_p^*$; because of the correlation between Ψ_1 and ϕ_Λ (again, even when integrating over all Λ s), $\langle \sin(\Psi_1 - \phi_p^*) \rangle (\phi_\Lambda - \phi_p^*)$ is sinusoidal. The amplitude of this curve is defined by v_1 and the phase is zero, but the vertical shift corresponds to the *true*, vorticity-driven Λ polarization, $\overline{P}_H^{\text{true}}$. Fig. 58 shows a fit to the data. This can be written as

$$\frac{8}{\pi \alpha_\Lambda} \frac{1}{R_{\text{EP}}^{(1)}} \langle \sin(\Psi_1 - \phi_p^*) \rangle^{\text{sig.}} = \overline{P}_H^{\text{true}} + c v_1 \sin(\phi_\Lambda - \phi_p^*). \quad (26)$$

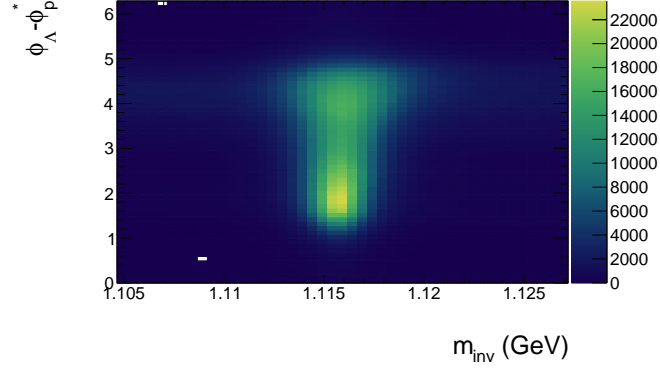


Figure 56: Here is shown the $m_{\text{inv.}}$ distribution as a function of $\phi_{\Lambda} - \phi_p^*$, and it is clear that the width of the distribution depends significantly on $\phi_{\Lambda} - \phi_p^*$...

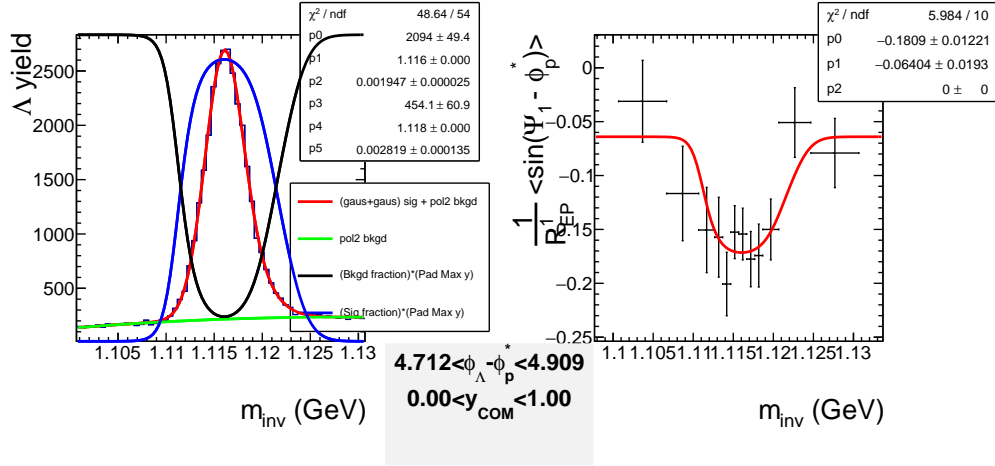


Figure 57: Here is shown the same procedure used in the “traditional” invariant-mass method except we constrain ourselves to regions of $\phi_{\Lambda} - \phi_p^*$. We see here that $\langle \sin(\Psi_1 - \phi_p^*) \rangle (m_{\text{inv.}})$ clearly follows the form expected, according to Eq. 25.

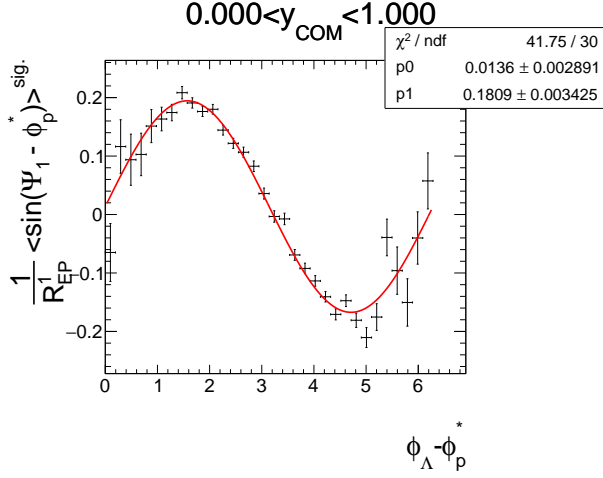


Figure 58: Here is shown the extracted $\langle \sin(\Psi_1 - \phi_p^*) \rangle^{\text{sig.}}$ with respect to $\phi_\Lambda - \phi_p^*$. We fit with a sine because of the correlation between v_1 and Ψ_1 ; the amplitude corresponds to the strength of v_1 and the vertical shift is the true, vorticity-driven polarization, \bar{P}_H^{true} .

Because this effect is in part driven by the sign of v_1 , we want to treat the cases $y < 0$ and $y > 0$ separately and average the results to get our final polarization measurement (Fig. 59). Using embedded Λ s with induced v_1 (as before), we can induce a known polarization and measure it using this method; Fig. 60 shows that, when using Λ s of positive and negative rapidity, the generalized invariant-mass method will under-report \bar{P}_H^{true} . Fig. 60 also demonstrates that we only need to treat positive and negative rapidities separately (“S” y bins, standing for “symmetric” rapidity bins) in order to accurately measure \bar{P}_H^{true} ; adding more bins in rapidity doesn’t help or hurt.

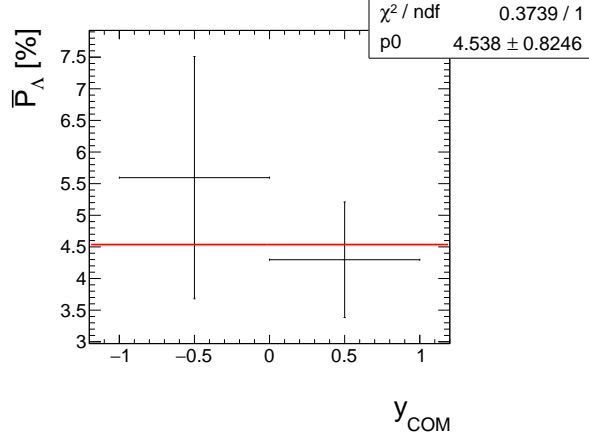


Figure 59: The true, vorticity-driven polarization extracted using the generalized invariant-mass method for negative and positive rapidity; this is fit with a horizontal line to extract the average value and statistical uncertainty.

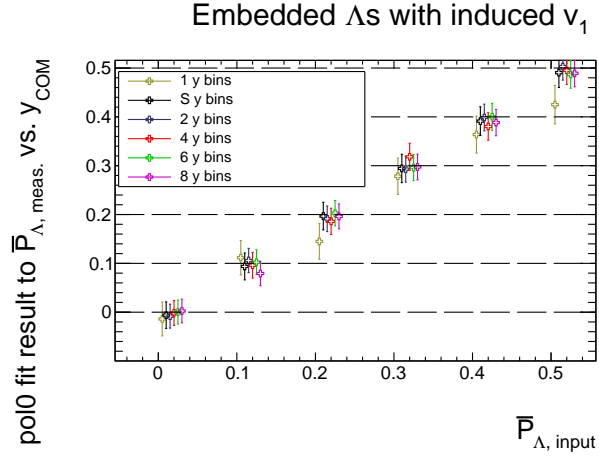


Figure 60: Measured polarization vs. input polarization for embedded Λ s with induced $v_1(y)$; we see that the polarization is under-reported if we use the generalized invariant-mass method on negative- and positive-rapidity Λ s together (“1 y bins”), but as long as we treat these two cases separately and average the results (“S y bins”, meaning symmetric bins in rapidity) then the polarization is accurately measured. More finely separating these rapidity bins neither helps nor hurts.

Fig. 60 also serves as a sort of confirmation of the generalization of this

method; we saw the same dipping and peaking structure in $\langle \sin(\Psi_1 - \phi_p^*) \rangle (m_{\text{inv.}})$ in the embedded Λ sample as we did in the real data and demonstrated that the structure lead to a false measurement, and with the generalized method we are able to reproduce the input \overline{P}_Λ .

After direct measurement of \overline{P}_Λ from this method, we apply a set of standard “efficiency corrections” due to the fact that we are not measuring all collision centralities with equal efficiency and we are not measuring all Λ s with equal efficiency. This process is described in E. Furthermore, we performed a detailed study both in search of unknown systematic effects and in quantification of the systematic uncertainties on our measurements; this is detailed in appendix F.

3.5 Results

Integrated over mid-centralty (20-50%), we measure $\overline{P}_\Lambda = 4.91 \pm 0.82(\text{stat.}) \pm 0.15(\text{syst})\%$. This result is shown in Fig. 61 alongside previous measurements [3, 7, 5, 4], which have been scaled according to the updated value of $\alpha_\Lambda = 0.732$ [70]. Also shown are calculations with various models at higher $\sqrt{s_{\text{NN}}}$ [37, 59] and recent calculations that extend to small $\sqrt{s_{\text{NN}}}$. These include the partonic AMPT model [29], the hadronic UrQMD model [24], and the 3-Fluid Hydrodynamics (3FD) model [31]. Details on the extraction of mid-centralty results from these models can be found in appendix G. While the 3FD and UrQMD models predict a sharply rising \overline{P}_Λ at $\sqrt{s_{\text{NN}}}$ below that of previous measurements, the AMPT model predicts a falling \overline{P}_Λ .

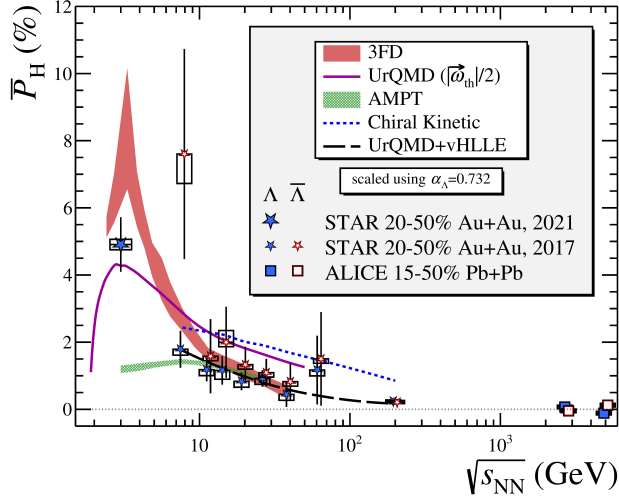


Figure 61: Statistically significant \bar{P}_Λ at $\sqrt{s_{NN}} = 3$ GeV is measured and plotted alongside previous studies [3, 7, 5, 4] and model predictions [37, 59, 29, 24, 31].

We also had sufficient statistics to study \bar{P}_Λ differentially. Shown in Fig. 62 is \bar{P}_Λ as a function of collision centrality. As was seen in a previous high-statistics data set at $\sqrt{s_{NN}} = 200$ GeV [50], as well as what is predicted by the various models [24, 29, 31], we observe increasing \bar{P}_Λ with collision centrality. What also stands in agreement with this previous measurement as well as the prediction by AMPT is the dependence (or lack thereof) of \bar{P}_Λ on p_T , shown in Fig. 63.

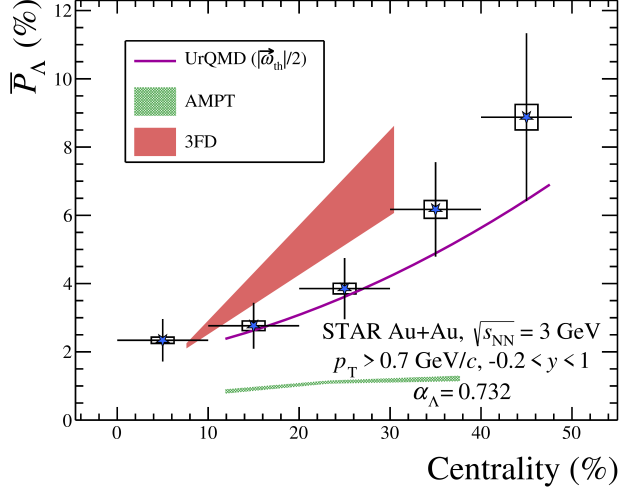


Figure 62: \bar{P}_Λ at $\sqrt{s_{NN}} = 3$ GeV, plotted with respect to centrality and alongside theory predictions at this energy [29, 24, 33]. We observe significant monotonic dependence of \bar{P}_Λ on centrality.

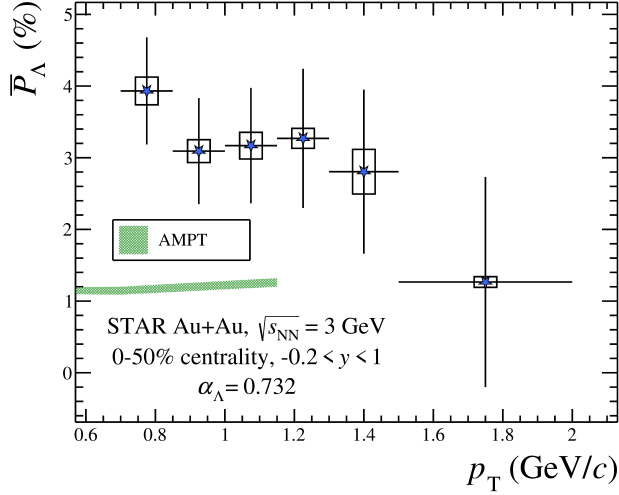


Figure 63: \bar{P}_Λ at $\sqrt{s_{NN}} = 3$ GeV, plotted with respect to p_T and alongside AMPT predictions at this energy [29]. We observe no significant dependence of \bar{P}_Λ on p_T .

The measurement of the dependence of \bar{P}_Λ on y is uniquely valuable at this collision energy and detector setup because, unlike at higher energies in collider mode, we have access to the most forward-rapidity Λ s. This is significant because many model calculations have predicted a migration of \bar{P}_Λ towards forward rapidities [36, 32, 66, 34, 33, 41, 23, 65, 67] and the most forward-rapidity regions have previously remained inaccessible. Our

measurement is shown in Fig. 64 and remarkably, we see no dependence of \bar{P}_Λ on y within statistical uncertainties. This stands in stark contrast with model predictions and casts doubt on the argument of vorticity migration towards forward rapidity as an explanation of the dependence of \bar{P}_Λ on $\sqrt{s_{\text{NN}}}$.

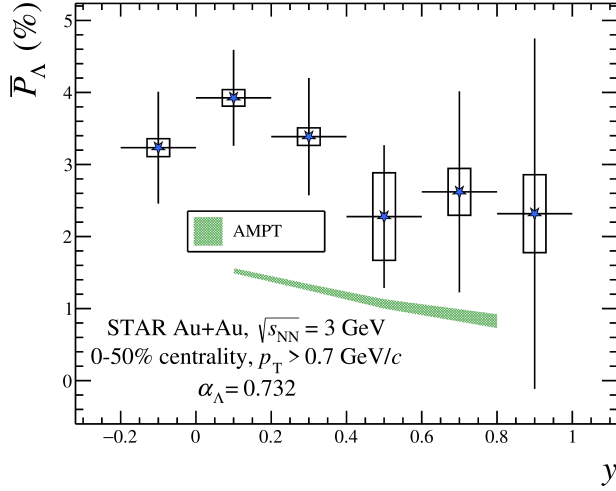


Figure 64: \bar{P}_Λ at $\sqrt{s_{\text{NN}}} = 3$ GeV, plotted with respect to y and alongside AMPT predictions at this energy [29]. We observe no significant dependence of \bar{P}_Λ on y .

3.6 Summary

This statistically significant measurement of \bar{P}_Λ at $\sqrt{s_{\text{NN}}} = 3$ GeV is the highest \bar{P}_Λ yet measured, and the lowest collision energy at which it has been measured. The result agrees roughly with predictions made within the context of the 3-Fluid Dynamics model when integrated over y ; however, it is dramatically larger than the prediction made within the AMPT framework. Low-energy extensions of the UrQMD study demonstrate striking agreement with our result despite over-estimation at higher energy; this should be taken with a grain of salt, however, as hadronization is drastically over-simplified by a simple scaling of thermal vorticity by 0.5.

The most interesting result obtained is the lack of dependence of \bar{P}_Λ on y within uncertainties. Various models have predicted an enormous dependence [36, 32, 66, 34, 33, 41, 23, 65, 67], and often one that becomes more dramatic as $\sqrt{s_{\text{NN}}}$ falls. While future measurements at higher $\sqrt{s_{\text{NN}}}$ using the STAR forward upgrade will certainly yield more insight, this data set's observed lack of such a dependence is highly valuable.

4 Initial-state fluctuations and angular momentum in heavy-ion collisions

4.1 Introduction

In non-central, high-energy heavy-ion collisions, there exists enormous system angular momentum, \vec{J}_{syst} . Across the energy range spanned by RHIC ($\sqrt{s_{\text{NN}}} = 3 - 200$ GeV), a mid-central ($b \approx 8$ fm) collision exhibits $|\vec{J}_{\text{syst}}| \sim \mathcal{O}(10^5 \hbar)$. For all but the most central collisions ($b \lesssim 2$ fm), the majority of \vec{J}_{syst} is transferred to the forward- and backward-going particles, which are dominated by spectator nucleons determined experimentally by $|y|, |\eta| \gtrsim 2 - 3$. Figure 65 demonstrates, in the simple Monte-Carlo Glauber model, an estimate of the fraction of total angular momentum carried by the spectators and by the participants, as a function of b .

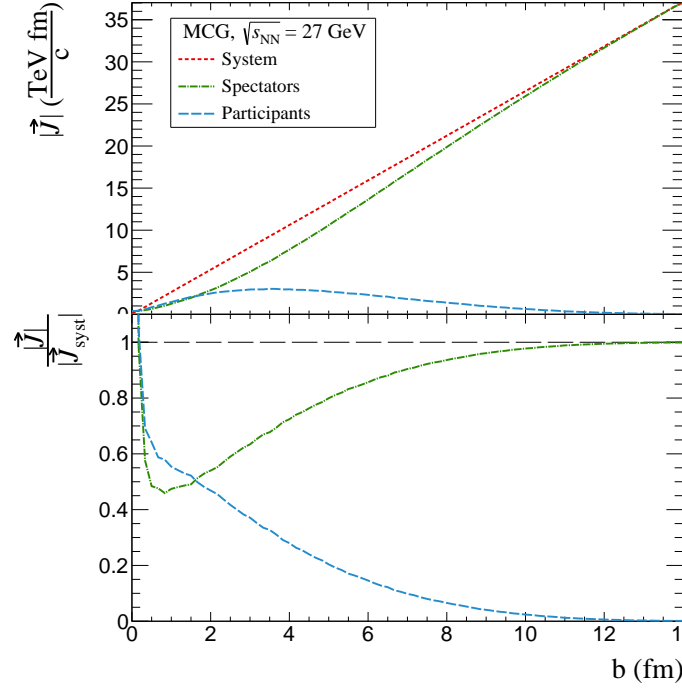


Figure 65: The magnitudes of angular momenta of the system, the participants, and the spectators, and the fraction of $|\vec{J}_{\text{syst}}|$ carried by the participants and spectators, as a function of b at $\sqrt{s_{\text{NN}}} = 27$ GeV in the Monte-Carlo Glauber model. Above $b \gtrsim 1$ fm we see $|\vec{J}_{\text{spec}}|$ take a larger fraction of $|\vec{J}_{\text{syst}}|$ as b becomes larger, since the number of spectators continually increases as does their average distance from the center of mass. Below $b \lesssim 1$ fm, however, we see $|\vec{J}_{\text{spec}}|/|\vec{J}_{\text{syst}}|$ as well as $|\vec{J}_{\text{part}}|/|\vec{J}_{\text{syst}}|$ rapidly increase as b becomes smaller, even to the point of becoming larger than 1. This is due to the fact that $|\vec{J}_{\text{syst}}| \rightarrow 0$ as $b \rightarrow 0$ while $\langle |\vec{J}_{\text{part}}| \rangle$ and $\langle |\vec{J}_{\text{spec}}| \rangle$ remain finite at $b = 0$ due to the extreme likelihood of spectators still existing for these cases.

While spectators carry most of the angular momentum of the system, the remaining $|\vec{J}_{\text{part}}|$ is still significant. The large $|\vec{J}_{\text{part}}|$ is necessary for the collision overlap region, whether there be QGP formation or not, to support vorticity aligned with \hat{J}_{part} . The vorticity, as detailed in section 3, allows us to

measure hadron spin alignment with \hat{J} , $\overline{P}_{H,J} \equiv \langle \vec{P}_H \cdot \hat{J} \rangle$. Theoretically [16, 42, 15, 17], \vec{B} is made to be parallel to \hat{x} so that \hat{J}_{syst} is parallel to $-\hat{y}$. When calculating the magnitudes of vorticity and spin polarization, these vectors are projected along $\hat{J}_{\text{syst}}||-\hat{y}$, under the correct assumption that $\hat{J}_{\text{part}}||\hat{J}_{\text{syst}}$ on average. Experimentally [3, 7, 4, 6], the azimuthal distribution of the spectators is used to calculate \hat{J}_{spec} which in turn is used in place of \hat{J}_{part} , under the correct assumption that $\hat{J}_{\text{part}}||\hat{J}_{\text{spec}}$ on average.

While it is true that $\hat{J}_{\text{part}}||\hat{J}_{\text{syst}}$ and $\hat{J}_{\text{part}}||\hat{J}_{\text{spec}}$ on average, event-by-event fluctuations will lead to $\langle \hat{J}_{\text{syst}} \cdot \hat{J}_{\text{part}} \rangle < 0$ as well as $\langle \hat{J}_{\text{spec}} \cdot \hat{J}_{\text{part}} \rangle < 0$. Although the effects of initial-state, event-by-event fluctuations have been studied in detail [12, 20, 19, 63, 54, 40, 53, 35, 44, 46, 26, 18, 45], the effects on $\langle \hat{J}_{\text{syst}} \cdot \hat{J}_{\text{part}} \rangle$ and $\langle \hat{J}_{\text{spec}} \cdot \hat{J}_{\text{part}} \rangle$ have yet to be studied.

4.2 Models

Monte-Carlo Glauber

The Monte-Carlo Glauber model is perhaps the simplest simulation of a heavy-ion collision. In essence, the nucleon positions for each nucleus are randomly sampled from a known distribution and taken to be spheres of a radius determined by $\sqrt{s_{\text{NN}}}$. The two nuclei are set a distance b apart, and two nucleons collide if they sufficiently overlap in the transverse plane. This obviously neglects many more realistic considerations, such as time evolution, deconfinement, etc., but it can serve as a baseline for expectations and is generally intuitive.

In the case of a non-deformed nucleus, such as Au, the sampling of the nucleon angular coordinates is trivial. The radial coordinate is randomly

sampled according to the Woods-Saxon distribution, given by

$$\rho(r) = \frac{\rho_0}{1 + e^{\frac{r-R}{a}}}. \quad (27)$$

Because of its common usage in heavy-ion collisions, we generate $^{197}_{97}\text{Au}$ nuclei, where $\rho_0 = 0.1693 \text{ fm}^{-3}$, $R = 6.38 \text{ fm}$, and $a = 0.535 \text{ fm}$ [25].

In Fig. 66 is shown a single *Au* nucleus with these randomly sampled nucleon positions, viewed in the transverse plane. From this we gain an intuitive sense of the degree of fluctuation of nucleon positions within the nucleus. In Fig. 67 is shown the nucleon density determined through the average of many randomly generated nuclei; there, the smoothness is obvious. An impact parameter is chosen according to $dN/db \propto b$ and the nucleons are shifted such that the centers of mass of the two nuclei are positioned at $(x, y) = (\pm b/2, 0)$. The separation between each pair of target-projectile nucleons, d , is tested, and a collision between the two nucleons occurs if $d < d_{\perp}$, where d_{\perp} is defined as [49]:

$$\begin{aligned} \sigma_{\text{NN}}^{\text{total}} &= 48 + 0.522(\ln p)^2 - 4.51 \ln p \\ \sigma_{\text{NN}}^{\text{elastic}} &= 11.9 + 26.9p^{-1.21} + 0.169(\ln p)^2 - 1.85 \ln p \\ d_{\perp} &= \sqrt{\frac{\sigma_{\text{NN}}^{\text{total}} - \sigma_{\text{NN}}^{\text{elastic}}}{\pi}} = \sqrt{\frac{\sigma_{\text{NN}}^{\text{inelastic}}}{\pi}}. \end{aligned} \quad (28)$$

The dependence of d_{\perp} on $\sqrt{s_{\text{NN}}}$ is weak. For a beam energy $\sqrt{s_{\text{NN}}} = 27 \text{ GeV}$, somewhat arbitrarily chosen for our calculations, $d_{\perp} = 0.984 \text{ fm}$. where $\sigma_{\text{inel}}^{\text{NN}}(\sqrt{s_{\text{NN}}}) \approx 3 \text{ fm}^2$ in the range $7.7 \text{ GeV} < \sqrt{s_{\text{NN}}} < 62.4 \text{ GeV}$; this is the so-called “black-disk approximation”. In Fig. 68 is shown a typical mid-

central heavy-ion collision, viewed in the transverse plane; the participant nucleons are outlined in black and the roughly ovular shape they make is apparent. In Fig. 69 is shown the average nucleon density at $b = 8$ fm determined by randomly sampling many such collisions; there, the overlap region is smooth and ovular.

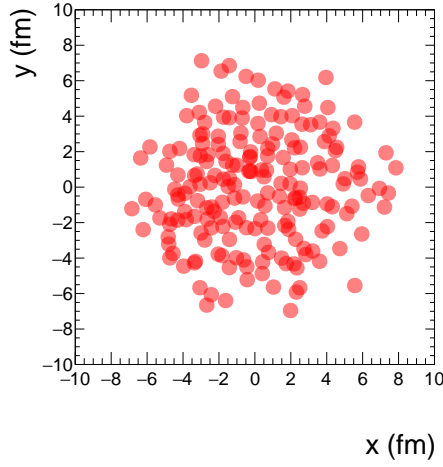


Figure 66: A $^{197}_{97}\text{Au}$ nucleus generated by random sampling of the appropriate distributions. The nucleon diameters are drawn as d_{\perp} (Eq. 28). From this picture we gain an intuitive sense of the level of nucleon position fluctuations.

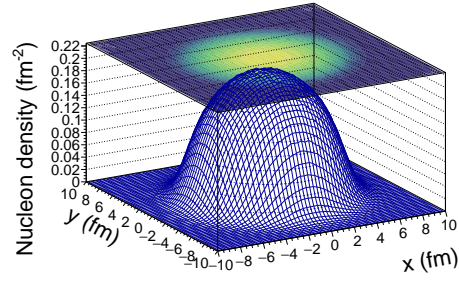


Figure 67: Averaged over many $^{197}_{97}\text{Au}$ nuclei, we see that the density profile is quite smooth and spherical symmetry holds to a very good degree of approximation.

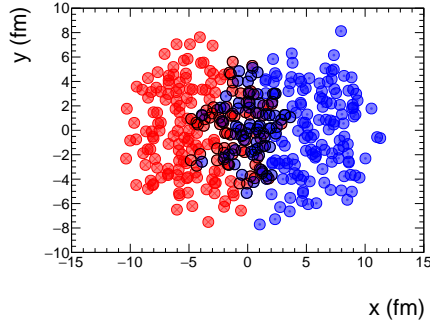
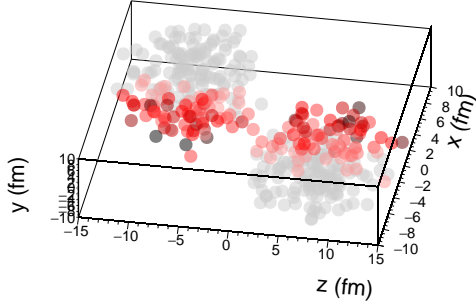


Figure 68: A $^{197}_{97}\text{Au} + ^{197}_{97}\text{Au}$ collision at $b = 8$ fm with nucleon diameters drawn as d (Eq. 28). In the upper panel, we see a three-dimensional cartoon where gray nucleons are spectators and the darkness of the red corresponds to the number of collisions a given participant nucleon undergoes. In the lower panel, we see a two-dimensional cartoon in the transverse ($x-y$) plane where participant nucleons are outlined in black.

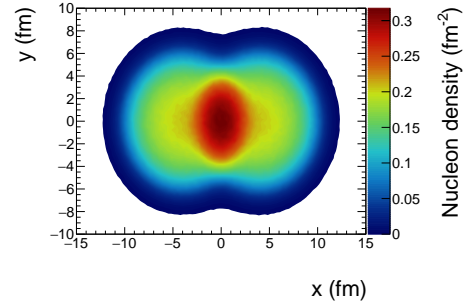
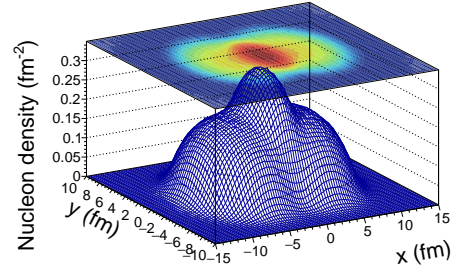


Figure 69: The nucleon density profile for collisions of $b = 8$ fm, averaged over many events; although a given collision's overlap region will be lumpy (Fig. 68), the overlap region is *on average* smooth.

The centrality of a collision is determined in models through the impact parameter distribution, but often only impact parameter is used. Experi-

mentally, the centrality is determined via the number of produced particles within a given region of acceptance which can only approximate the true impact parameter. Using a set of assumptions to extract the expected multiplicity within the MCG model, detailed in appendix H.1, we compared our observable of interest (detailed later on) as a function of centrality as determined using impact parameter and multiplicity. In Fig. 70 is shown this comparison, and there is no obvious distinction between the two methods; we therefore avoid the use of multiplicity in the case of MCG as it adds complication without further insight.

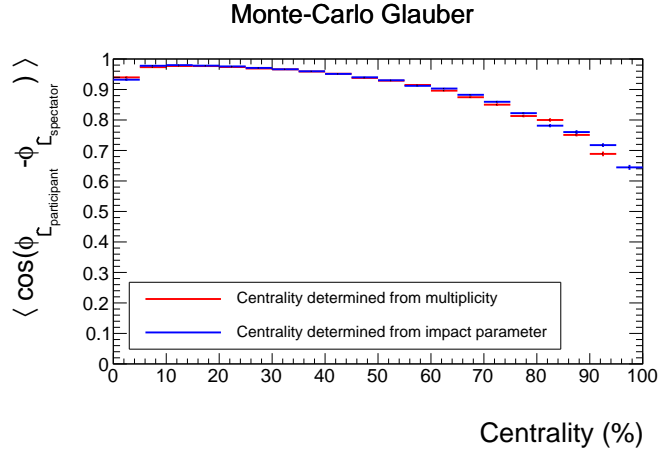


Figure 70: The angular-momentum correlation between participants in the MCG model with respect to collision centrality as determined by b or multiplicity. There is clearly no difference between the two methods of centrality determination.

AMPT

The “A Multi-Phase Transport” (AMPT) model performs a series of treatments of the collision system for various stages of evolution. The initial con-

ditions are given by the Heavy Ion Jet Interaction Generator (HIJING) [30] and the results are fed into Zhang’s Parton Cascade (ZPC) [68]. For treating hadronization and hadronic scatterings, the Lund string fragmentation model and the “A Relativistic Transport” (ART) models are used, respectively. Angular momentum is approximately conserved in AMPT (see appendix I).

While we can have AMPT carry out calculations to late stage ($\mathcal{O}(100\text{fm}/c)$), we are concerned with angular momentum in the QGP phase (as that is the stage of evolution in which the vorticity is large and spin-orbit coupling drives parton polarization). Additionally, we do not want late-stage hadronic interactions and decays to act with disproportionately large lever arm on the angular momentum of the mid-rapidity region. For this reason, we use parton position and momentum information at the moment of hadronization by reading out information at the end of the ZPC stage. While it is true that hadronization will redistribute angular momentum in rapidity, this is a far sub-dominant effect.

We have control of quite a few parameters in AMPT, but everything remains in the default setting with exception of $\sqrt{s_{\text{NN}}}$, b_{max} , and the number of collisions. For each $\sqrt{s_{\text{NN}}}$ we generate 50k events. For $\sqrt{s_{\text{NN}}} > 100 \text{ GeV}$ we generate 100k events as the particle count within $|y| < 1$ becomes statistically challenging.

In both the MCG and AMPT model, impact distributions are sampled according to $dN/db \propto b$ which mimics the physical distribution. The number of input events that result in any nucleons colliding is distributed linearly as well, up to some $b \approx 2R_0$ above which an input event is “hit or miss” due to nucleon position fluctuations (see Fig. 71). The event statistics for

very peripheral and very central collisions therefore drops off significantly and affects statistical uncertainty, as happens as well experimentally.

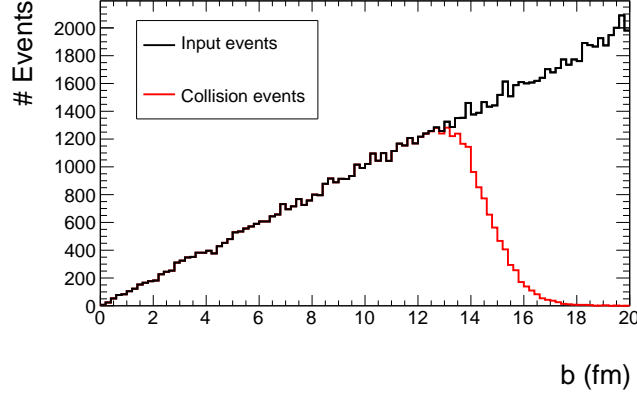


Figure 71: The distribution of impact parameter for all input events and input events that resulted in at least one nucleon-nucleon collision. Clearly the collision event yield above $b \approx 2R_0$ drops, but the drop is smooth due to nucleon position fluctuations.

Overlap geometry characterization

The collision overlap region is approximately elliptic; on average, the major axis of the ellipse is parallel to \hat{y} with some event-by-event fluctuation.

In order to determine the orientation of the elliptic shape, we can fit the participants to an ellipse and study the correlation between the major axis of the ellipse and \hat{J}_{part} . The geometric shape is characterized through so-called harmonic eccentricity coefficients ε [55]:

$$\varepsilon_n e^{in\Phi_n} = -\frac{\int r dr d\phi r^n e^{in\phi} e(r, \phi)}{\int r dr d\phi r^n e(r, \phi)}. \quad (29)$$

In this case, we take $n = 2$. $e(r, \phi)$, the energy density distribution at the

moment of impact, is simply a sum of δ functions. We then arrive at:

$$\Phi_2 = \frac{1}{2} \left[\arctan \frac{\sum_i r_{\perp,i}^2 \sin(2\phi_i)}{\sum_i r_{\perp,i}^2 \cos(2\phi_i)} + \pi \right], \quad (30)$$

where (r_{\perp}, ϕ) are the polar coordinates, in the transverse plane, of the participant nucleons. Note here that we must take the center of mass of the participants as the origin, as opposed to the center of mass of the collision system. Figure 72 demonstrates in yellow dashed lines the elliptic fits, with lines through the major axes, to a handful of collisions in the MCG model at varying b .

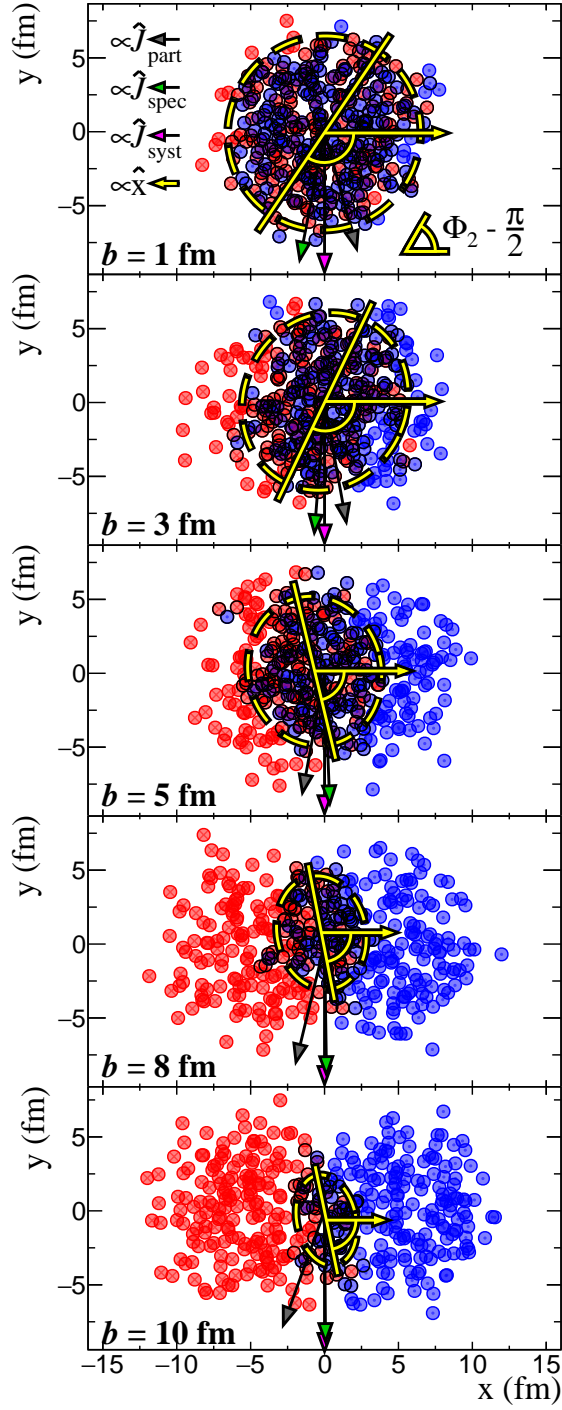


Figure 72: The MCG model is used to generate a handful of collisions at varying b . The z dimension is irrelevant in this model and the collisions are viewed in the transverse plane. Black outlines denote participant nucleons, and yellow dashed lines denote the elliptic fit to the collision overlap region. Each event is typical, in that $\hat{J}_{\text{spec}} \cdot \hat{J}_{\text{part}}|_b \approx \left\langle \hat{J}_{\text{spec}} \cdot \hat{J}_{\text{part}} \right\rangle \Big|_b$ and $\Phi_2|_b \approx \langle \Phi_2 \rangle|_b$.

4.3 Correlation results

\hat{J}_{part} correlations with \hat{J}_{syst} and \hat{J}_{spec}

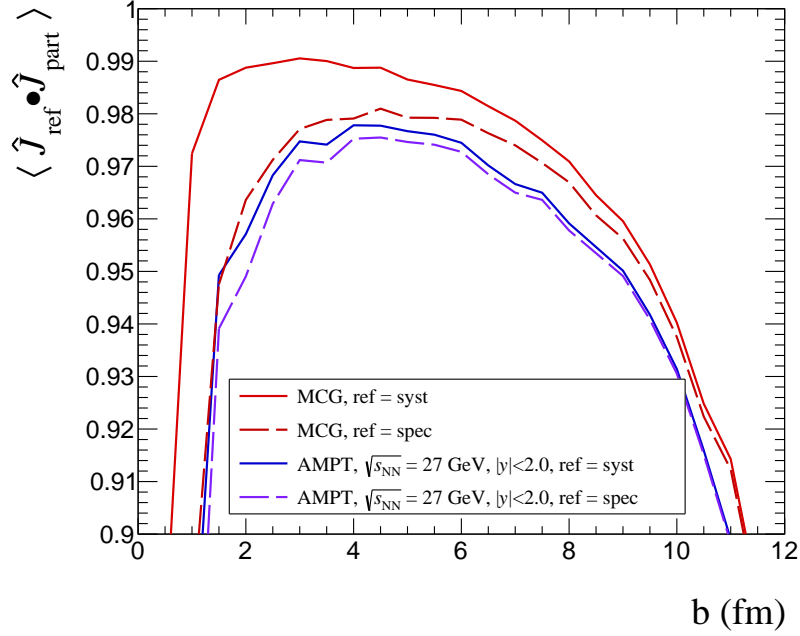


Figure 73: The correlation between \hat{J}_{syst} and \hat{J}_{part} . There is significant decorrelation for peripheral and central events, but good correlation for mid-central collisions. There is an enhanced correlation between \hat{J}_{syst} and \hat{J}_{part} which arises from conservation of angular momentum. In AMPT, spectators are defined with $|y| > 2$.

In central heavy-ion collisions ($b \lesssim 3$ fm), $|\vec{J}_{\text{syst}}|$ and $|\vec{J}_{\text{part}}|$ become smaller as $b \rightarrow 0$ while $|\vec{J}_{\text{spec}}|$ remains large; many spectators still exist in these collisions (as seen for example in Fig. 72) which carry a large lever arm. Because of this, $|\vec{J}_{\text{spec}}|$ and $|\vec{J}_{\text{part}}|$ are non-zero even as $b \rightarrow 0$ (see Fig. 65). As $b \rightarrow 0$, \hat{J}_{spec} becomes more random and so, therefore, does \hat{J}_{part} due

to conservation of angular momentum. In peripheral collisions ($b \gtrsim 9$ fm) $|\vec{J}_{\text{spec}}|$ dominates the contribution to $|\vec{J}_{\text{syst}}|$ but the effects of initial-state fluctuations on \hat{J}_{spec} diminish as the number of spectators increases, so \hat{J}_{spec} becomes well aligned with \vec{J}_{syst} ; however, the number of participants drops as does the contribution of \vec{J}_{part} to \vec{J}_{syst} , so initial-state fluctuations play a significant role in the orientation of \hat{J}_{part} . We therefore expect \hat{J}_{part} and \hat{J}_{syst} to be poorly correlated in central and peripheral collisions. In mid-central collisions, however, there are enough of both participants and spectators that initial-state fluctuations play a small role in the orientations of \hat{J}_{part} and \hat{J}_{spec} and we therefore would expect them to be well correlated in these collisions. We indeed see this behavior in the solid lines in Fig. 73 measuring $\hat{J}_{\text{syst}} \cdot \hat{J}_{\text{part}}$ with the MCG and AMPT models. Here and henceforth we use the rapidity cut $|y| > 2$ to approximately isolate the spectators, as would be done experimentally. When choosing the upper limit of $|y| = 2$ to define the participant region in AMPT, no particles are excluded and we therefore see quite good agreement between the two models.

When instead measuring the correlation between the participants and the spectators, we see $\hat{J}_{\text{spec}} \cdot \hat{J}_{\text{part}} < \hat{J}_{\text{syst}} \cdot \hat{J}_{\text{part}}$; this is true both on average as well as event by event, and must be so because of conservation of angular momentum. This is represented in Fig. 72 as a cartoon of mid-central collisions within the MCG model viewed in the transverse plane. By design, $\hat{J}_{\text{syst}} \parallel -\hat{y}$ but initial-state fluctuations will generate a deviation of $\hat{J}_{\text{part}}(\hat{J}_{\text{spec}})$ from $-\hat{y}$ and because of angular-momentum conservation $\hat{J}_{\text{spec}}(\hat{J}_{\text{part}})$ must point along the “other side” of $-\hat{y}$; i.e. the angle between \hat{J}_{part} and \hat{J}_{spec} must be larger than the angle between \hat{J}_{part} and \hat{J}_{syst} .

Experiments are typically set up to identify particles with tracking at mid-rapidity (e.g. with time projection chambers) while particle-type-insensitive detectors are placed at forward and backward rapidities (e.g. with calorimeters). When measuring phenomena driven by angular momentum within the QGP (e.g. global spin alignment with \hat{J}_{part}), QGP byproducts are reconstructed at mid-rapidity while \vec{J}_{spec} is measured using the azimuthal distribution of forward/backward-going particles as an approximation of \vec{J}_{part} ; however, such an approximation is subject not only to the effects seen in Fig. 73 but also to the reduction of particles measured at mid-rapidity. As we constrain the rapidity window used in the participant region, we reduce the number of particles in that region and random fluctuations play a larger role in the decorrelation between \hat{J}_{spec} and \hat{J}_{part} . We see this effect in Fig. 74 within the AMPT model; for mid-central collisions, the mid-rapidity angular momentum \hat{J}_{part} is well aligned with \hat{J}_{sys} when considering $|y| < 2$; however, the degree of alignment drops substantially when considering the region $|y| < 1$ typically used. This is striking; if taken at face value, this would translate to a correction of roughly 25% on the observable of interest.

At higher energies, the fraction of all particles that lie in the rapidity window $|y| < 1$ becomes smaller; we might therefore expect the correlator $\hat{J}_{\text{spec}} \cdot \hat{J}_{\text{part}}$ to become smaller with increasing $\sqrt{s_{\text{NN}}}$ and indeed we see such behavior in Fig. 75. The correlations depend strongly on $\sqrt{s_{\text{NN}}}$, differing by more than a factor of 2 between the lowest and highest collision energies. In Fig. 76 is shown $\langle \hat{J}_{\text{spec}} \cdot \hat{J}_{\text{part}} \rangle$ for mid-central collisions, defined in a number of ways that yield very similar results, as a function of $\sqrt{s_{\text{NN}}}$. Any $\sqrt{s_{\text{NN}}}$ -dependent experimental observable driven by angular momentum within the

QGP would be corrected in such a manner, by $\langle \hat{J}_{\text{spec}} \cdot \hat{J}_{\text{part}} \rangle^{-1}$. Similarly, it is important for model predictions to use \hat{J}_{part} , rather than \hat{J}_{syst} , when calculating phenomena driven by angular momentum within the QGP. Without doing so there will be an apparent dependence on $\sqrt{s_{\text{NN}}}$ driven at least in part by the behavior observed in Fig. 76 (recall that $\langle \hat{J}_{\text{syst}} \cdot \hat{J}_{\text{part}} \rangle \approx \langle \hat{J}_{\text{spec}} \cdot \hat{J}_{\text{part}} \rangle$ as seen in Fig. 73).

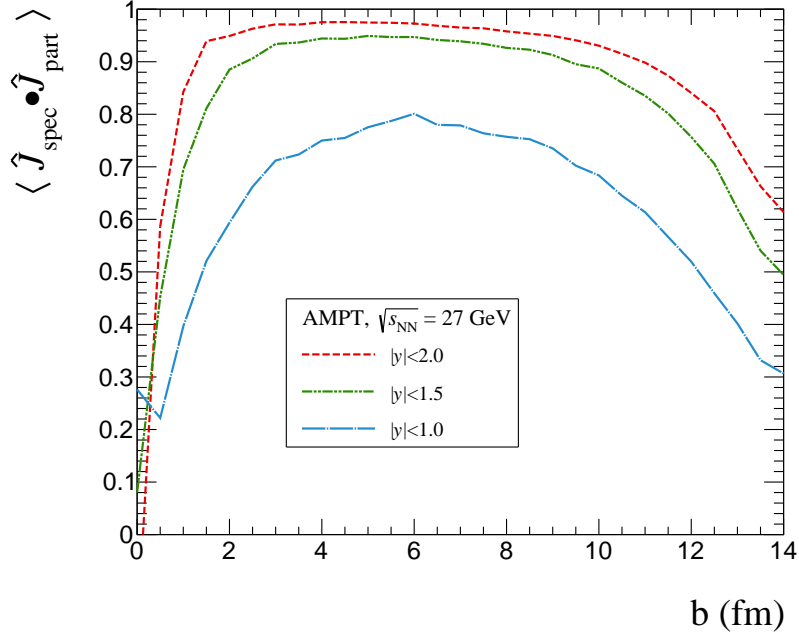


Figure 74: The correlation between \hat{J}_{part} and \hat{J}_{spec} becomes smaller as we further constrain the size of the rapidity window used for the calculation of \hat{J}_{part} where initial-state fluctuations play a larger role. Experiments typically are limited to $|y| < 1$.

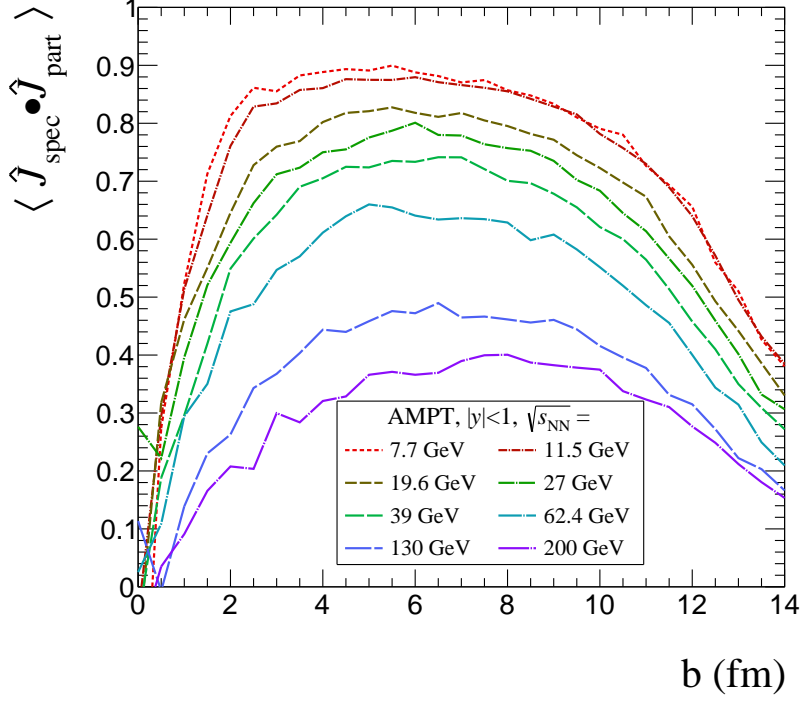


Figure 75: The correlation between \hat{J}_{part} and \hat{J}_{spec} becomes smaller as we increase $\sqrt{s_{\text{NN}}}$ where a given rapidity window includes a smaller fraction of all particles and initial-state fluctuations play a larger role. This is similar to the effects driving the observation in Fig. 74. The values of $\sqrt{s_{\text{NN}}}$ are chosen to match those of the RHIC Beam Energy Scan (BES).

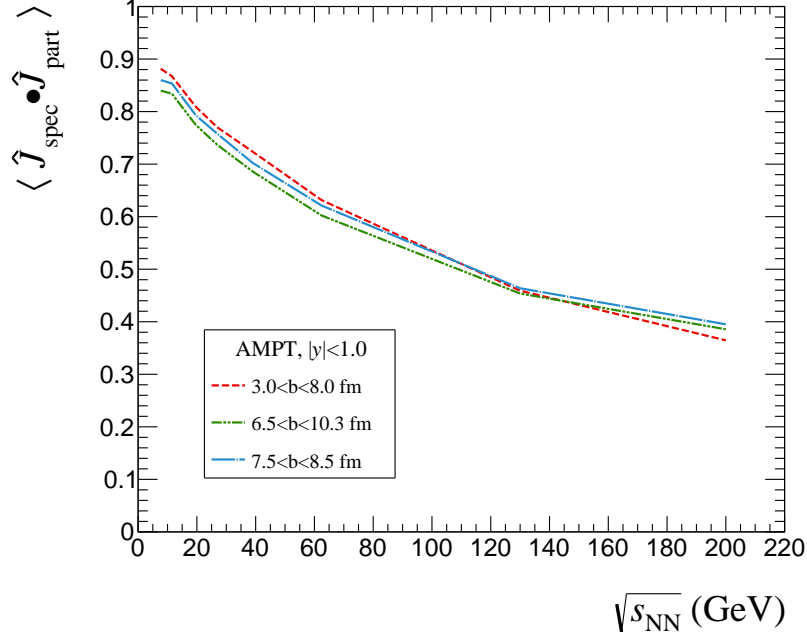


Figure 76: The correlation between \hat{J}_{part} and \hat{J}_{spec} for mid-central collisions, the event class used when studying angular-momentum-driven phenomena, falls with $\sqrt{s_{\text{NN}}}$. $3 < b < 8$ fm describes the region from Fig. 75 where the correlation is flat, and $6.5 < b < 10.3$ fm and $7.5 < b < 8.5$ fm are two ways of approximating 20-50% central collisions.

In order to ensure that the observed correlations are not relative, we should examine the behavior of $\frac{\langle \vec{J}_{\text{spec}} \cdot \vec{J}_{\text{part}} \rangle}{\langle |\vec{J}_{\text{spec}}| \rangle \langle |\vec{J}_{\text{part}}| \rangle}$ (Fig. 77).

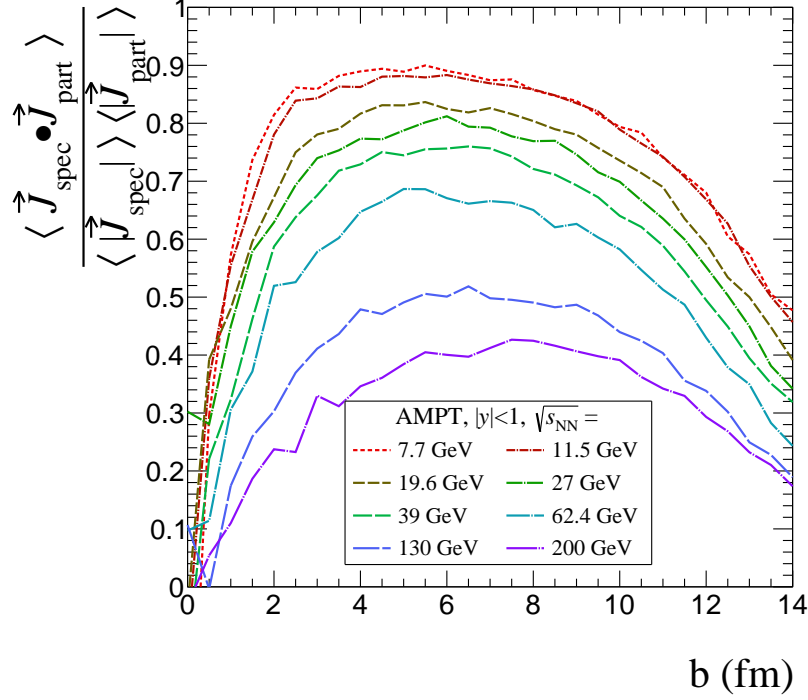


Figure 77: Here we examine the behavior of $\frac{\langle \vec{J}_{\text{spec}} \cdot \vec{J}_{\text{part}} \rangle}{\langle |\vec{J}_{\text{spec}}| \rangle \langle |\vec{J}_{\text{part}}| \rangle}$ and see it is nearly identical to that of $\hat{J}_{\text{spec}} \cdot \hat{J}_{\text{part}}$.

\hat{J}_{part} correlations with geometry

The overlap region of a heavy-ion collision is roughly ovular on average, with the major axis of the ellipse aligned with \hat{y} . We can fit the participant coordinates to an ellipse in order to determine its orientation and study the correlation between \hat{J}_{part} and this orientation. We characterize the initial shape through harmonic eccentricity coefficients ε_n and event plane angles Φ_n [55]:

$$\varepsilon_n e^{in\Phi_n} = -\frac{\int r dr d\phi r^n e^{in\phi} e(r, \phi)}{\int r dr d\phi r^n e(r, \phi)}. \quad (31)$$

By taking $n = 2$ and treating the initial energy density distribution $e(r, \phi)$ as a sum of delta functions, each at the position of a nucleon, this reduces to:

$$\Phi_2 = \frac{1}{2} \left[\arctan \frac{\sum_i r_{\perp,i}^2 \sin(2\phi_i)}{\sum_i r_{\perp,i}^2 \cos(2\phi_i)} + \pi \right], \quad (32)$$

where r_{\perp} and ϕ are the polar coordinates of the participant nucleons in the transverse plane, as measured from the center of mass of the participants. This is only sensible when considering initial-state positions, which disallows us from studying rapidity windows in AMPT and restricts us to using the MCG model only. These elliptic fits to the participants are shown in Fig. 72, with lines drawn through the major axes.

For central collisions, the overlap region is quite circular and for very peripheral collisions only a small number of nucleons participate; in both cases, initial-state fluctuations play a large role in the orientation of the elliptic fit and therefore on Φ_2 . In mid-central collisions, the overlap region is sufficiently elliptic and there are enough participants that initial-state fluctuations will be sub-dominant; we might therefore expect Φ_2 to be best aligned with $\phi_{\hat{j}_{\text{syst}}} \pm \pi/2$ for mid-central collisions. We see such behavior in the solid line in Fig. 78.

We might also intuitively make the naïve assumption that the somewhat-elliptic participant region would be spinning about its major axis and therefore expect better alignment when instead looking at the correlation between Φ_2 and $\phi_{\hat{j}_{\text{part}}}$; however, when looking again at Fig. 78 is shown that the opposite is true. This can be understood by dividing a given tilted elliptic overlap region in two, lengthwise, and considering that one half is dominated by forward-going nucleons while the other is dominated by backward-going

nucleons. By applying the right-hand rule to these two halves it is clear that \hat{J}_{part} will tilt to the left as the elliptic overlap region tilts to the right, and vice versa.

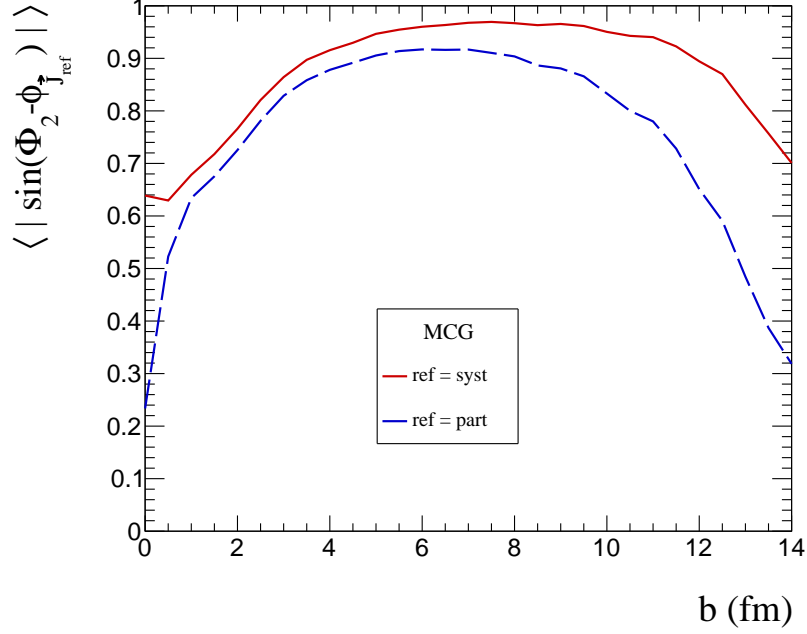


Figure 78: The correlation between the orientation of the elliptic overlap region and \hat{J}_{syst} is largest for mid-central collisions, in line with expectations. Counter-intuitively, however, there is a smaller correlation between the orientation of the ellipse and \hat{J}_{part} . The absolute value of $\sin(\Phi_2 - \phi_{\vec{J}_{\text{ref}}})$ is used since Φ_2 is physically indistinguishable from $\Phi_2 \pm \pi$.

While it is not trivial to extract the initial-state ellipticity of the overlap region corresponding to a given final-state rapidity window, Φ_2 can be approximated with the second-order event-plane angle,

$$\Psi_2 = \frac{1}{2} \text{atan2} \left(\sum_i^{\# \text{Particles}} w_i \sin(\phi_i), \sum_i^{\# \text{Particles}} w_i \cos(\phi_i) \right), \quad (33)$$

which is experimentally determined within a region of $|y|$ or η ; the weight, w_i , is typically the transverse momentum, p_T . We expect the correlation $\left\langle \left| \sin(\Phi_2 - \phi_{\hat{J}_{\text{part}}}) \right| \right\rangle$ to again decrease when considering $|y| < 1$, as well as decrease with $\sqrt{s_{\text{NN}}}$ as the fraction of all particles contained in $|y| < 1$ becomes smaller.

The poor correlation between the orientation of the elliptic overlap region and \hat{J}_{part} in addition to the relative difficulty in calculating a correction factor accounting for the decorrelation between Φ_2 and $\phi_{\hat{J}_{\text{part}}} \pm \pi/2$ within a given $|y|$ window are reasons to avoid using Ψ_2 in estimating the direction of \hat{J}_{part} when measuring angular-momentum-driven phenomena.

4.4 Summary

Initial-state fluctuations drive a decorrelation between \hat{J}_{syst} and \hat{J}_{part} , which is the largest for central and peripheral collisions. Conservation of angular momentum drives an even larger decorrelation between \hat{J}_{spec} and \hat{J}_{part} ; only \hat{J}_{spec} is experimentally accessible, and is used as an approximation of \hat{J}_{part} . As the range of $|y|$ used in qualifying participants shrinks, the decorrelation between \hat{J}_{spec} and \hat{J}_{part} grows larger. Similarly, this decorrelation becomes larger with increasing $\sqrt{s_{\text{NN}}}$.

The orientation of the elliptic overlap region has a smaller correlation with \hat{J}_{part} than \hat{J}_{syst} , in conflict with potential intuitive expectations. The correlation between the orientation of elliptic shape and \hat{J}_{part} will grow worse when considering $|y| < 1$, as well as with increasing $\sqrt{s_{\text{NN}}}$; therefore, deducing \hat{J}_{part} from Φ_2 or Ψ_2 is not a viable method to avoid the decorrelation between \hat{J}_{part} and \hat{J}_{spec} .

The findings presented hold significant implications for measurements of phenomena driven by angular momentum within the QGP, and particularly for those interested in the dependence on $\sqrt{s_{\text{NN}}}$. Based on our model-dependent study, it is crucial for $\sqrt{s_{\text{NN}}}$ -dependent studies of angular-momentum-driven phenomena to correct for the decorrelation between \hat{J}_{spec} and \hat{J}_{part} in a $\sqrt{s_{\text{NN}}}$ -dependent manner, and for model predictions of such phenomena to use \hat{J}_{part} instead of \hat{J}_{syst} ; otherwise any observed dependence will be driven at least in part by this decorrelation.

5 Summary and future work

Experimental studies of heavy ion collisions require a vast array of detector subsystems, each responsible for specific observables and each with vastly different technology. A crucial observable is that of the collision's orientation, which is estimated by the first-order event-plane angle, $\Psi_{\text{EP},1}$ determined with the azimuthal distribution of emitted particles at forward rapidity. For over a decade, the BBC served as the primary subsystem within the STAR detector for determining $\Psi_{\text{EP},1}$; however, its resolution was generally poor owing to the large size of the BBC tiles and the small coverage in η .

In 2017-2018 the EPD was constructed as a replacement of the BBC. While many institutions were involved in various stages (including prototyping, construction, software design, etc.), the EPD was constructed and assembled in large part in the Ohio State University's High-Energy Nuclear Physics laboratory within the Department of Physics. Extreme care was required in the various stages of construction and assembly, and unique challenges were regularly confronted. Thorough testing was conducted on each of the twenty-four used plus three spare supersectors using a radioactive source mounted on rails that were moved via program-controlled motors and using cosmic rays. Ultimately, the EPD was successfully installed as the replacement for the BBC and maintains very good performance, and serves as an indispensable tool to measure, for example, the direction of system angular momentum from the collision.

Large system angular momentum, \vec{J}_{syst} , is critical for the generation of vorticity within the collision which leads to the spin alignment of hadrons with \hat{J}_{syst} . This spin polarization has been measured via the decay of the Λ hyperon, which preferentially emits its daughters along the direction of its spin, across a wide range of $\sqrt{s_{\text{NN}}}$. The trend strongly suggests that \bar{P}_{Λ} decreases monotonically with $\sqrt{s_{\text{NN}}}$. A simple extrapolation of this trend would show \bar{P}_{Λ} becoming very large at small $\sqrt{s_{\text{NN}}}$; however, \bar{P}_{Λ} must go to zero at $\sqrt{s_{\text{NN}}} = 2m_{\text{N}}$. A peak \bar{P}_{Λ} therefore likely lies in the region $2m_{\text{N}} < \sqrt{s_{\text{NN}}} < 7.7$ GeV, which is the lowest energy at which \bar{P}_{Λ} has yet been measured.

In 2018, the STAR collaboration achieved a high-statistics data set of Au+Au collisions at its lowest-yet center-of-mass collision energy of $\sqrt{s_{\text{NN}}} = 3$ GeV. Despite these challenges, a measurement of an integrated, mid-rapidity \bar{P}_{Λ} larger than any yet-observed \bar{P}_{Λ} with a statistical significance of $\approx 6\sigma$ was achieved. Furthermore, the statistics allowed for differential measurements; the measurement of \bar{P}_{Λ} with respect to centrality and p_{T} confirmed previously observed dependencies, namely that \bar{P}_{Λ} increases with centrality and doesn't depend on p_{T} within uncertainties. The measurement of \bar{P}_{Λ} with respect to y was uniquely valuable because the detector setup and collision energy allowed for the measurement of the most-forward Λ s while previous measurements of \bar{P}_{Λ} with respect to y were constrained to only measure the mid-rapidity Λ s. The lack of any observed dependence of \bar{P}_{Λ} on y stands in stark contrast to the number of model calculations that predict a rising or falling \bar{P}_{Λ} with y and to any arguments that the falling \bar{P}_{Λ} with $\sqrt{s_{\text{NN}}}$ can be explained by a migration of \bar{P}_{Λ} towards forward rapidity.

Experimental measurements and model calculations of \overline{P}_Λ assume that the net vorticity within the collision overlap region, which is parallel to the participant angular momentum \vec{J}_{part} , is parallel to \vec{J}_{syst} . For example, models generate nucleon positions about nuclei centers which exist on the \hat{x} axis, so that $\hat{b}||\hat{x}$ and in turn $\hat{J}_{\text{syst}}||-\hat{y}$. Vorticity and polarization vectors are then projected onto $-\hat{y}$ in order to calculate \overline{P}_Λ . Experimentally, the additional assumption is made that the spectator angular momentum, \vec{J}_{spec} , is also parallel to \vec{J}_{syst} and \vec{J}_{part} ; the spectators are measured at forward rapidity (by the EPD for example) and \vec{J}_{spec} is taken as \vec{J}_{part} or \vec{J}_{syst} to be correlated with \vec{S}_Λ which is measured at mid-rapidity and is a product of the participant region of the collision.

While these assumptions are true on average, event-by-event fluctuations dictate that they are flawed in any given event. Through the use of a simple Monte-Carlo Glauber model and a more realistic transport model, we quantified the effects of initial-state fluctuations on the correlations between \hat{J}_{spec} , \hat{J}_{syst} , and \hat{J}_{part} . While angular momentum conservation suppresses these correlations slightly, rapidity-window restriction (which is carried out experimentally) and fluctuations have a large effect on these correlations. At lower $\sqrt{s_{\text{NN}}}$ the effects are small, but become worse as $\sqrt{s_{\text{NN}}}$ becomes larger. While not a significant enough effect to explain the observed $\sqrt{s_{\text{NN}}}$ dependence of \overline{P}_Λ , this is still a very important corrective factor; if ignored, the $\sqrt{s_{\text{NN}}}$ dependence of \overline{P}_Λ will be exaggerated. Furthermore, we find that the orientation of the elliptic overlap region is decorrelated with \hat{J}_{part} which disallows the “escape” of this problem via mid-rapidity particles.

Beyond the importance of understanding the dependence of \overline{P}_Λ on $\sqrt{s_{\text{NN}}}$,

which we've shown is not likely explained by a dependence on y and is overestimated due to these event-by-event fluctuations, \overline{P}_Λ can be used as a tool for understanding other phenomena. For example, while vorticity within the collision overlap region will polarize Λ and $\bar{\Lambda}$ hyperons equally, the two have opposite magnetic moments and therefore a given magnetic field sustained by the QGP will enhance $\overline{P}_{\bar{\Lambda}}$ and suppress \overline{P}_Λ . Because of this, a splitting between \overline{P}_Λ and $\overline{P}_{\bar{\Lambda}}$ can be used as a measurement of the magnetic field strength sustained by the QGP and in turn as a measurement of the magnetic susceptibility of the QGP. This process is complicated, however, by other driving mechanisms of such a splitting, such as the difference in emission time from the QGP between Λ s and $\bar{\Lambda}$ s.

Nevertheless, studying such a splitting between \overline{P}_Λ and $\overline{P}_{\bar{\Lambda}}$ is of much experimental interest. In 2018, STAR collected a high-statistics data set of Au+Au collisions at $\sqrt{s_{\text{NN}}} = 27$ GeV, motivated in part by this potential splitting. Numerous complicating factors, however, affected this analysis; while a significant effort was put forth in order to account for these complicating factors, the measurements of \overline{P}_Λ and $\overline{P}_{\bar{\Lambda}}$ repeatedly failed checks for systematic errors and sufficient confidence could not be gained that such a charge-sensitive analysis would ultimately be free of unknown systematic effects. Details on this inconclusive study can be found in appendix J. The following year, the STAR collaboration had taken another high-statistics data set at $\sqrt{s_{\text{NN}}} = 19.6$ GeV which included significant detector upgrades and is free of the problems present in the 2018 data set at $\sqrt{s_{\text{NN}}} = 27$ GeV; however, new problems are present. Still, the data set is promising and remains a top priority in my post-graduation research.

Appendices

A Details on event and Λ selection

A.1 Details on event selection

Minimum-bias Au+Au collisions were taken in 2018 in fixed-target mode; the Eastward beam (with nucleon energy 3.85 GeV) was steered down (i.e. to $-y$ in STAR geometry, towards the ground) to hit 1 mm-thick Au foil sitting at $z = 200$ cm (see Fig. 37) leading to collisions with center-of-mass energy $\sqrt{s_{\text{NN}}} = 3$ GeV. Triggered events were those that had at least one hit in the East BBC and in the TOF; we use the trigger with label “bbce_tofmult1”, ID 620052. This represents 95.6% of all triggered events for a total of ≈ 337 M events. The dataset was calibrated and produced twice, with only minor corrections for the second production. In an .xml file to submit jobs, one can access the appropriate files with the SL20d library (corresponding to the second production) in two ways:

- `<input URL="catalog:star.bnl.gov?filetype=daq_reco_picoDst, trgsetupname=production_3p85GeV_fixedTarget_2018, library=SL20d, tpx=1, filename st_physics, sanity=1, storage!=hpss, daynumber=154" preferStorage="local" singleCopy="true" nFiles="all" />`

- `<input URL="filelist:/star/u/bkimel/3GeV_newProd_Robust_GoodList.list" nFiles="all" />`

Primary vertex cuts were chosen to match the centrality study performed by the UC Davis group. The v_z distribution is sharply peaked about $\langle v_z \rangle = 200.7$ cm and we therefore impose a cut of 200 ± 2 cm (Fig. 79). The beam is steered down from $(x, y) = (0, 0)$ in order to hit the gold foil; we therefore impose a cut on v_T about the beam spot, $(0, -2)$ (as opposed to cutting about $(0, 0)$ as is done in collider mode) of 1.5 cm (Figures 80, 81).

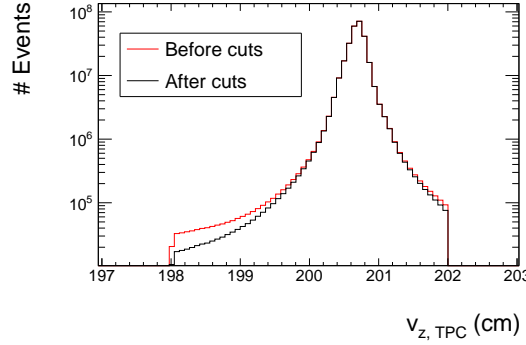


Figure 79: The v_z distribution is sharply peaked about $\langle v_z \rangle = 200.7$ cm. This cut is actually redundant, as the trigger ID selection excludes events with v_z outside of 200 ± 2 cm. Without the trigger selection, many smaller peaks appear due to out-of-time events/tracks. The peak is wider than the target width in \hat{z} of 1 mm; this is due to peripheral events which have poor resolution of the primary vertex.

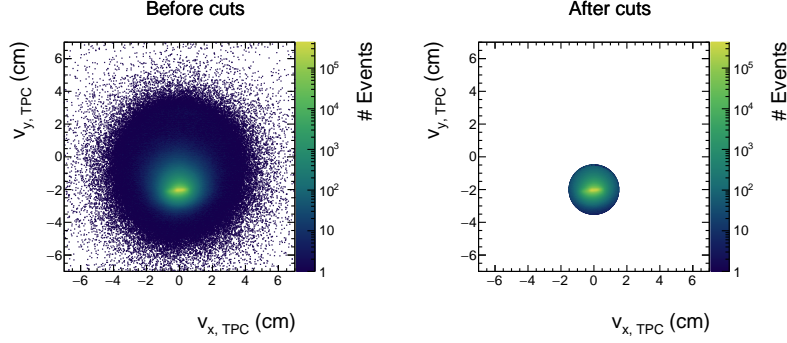


Figure 80: We impose a cut on v_T about the beam spot (0,-2) instead of (0,0) (as is typically done in collider mode) because the beam is steered downwards.

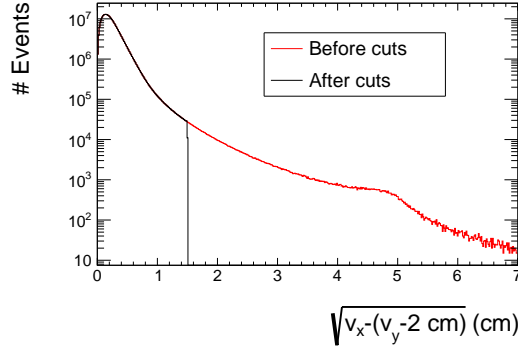


Figure 81: We impose a cut on v_T about the beam spot (0,-2) instead of (0,0) (as is typically done in collider mode) because the beam is steered downwards.

The QA studies performed by the UC Davis group [39] yield a list of runs that were rejected for various reasons (Fig. 84). The pileup cut and centrality definitions were also determined by the UC Davis group [60]; comparisons between measured charged-particle multiplicity and a Glauber model (Fig. 82)

help give the centrality definitions at this energy. The inclusive lower limits on the centralities are shown in Fig. 83 (e.g. 5-10% centrality is given by events with $119 \leq \text{mult.} < 141$). It is worth noting here that the fixed-target multiplicity is given simply by the number of primary tracks. A cut of multiplicity *larger than* 195 is applied to remove pile-up events.

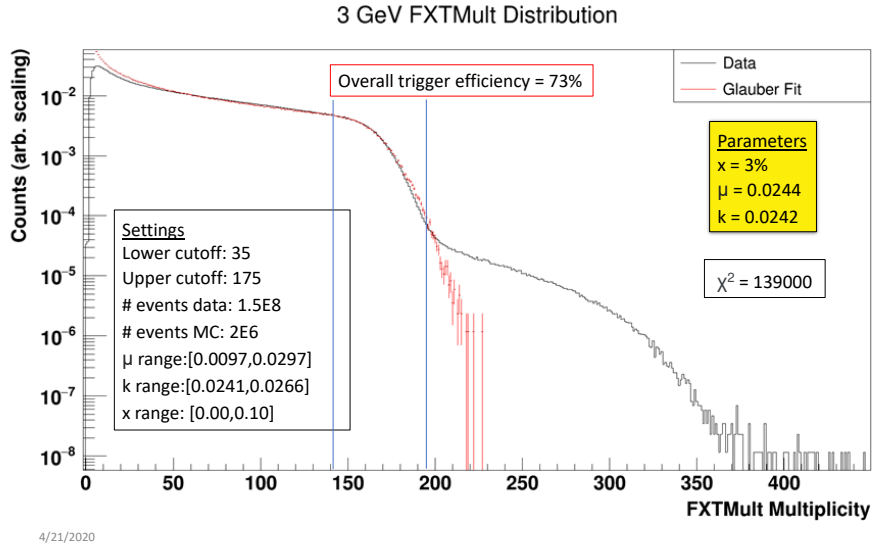


Figure 82: Comparing the distribution of number of primary tracks in an event to a Glauber model. Glauber fits the data well besides low multiplicity where triggering becomes difficult and high multiplicity where pileup is evident. Events with more than 195 primary tracks are obviously dominated by pileup. This slide from [21].

Comparison to old data

Centrality	STAR 3.0	STAR Scaled	E895 6AGeV
0-5%	141	218	218
5-10%	118	184	187
10-15%	99	154	159
15-20%	83	129	133
20-25%	69	107	109
25-30%	57	89	86
30-35%	47	74	69
35-40%	38	59	57
40-45%	30	47	48
45-50%	24	37	40
50-55%	18	28	32
55-60%	14	22	24
60-65%	10	16	16

4/21/2020

We can ask the question of whether the Glauber model is accurate at these energies. For comparison, we compare the STAR centrality cuts at 3.0 GeV to the E895 centrality cuts at 3.83 GeV. The STAR cuts are scaled up by a factor of 1.557.

E895 did not use a Glauber model for centrality. Every gold ion incident on the target was counted and the trigger cross-section as a function of multiplicity was determined. The overall trigger cross section was 4.63 barns

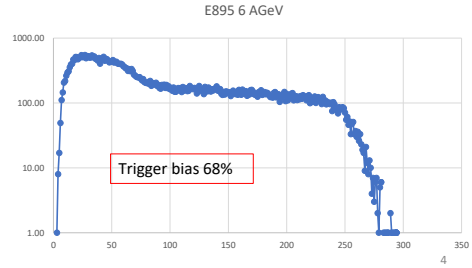


Figure 83: Comparing the distribution of number of primary tracks in an event to fixed-target E895 data. This slide from [21].

Bad Run List (Robust Analyses) - removes 35M Events

[24]=

**19151029,19151045,19152001,19152078,19153023,
19153032,19153065,19154012,19154013,19154014,
19154015,19154016,19154017,19154018,19154019,
19154020,19154021,19154022,19154023,19154024,
19154026,19154046,19154051,19154056**

19151029 → First physics run, filled w/ 24 bunches not 12
19151045 → No ETOW, collimator adjustments
19152001 → Only 1 event
19152078 → 1 minute run, not in log book
19153023 → 3.4 minute run, getting no rate, TPC trips
19153032 → 35 second run, TPC trips
19153065 → 35 second run, TPC trips
19154012 through 19154024 → TPX 14 (4 RDOs) out
19154026 → No BTOW
19154046 → 3 minute run, Trigger 100% dead
19154051 → 30 second run, TPC trips
19154056 → 2 minute test w/o EVB 6/7/8

This list is mostly identical to original production bad run list (inclusion of runs 19151045, 19154046, and 19154056 to this list are only change)

14

Ben Kimelman

Nov. 6, 2020

Figure 84: The bad run list compiled through various QA studies performed by the UC Davis group. Figure from [39].

A.2 Details on Λ selection

We are interested in measuring \overline{P}_H using Λ hyperons, through the decay $\Lambda \rightarrow p^+ + \pi^-$. For simplicity, we use the KFParticle package with two modifications:

- `StKFParticleInterface::instance()->CleanLowPVTrackEvents()`
- `StKFParticleInterface::instance()->SetChiPrimaryCut(10)`

Other modifications on the default cut set were investigated for potential

improvement on the significance, but no better set was found. For both p^+ and π^- the following cuts on global tracks are applied by KFParticle (where TOF cuts are only applied when TOF information is available):

- $n\text{HitsFit} \geq 15$
- $0.04 \leq d\text{EdxError} \leq 0.12$
- $|\text{nSigma}| < 3.$
- $-0.15 < m^2 < 0.15 \text{ GeV}^2$ for π^-
- $0.5 < m^2 < 1.5 \text{ GeV}^2$ for p^+

Additionally, we apply the cuts:

- $p_{\text{T}} \geq 0.15 \text{ GeV}/c$ for π^-
- $p_{\text{T}} \geq 0.4 \text{ GeV}/c$ for p^+
- $p_{\text{T}} \geq 0.7 \text{ GeV}/c$ for Λ
- $\vec{p}_{\Lambda} \cdot \vec{r}_{\Lambda} > 0$
- $-0.2 < y_{\Lambda} < 1$

where \vec{r}_{Λ} is the vector from the primary vertex to the Λ decay vertex. The lower-bound $p_{\text{T},\pi}$ cut is applied because of low tracking efficiency. The lower-bound $p_{\text{T},p}$ cut is applied to avoid spallation protons. The lower-bound $p_{\text{T},\Lambda}$ cut is applied because efficiency corrections were very large (see Fig. 119) and polarization measurements were unstable below $p_{\text{T},\Lambda} = 0.7 \text{ GeV}$ when

comparing cut sets. The lower-bound rapidity cut is applied because efficiency corrections were very large (see Fig. 119), polarization measurements for $y_\Lambda < -0.2$ were unstable, and when including such Λ s, there were discrepancies between the integrated result and the averages of the differential measurements. The $m_{\text{inv.}}$ distribution of these Λ s is shown in Fig. 90.

Though we did not find Λ s the typical (“manual”) way, we did use two sets of topological cuts in order to test for any change of the result between Λ identification methods (see Table 1. For each of these, we require some basic track cuts for the daughters (again, where TOF cuts are only applied when TOF information is available):

- $p_T \geq 0.15 \text{ GeV}/c$ for π^-
- $p_T \geq 0.4 \text{ GeV}/c$ for p^+
- $\text{nHitsPoss} \geq 5$
- $\text{nHits} \geq 15$
- $\text{nHitsFit}/\text{nHitsPoss} \geq 0.52$
- $|\text{nSigma}| < 3.$
- $-0.6 < m^2 < 0.1 \text{ GeV}^2$ for π^-
- $0.5 < m^2 < 1.5 \text{ GeV}^2$ for p^+

Λ hyperons reconstructed using KFParticle sometimes share daughter protons or pions. Obviously, though a given proton may be paired with multiple pions that together pass Λ cuts (and vice versa), this is not physical.

Topological featue	Cut set 1	Cut set 2
Min. decay length (cm)	2.5	3.5
Max. p DCA to π (cm)	1	1
Min. p DCA to PV (cm)	0.15	0.5
Min. π DCA to PV (cm)	0.8	1.5
Max. Λ DCA to PV (cm)	1.2	0.75

Table 1: Topological cuts used to reconstruct $\Lambda \rightarrow p + \pi^-$ decays for comparison with KFParticle. Here, DCA denotes distance at closest approach and PV denotes the location of the primary vertex.

We can account for this by evaluating these daughter-sharing Λ s and choosing the “best” one while ignoring the others; this process we call “Thunderdome”. The most straightforward way to measure the “quality” of a Λ is by its $m_{\text{inv.}}$; simply choose the reconstructed Λ candidate that has the smallest $|m_{\text{inv.}} - m_{\Lambda, \text{PDG}}|$ (Fig. 85).

Because only a small fraction of reconstructed Λ s share daughters, we know that this should be a small effect on \overline{P}_Λ . Indeed, when comparing the \overline{P}_Λ measurements we see a fractional change of 3%, and the difference in \overline{P}_Λ (when *subtracting* uncertainties in quadrature, as we ought to) between the two methods is less than a 2σ effect. This is a useful check because other Thunderdome methods that we checked (e.g. optimizing daughter DCA) do *not* yield consistent measurements. We won’t go in to detail here on the causes of such discrepancies other than to say that, as with other surprising effects in this analysis, it is ultimately caused in part by an asymmetric collider system. Since optimizing $m_{\text{inv.}}$ is the natural choice and yields a small difference in \overline{P}_Λ as we expect, this is our optimization variable of choice.

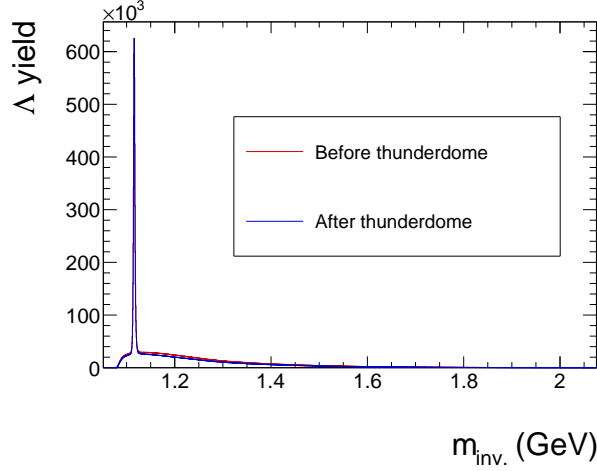


Figure 85: The Λ $m_{\text{inv.}}$ distribution before and after applying the Thunderdome filter. The effect is small and mostly concentrated at $m_{\text{inv.}} > m_{\Lambda, \text{PDG}}$.

Because using KFParticle is a new tool to the STAR collaboration to find Λ s, we want to check how our results compare when using the more traditional topological cut method. Table 1 shows two common sets of topological cuts (both of which were used in the Nature publication) that we use for this check. For each of these cut sets, we look at the difference between the polarization measurements using KFParticle and using that cut set, again, *subtracting* statistical uncertainties in quadrature as we ought to. We observe the differences of integrated \overline{P}_{Λ} as well as the dependences of the differences on p_T , y , and centrality.

The kinematics of the measured Λ s after *all* cuts are shown below:

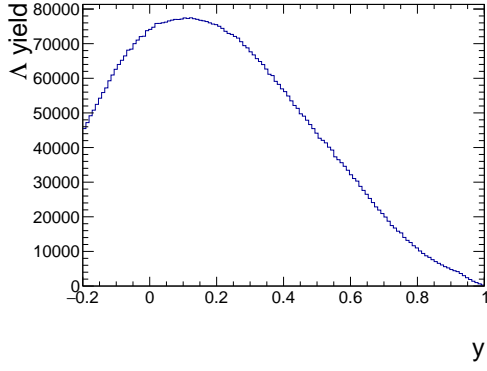


Figure 86: The rapidity distribution of measured Λ s using the final set of cuts.

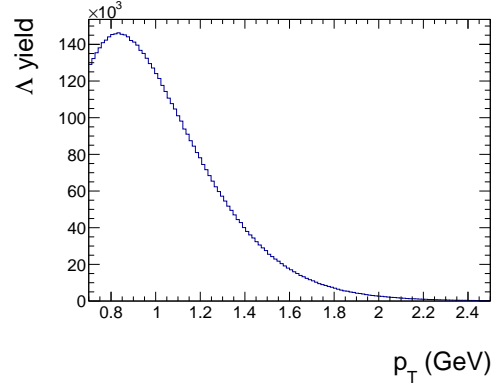


Figure 87: The p_T distribution of measured Λ s using the final set of cuts.

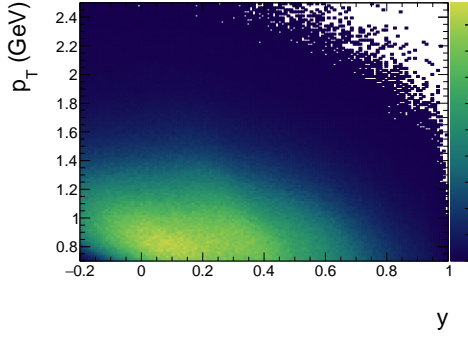


Figure 88: The $y - p_T$ distribution of measured Λ s using the final set of cuts.

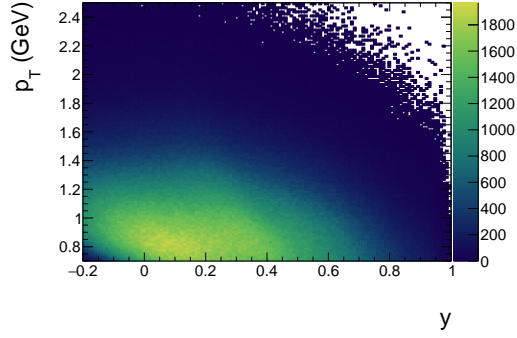


Figure 89: The $y - p_T$ distribution of measured Λ s using the final set of cuts.

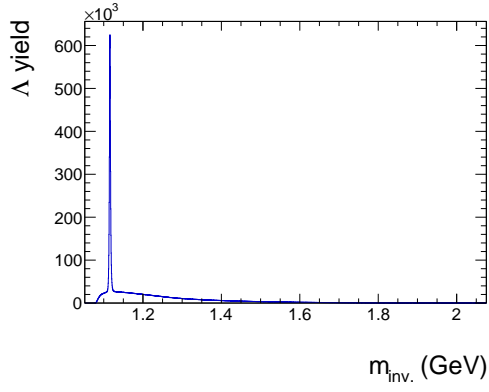


Figure 90: The $m_{\text{inv.}}$ distribution of measured Λ s using the final set of cuts.

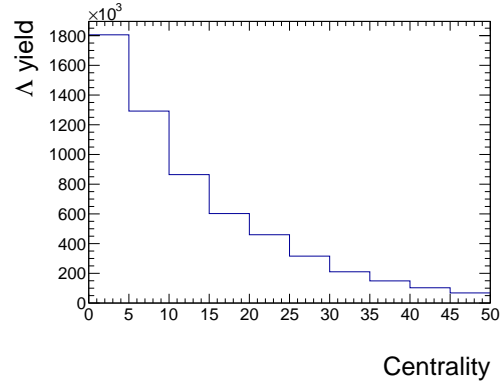


Figure 91: Λ yield as a function of centrality; the drop in yield is significant.

B Determination of subevents

B.1 EPD

Momentum-conservation effects are obvious when looking at $R_{\text{EP}}^{(1)}$ vs. centrality (Fig. 92). When using the entire EPD, $R_{\text{EP}}^{(1)}$ remains very large even for peripheral events; however, when dramatically reducing the number of tracks used in Ψ_1 determination we see $R_{\text{EP}}^{(1)}$ drop for more peripheral collisions, indicating reduced effects of momentum conservation on the measurement (and, yes, and actual reduction in $R_{\text{EP}}^{(1)}$).

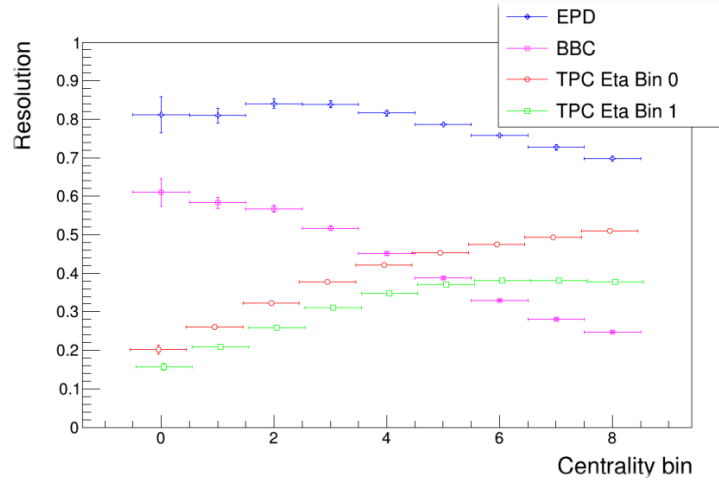


Figure 92: $R_{\text{EP}}^{(1)}$ for the EPD with no momentum-conservation considerations (i.e. using large subevents that capture a significant fraction of all produced particles. Here, especially at more central events (smaller “centrality bin” is shown), $R_{\text{EP}}^{(1)}$ is noticeably and artificially enhanced.

For our measurement of Ψ_1 we use EPD hits from rings 13-16 only ($-2.9 \lesssim \eta \lesssim -2.5$). For rings 12 and below, with $\eta \lesssim -2.9$, there is unstable behavior in $R_{\text{EP}}^{(1)}$; we found that the measured $R_{\text{EP}}^{(1)}$ depended strongly on the choice of reference subevents. Also, when looking at $dN/d\eta$ (Fig. 93), we see an unexpected surplus in yield starting at ring 12. Furthermore, although we know that rapidity and pseudorapidity are not equivalent, we can at least use η as a measure of y ; remembering that $y_{\text{beam}} = -2.09$, we may be able to attribute behavior in ring 12 and below to anything “forward” of y_{beam} , which is not sensible for Ψ_1 measurement. We also saw jumps in \vec{B}_{STAR} -driven Ψ_1 rotation (elaborated later on) between ring 12 and 13, and the list goes on. Because of its unstable behavior, and because we also don’t want a large subevent for Ψ_1 calculation (due to momentum-conservation concerns), we are perfectly justified in ignoring EPD rings 12 and below.

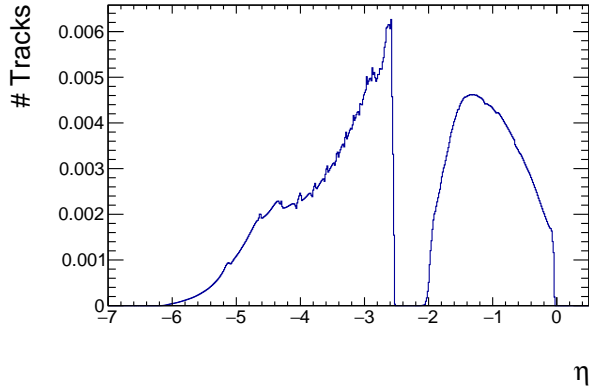


Figure 93: The $dN/d\eta$ distribution, using the TPC and EPD; the η gap between the two detectors is clear. In the TPC, we can see the tracking efficiency dropping sharply around $\eta \sim -1.4$. In the EPD, we can see small spikes, which are attributed to individual tiles; when choosing a random point in tile, the associated η distribution does not match reality, so a more ideal choice would be to have η bin widths match the widths of EPD rings in η . We can see jumps in yield at $\eta \sim -3$ and $\eta \sim -4.4$; these may or may not be physical, and no model would be very useful at describing behavior at such forward rapidities.

In principle, any two groups of particles originating from the same collision will be correlated, at least in part, by momentum-conservation effects. The simplest example is that of two subevents each comprised of one-half of the total emitted particles; the net momentum of one is necessarily equal and opposite the net momentum of the other. As the number of particles in the two subevents approaches zero these effects become negligible. In collider mode, where many particles are produced relative to the number of particles used for subevents, momentum conservation effects are negligible and often ignored; however, at the much lower energy of 3 GeV we must be

more careful. With the exception of the most central events, the number of primary tracks measured in the TPC are fewer than 100; also, we are forced to choose three subevents for an accurate $R_{\text{EP}}^{(1)}$ calculation, as opposed to the two required in collider mode (because of a symmetric collision system). We therefore want to choose TPC subevents with small enough widths in η to minimize these effects but large enough to have a meaningful v_1 associated with them. As discussed earlier, we only want to consider rings 13 and above in the EPD. TPC subevents with η width 0.1 are roughly as small as can be before lack of hits becomes a problem (Fig. 94), while still showing meaningful correlation. For this short study on momentum conservation, we somewhat arbitrarily choose TPC subevents 1 (with $-0.9 < \eta < -0.8$) and 7 (with $-0.3 < \eta < -0.2$), since they are separated well enough in η as to have negligible non-flow correlations; their event-plane correlations are shown in Fig. 95.

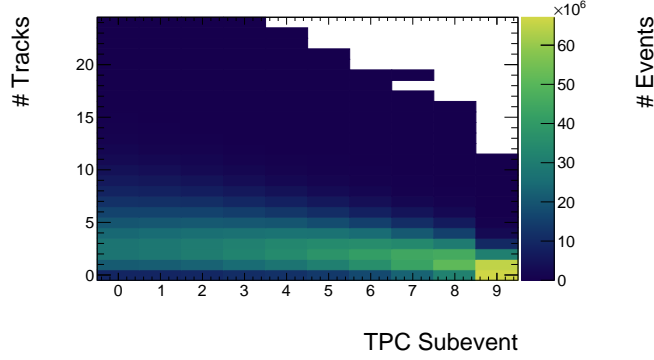


Figure 94: The distribution of number of tracks for each TPC subevent (excuse the label; TPC subevent 0 covers $-1 < \eta < -0.9$, subevent 1 covers $-0.9 < \eta < -0.8$, and so on). We see here that if the subevents were any smaller than 0.1 in η , we would see too many events with “empty” TPC subevents.

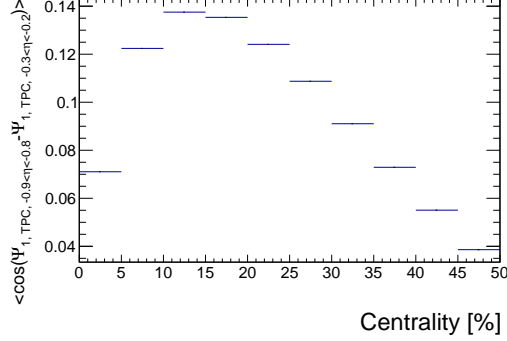


Figure 95: The Ψ_1 correlation of the two TPC subevents chosen for this momentum-conservation study; we see that, although the subevents often have only a small handful of tracks, the correlation between the subevents is still meaningful.

To correct for any momentum-conservation effects present in the EPD is impossible, since doing so would demand knowledge of the track momenta; all we can hope to do is to fold any measured momentum-conservation effect into our systematic uncertainty. Although we cannot reduce TPC subevent sizes any further, we can restrict ourselves to individual EPD rings, which have enough hits on average to make meaningful Ψ_1 measurements. The only obvious way, then, to check for momentum-conservation effects on the polarization observable is to compare polarization measurements using EPD ring 13 alone (“EPD Ring Group 0”), rings 13 and 14 (“EPD Ring Group 1”), rings 13-15 (“EPD Ring Group 2”) and compare it to the group of rings 13-16 used for the final measurement (“EPD Ring Group 3”). It is important when comparing the results to measure the difference between the measurements using various methods (EPD Ring Groups 0, 1, and 2) and the “chosen” method (EPD Ring Group 3) *with the uncertainties subtracted in quadrature*, rather

than simply plotting them side by side. Fig. 96 demonstrates this difference in polarization for the various EPD Ring Groups. If momentum-conservation effects were measurable, we would observe a drop in polarization with EPD Ring Group, as an artificially large $R_{\text{EP}}^{(1)}$ would over-correct the polarization measurement. Since we see no such dependence (in fact all measurements of polarization are consistent), momentum-conservation effects are demonstrably negligible and we need no such corrections or contributions to systematic uncertainties.

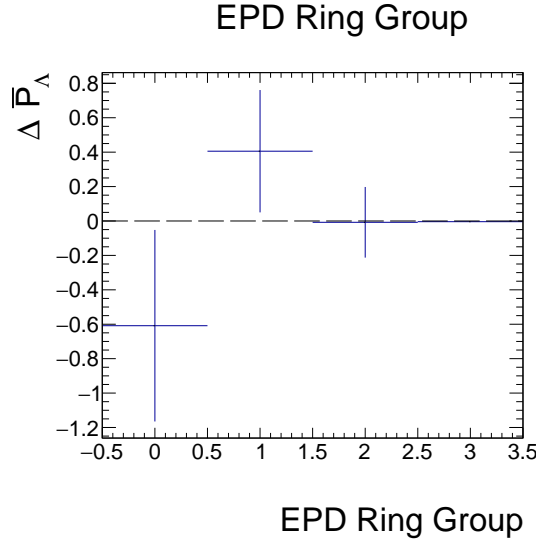


Figure 96: The difference between polarization measurements using various EPD Ring Groups and that using EPD Ring Group 3, with the uncertainties subtracted in quadrature. There is no observable drop in polarization with EPD Ring Group that would arise from momentum-conservation effects.

B.2 TPC

Even without any flow or momentum-conservation effects, Ψ_1 measurements between two subevents can be correlated; if subevents contain particles originating from the same “region” of the QGP, then any relevant physics determining the momenta of the particles will necessarily affect both subevents similarly. We of course want our $R_{\text{EP}}^{(1)}$ measurement (determined with multiple subevents) to be free of such non-flow effects and therefore be accurately represented; if that is not possible, then we would at least hope to be able to correct for such a systematic effect or as a last resort fold various measurements into the systematic uncertainties. As discussed earlier, we are more or less set on EPD rings 13-16 as the “ Ψ_1 -determination subevent”; therefore, the only obvious way to check for non-flow contributions to $R_{\text{EP}}^{(1)}$ is to pick various reference subevent pairs for Eq. 9. In Fig. 97 is shown that, for TPC reference subevents closer in η to the EPD, $R_{\text{EP}}^{(1)}$ becomes artificially large due to non-flow correlations, yet any non-flow correlations between TPC subevents close in η has no effect on $R_{\text{EP}}^{(1)}$ since those contributions are cancelled out (see Eq. 9). We also see that, luckily enough, we are able to find subevents within the TPC far enough from the EPD to minimize these effects; in fact, for TPC subevents 5 and greater (with $\eta > -0.5$), there are no observed non-flow contributions to the $R_{\text{EP}}^{(1)}$ measurement (this is highlighted in Fig. 98). Within this handful of reference subevents, we see no pattern as in Fig. 97, so we need not correct or incorporate differences into systematic uncertainties. We also may freely choose any pair of reference subevents, so arbitrarily we choose TPC subevents 5 ($-0.5 < \eta < -0.4$) and 8 ($-0.2\eta < -0.1$).

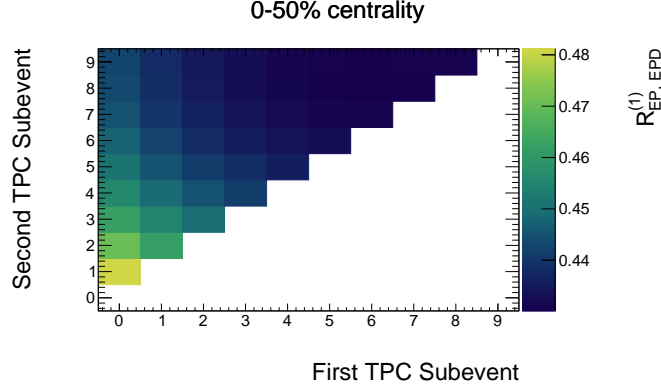


Figure 97: $R_{\text{EP}}^{(1)}$ of the EPD with a variety of TPC subevent choices (excuse the label; TPC subevent 0 covers $-1 < \eta < -0.9$, subevent 1 covers $-0.9 < \eta < -0.8$, and so on). As TPC reference subevents approach zero (i.e. approach $\eta = -1$), $R_{\text{EP}}^{(1)}$ is artificially inflated due to non-flow correlations with the EPD; however, the η gap between TPC subevents is not relevant as such non-flow correlations are cancelled out (see Eq. 9).

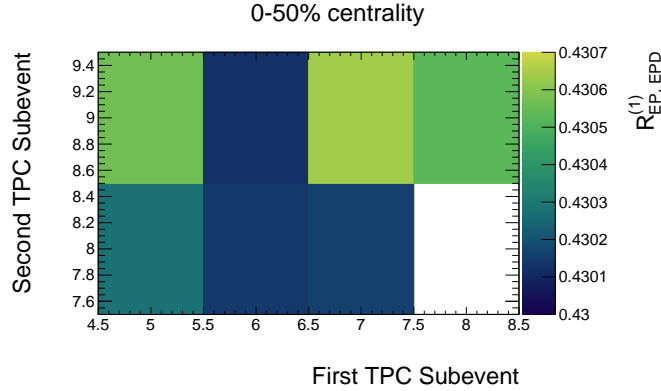


Figure 98: Here is the same plot as in Fig. 97, zoomed and re-scaled onto the region of the TPC far enough from the EPD to have no observable non-flow contributions to $R_{\text{EP}}^{(1)}$.

C Flattening of the event-plane distributions

For $\Psi_{1,\text{Ref.1}}$ we use TPC tracks with $-0.5 < \eta < -0.4$ and for $\Psi_{1,\text{Ref.2}}$ we use TPC tracks with $-0.2 < \eta < -0.1$. In order to reduce the effects of TPC non-uniformity, we weight each track (only when measuring $\Psi_{1,\text{Ref.2}}$) with w_{yield} such that the ϕ distribution of tracks is flat on an η, p_T -dependent basis. For measuring Ψ_1 with the TPC, we use (from Eq. 8) $w = p_T w_{\text{yield}}$ and only consider tracks with $0.15 < p_T < 1.2 \text{ GeV}/c$ (since yield is very low above $1.2 \text{ GeV}/c$ and yield weighting becomes impractical).

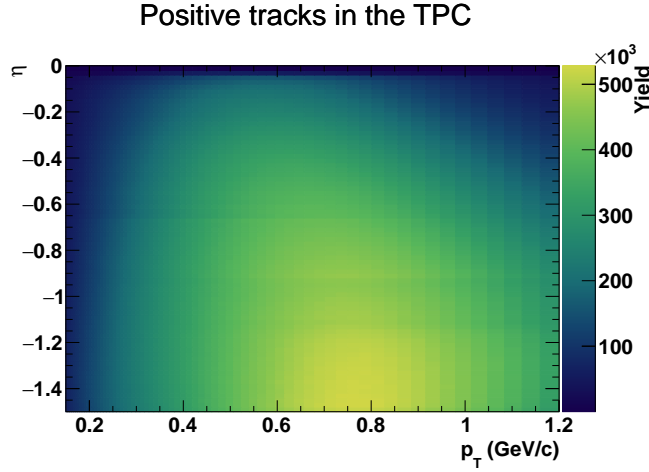


Figure 99: TPC Positive-track yield as a function of p_T and η .

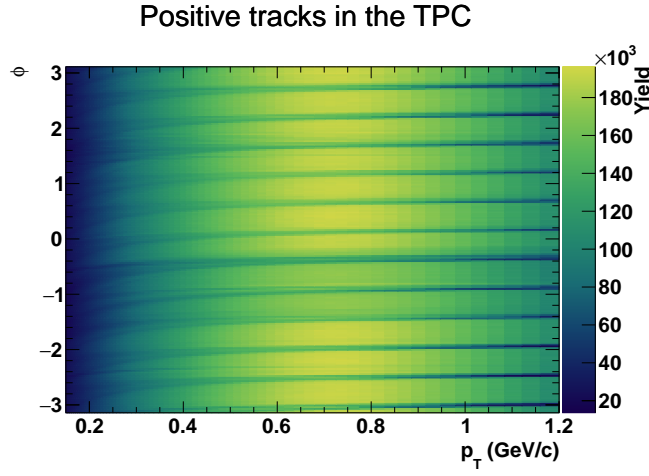


Figure 100: TPC Positive-track yield as a function of p_T and ϕ ; sector boundaries and TPC non-uniformity are obvious.

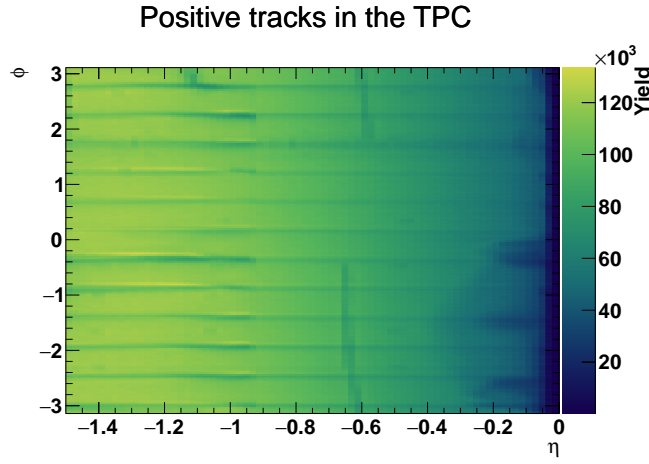


Figure 101: TPC Positive-track yield as a function of η and ϕ ; sector boundaries and TPC non-uniformity are obvious.

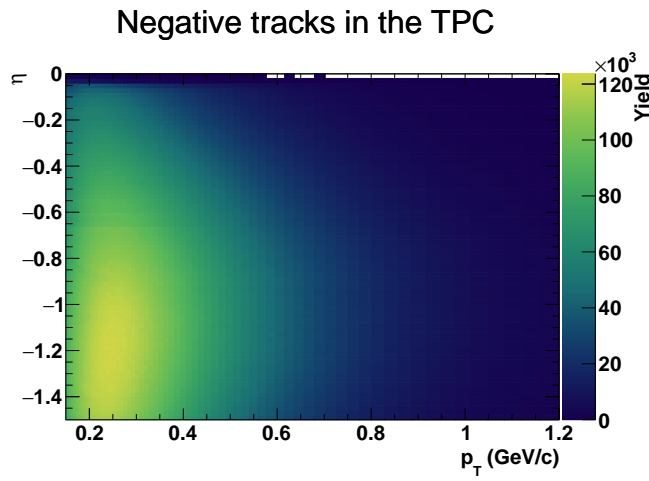


Figure 102: TPC Negative-track yield as a function of p_T and η .

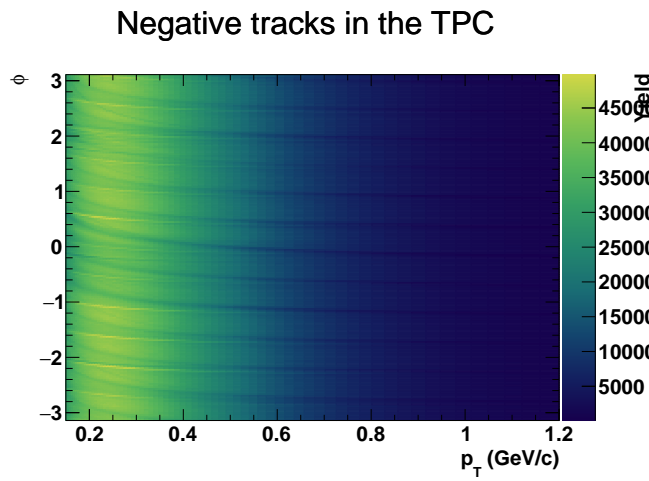


Figure 103: TPC Negative-track yield as a function of p_T and ϕ ; sector boundaries and TPC non-uniformity are obvious.

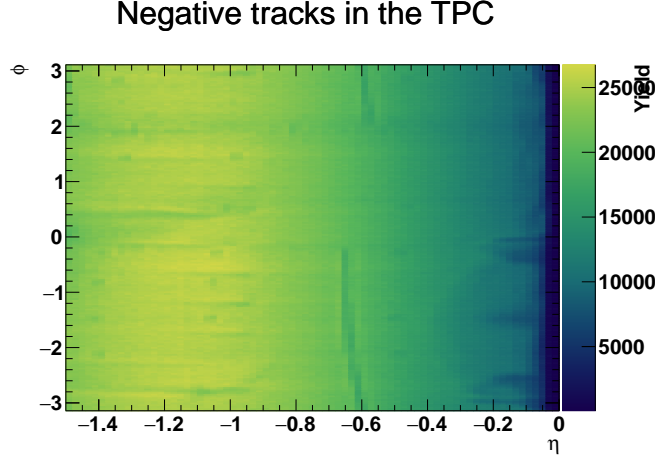


Figure 104: TPC Negative-track yield as a function of η and ϕ ; sector boundaries and TPC non-uniformity are obvious.

For each Ψ_1 , we enforce a flat distribution so that $R_{\text{EP}}^{(1)}$ is not affected by any acceptance (or otherwise unrelated to the collision)-driven correlations. This is done through the standard Fourier-shifting method, using 24 terms:

$$\Delta\Psi_1 = \sum_{i=1}^{24} \frac{2}{i} [\langle \cos(i\Psi_1) \rangle \sin(i\Psi_1) - \langle \sin(i\Psi_1) \rangle \cos(i\Psi_1)]. \quad (34)$$

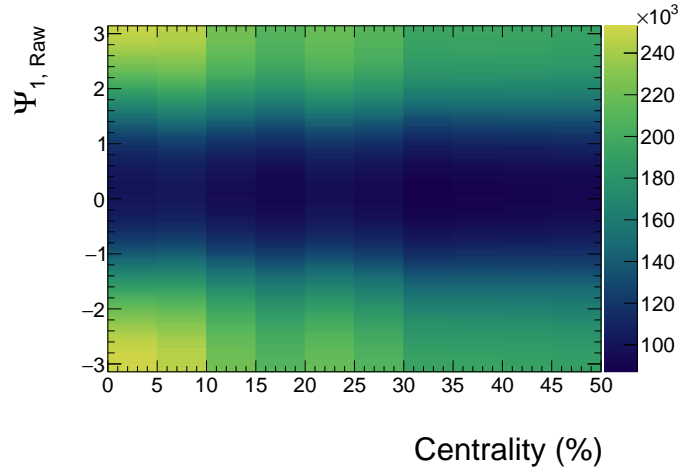


Figure 105: The raw Ψ_1 distribution with respect to centrality; non-uniformity is obvious.

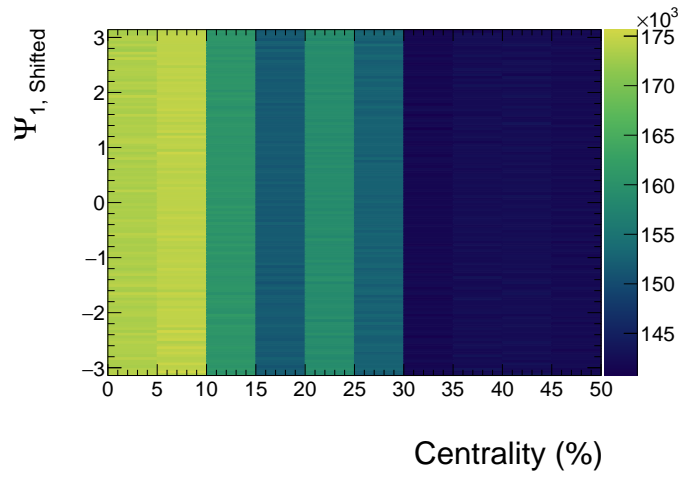


Figure 106: The shifted Ψ_1 distribution with respect to centrality; flatness is obvious.

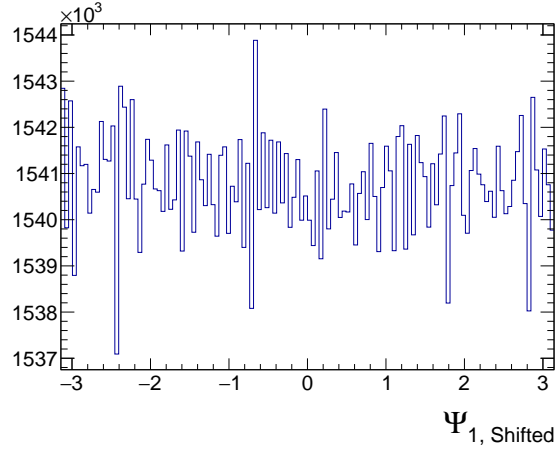


Figure 107: The projection of the above histogram across centrality; flatness is obvious.

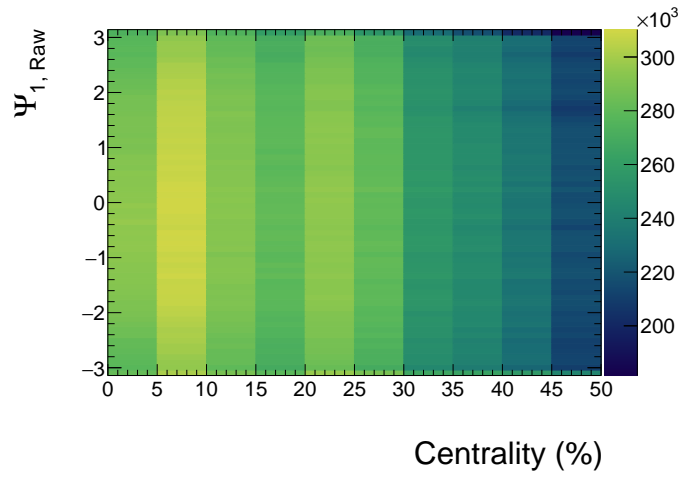


Figure 108: The raw Ψ_1 distribution with respect to centrality; non-uniformity is obvious.

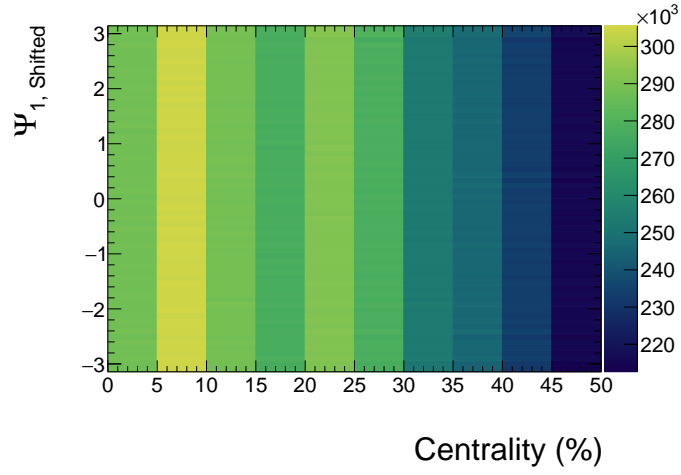


Figure 109: The shifted Ψ_1 distribution with respect to centrality; flatness is obvious.

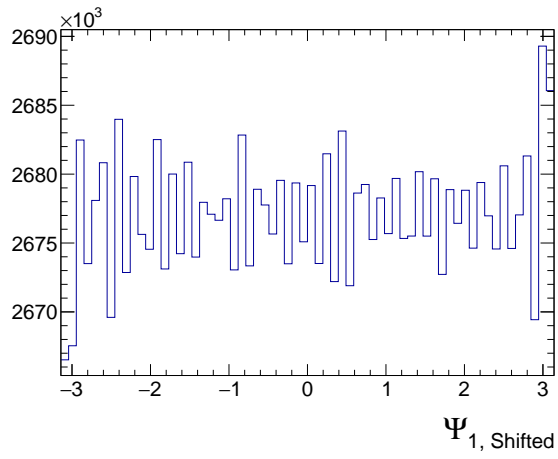


Figure 110: The projection of the above histogram across centrality; flatness is obvious.

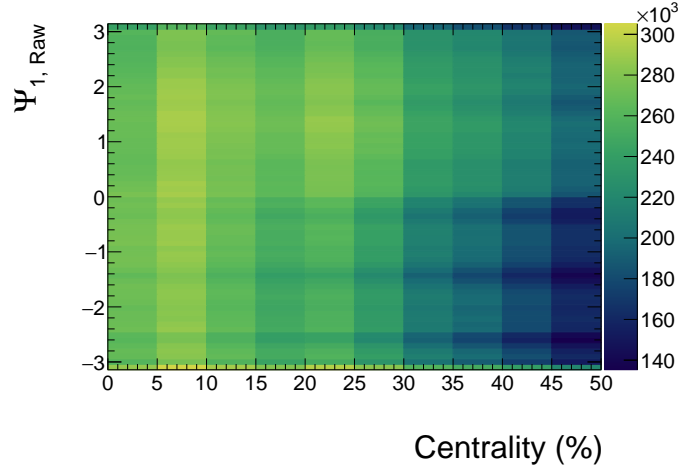


Figure 111: The raw Ψ_1 distribution with respect to centrality; non-uniformity is obvious.

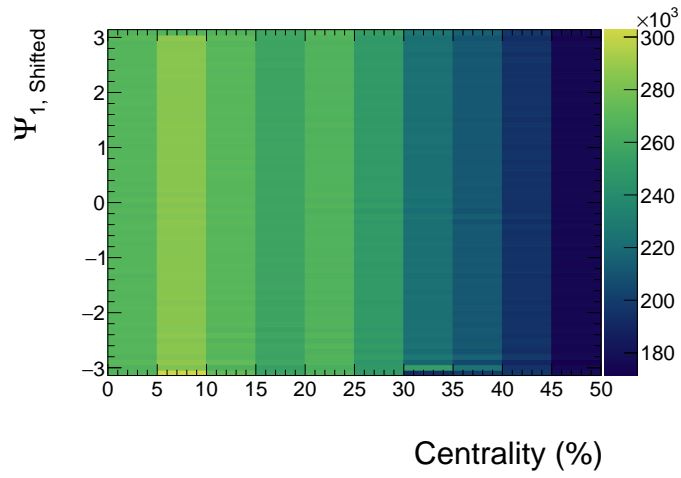


Figure 112: The shifted Ψ_1 distribution with respect to centrality; flatness is obvious.

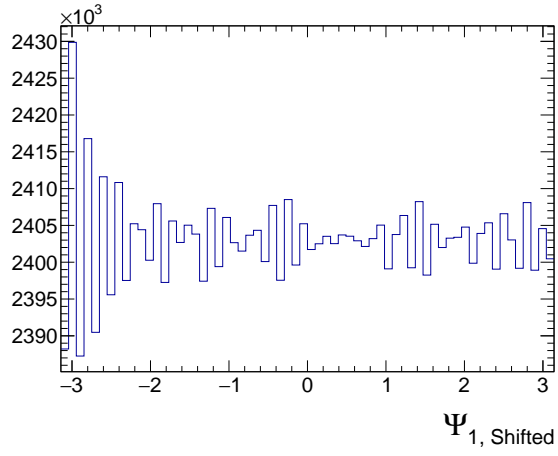


Figure 113: The projection of the above histogram across centrality; flatness is obvious.

D Position of EPD tile hit

Typically, when finding any event-plane angle from the EPD, one will use the geometric center of the tile for determining the ϕ, η of the corresponding hit(s) (though a non-flat $dN/d\eta$ distribution means the average hit location will be slightly farther radially from the tile center, the effect would be quite small). At such a low energy, where it is common to have only a small handful of hits in the EPD, we start to see the azimuthal structure of the EPD in the Ψ_1 distribution, even after Fourier shifting with 48 terms (which is twice the number of sectors in the EPD). A flat Ψ_1 distribution could be achieved by using a random point within the tile for determining the ϕ of the corresponding hit; Fig. 114 shows the Fourier-shifted Ψ_1 distributions using these two methods, and it is clear that using a random point within each tile leads to a flat Ψ_1 distribution.

One could include more Fourier terms than 48, since any distribution will approach perfect flatness as the number of Fourier terms approaches infinity. Fig. 115 shows these shifting terms out to $i_{\text{Fourier}} = 256$, where these shifting terms are still significant. Carrying out shifting to terms in the thousands would be computationally expensive and anyways unnecessary; Fig. 116 shows that there is no preferred direction of Ψ_1 in any of the rings and the distribution is sufficiently flat, even when using the tile center. This may seem dubious, but keep in mind that virtually any plotted Ψ_1 distribution is hiding similar “spikey” behavior; if we used sufficiently fine binning for

the TPC, we would see spikes corresponding to the limits of floating-point precision, and we would use $\langle \sin(\Psi_1) \rangle, \langle \cos(\Psi_1) \rangle$ just as in Fig. 116 to justify the non-flat Ψ_1 distribution being okay.

The next question might address how the resolutions compare between the two methods. We can simply correlate the Ψ_1 measurements between the EPD rings and an arbitrary TPC subevent, and take the ratio between these correlations using the two methods. This is shown in Fig. 117 and, besides the first ring wherein tiles have twice the azimuthal width as any other (and the ratio is anyways still near 1 and, as we'll see later, it has a relatively small $R_{\text{EP}}^{(1)}$), the two methods yield essentially the same result.

The message of this study is that the choice to use the tile center or a random point within the tile when assigning a ϕ to an EPD hit for the Ψ_1 measurement is, more or less, an arbitrary one. Because of this, we arbitrarily choose the one that produces a visually flat distribution (see Fig. 114).

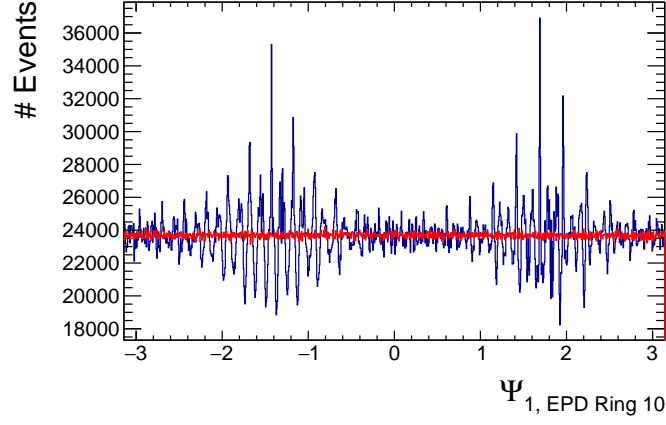
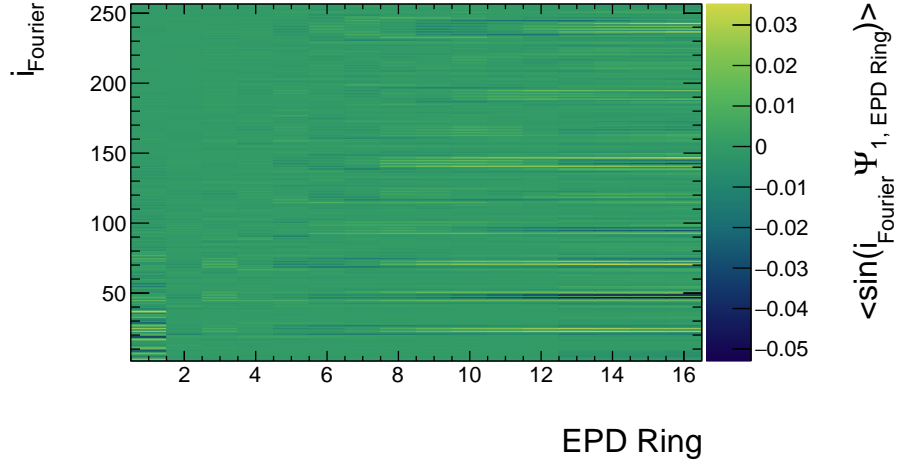
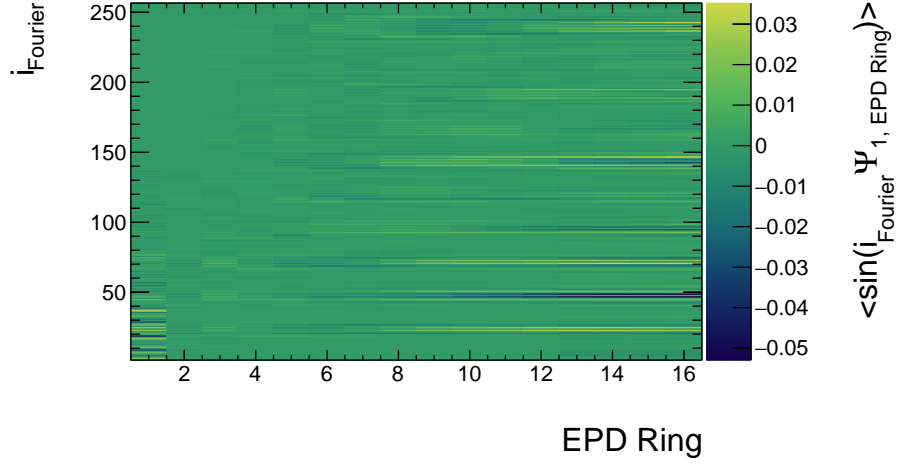


Figure 114: Fourier-shifted Ψ_1 distributions of an arbitrarily selected EPD ring with 48 terms. Using the tile center for the ϕ of each EPD hit (shown in blue) reveals the azimuthal structure of the EPD and using a random point within the tile of each EPD hit (shown in red) “washes out” the structure and allows for a flat distribution.



(a)



(b)

Figure 115: Fourier-shifting terms for the EPD, using the tile center for the ϕ of the EPD hit, excluding the $i_{\text{Fourier}} = 1$ since it is the largest and dominates the color scale. We see significant behavior for $i_{\text{Fourier}} \sim n_{24}$, corresponding the the number of azimuthal divisions (sectors) in the EPD.

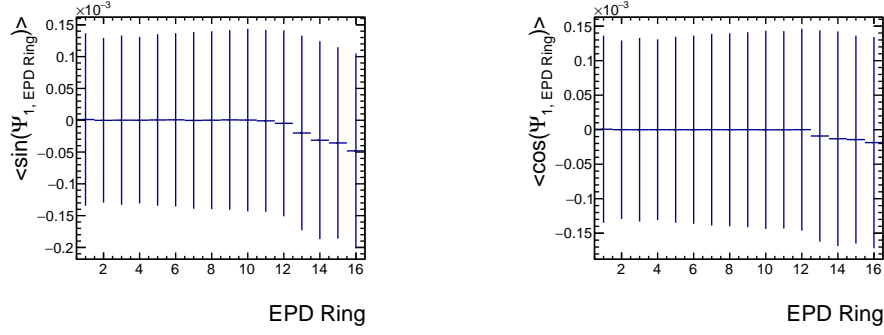


Figure 116: Despite the structure in the Ψ_1 distribution when using the tile center (seen in Fig. 114), we see no preferred direction.

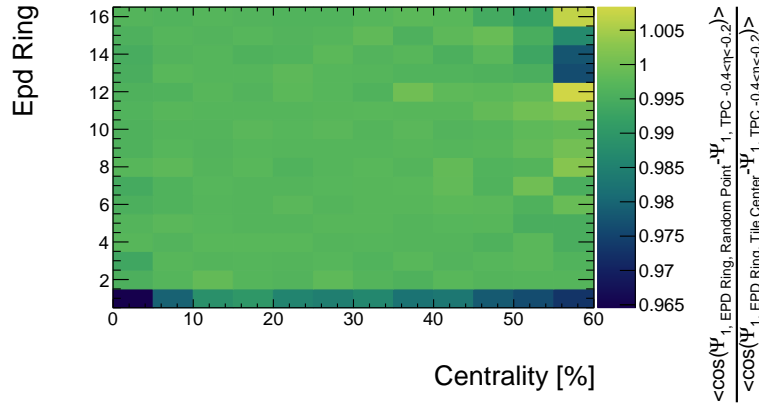


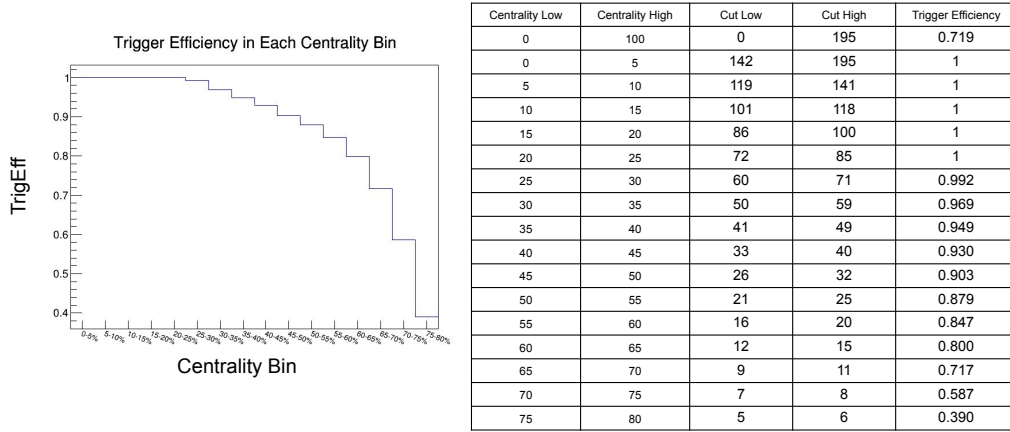
Figure 117: Correlating Ψ_1 measurements between the EPD and TPC and taking the ratio of the results between the two methods (using EPD tile centers or random points on the tile), we see virtually no difference besides in the first ring, where the tiles have twice the azimuthal width as any other.

E Efficiency Corrections

E.1 Trigger Efficiency

As in the centrality study, performed by the UC Davis group [60], the efficiency of the trigger to measure when a legitimate collision happened is determined by comparing the measured track-multiplicity distribution to that of a Glauber model (with parameters chosen through fitting). Fig. 118 shows the trigger efficiency as a function of centrality. We simply weight a Λ hyperon's contribution to \bar{P}_Λ by the inverse of this trigger efficiency.

BES-II FXT 3.0 GeV (2018)



Zachary Sweger 11/17/2020

15

Figure 118: Trigger efficiency as a function of collision centrality.

E.2 Λ -measurement efficiency

Due to various factors associated both with the detector system and the Λ -finding algorithm, there is a smaller-than-one probability that a given Λ will be measured, and this probability depends on p_T and y . It is important then to appropriately correct any integrated measurements for this Λ -measurement efficiency. Consider for example a \bar{P}_Λ that rises with $|y|$ and an efficiency that falls with $|y|$; without any correction, we would under-report contributions to \bar{P}_Λ from Λ s with larger $|y|$ and the integrated \bar{P}_Λ measurement would therefore be lower than the true value.

In order to appropriately correct for this effect we want to know the *true* Λ yield with respect to p_T and y ; it may seem impossible to know this, but by using simulations we may generate a given number of Λ s with some arbitrary dependence on p_T and y (usually flat), embed them into real data (flagging whichever protons and pions came from the embedding), and then reconstruct Λ s as usual. We then simply divide the measured Λ yield by the input Λ yield (as functions of p_T and y) in order to measure the efficiency. We must take care to use the same exact Λ -finding algorithms (including any kinematic or topological cuts) for these embedded Λ s as we use for the \bar{P}_Λ measurement.

For our study, we used an embedded Λ sample provided by Yue-Hang Leung (LBNL); 3M Λ s were embedded with a flat p_T and y distributions in the range $0 < p_T < 3$ GeV and $-2 < y_{\text{Lab}} < 0$. Fig. 119 shows the efficiency calculated for our Λ -finding algorithm.

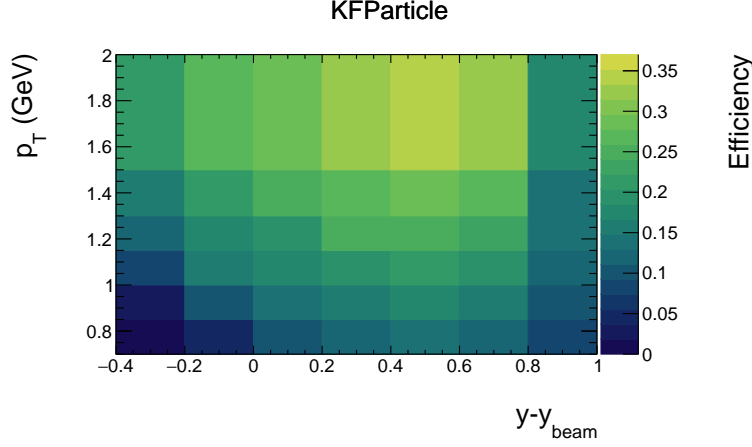


Figure 119: The ratio of embedded Λ s to *measured* embedded Λ s with respect to p_T and y ; this ratio measures the efficiency of identifying Λ s as affected by both the STAR detector and the Λ -finding algorithm.

E.3 Acceptance efficiency

Eq. 24 derives from the global polarization definition,

$$\frac{dN}{d \cos \delta} = \frac{1}{2} (1 + \alpha_H P_H \cos \delta), \quad (35)$$

where $\cos \delta = \vec{J}_{\text{sys.}} \cdot \hat{p}_p^*$; however, this derivation assumes that the integral over the solid angle $d\Omega_p^* = d\phi_p^* d\sin\theta_p^* d\theta_p^*$ is unaffected by detector acceptance correction. If we appropriately account for this detector acceptance, we instead have

$$\begin{aligned} \frac{8}{\pi\alpha} \langle \sin(\Psi_1 - \phi_p^*) \rangle &= \frac{4}{\pi} \langle \sin\theta_p^* \rangle P_H - \frac{2}{\pi} \langle \sin\theta_p^* \cos[2\langle \phi_H - \phi_p^* \rangle] \rangle P_H^{(2)} \\ &= A_0 P_H - A_2 P_H^{(2)}. \end{aligned} \quad (36)$$

The full derivation is in the 2007 STAR polarization paper. The second term in Eq. 36 is actually negligible; $A_2 \sim \mathcal{O}(10\%)$ (Fig. 120) and $P_H^{(2)} \sim \mathcal{O}(0.1\%)$ (Fig. 121). We are left with an $\mathcal{O}(0.01\%)$ effect and we therefore ignore this correction. We then only need to scale our measurement by A_0^{-1} in order to correct for this acceptance efficiency.

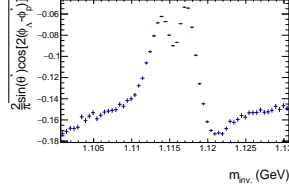


Figure 120: The second-harmonic acceptance-correction term A_2 , from Eq. 36; we see that, although there is a dependence on $m_{\text{inv.}}$, the term is less than 10% within the Λ mass peak.

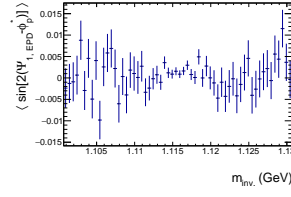


Figure 121: The second-harmonic polarization term $P_H^{(2)}$, from Eq. 36; we don't see a strong dependence on $m_{\text{inv.}}$, and the term is less than 0.1% within the Λ mass peak.

The first term in Eq. 36, A_0 , is of order $A_0 \sim \mathcal{O}(7\%)$ and depends on $m_{\text{inv.}}$.

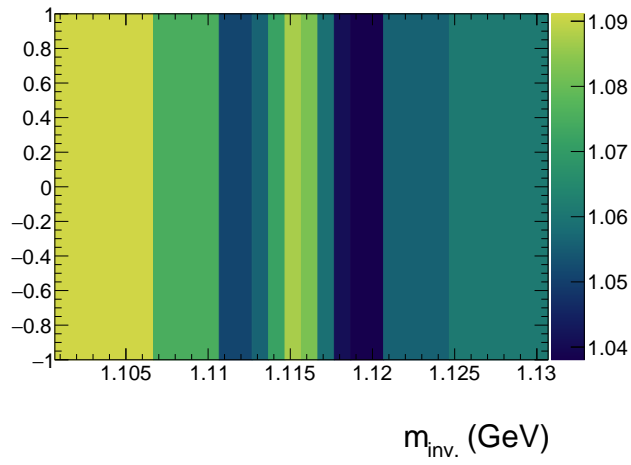


Figure 122: The A_0 term from Eq. 36 as a function of $m_{\text{inv.}}$; the dependence is quite strong.

This term also shows significant dependence on each of the differential variables studied.

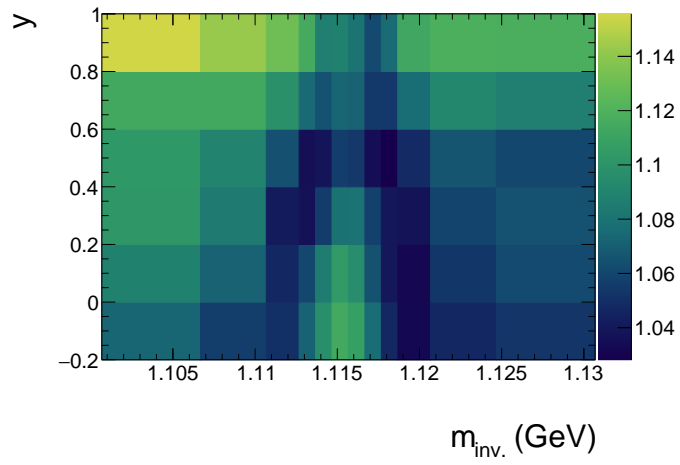


Figure 123: The A_0 term from Eq. 36 as a function of $m_{\text{inv.}}$ and y .

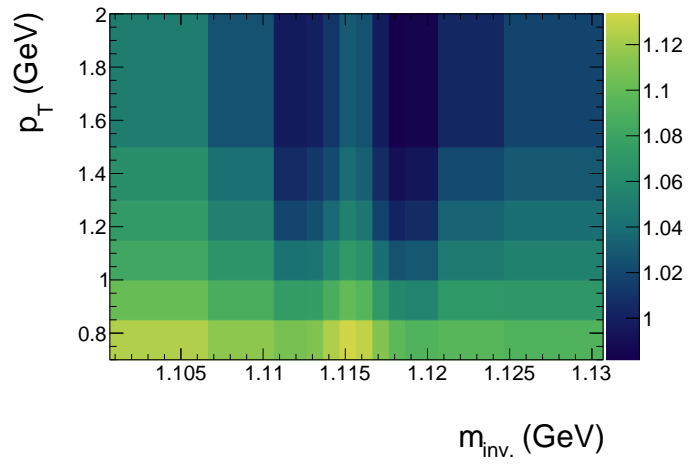


Figure 124: The A_0 term from Eq. 36 as a function of $m_{\text{inv.}}$ and p_T .

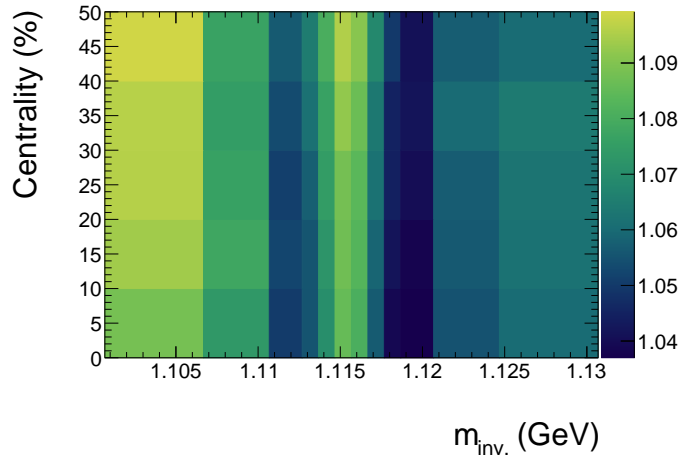


Figure 125: The A_0 term from Eq. 36 as a function of $m_{\text{inv.}}$ and Centrality.

In fact, whenever we compare polarizations between two methods in order to check for systematic mistakes or to quantify systematic uncertainties, we always correct for A_0 with respect to both $m_{\text{inv.}}$ and whichever differential variable is being studied.

F Systematic uncertainties

F.1 Overview

In this section, we will take care to appropriately use systematic parlance: systematic effects (reproducible inaccuracies due to detector calibration, measurement technique, etc., for which there must be corrections), systematic errors (failings to account for systematic effects), and systematic uncertainties (uncertainties associated with the corrections for the systematic effects). There are also *checks* for systematic effects, which are often confused with *true* systematic effects themselves. For example, it is not uncommon for analyzers to vary arbitrarily chosen cuts arbitrary amounts and fold the variations in the final observable into the total systematic uncertainties *regardless of whether any significant variations existed*; the appropriate thing to do would instead be to *check* whether any significant variations exist (so long as none are expected in the first place) (where significance can be determined by comparing the separate measurements, each using different cuts, through the difference in those measurements with their statistical uncertainties *subtracted* in quadrature). If no such variation is observed, then the check passed the test and the analyzer can then move on; otherwise, the analyzer must understand *why* such a variation occurred and correct for it, folding any uncertainties deriving from that correction into the final systematic uncertainty. Only when one is “truly at thy wit’s end” in investigating the systematic ef-

fect may they fold such variations into the systematic uncertainty; this is only valid as a last resort. The e-print by Roger Barlow, “Systematic Errors: Facts and Fictions” (<https://arxiv.org/pdf/hep-ex/0207026.pdf>), would be very useful to anyone interested in further discussion or clarification.

F.2 Checks for systematic mistakes

We further checked for systematic errors by varying things that we didn’t expect to change the measurement of \overline{P}_Λ , which included altering the Λ -finding algorithm (using our own sets of topological cuts as opposed to KFParticle) and using different subevents for the measurement of Ψ_1 . The cut-set topological cuts are given in Tab. 1.

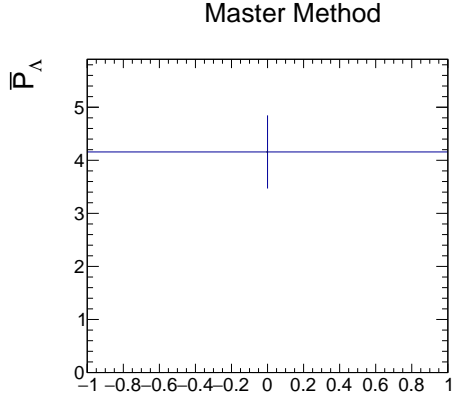


Figure 126: Difference between polarization using the standard KFParticle-found Lambdas and using the “manually”-found Lambdas (using the first cut set). This is the integrated result and the x axis is simply a meaningless placeholder.

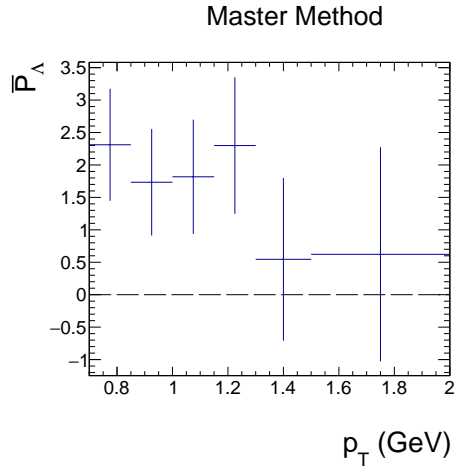


Figure 127: Difference between polarization using the standard KFParticle-found Lambdas and using the “manually”-found Lambdas (using the first cut set).

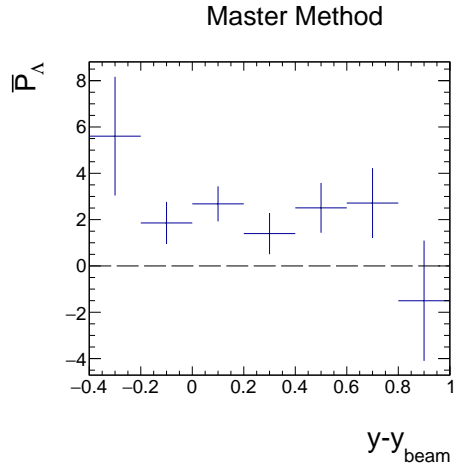


Figure 128: Difference between polarization using the standard KFParticle-found Lambdas and using the “manually”-found Lambdas (using the first cut set).

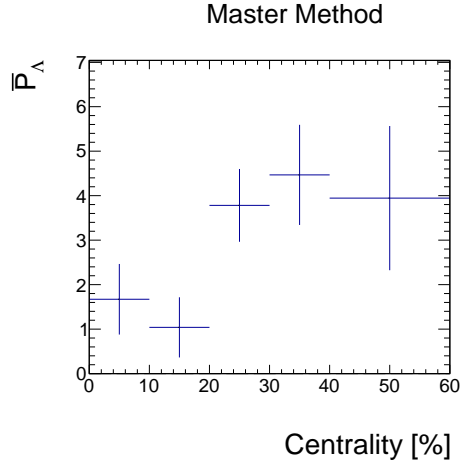


Figure 129: Difference between polarization using the standard KFParticle-found Lambdas and using the “manually”-found Lambdas (using the first cut set).

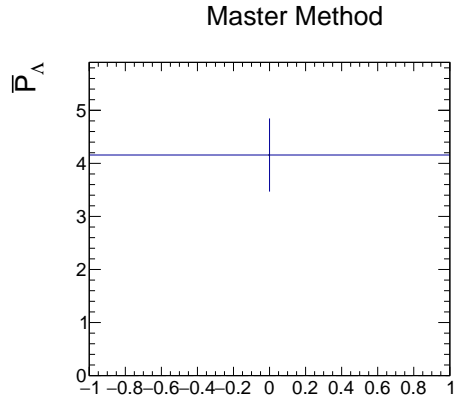


Figure 130: Difference between polarization using the standard KFParticle-found Lambdas and using the “manually”-found Lambdas (using the second cut set). This is the integrated result and the x axis is simply a meaningless placeholder. Note: this is not simply a plot of \bar{P}_Λ vs. Placeholder; we subtract the integrated result *and* subtract the statistical uncertainties in quadrature.

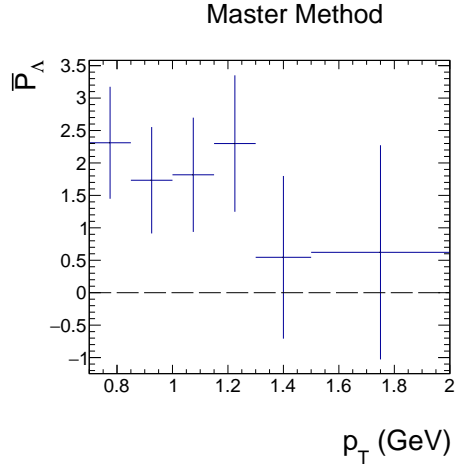


Figure 131: Difference between polarization using the standard KFParticle-found Lambdas and using the “manually”-found Lambdas (using the second cut set). Note: this is not simply a plot of \overline{P}_Λ vs. p_T ; we subtract the integrated result *and* subtract the statistical uncertainties in quadrature.

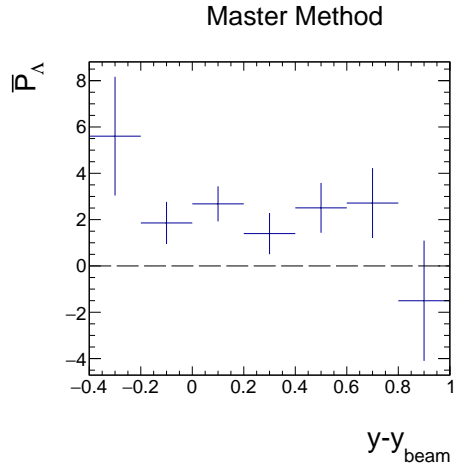


Figure 132: Difference between polarization using the standard KFParticle-found Lambdas and using the “manually”-found Lambdas (using the second cut set). Note: this is not simply a plot of \overline{P}_Λ vs. ComRapidity; we subtract the integrated result *and* subtract the statistical uncertainties in quadrature.

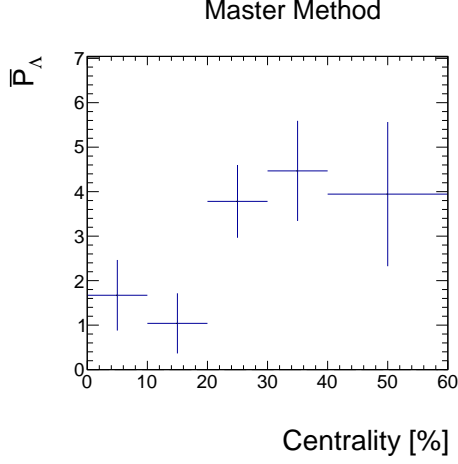


Figure 133: Difference between polarization using the standard KFParticle-found Lambdas and using the “manually”-found Lambdas (using the second cut set). Note: this is not simply a plot of \bar{P}_{Λ} vs. Centrality; we subtract the integrated result *and* subtract the statistical uncertainties in quadrature.

We also need to check for dependences of \bar{P}_{Λ} related to STAR geometries, RHIC state, weather, etc. To this end, we studied the dependence of \bar{P}_{Λ} on the background and true event rates, day of the run, day of the week, hour of the day, and ϕ_{Λ} . When studying this, instead of simply plotting \bar{P}_{Λ} against each of these variables, we instead subtract the integrated \bar{P}_{Λ} from \bar{P}_{Λ} plotted against each of the variables, and subtract statistical uncertainties in quadrature. For these checks, we did not find any systematic effects

F.3 Contributions to the total systematic uncertainty

Various checks for systematic effects are explained in previous sections. The legitimate systematic uncertainties come from the following:

- Uncertainty in the A_0 correction term: σA_0
- Statistical uncertainty in α_{Λ} : $\sigma \alpha_{\Lambda}$
- Statistical uncertainty in $R_{EP}^{(1)}$: $\sigma R_{EP}^{(1)}$

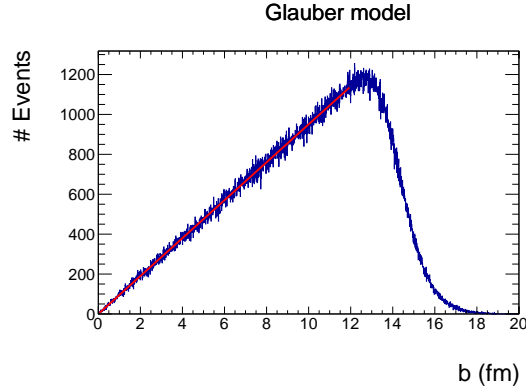
- Uncertainty in $\Delta\Psi_{1,EPD}$: $\sigma\Delta\Psi_{1,EPD}$
- Uncertainty in the dependence of $\overline{P}_\Lambda^{\text{bgd.}}$ on $m_{\text{inv.}}$ (flat or linear): $\sigma\overline{P}_\Lambda^{\text{bgd.}}$

For each of the known systematic effects, we measure \overline{P}_Λ vs. each differential variable (centrality, p_T , y , and integrated) with the appropriate change (e.g. taking $\alpha_\Lambda = \alpha_\Lambda \pm \sigma\alpha_\Lambda$ to measure the effect of the uncertainty in the α_Λ correction) and take the difference between the new measurement and the “standard” measurement ($\overline{P}_\Lambda^{\text{bgd.}} - \overline{P}_{\Lambda\text{Standard}}$). The square root of the sum of these differences for each individual data point for each differential measurement represents the systematic uncertainty on that data point. Below we show these differences for each systematic effect, and for each differential variable. Note that the statistical uncertainties are subtracted in quadrature; this is useful for determining whether a given effect is truly systematic. For the purposes of measuring the systematic uncertainty, we do not use them.

G Comparing \overline{P}_Λ measurements with theory

G.1 Extracting centrality from impact parameter

Model predictions serve obvious benefits for comparison with measurements, but polarizations and vorticities are often given in terms of impact parameter, rather than centrality. The simplest way to extract the model predictions of polarization and vorticity corresponding to 20-50% centrality or other centralities would involve analyzing the impact-parameter distribution. By using a Glauber model, we see that $dN/db \propto b$ in the range $0 < b < 12$ fm (where the fit and Glauber model no longer match):



[H]

Figure 134: The impact-parameter distribution using a Glauber model

If the fit to this distribution is extrapolated to $b = 14.5$ fm, then the integral recovers the total number of simulated events; therefore, we can

normalize such that:

$$\int_0^{14.5 \text{ fm}} \frac{dn}{db} db = 1, \quad n = N^{-1} \quad (37)$$

and centrality can therefore be recovered from impact parameter, valid up to $b = 12 \text{ fm}$.

$$\frac{dn}{db} = cb, \quad c = \left[\frac{(14.5 \text{ fm})^2}{2} \right]^{-1} \quad (38)$$

$$n = \frac{cb_{\text{max}}^2}{2} = \frac{b_{\text{max}}^2}{(14.5 \text{ fm})^2} \quad (39)$$

$$b_{\text{max}} = 14.5 \text{ fm} \sqrt{n} \quad (40)$$

$$b_{20\%} = 14.5 \text{ fm} \sqrt{0.2} = 6.5 \text{ fm} \quad (41)$$

$$b_{50\%} = 14.5 \text{ fm} \sqrt{0.5} = 10.3 \text{ fm} \quad (42)$$

$$(43)$$

We find here that $b \approx 8 \text{ fm}$ corresponds to 20-50% centrality, and since most predictions include results at $b = 8 \text{ fm}$, this suffices. If we want to extract the prediction's dependence on centrality (as determined through multiplicity) in order to make a comparison to our measured dependence of polarization on centrality, we simply follow the same procedure as above, extracting the centrality from the given impact parameters.

One problem with this simple approach is that it does not take into account the dependence of Lambda yield on centrality. \overline{P}_Λ (according to any model or observation) increases with centrality, but we also measure fewer Λ s at larger centrality; therefore, a *measurement* of \overline{P}_Λ in a given centrality window will be dominated by the lower end of centrality and will be smaller than

what a theory prediction might suggest with the above picture. To quantify the effect, we use data from a Glauber model provided by Zachary Sweger of the UC Davis group who conducted the centrality study relevant for this data set [60]. We use our *measured* multiplicity distribution to appropriately scale the multiplicity distribution from the Glauber model (since the Glauber multiplicity does not “miss” any particles due to detector efficiencies).

Multiplicity from the Glauber model is achieved through sampling a negative binomial distribution m times; m is given by

$$m = xN_{\text{coll.}} + \frac{(1-x)}{2}N_{\text{part.}}, \quad (44)$$

where x is the “hardness” parameter, $N_{\text{coll.}}$ is the number of nucleon collisions, and $N_{\text{part.}}$ is the number of participant nucleons. x is achieved through fitting and found to be zero. The parameterization of the negative binomial distribution is also found through fitting and $\mu = 0.9000$, $k = 39.984$ are achieved. Details can be found in Ref. [60].

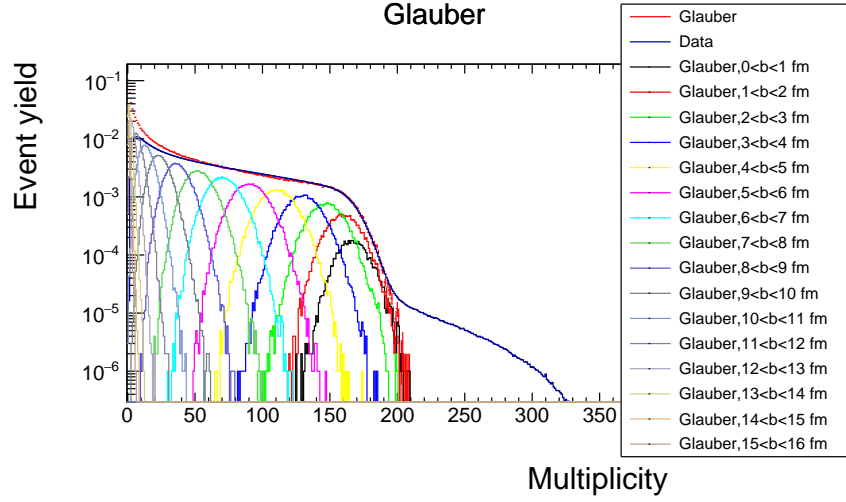


Figure 135: The multiplicity distributions from both data and Glauber. For Glauber, we can also see the multiplicity distributions corresponding to each 1 fm impact-parameter window. The trigger efficiency at low multiplicity is obvious.

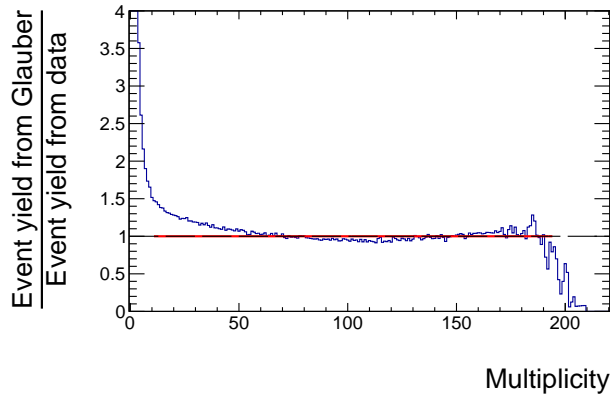


Figure 136: The ratio of multiplicity distributions from both data and Glauber. In the range $40 \lesssim \text{multiplicity} \lesssim 190$ the Glauber model reproduces the observed multiplicity fairly well.

We can then achieve the estimated multiplicity distribution of Λ yield (rather than event yield) with trigger efficiency correction for each 1 fm impact-parameter yield by simply scaling the *normalized* Glauber (Event yield vs.) Multiplicity distribution histogram for each impact-parameter window by the measured Λ yield vs. Multiplicity distribution histogram.

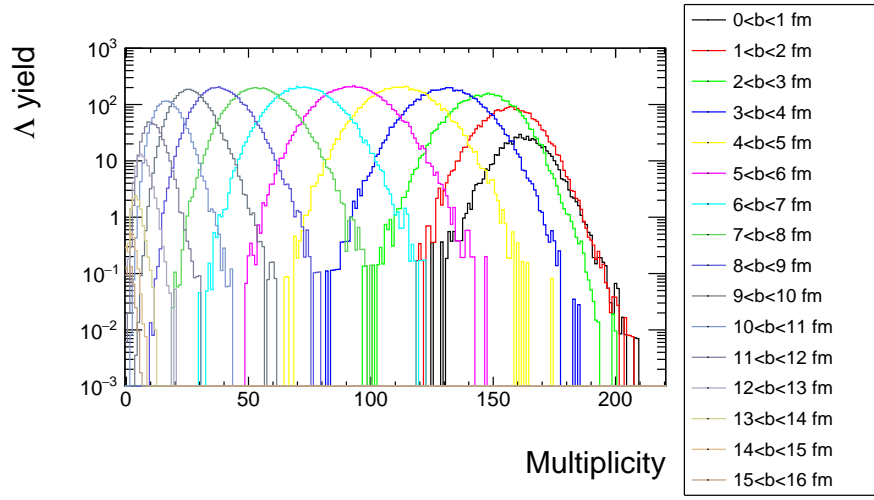


Figure 137: The estimated trigger-efficiency-corrected Λ yield vs. multiplicity distribution for each 1 fm impact-parameter window. We see a stark difference compared to Fig. 135; here, above $b = 3$ fm, Λ yield falls with centrality whereas event yield rises.

Then, for a model prediction with a few given impact parameters, we can extrapolate polarization for any impact parameter by assuming zero vorticity and polarization at $b = 0$ fm, fitting each adjacent pair of points with a straight line, and using the last such slope for $b > b_{\max}$ (see Fig. 138).

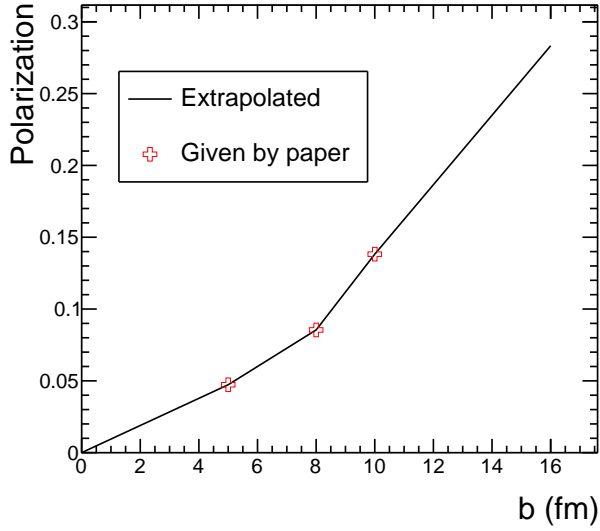


Figure 138: Theory polarization extrapolated from three given impact parameters across the range $0 < b < 16$ fm. We assume zero polarization and vorticity at $b = 0$ fm and take the last linear fit beyond the last data point. The values shown here are from UrQMD predictions at low energy [24].

Then, for a given multiplicity range, we can get the normalized Λ yield vs. impact parameter:

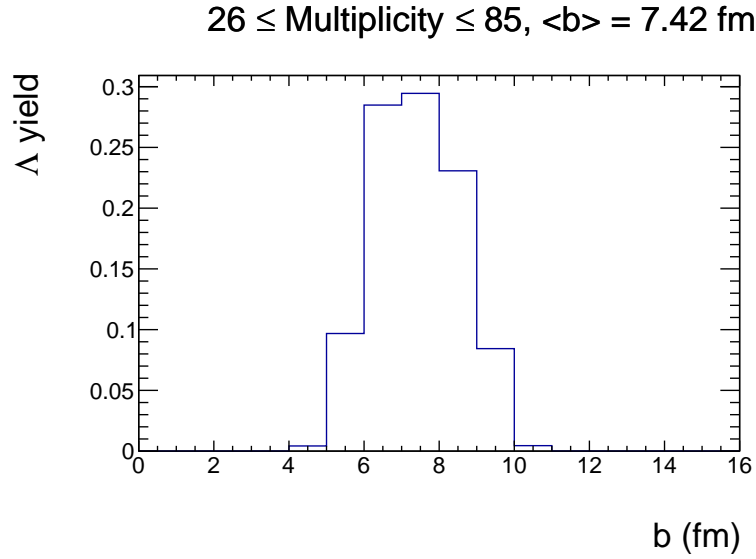


Figure 139: Λ yield vs. impact parameter for the 20-50% centrality window.

With both this extrapolated theory polarization vs. impact parameter (Fig. 138) and the Λ yield vs. impact parameter (Fig. 139), we can estimate the theory polarization in a given centrality window by simply summing the product of the normalized Λ yield and the extrapolated theory polarization for each 1 fm impact-parameter window.

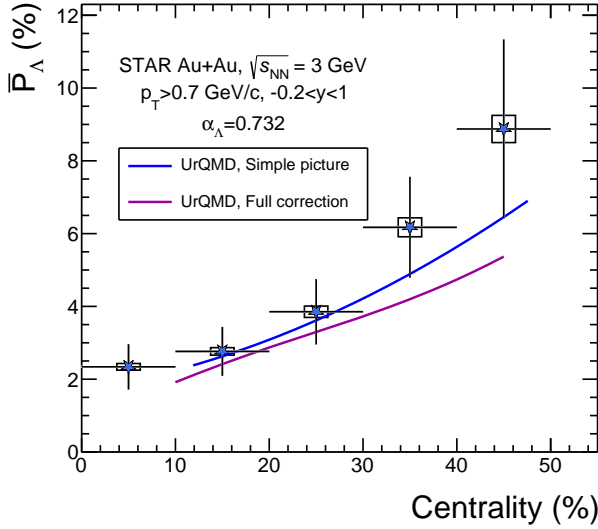


Figure 140: Polarization vs. centrality, compared to UrQMD [24] using the two methods described here. The “simple picture” uses Eq. 40 and only the three impact parameters given by the model calculation, and the “full correction” uses the Glauber-model Λ -yield weighting and theory extrapolation described above.

Since these methods agree fairly well, the choice of method used in the publication is not clear. On one hand, the “full correction” corrects for the poor assumptions made in Eq. 40 and therefore may more accurately reflect the expectation from a model; on the other hand, the “simple picture” is far easier to reproduce and understand by the reader, and there are always imperfections with the “full correction” method (Fig. 136 shows discrepancies between the measured and expected multiplicities, we need to make assumptions about values not quoted by the theory study, etc.). Since reproducibility and understandability are important, and there is always not a substantial difference between the two methods, we will use the “simple

picture” method.

G.2 Extracting exclusive y ranges from inclusive y ranges

Some theory predictions give polarizations with a variety of inclusive ranges. The 3-Fluid Dynamics calculations [31], for example, give three inclusive *hydrodynamic* rapidity ranges for polarization:

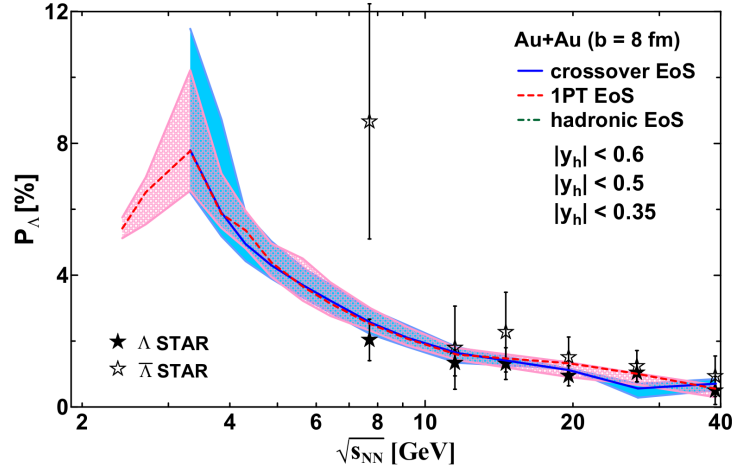


Figure 141: Polarization calucations using the 3-Fluid-Dynamics model [31]. Three inclusive *hydrodynamic* rapidity windows are shown as the uncertainties.

We can clearly see in Fig. 141 that \overline{P}_Λ increases strongly with rapidity; however, the inclusivity of these ranges makes it hard to compare with our measurements. We know that Λ yield drops off with y , and the more sharply it does the stronger the corresponding *exclusive* \overline{P}_Λ will be; recall

from algebra:

$$\overline{P}_{\Lambda,|y|<1} = \frac{N_{\Lambda,|y|<0.5}\overline{P}_{\Lambda,|y|<0.5} + N_{\Lambda,0.5<|y|<1}\overline{P}_{\Lambda,0.5<|y|<1}}{N_{\Lambda,|y|<0.5} + N_{\Lambda,0.5<|y|<1}} \quad (45)$$

$$\overline{P}_{\Lambda,0.5<|y|<1} = \frac{N_{\Lambda,|y|<1}\overline{P}_{\Lambda,|y|<1} - N_{\Lambda,|y|<0.5}\overline{P}_{\Lambda,|y|<0.5}}{N_{\Lambda,0.5<|y|<1}} \quad (46)$$

For example, if $\overline{P}_{\Lambda,|y|<1}$ was twice as strong as $\overline{P}_{\Lambda,|y|<0.5}$, but $N_{\Lambda,0.5<|y|<1}$ was one-tenth $N_{\Lambda,|y|<0.5}$, then $\overline{P}_{\Lambda,|y|<0.5}$ would be *twelve* times $\overline{P}_{\Lambda,|y|<0.5}$.

Looking at Fig. 141 and referring to Eq. 46, we can deduce that the polarization rises sharply with y in this model. The problem in applying Eq. 46 is that, although we know the rapidity distribution in our own data set, we don't know what is used in the model. The most conservative estimate would come from assuming a flat distribution, which would give us $\overline{P}_{\Lambda,|y_h|<0.35} = 6.037\%$ and $\overline{P}_{\Lambda,0.35<|y_h|<0.6} = 12.17\%$ – an increase by a factor of two!

H Model-based determinations of centrality

H.1 Monte-Carlo Glauber

When calculating multiplicity in the MCG model we must track the number of participants as well as the total number of nucleon-nucleon (“binary”) collisions. These distributions are shown in Figures 142 and 143, respectively. To determine the multiplicity, we sample for each participant the negative

binomial distribution (NBD),

$$P(n) = \frac{\Gamma(n+k)}{\Gamma(n+1)\Gamma(k)} \frac{\left(\frac{\mu}{k}\right)^n}{\left(\frac{\mu}{k} + 1\right)^{n+k}}, \quad (47)$$

where μ and k are determined through fitting experimental data and account for $\sqrt{s_{\text{NN}}}$ and detector efficiency effects. As an example we use a study of low-energy ($\sqrt{s_{\text{NN}}} = 3$ GeV) data [60] where $\mu = 0.9$ and $k = 39.984$ were achieved; the corresponding NBD is shown in Fig. 144. An interesting point about Fig. 142 is that even with a large number of events, we see none in which all nucleons are participants; this extreme rarity of spectator-less collisions is due both to the low nucleon density at the edges (“skins”) of the nuclei along with position fluctuations as usual, as well as the rarity of 100% central ($b = 0$ fm) events (Fig. 71). While some methods of multiplicity calculation use the binary collision count along with a collision “hardness” parameter x also found through fitting, we calculate multiplicity according to the sampling of Eq. 47 once for each participant; we achieve a multiplicity distribution shown in Fig. 145.

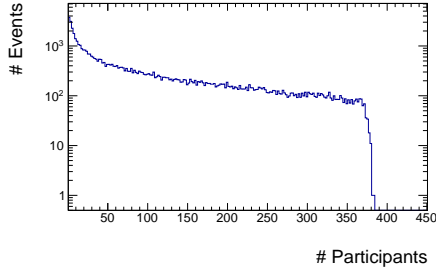


Figure 142: The distribution of participant count over many events; we see a peak near zero due to the relatively large number of peripheral events and a sudden drop-off near $2 * 197 = 394$, which is of course the maximum number of participants allowed in a $^{197}\text{Au} + ^{197}\text{Au}$ collision. Interestingly, we see no counts at the maximum number of allowed participants due to the extreme rarity of spectator-free collisions, even in *100% central events*.

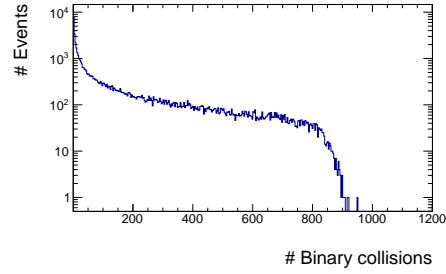


Figure 143: The distribution of binary collision count over many events; we see a peak near zero due to the relatively large number of peripheral events and a drop-off more gradual than in Fig. 142 due of course to the fact that a given nucleon may collide with more than one nucleon.

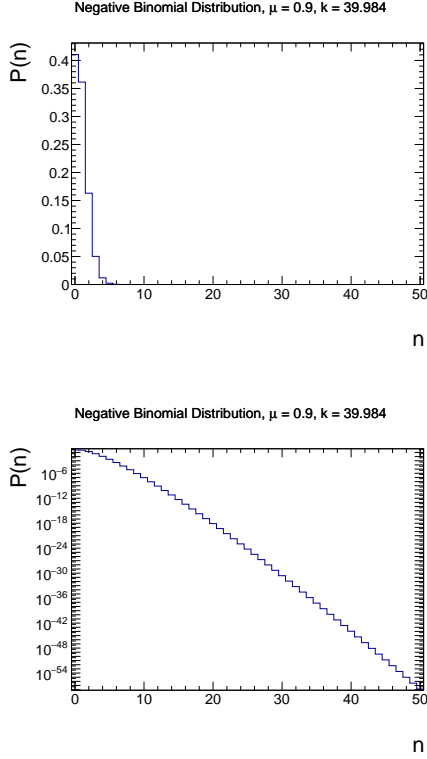


Figure 144: The negative binomial distribution (Eq. 47 with $\mu = 0.9$ and $k = 39.984$). This describes the distribution of produced charged particles per participant. Clearly this drops sharply after a few non-negligible values.

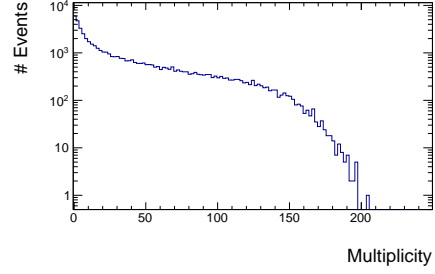


Figure 145: The multiplicity distribution achieved by randomly sampling Eq. 47 for each participant; we see a peak near zero due to the relatively large number of peripheral events and a drop-off more gradual than in Fig. 142 due to the “smearing” effect of Eq. 47.

As described previously, we can extract the centrality from the impact-parameter and multiplicity distributions. To extract the centrality that corresponds to a given impact parameter or centrality, we simply take the fraction of total events with impact parameter at or *below* a given impact parameter or the fraction of total events with multiplicity at or *above* a given multiplicity; these are shown in Figures 146 and 147.

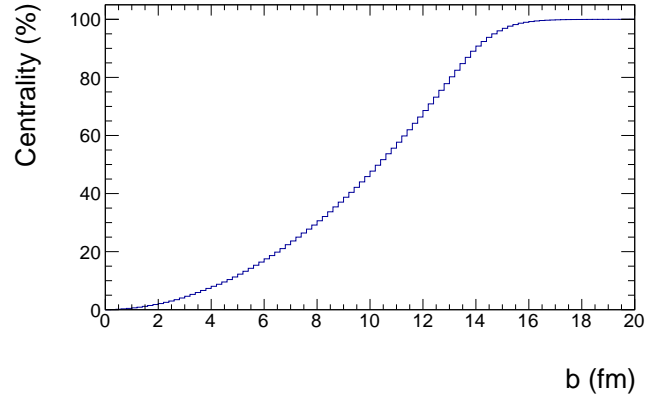


Figure 146: Centrality as a function of b ; we simply take from Fig. 71 the fraction of total collision events at or below a given impact parameter.

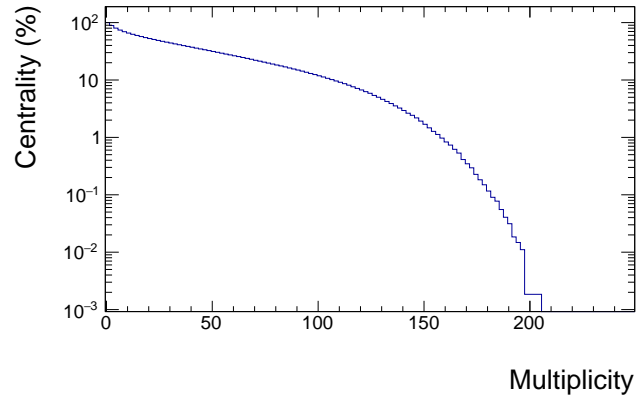


Figure 147: Centrality as a function of MCG multiplicity; we simply take from Fig. 145 the fraction of total collision events at or above a given multiplicity.

H.2 AMPT

Centrality determination in AMPT is quite straightforward. Without any filtering, we are left with an impact-parameter distribution as in Fig. 148.

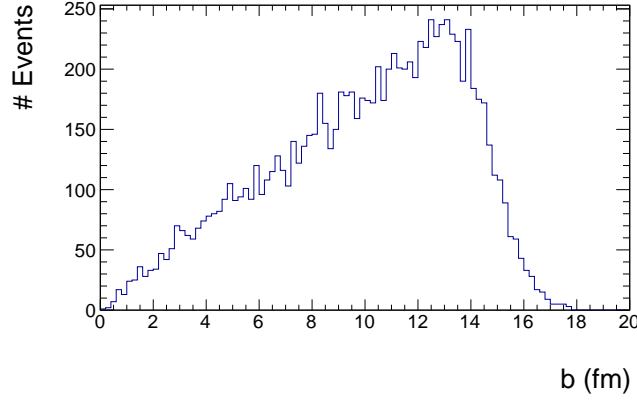


Figure 148: The impact-parameter distribution in AMPT without event filtering; we see that “non-collision events are not stored. Clearly, at $b \gtrsim 2R_A$, we see a gradual drop consistent with the fluctuating nucleon positions on the “skin” of the nucleus as opposed to a sudden drop-off as one would expect from a hard-shell model.

Our choice of multiplicity definition by η window is somewhat arbitrary, and when it comes to deriving centrality from an η window the choice does not matter much. We choose $|\eta| < 1$ and arrive at a multiplicity distribution as in Fig. 151.

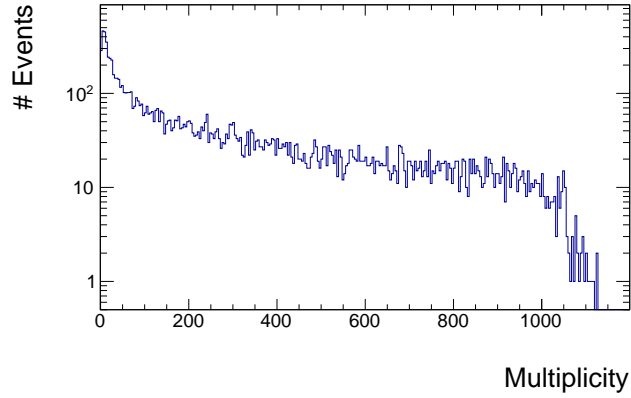


Figure 149: The multiplicity distribution of $|\eta| < 1$ in AMPT.

To then extract the centrality that corresponds to a given impact parameter or centrality, we simply take the fraction of total events with impact parameter at or *below* a given impact parameter or the fraction of total events with multiplicity at or *above* a given multiplicity (Figures 150 and 151, respectively).

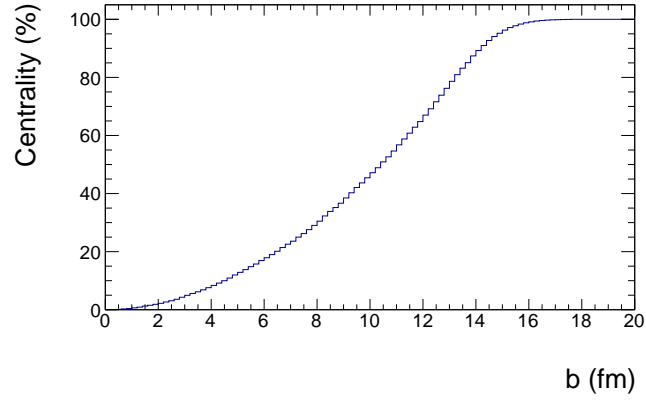


Figure 150: Centrality as a function of b ; we simply take from the impact parameter distribution the fraction of total collision events at or below a given impact parameter.

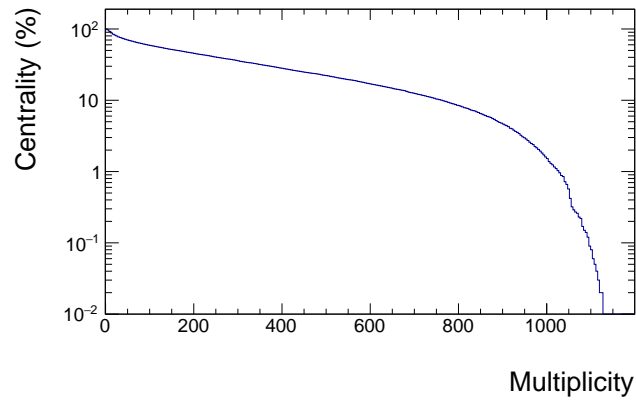


Figure 151: Centrality as a function of multiplicity in the range $|\eta| < 1$; we simply take from Fig. 149 the fraction of total collision events at or above a given multiplicity.

In order to simplify centrality determination without the need to invoke

assumptions needed for multiplicity determination, we will henceforth use the impact-parameter distribution for centrality determination.

I Angular-momentum conservation in AMPT

The system angular momentum, $\vec{J}_{\text{sys.}}$, can be approximated with the sum:

$$\vec{J}_{\text{sys.}} \approx \sum_i \vec{L}_i = \sum_i \vec{r}_i \times \vec{p}_i. \quad (48)$$

As models generally don't propagate spin fully, this is only an approximation; however, we expect spin contributions to be much smaller than contributions from \vec{L} . This approximation should therefore follow

$$\vec{J}_{\text{sys.}} \approx A|\vec{b}||\vec{L}_N|. \quad (49)$$

Running AMPT “out of the box”, however, (only changing b_{max} and $\sqrt{s_{\text{NN}}}$) we see an enormous discrepancy.

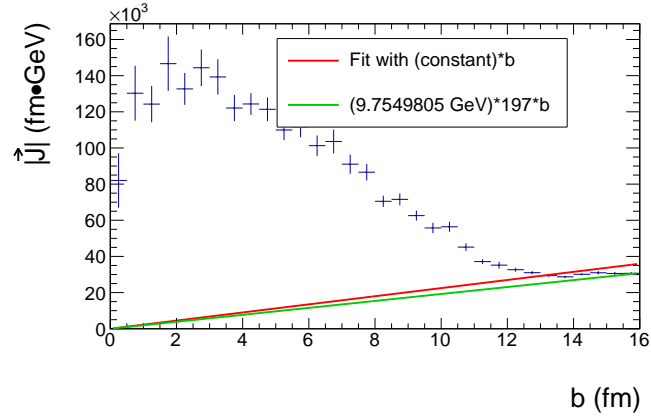


Figure 152: AMPT system angular momentum estimated according to Eq. 48; we see that it does not follow the form of Eq. 49. In fact, the dependence on b seems completely incorrect; this turns out to be a problem with running AMPT “out of the box” with low precision.

Another sign of a problem can be found by looking at the component of $\hat{J}_{\text{sys.}}$ along the $-\hat{y}$ direction, $\hat{J}_{\text{sys.}} \cdot (-\hat{y})$, which should be 1 since the impact parameter is set to be parallel to \hat{x} .

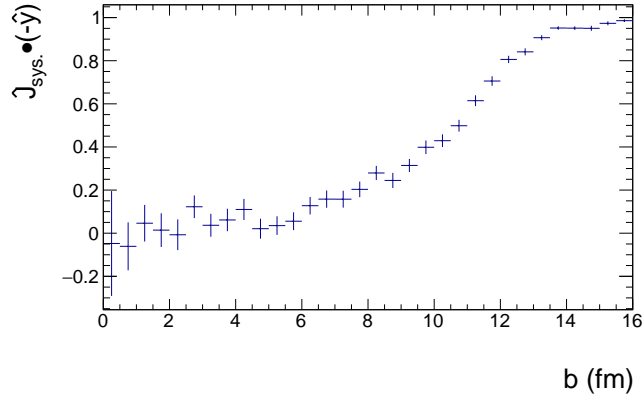


Figure 153: AMPT system angular momentum along $-y$ estimated according to Eq. 48; we see that it is not roughly constant at 1. In fact, the dependence on b seems completely incorrect; this turns out to be a problem with running AMPT “out of the box” with low precision.

This is ultimately due to the limited precision of particles with very large angular momenta at the moment of freezeout. To increase the precision, one simply needs to change the 3 lines in `linana.f` that contain “`write(16,200)...`” or “`write(16,201)...`” to “`write(16,*)...`”. With that change, we see more sensible plots. Notably, in Fig. 154, we see that this approach of neglecting spin contributions to $\vec{J}_{\text{sys.}}$ and imperfect angular-momentum conservation by simply using Eq. 48 is valid. In Fig. 155 we still see $\hat{J}_{\text{sys.}} \cdot (-\hat{y})$ falling below 1, but only for very central collisions; this arises from the fact that the nuclei are generated according to appropriate distributions centered according to the randomly sampled impact parameter, but the centers of the nuclei do not end up exactly at the centers of the distributions. We could correct for this by appropriately rotating all positions and momenta, but there is no need since we are ultimately not correlating with \hat{y} (this was only made as a sort

of sanity check).

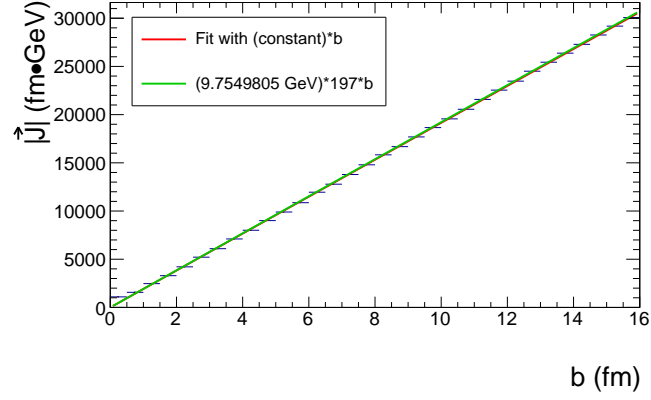


Figure 154: AMPT system angular momentum estimated according to Eq. 48, with increased output-file precision; we see that it does closely follow the form of Eq. 49.

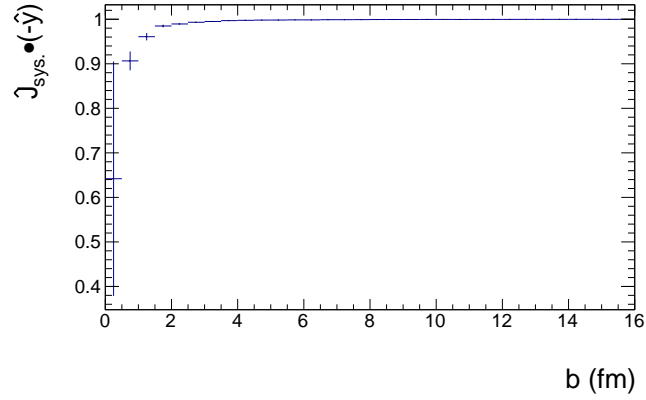


Figure 155: AMPT system angular momentum along $-y$ estimated according to Eq. 48; we see that it is roughly constant at 1. The dot product falling below 1 for more central collisions comes from the fact that incoming nuclei are build from nucleons randomly generated according to the appropriate distributions with nuclei separation according to a randomly-chosen b . The centers-of-mass of the two nuclei thus have a variation from the point about which the nucleons were generated which becomes more noticeable by this dot product as $b \rightarrow 0$ fm.

J A search for the magnetic field in the QGP

J.1 Introduction

Global polarization of hadrons emitted by the QGP, \overline{P}_H , is measurable via the decay of the Λ hyperon, as it preferentially emits its proton daughter in the direction of its spin. This was measured by the STAR collaboration via the RHIC BES program [7] and subsequently studied in more detail with higher statistics at $\sqrt{s_{NN}} = 200$ GeV [50] where the dependence of \overline{P}_Λ on azimuthal angle ϕ , pseudo-rapidity η , and transverse momentum p_T .

Particularly in the RHIC Beam Energy Scan range of $\sqrt{s_{NN}}$ studied so far, one can see that apparently $\overline{P}_{\overline{\Lambda}} > \overline{P}_\Lambda$, though the difference is not statistically significant (Fig. 36). This splitting becomes more pronounced at lower $\sqrt{s_{NN}}$. One may, by hand, combine the measurements at varying $\sqrt{s_{NN}}$ to obtain an overall splitting of significance 2σ ; enticing, but certainly not convincing. If such a splitting was statistically significant, it could point to a strong, late-stage magnetic field sustained by the QGP and thereby serve as a measure of the magnetic susceptibility of the QGP, χ_{QGP} [14, 58], which is of significant theoretical importance [47]. For example, a large magnetic field is a crucial ingredient required to measure the so-called “Chiral Magnetic Effect” which would be evidence of $\mathcal{C} - \mathcal{P}$ violation [38].

If one were to take the average enhancement of $\overline{P}_{\bar{\Lambda}}$ over \overline{P}_{Λ} and extract a magnetic field at face value (despite various potential problems with so doing) according to [14], they would arrive at $|\vec{B}|_{\text{QGP}} = 6.0 \pm 5.5 \cdot 10^{13} \text{ T}$, which would be enormous. Such a simple extraction, however, is dubious, as other potential explanations for a splitting between $\overline{P}_{\bar{\Lambda}}$ and \overline{P}_{Λ} exist. One such explanation is the potential difference in origination points between $\bar{\Lambda}$ and Λ hyperons from within the QGP [61].

Despite these potential problems, it is still worthwhile to study the splitting in a high-statistics data set. In 2018, RHIC/STAR collided Au+Au at $\sqrt{s_{\text{NN}}} = 27 \text{ GeV}$, collecting sufficient events to study this effect. At this collision energy there is sufficient Λ production, and the ability to resolve the first-order event plane is quite good; therefore it is an ideal data set to look for such an effect.

J.2 Ψ_1 flatness and \overline{P}_{Λ} , $\overline{P}_{\bar{\Lambda}}$ variations

Recall that the first-order event-plane angle, Ψ_1 , is described by the azimuthal distribution of (typically) higher-rapidity particles ($|y| > 3$). The then-newly-installed Event-Plane Detector (EPD) provided ideal coverage and granularity in order to provide measurements of Ψ_1 with good resolution,

$$R_{\text{EP}}^{(1)} \approx \sqrt{2 \left\langle \cos(\Psi_1^{\text{ref}.1} - \Psi_2^{\text{ref}.2}) \right\rangle}, \quad (50)$$

where $\Psi_1^{\text{ref}.1}$ and $\Psi_1^{\text{ref}.2}$ are measurements from two subevents which together make up the subevent used for Ψ_1 . Eq. 50 is only valid when these two subevents have symmetric acceptances; hence it is invalid in the fixed-target

setup discussed earlier. In collider mode, our acceptance is symmetric between the two EPD wheels, so Eq. 50 is valid.

Before applying Eq. 50 it is necessary to first “flatten” the Ψ_1 distribution. For a variety of reasons, including non-uniform detector acceptance, beam characteristics, and other material near the beam pipe, there will be an artificial (i.e. not representative of reality) non-uniformity; this is seen in Fig. 156.

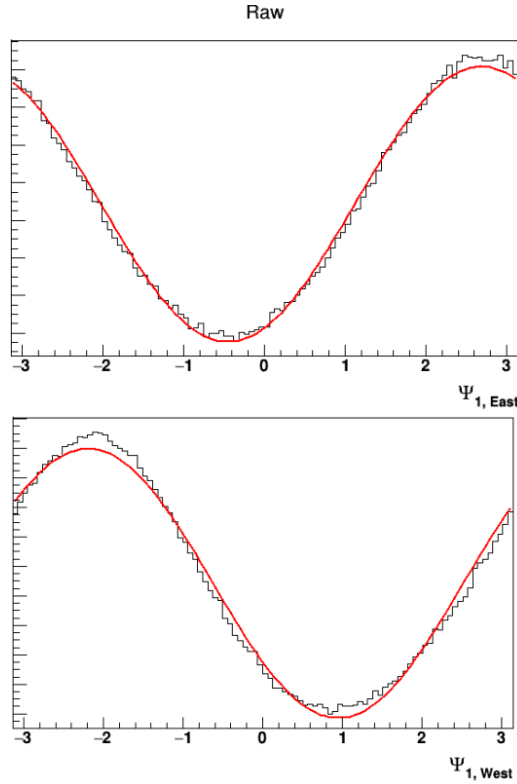


Figure 156: The raw Ψ_1 distribution for each EPD wheel. The red lines are sinusoidal fits, which approximate the data quite well.

In Fig. 156 is shown that the raw Ψ_1 distribution is quite sinusoidal. If we were to normalize it, we could extract the amplitude and phase shift

according to:

$$A = 2\sqrt{\langle \sin \Psi_1 \rangle^2 + \langle \cos \Psi_1 \rangle^2} \quad (51)$$

$$\phi = \tan^{-1} \left[-\frac{\langle \sin \Psi_1 \rangle}{\langle \cos \Psi_1 \rangle} \right]. \quad (52)$$

In figures 157 and 158 is shown these amplitudes and phase shifts for independent (45 min.) runs; the level of fluctuation compared to the uncertainties would indicate a potential problem.

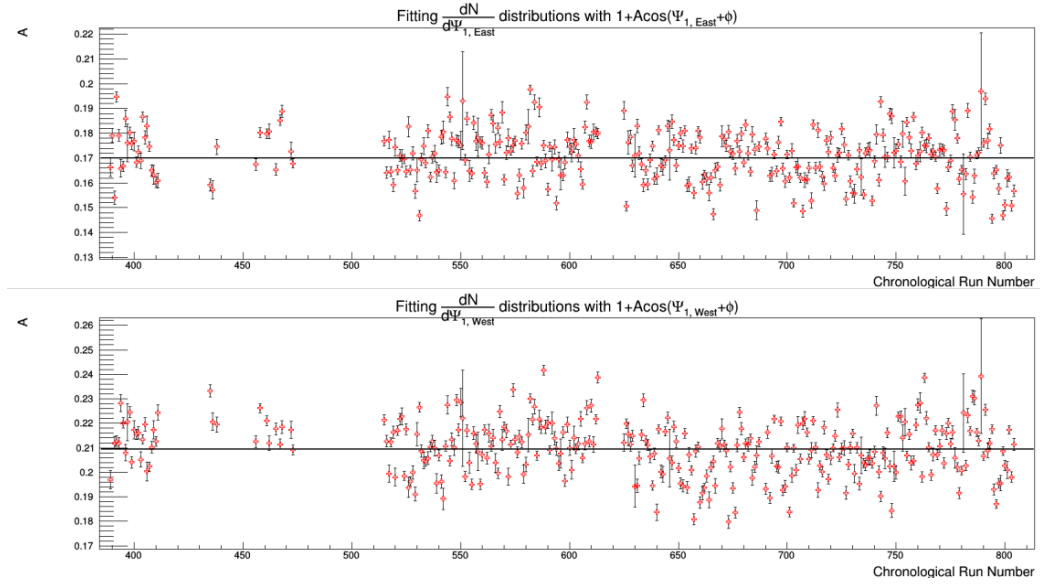


Figure 157: The amplitude of the sinusoidal fit to the normalized Ψ_1 distribution over time. We see clearly that the sizes of the uncertainties do not match the scatter, indicating that the amplitude is changing significantly on a run-by-run basis.

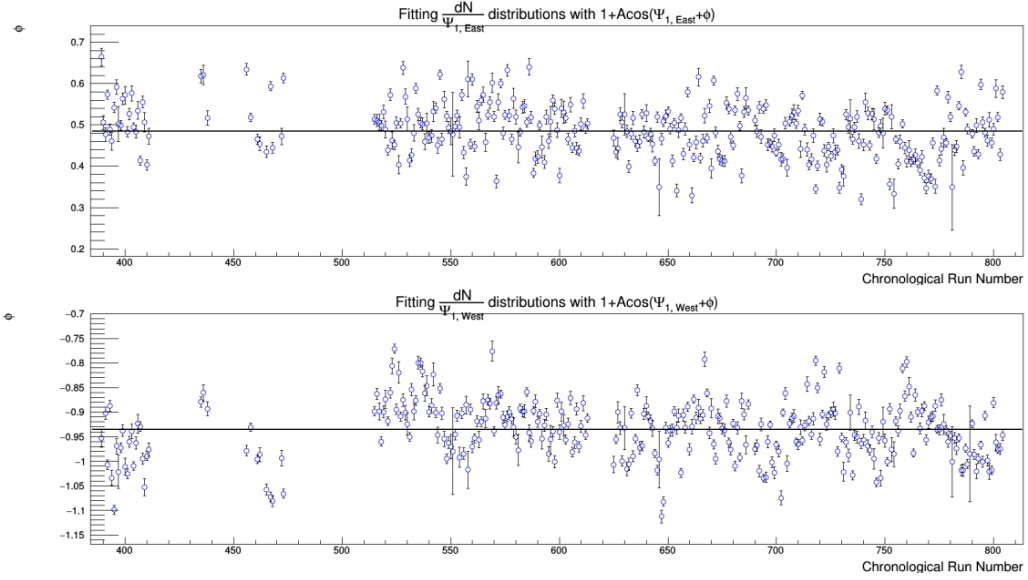


Figure 158: The phase shift of the sinusoidal fit to the normalized Ψ_1 distribution over time. We see clearly that the sizes of the uncertainties do not match the scatter, indicating that the phase is changing significantly on a run-by-run basis.

Understanding the behavior in figures 157 and 158 requires looking within a run. In Fig. 159 we can see that the shape of the Ψ_1 distribution evolves smoothly with time within each run; however, in Fig. 160 (on another day of running) we see sharp jumps between runs.

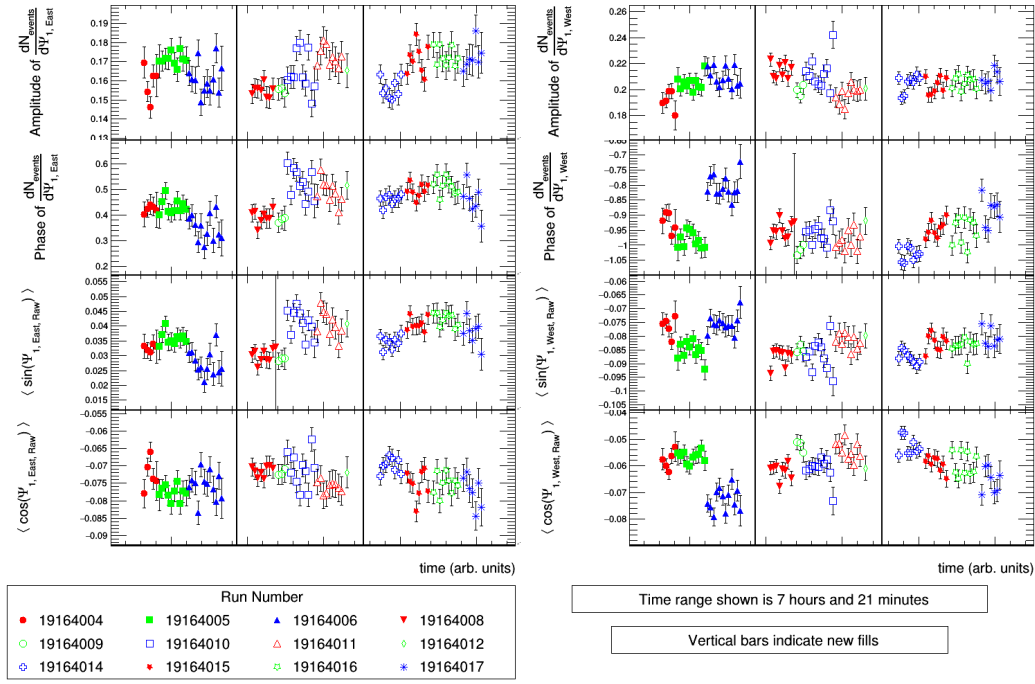


Figure 159: Here is shown that the characteristics of the Ψ_1 distribution shape evolve smoothly with time within fills. In between fills (as indicated with solid black vertical lines in time) we do not see jumps.

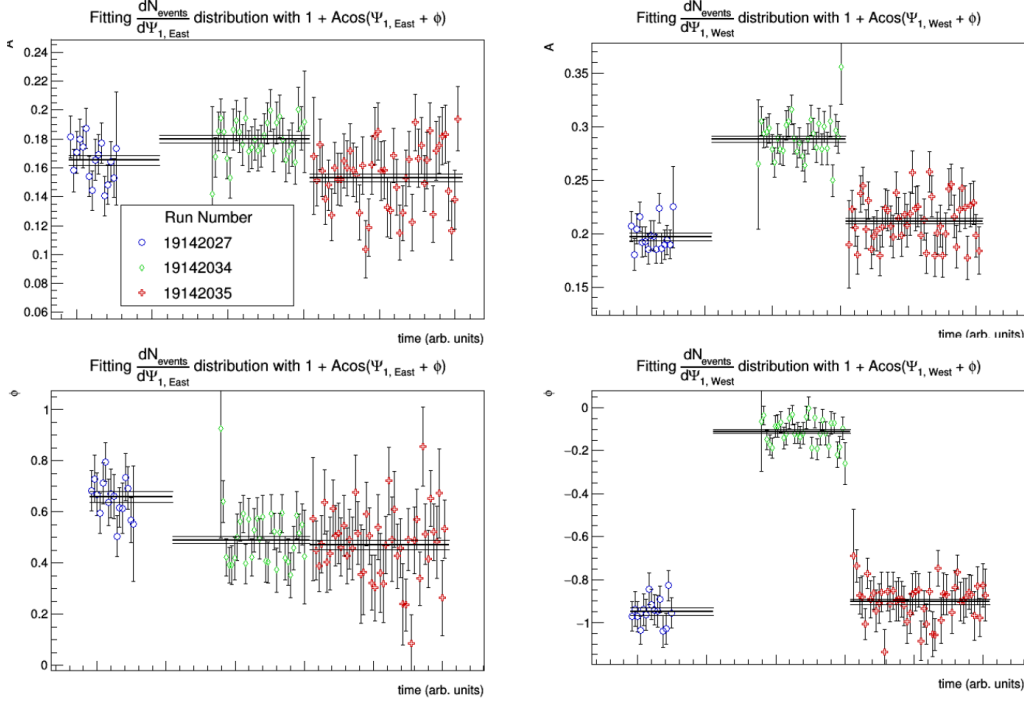


Figure 160: Here, in contrast to Fig. 159, we see that the characteristics of the Ψ_1 distribution shape can jump suddenly between runs, even without a fill in between.

While the behavior of Ψ_1 with time is not fully understood in the EPD, we have sufficient statistics in each run to shift; therefore, we apply the shifting technique to ensure a flat distribution on a run-by-run basis as well as calculating $R_{\text{EP}}^{(1)}$ on a run-by-run basis.

When checking for flatness of Ψ_1 against other parameters, we sometimes see an unexpected dependence. Fig. 161 for example shows no obvious dependence of Ψ_1 on v_z ; however, when looking at the dependence of Ψ_1 on the difference between v_z calculated in the TPC and VPD, $|v_{z,\text{TPC}} - v_{z,\text{VPD}}|$, we do in fact see an obvious dependence (Fig. 162). Although we investigated potential causes of such a dependence, we found none. For the time

being, we simply decide to shift to enforce a flat distribution with respect to $|v_{z,\text{TPC}} - v_{z,\text{VPD}}|$ (Fig. 163).

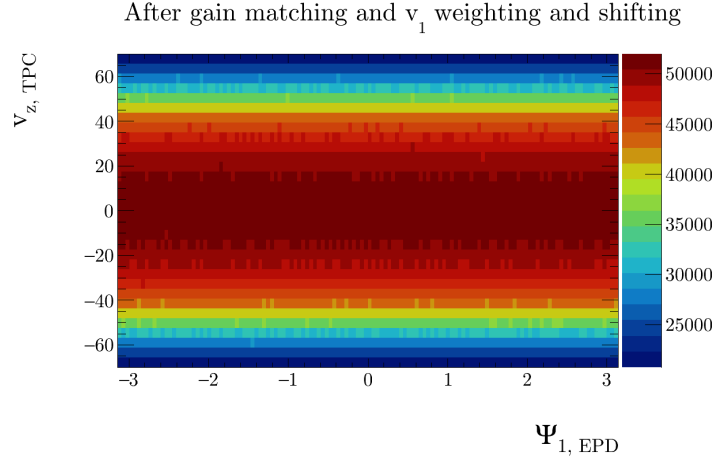


Figure 161: The Ψ_1 distribution with respect to $v_{z,\text{TPC}}$ is apparently flat.

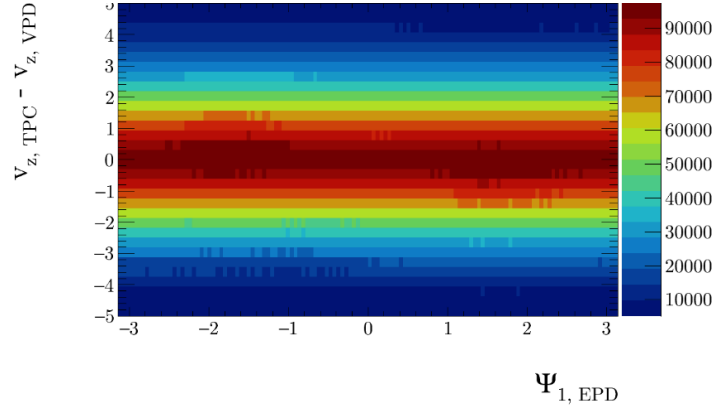


Figure 162: The Ψ_1 distribution with respect to $|v_{z,\text{TPC}} - v_{z,\text{VPD}}|$ is obviously non-flat.

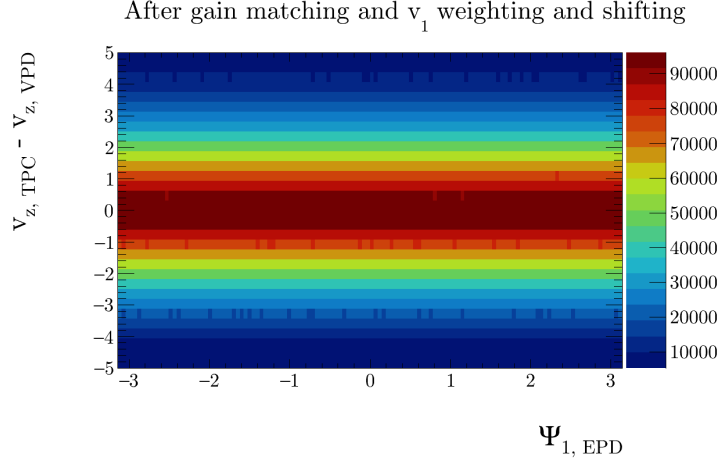


Figure 163: We shift Ψ_1 with respect to $|v_{z,\text{TPC}} - v_{z,\text{VPD}}|$ to ensure its flatness.

It is surprising to see the effects of such a slightly non-flat distribution (as seen in Fig. 162). In this data set an entire inner sector of the TPC was missing, due to testing. Because of this, non-flatness of the Ψ_1 distribution on the order of a few percent will strongly affect polarization. In Fig. 164 is shown a dramatic dependence of $\overline{P}_{\bar{\Lambda}}$ and \overline{P}_{Λ} on $|v_{z,\text{TPC}} - v_{z,\text{VPD}}|$, and the trends are opposite. This comes from the combined broken symmetries between the helicity efficiency effect 165 and the missing iTPC sector. In Fig. 166 is shown that this behavior is isolated to the East side of the TPC, demonstrating that without the broken symmetry caused by the missing iTPC sector we wouldn't have the problems seen in Fig. 164.

20-50% centrality, before v_z -dependent shifting

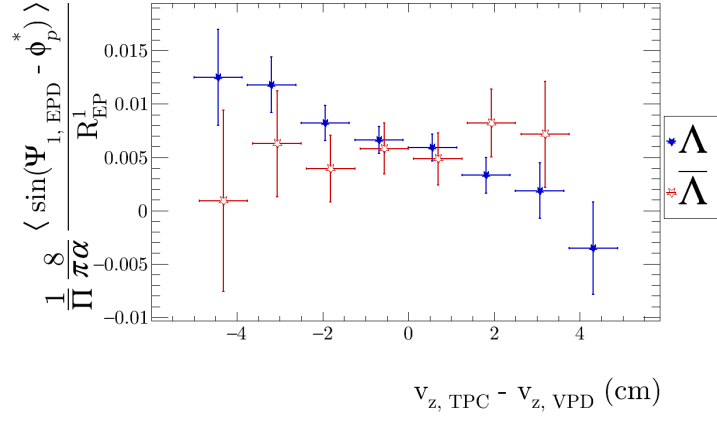


Figure 164: The behavior of \bar{P}_Λ vs. $|v_{z, \text{TPC}} - v_{z, \text{VPD}}|$ is drastically different than that of $\bar{P}_{\bar{\Lambda}}$ vs. $|v_{z, \text{TPC}} - v_{z, \text{VPD}}|$.

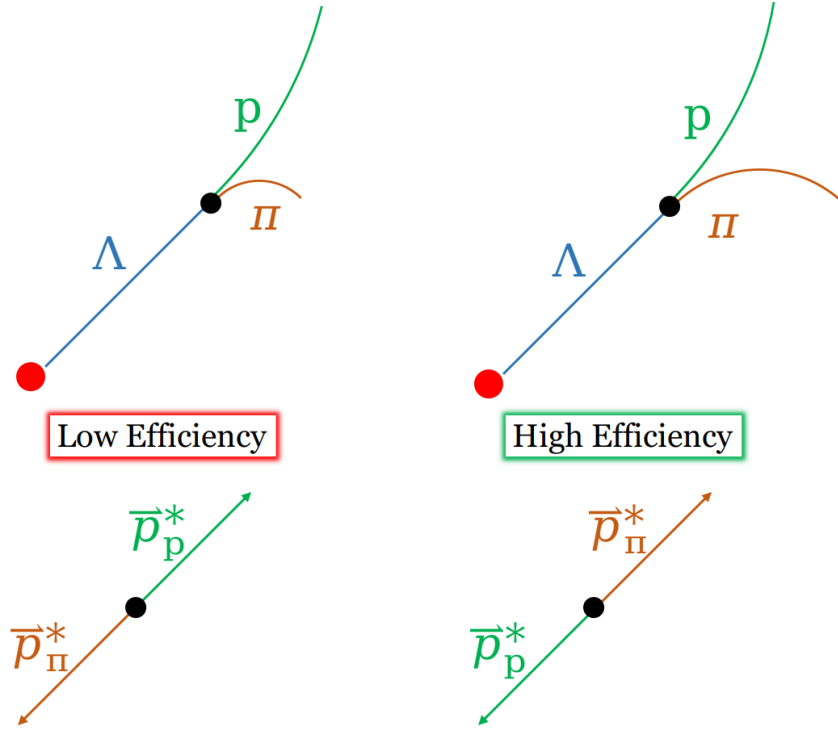


Figure 165: The so-called “helicity efficiency effect” wherein a Λ emitting its pion daughter “backwards” in the Λ rest frame has substantially lower p_T than a pion emitted “forward” in the Λ frame. The proton’s momentum is only slightly affected. Lower- p_T tracks are more difficult to measure in the STAR TPC.

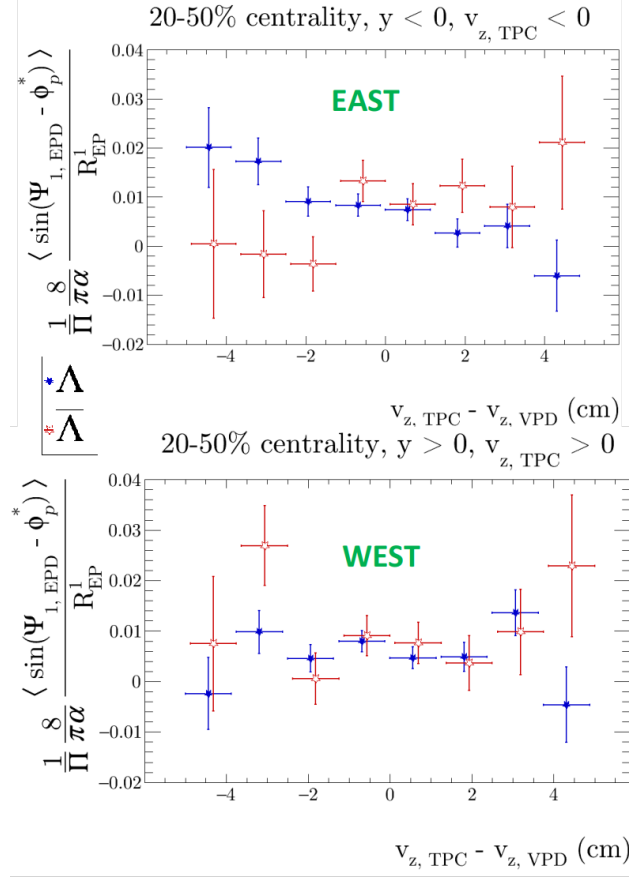


Figure 166: The difference in behavior seen in Fig. 164 is dramatically worse on the East side of the TPC, due to a missing iTPC sector.

After finding all known Ψ_1 dependences and shifting accordingly (even when the causes of such dependences were not fully understood), we check that $\overline{P}_{\bar{\Lambda}}$ and \overline{P}_{Λ} do not depend on the two separate productions. In Fig. 167 is shown that, between two productions, it appears as if $\overline{P}_{\bar{\Lambda}}$ jumps up while \overline{P}_{Λ} jumps down; however, this is not statistically significant. This observation does, however, deserve special attention. We can try to isolate the behavior from the missing iTPC sector, since that has caused other issues. In Fig. 168

we do so, separating Λ s by $v_{z,\text{TPC}}$; however, we see the behavior persist.

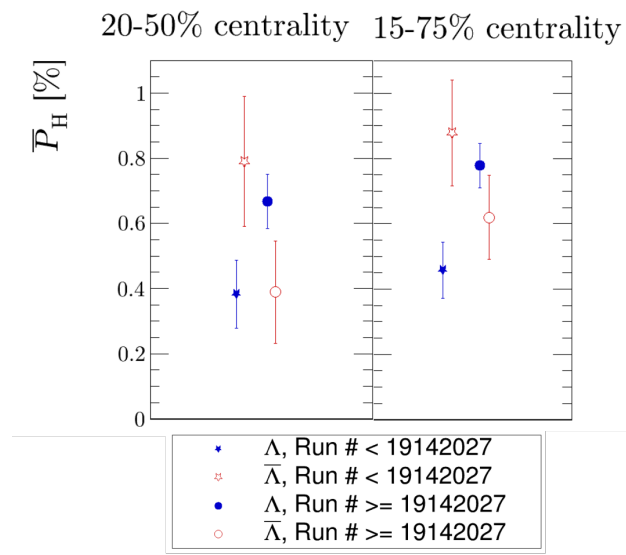


Figure 167: Here is shown the suggested jump in $\bar{P}_{\bar{\Lambda}}$ and \bar{P}_{Λ} between the two productions. \bar{P}_{Λ} seems to rise and $\bar{P}_{\bar{\Lambda}}$ seems to fall. This is within statistical uncertainties, however, and only suggests a problem.

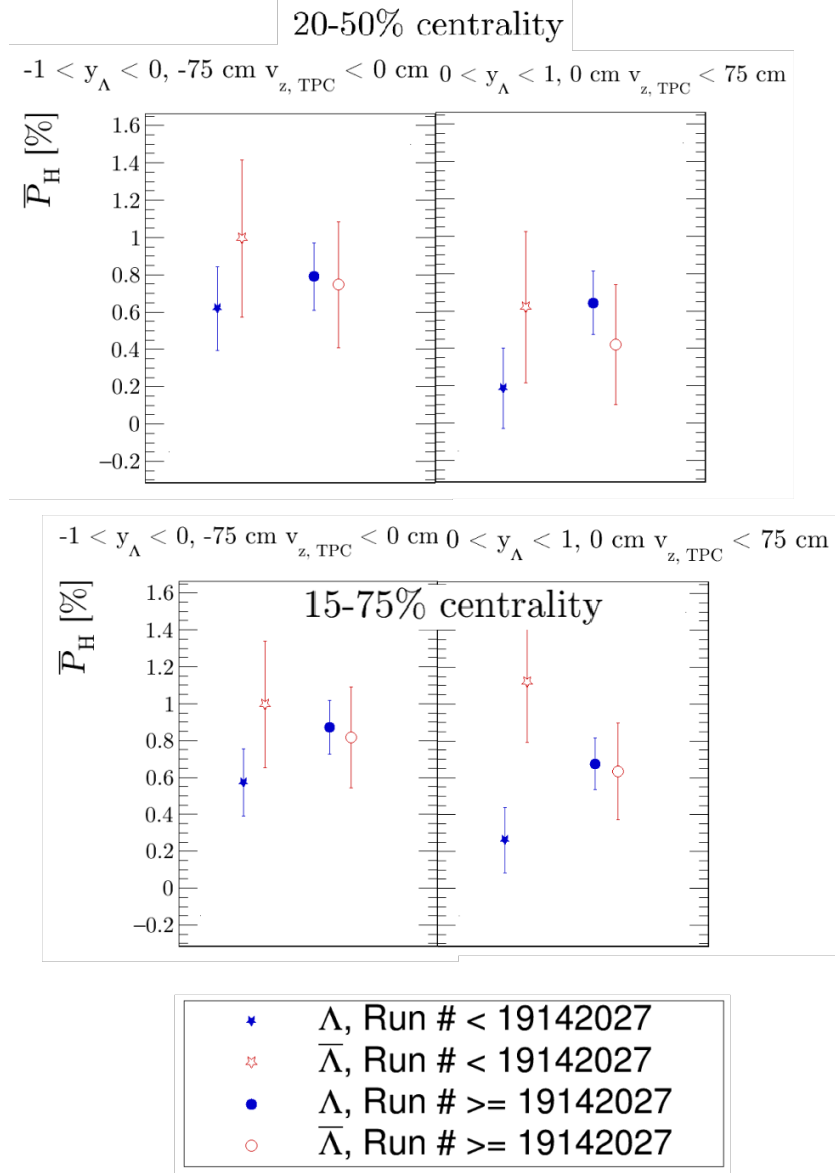


Figure 168: Here is shown the suggested jump in $\bar{P}_{\bar{\Lambda}}$ and \bar{P}_{Λ} between the two productions, which remains when isolating the missing iTPC section of y_{Λ} . For both sections, \bar{P}_{Λ} still seems to rise and $\bar{P}_{\bar{\Lambda}}$ seems to fall. This is within statistical uncertainties, however, and only suggests a problem.

In Fig. 169 is shown that the behavior is not limited solely to the two

separate productions; there is in fact a suggested linear dependence on both \bar{P}_Λ and $\bar{P}_{\bar{\Lambda}}$. A potential explanation would be a dependence of $R_{\text{EP}}^{(1)}$ on time, but Fig. 170 clears such suspicions.

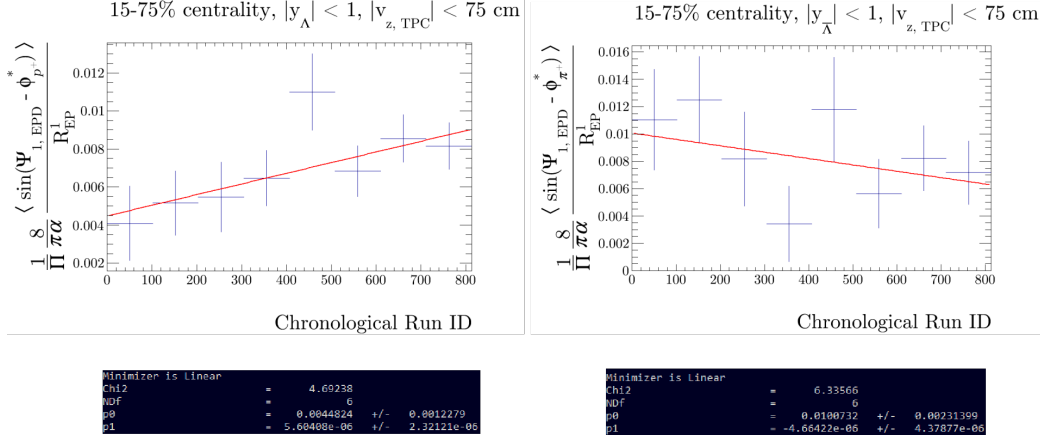


Figure 169: Here is shown a more detailed dependence of $\bar{P}_{\bar{\Lambda}}$ and \bar{P}_Λ on time; for \bar{P}_Λ especially, the dependence appears to be linear, but the linear fit term (fitting with $p_0 + p_1 \bar{P}_\Lambda$ is only of significance 2.3σ .

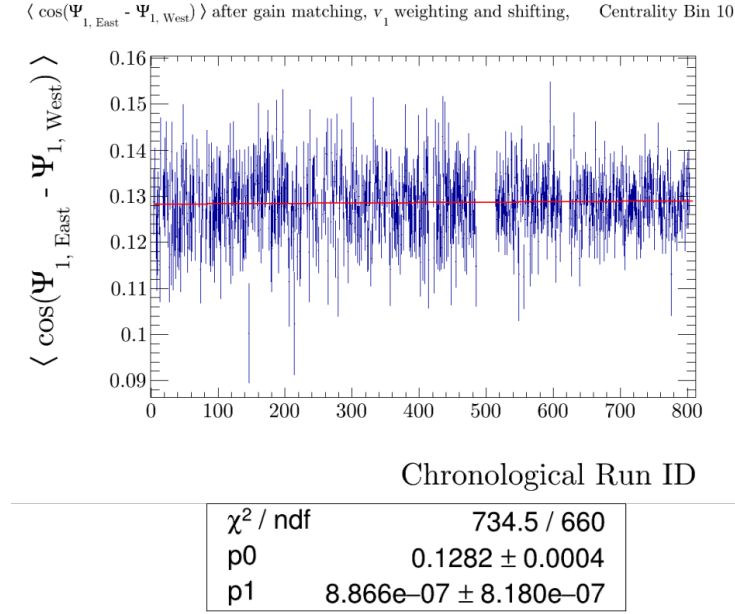


Figure 170: There is no apparent dependence of $R_{\text{EP}}^{(1)}$ on time, which would be a potential explanation of the behavior seen in Fig. 169

Other various quantities do depend on time in this run, due to various problems with the collider and detector system unfortunately experienced during this run. In figures 171 and 172 is shown a few such examples. For many of these there is a sudden jump between the two productions, rather than a linear dependence seen in Fig. 169.

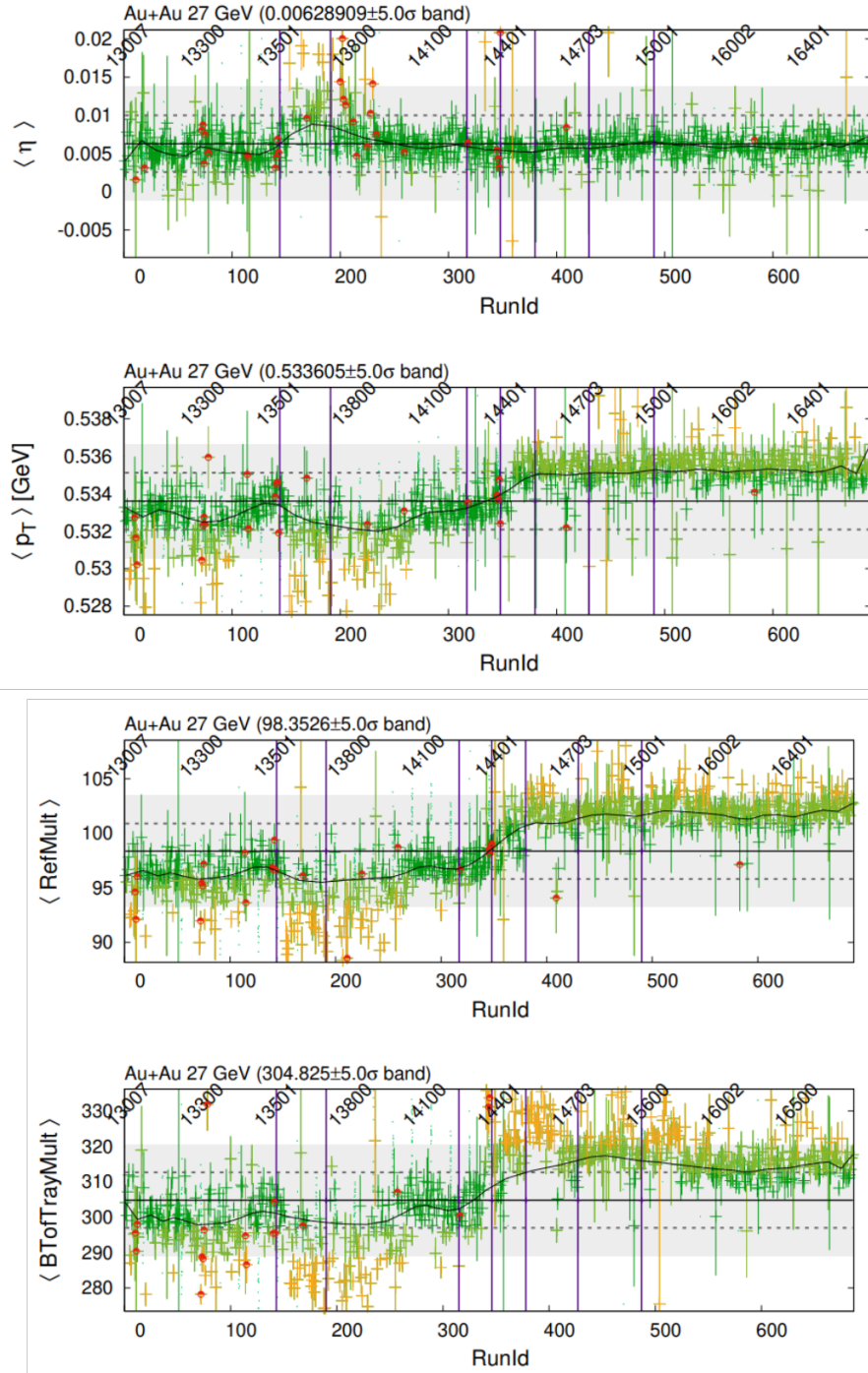


Figure 171: The dependence of multiplicities and particle quantities on time; there is an obvious jump between the two productions.

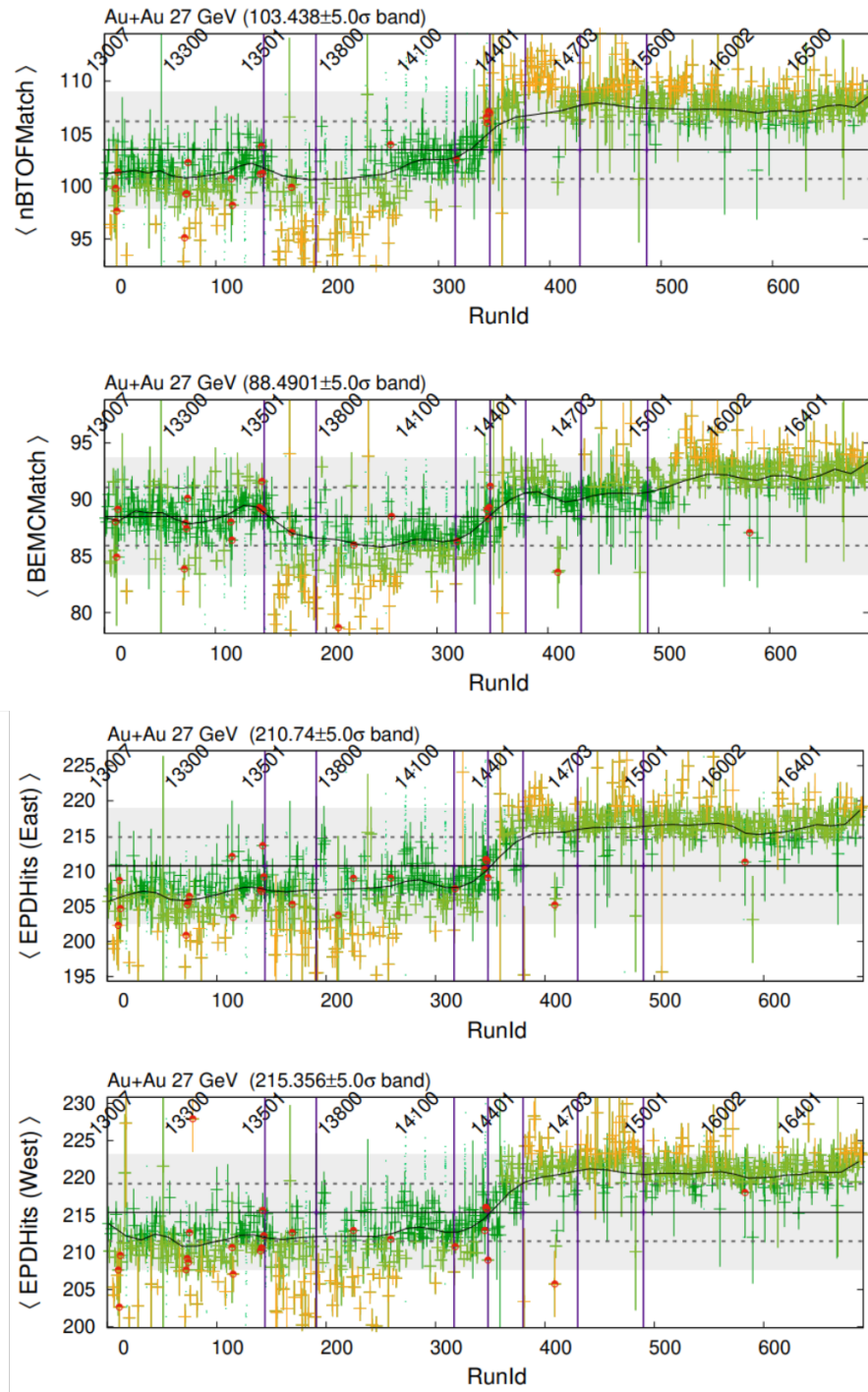


Figure 172: The dependence of particle matches and hits on time; there is an obvious jump between the two productions.

J.3 Summary, and search at $\sqrt{s_{\text{NN}}} = 19 \text{ GeV}$

Although the high-statistics dataset taken at $\sqrt{s_{\text{NN}}} = 27 \text{ GeV}$ was a promising candidate to study $\bar{P}_{\Lambda} - \bar{P}_{\Lambda}$ splitting, there are too many broken symmetries. With such a charge-sensitive analysis, we simply can not guarantee that all systematic effects will be fully accounted for.

Since RHIC/STAR has since taken a high-statistics data set at $\sqrt{s_{\text{NN}}} = 19.6 \text{ GeV}$, which will be fully calibrated and ready for analysis in roughly two weeks, we will turn our attention there. Initial looks at $R_{\text{EP}}^{(1)}$ at that data set are promising (Fig. 173).

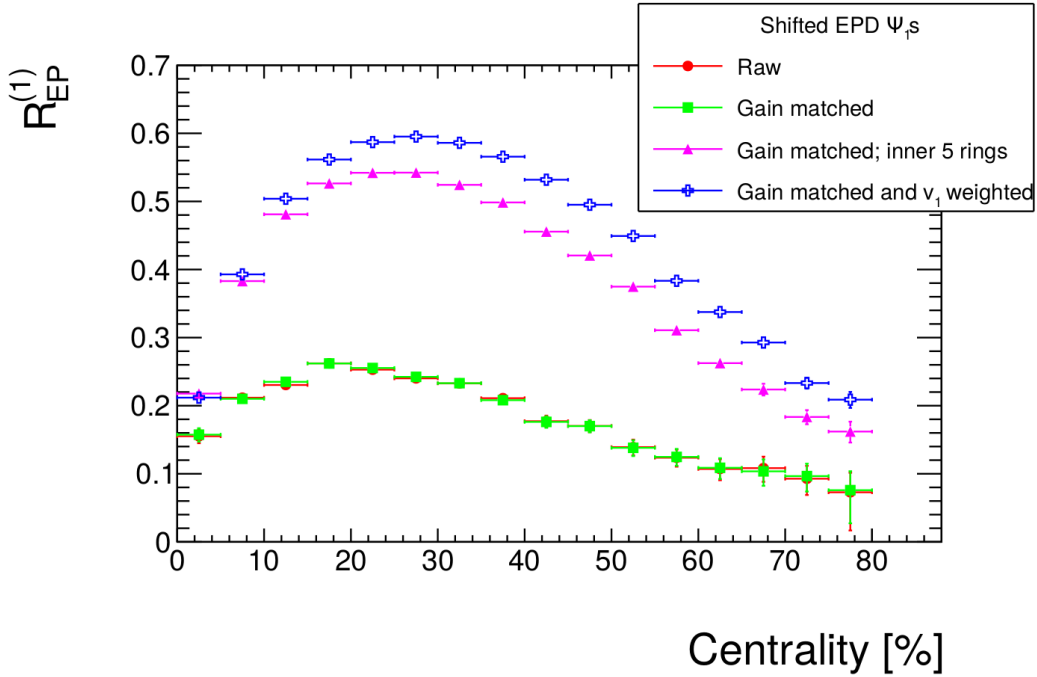


Figure 173: $R_{\text{EP}}^{(1)}$ in uncalibrated $\sqrt{s_{\text{NN}}} = 19.6 \text{ GeV}$ data; there is a 15% increase over $R_{\text{EP}}^{(1)}$ seen at $\sqrt{s_{\text{NN}}} = 27 \text{ GeV}$, with comparable Λ statistics. v_1 weighting is achieved on a η -dependent basis (Fig. 174).

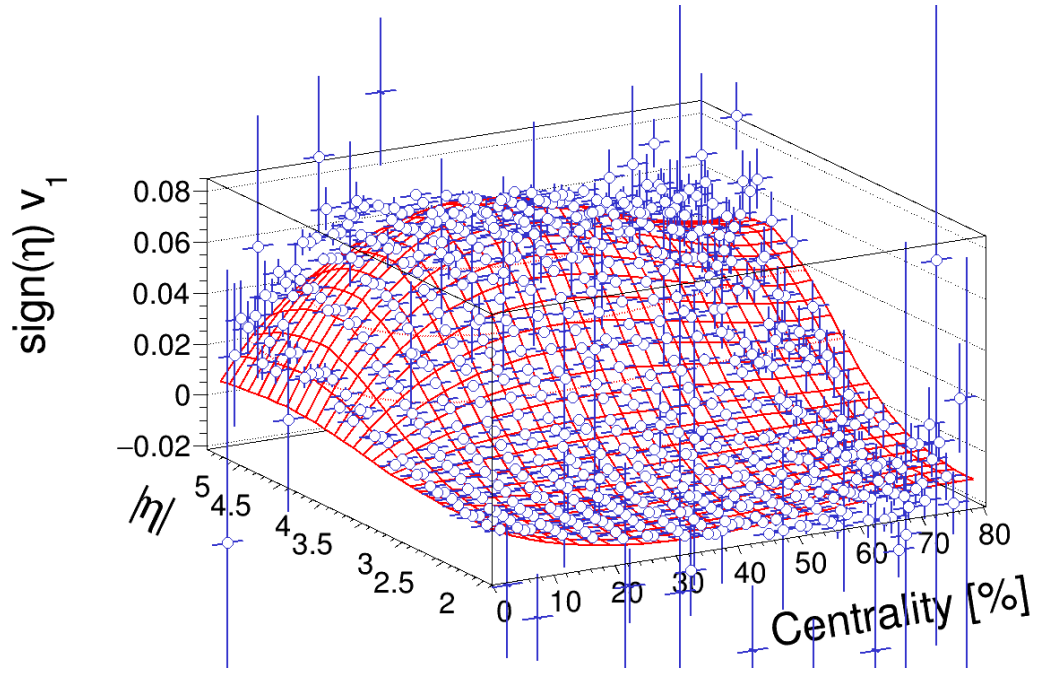


Figure 174: v_1 weights are achieved by measuring $\langle \cos(\Psi_1 - \phi) \rangle (\eta)$ where Ψ_1 is determined by the opposite EPD wheel.

Bibliography

- [1] Us department of energy office of science. `science.osti.gov`. Accessed: 2021-07-11.
- [2] B. I. Abelev et al. Global polarization measurement in Au+Au collisions. *Phys. Rev. C*, 76:024915, 2007. [Erratum: *Phys.Rev.C* 95, 039906 (2017)].
- [3] B. I. Abelev et al. Global polarization measurement in Au+Au collisions. *Phys. Rev. C*, 76:024915, 2007. [Erratum: *Phys.Rev.C* 95, 039906 (2017)].
- [4] Shreyasi Acharya et al. Global polarization of $\Lambda\bar{\Lambda}$ hyperons in Pb-Pb collisions at $\sqrt{s_{NN}} = 2.76$ and 5.02 TeV. *Phys. Rev. C*, 101(4):044611, 2020.
- [5] Jaroslav Adam et al. Global polarization of Λ hyperons in Au+Au collisions at $\sqrt{s_{NN}} = 200$ GeV. *Phys. Rev. C*, 98:014910, 2018.
- [6] Jaroslav Adam et al. Global polarization of Ξ and Ω hyperons in Au+Au collisions at $\sqrt{s_{NN}} = 200$ GeV. *Phys. Rev. Lett.*, 126(16):162301, 2021.
- [7] L. Adamczyk et al. Global Λ hyperon polarization in nuclear collisions: evidence for the most vortical fluid. *Nature*, 548:62–65, 2017.
- [8] Joseph Adams et al. The STAR Event Plane Detector. *Nucl. Instrum. Meth. A*, 968:163970, 2020.

- [9] C. Adler et al. Multiplicity distribution and spectra of negatively charged hadrons in Au+Au collisions at $\sqrt{s(NN)} = 130$ -GeV. *Phys. Rev. Lett.*, 87:112303, 2001.
- [10] Yasuyuki Akiba et al. The Hot QCD White Paper: Exploring the Phases of QCD at RHIC and the LHC. 2 2015.
- [11] Mark G. Alford, Andreas Schmitt, Krishna Rajagopal, and Thomas Schäfer. Color superconductivity in dense quark matter. *Rev. Mod. Phys.*, 80:1455–1515, 2008.
- [12] B. Alver and G. Roland. Collision geometry fluctuations and triangular flow in heavy-ion collisions. *Phys. Rev. C*, 81:054905, 2010. [Erratum: *Phys.Rev.C* 82, 039903 (2010)].
- [13] M. Anderson et al. The Star time projection chamber: A Unique tool for studying high multiplicity events at RHIC. *Nucl. Instrum. Meth. A*, 499:659–678, 2003.
- [14] F. Becattini, I. Karpenko, M. Lisa, I. Upsal, and S. Voloshin. Global hyperon polarization at local thermodynamic equilibrium with vorticity, magnetic field and feed-down. *Phys. Rev. C*, 95(5):054902, 2017.
- [15] F Becattini and F Piccinini. The effects of angular momentum conservation in relativistic heavy-ion collisions at the LHC. *J. Phys. G*, 35(5):054001.155, 2008.
- [16] Francesco Becattini and Michael A. Lisa. Polarization and Vorticity in the Quark–Gluon Plasma. *Ann. Rev. Nucl. Part. Sci.*, 70:395–423, 2020.

- [17] Barbara Betz, Miklos Gyulassy, and Giorgio Torrieri. Polarization probes of vorticity in heavy ion collisions. *Phys. Rev. C*, 76:044901, 2007.
- [18] Rajeev S. Bhalerao, Giuliano Giacalone, Pablo Guerrero-Rodríguez, Matthew Luzum, Cyrille Marquet, and Jean-Yves Ollitrault. Relating eccentricity fluctuations to density fluctuations in heavy-ion collisions. *Acta Phys. Polon. B*, 50:1165–1176, 2019.
- [19] John Błoczyński, Xu-Guang Huang, Xilin Zhang, and Jinfeng Liao. Azimuthally fluctuating magnetic field and its impacts on observables in heavy-ion collisions. *Phys. Lett. B*, 718:1529–1535, 2013.
- [20] Adam Bzdak and Vladimir Skokov. Event-by-event fluctuations of magnetic and electric fields in heavy ion collisions. *Phys. Lett. B*, 710:171–174, 2012.
- [21] Daniel Cebra. Centrality – 3.85 (3.0) GeV FXT. https://drupal.star.bnl.gov/STAR/system/files/\Daniel2020Apr22_Centrality_3p85.pdf. Presentation to the STAR Bulk Correlations Weekly Meeting, 2020-04-22.
- [22] M. Cheng et al. The QCD equation of state with almost physical quark masses. *Phys. Rev. D*, 77:014511, 2008.
- [23] Wei-Tian Deng and Xu-Guang Huang. Vorticity in Heavy-Ion Collisions. *Phys. Rev. C*, 93(6):064907, 2016.

- [24] Xian-Gai Deng, Xu-Guang Huang, Yu-Gang Ma, and Song Zhang. Vorticity in low-energy heavy-ion collisions. *Phys. Rev. C*, 101(6):064908, 2020.
- [25] G. Fricke and K. Heilig. Nuclear charge radii · 79-au gold: Datasheet from landolt-börnstein - group i elementary particles, nuclei and atoms · volume 20: “nuclear charge radii” in springermaterials (https://doi.org/10.1007/10856314_81). Copyright 2004 Springer-Verlag Berlin Heidelberg.
- [26] Fernando G. Gardim, Giuliano Giacalone, Matthew Luzum, and Jean-Yves Ollitrault. Effects of initial state fluctuations on the mean transverse momentum. *Nucl. Phys. A*, 1005:121999, 2021.
- [27] S. Gorbunov. Ph.D. thesis, Johann Wolfgang Goethe University, 2013.
- [28] D. De Gruttola et al. A multigap resistive plate chamber array for the Extreme Energy Events project. *JINST*, 9(10):C10024, 2014.
- [29] Yu Guo, Jinfeng Liao, Enke Wang, Hongxi Xing, and Hui Zhang. Locating the most vortical fluid in nuclear collisions with beam energy scan, 2021.
- [30] Miklos Gyulassy and Xin-Nian Wang. HIJING 1.0: A Monte Carlo program for parton and particle production in high-energy hadronic and nuclear collisions. *Comput. Phys. Commun.*, 83:307, 1994.
- [31] Yu B. Ivanov. Global Λ polarization in moderately relativistic nuclear collisions. *Phys. Rev. C*, 103(3):L031903, 2021.

- [32] Yu B. Ivanov and A. A. Soldatov. Vortex rings in fragmentation regions in heavy-ion collisions at $\sqrt{s_{NN}} = 39$ GeV. *Phys. Rev. C*, 97(4):044915, 2018.
- [33] Yu. B. Ivanov and A. A. Soldatov. Correlation between global polarization, angular momentum, and flow in heavy-ion collisions. *Phys. Rev. C*, 102(2):024916, 2020.
- [34] Yu B. Ivanov, V. D. Toneev, and A. A. Soldatov. Estimates of hyperon polarization in heavy-ion collisions at collision energies $\sqrt{s_{NN}} = 4\text{--}40$ GeV. *Phys. Rev. C*, 100(1):014908, 2019.
- [35] Jiangyong Jia. Event-shape fluctuations and flow correlations in ultra-relativistic heavy-ion collisions. *J. Phys. G*, 41(12):124003, 2014.
- [36] Yin Jiang, Zi-Wei Lin, and Jinfeng Liao. Rotating quark-gluon plasma in relativistic heavy ion collisions. *Phys. Rev. C*, 94(4):044910, 2016. [Erratum: Phys.Rev.C 95, 049904 (2017)].
- [37] I. Karpenko and F. Becattini. Study of Λ polarization in relativistic nuclear collisions at $\sqrt{s_{NN}} = 7.7\text{--}200$ GeV. *Eur. Phys. J.*, C77(4):213, 2017.
- [38] Dmitri E. Kharzeev, Larry D. McLerran, and Harmen J. Warringa. The Effects of topological charge change in heavy ion collisions: 'Event by event P and CP violation'. *Nucl. Phys.*, A803:227–253, 2008.
- [39] Ben Kimelman. 3GeV FXT 2018 New Production QA and Bad Runs. <https://drupal.star.bnl.gov/STAR/system/files/>

\Kimelman_3GeV_run_by_run_QA_badRuns_0.pdf. Presentation to the STAR Bulk Correlations Weekly Meeting, 2020-11-06.

- [40] Roy A. Lacey, Rui Wei, N. N. Ajitanand, and A. Taranenko. Initial eccentricity fluctuations and their relation to higher-order flow harmonics. *Phys. Rev. C*, 83:044902, 2011.
- [41] Zuo-Tang Liang, Jun Song, Isaac Upsal, Qun Wang, and Zhang-Bu Xu. Rapidity dependence of global polarization in heavy ion collisions. *Chin. Phys. C*, 45(1):014102, 2021.
- [42] Zuo-Tang Liang and Xin-Nian Wang. Globally polarized quark-gluon plasma in non-central A+A collisions. *Phys. Rev. Lett.*, 94:102301, 2005. [Erratum: *Phys.Rev.Lett.* 96, 039901 (2006)].
- [43] W. J. Llope et al. The TOFP / pVPD time-of-flight system for STAR. *Nucl. Instrum. Meth. A*, 522:252–273, 2004.
- [44] Matthew Luzum and Hannah Petersen. Initial State Fluctuations and Final State Correlations in Relativistic Heavy-Ion Collisions. *J. Phys. G*, 41:063102, 2014.
- [45] L. Ma, G. L. Ma, and Y. G. Ma. Initial partonic eccentricity fluctuations in a multiphase transport model. *Phys. Rev. C*, 94(4):044915, 2016.
- [46] Niseem Magdy, Xu Sun, Zhenyu Ye, Olga Evdokimov, and Roy Lacey. Investigation of the Elliptic Flow Fluctuations of the Identified Particles Using the a Multi-Phase Transport Model. *Universe*, 6(9):146, 2020.

- [47] L. McLerran and V. Skokov. Comments About the Electromagnetic Field in Heavy-Ion Collisions. *Nucl. Phys. A*, 929:184–190, 2014.
- [48] Kathryn Meehan. The Fixed-Target Experiment at STAR. https://www.bnl.gov/aum2016/content/workshops/Workshop_1b/\meehan.pdf. 2016 RHIC & AGS Users’ Meeting, 2016-06-07.
- [49] L. Montanet et al. Review of particle properties. Particle Data Group. *Phys. Rev. D*, 50:1173–1823, 1994.
- [50] Takafumi Niida. Global and local polarization of Λ hyperons in Au+Au collisions at 200 GeV from STAR. *Nucl. Phys. A*, 982:511–514, 2019.
- [51] M. Olsson, P. de Barbaro, A. Bodek, Howard Scott Budd, P. Koehn, M. Pillai, W. Sakumoto, R. C. Walker, and B. Winer. Techniques for optical isolation and construction of multitile assemblies in scintillator tile - fiber calorimeters using white epoxy, 1995.
- [52] Arthur M. Poskanzer and S. A. Voloshin. Methods for analyzing anisotropic flow in relativistic nuclear collisions. *Phys. Rev. C*, 58:1671–1678, 1998.
- [53] Jing Qian and Ulrich Heinz. Hydrodynamic flow amplitude correlations in event-by-event fluctuating heavy-ion collisions. *Phys. Rev. C*, 94(2):024910, 2016.
- [54] Guang-You Qin, Hannah Petersen, Steffen A. Bass, and Berndt Muller. Translation of collision geometry fluctuations into momentum anisotropies in relativistic heavy-ion collisions. *Phys. Rev. C*, 82:064903, 2010.

- [55] Zhi Qiu and Ulrich Heinz. Hydrodynamic event-plane correlations in Pb+Pb collisions at $\sqrt{s} = 2.76$ ATeV. *Phys. Lett. B*, 717:261–265, 2012.
- [56] Alex Schmah, Rosi Reed, and Michael Lisa. An Event Plane Detector for STAR - Construction Proposal 2016. 2 2020.
- [57] T. M. Schwarz, S. P. Klevansky, and G. Papp. The Phase diagram and bulk thermodynamical quantities in the NJL model at finite temperature and density. *Phys. Rev. C*, 60:055205, 1999.
- [58] V. Skokov, A. Yu. Illarionov, and V. Toneev. Estimate of the magnetic field strength in heavy-ion collisions. *Int. J. Mod. Phys.*, A24:5925–5932, 2009.
- [59] Yifeng Sun and Che Ming Ko. Λ hyperon polarization in relativistic heavy ion collisions from a chiral kinetic approach. *Phys. Rev. C*, 96(2):024906, 2017.
- [60] Zachary Sweger. Fixed Target $\sqrt{s_{NN}} = 3.0$ GeV (2018) Centrality. https://drupal.star.bnl.gov/STAR/system/files/3p0GeV_Standard_0.pdf. Presentation to the STAR Bulk Correlations Weekly Meeting, 2020-11-17.
- [61] O. Vitiuk, L. V. Bravina, and E. E. Zabrodin. Is different Λ and $\bar{\Lambda}$ polarization caused by different spatio-temporal freeze-out picture? *Phys. Lett. B*, 803:135298, 2020.
- [62] Sergei A. Voloshin, Arthur M. Poskanzer, and Raimond Snellings. Collective phenomena in non-central nuclear collisions. *Landolt-Bornstein*, 23:293–333, 2010.

- [63] V. Vovchenko, D. Anchishkin, and L. P. Csernai. Longitudinal fluctuations of the center of mass of the participants in heavy-ion collisions. *Phys. Rev. C*, 88(1):014901, 2013.
- [64] Gang Wang and Liwen Wen. Experimental results on chiral magnetic and vortical effects. *Adv. High Energy Phys.*, 2017:9240170, 2017.
- [65] De-Xian Wei, Wei-Tian Deng, and Xu-Guang Huang. Thermal vorticity and spin polarization in heavy-ion collisions. *Phys. Rev. C*, 99(1):014905, 2019.
- [66] Hong-Zhong Wu, Long-Gang Pang, Xu-Guang Huang, and Qun Wang. Local spin polarization in high energy heavy ion collisions. *Phys. Rev. Research.*, 1:033058, 2019.
- [67] Yilong Xie, Dujuan Wang, and Laszlo Pal Csernai. Fluid dynamics study of the Λ polarization for Au + Au collisions at $\sqrt{s_{NN}} = 200$ GeV. *Eur. Phys. J. C*, 80(1):39, 2020.
- [68] Bin Zhang. ZPC 1.0.1: A Parton cascade for ultrarelativistic heavy ion collisions. *Comput. Phys. Commun.*, 109:193–206, 1998.
- [69] P. A. Zyla et al. Review of Particle Physics. *PTEP*, 2020(8):083C01, 2020.
- [70] P.A. Zyla et al. Review of particle physics. *Prog. Theor. Exp. Phys.*, page 083C01, Aug 2020.
- [71] M. Zyzak. Ph.D. thesis, Johann Wolfgang Goethe University, 2015.